Development of a generic analytical model for optimizing the energy production of a tidal turbine park

Kabir Bashir Shariff

Normandie Université

UNIVERSITÉ CAEN NORMANDIE

THÈSE

Pour obtenir le diplôme de doctorat

Spécialité MECANIQUE DES FLUIDES, ENERGETIQUE, THERMIQUE, COMBUSTION, ACOUSTIQUE

Préparée au sein de l'Université de Caen Normandie

Development of a generic analytical model for optimizing the energy production of a tidal turbine park

Présentée et soutenue par
KABIR BASHIR SHARIFF

Thèse soutenue le 18/10/2023 devant le jury composé de		
M. GUILLAUME BALARAC	Professeur des universités, Ecole Nationale Supérieure de l'Energie, l'Eau et l'Environnement de Grenoble	Rapporteur du jury
MME ANNIE-CLAUDE BAYEUL-LAINÉ	Maître de conférences HDR, ENSAM CER LILLE	Rapporteur du jury
M. PIERRE-LUC DELAFIN	Maître de conférences, Ecole Nationale Supérieure de l'Energie, l'Eau et l'Environnement de Grenoble	Membre du jury
M. ABDELLATIF OUAHSINE	Professeur des universités, UNIV TECHNOLOGIE COMPIEGNE UTC COMPIEGNE	Président du jury
M. SYLVAIN GUILLOU	Professeur des universités, Université de Caen Normandie	Directeur de thèse

Thèse dirigée par SYLVAIN GUILLOU (Laboratoire universitaire des sciences appliquées de cherbourg (Caen))

ED 591 PSIME

LUSAC

This thesis was carried out at the Laboratoire Universitaire des Sciences Appliquées de Cherbourg.

I would like to show my gratitude and sincere appreciation to the Région Normandie and the Communauté d'Agglomération du Cotentin for financing my thesis.

Calculations were performed on the Myria server of the Centre Regional Informatique et d'Applications d'Applications Numeriques de Normandie (CRIANN).

to my parents;
Bashir Abba Shariff & Zakiyya Bashir Abba
to my siblings,
and to my Noury, Fatima

Acknowledgements

First of all, I would like to show my sincere appreciation to my thesis reporters M. Guillaume Balarac and Mme. Annie-Claude Bayeul-Laine for assessing my work. I would also like to thank M.Abdellatif Ouahsine and M. Pierre-Luc Delafin for accepting to serve as a jury in my thesis defense. A special vote of thanks to my CSI members M. Philippe Gleizon and M. Pierre-Luc Delafin. Moreover, M. Pierre-Luc Delafin who not only serves as a jury member of my thesis defense and also a CSI member along with M. Philippe Gleizon during my thesis. He was my professor and school supervisor during my master's dissertation at Grenoble INP.

I would like to express my sincere gratitude to Région Normandie and the Communauté du Agglomération du Cotentin for their generous funding and unwavering belief in the importance of this research. Without their financial backing, this thesis would not have been possible. Their investment in my education and academic pursuits has been instrumental in bringing this project to fruition. Thank you for your invaluable contribution to my academic journey. I would also like to acknowledge the support of the TIGER project for your invaluable contribution.

To my thesis director, M. Sylvain Guillou, I want to take this moment to express my most profound appreciation for your generous support throughout my thesis journey. I would like to thank you again for giving me access, time, and support during my PhD studentship at LUSAC. Your support has not only helped me achieve my academic goal but also strengthened my passion for the subject matter. In addition, I would also like to thank Mrs. Fredrique Guillou for your generosity and for hosting us in your compound on several occasions.

To my LUSAC colleagues, a special thanks to all the staff and colleagues in LUSAC. I thank you for your support during my thesis. A special thanks to Alina, Philippe, Haiyen, Jerome and Mikaël, and Adeline. I would also like to thank my friends and colleagues Chaker, Israa, Morgane, Laurie, Anju, Fatiha, and Kim. A special thanks to my dear friend Hamza. I wish you all a successful Ph.D. journey ahead.

I want to express my heartfelt gratitude to my loving parents Abba and Mama, for your unwavering support, encouragement and love throughout my academic journey. Your constant belief in me and your sacrifices have been instrumental in enabling me to reach this milestone. *Iyayena*, your prayers, guidance, and wisdom have shaped my academic pursuits and my character. Your sacrifices, both big

and small, have taught me the true value of determination and hard work. Your unconditional love has been my constant source of strength, motivating me to overcome challenges and strive for excellence.

To my siblings; Samira, Ummi, Surayya, Hafsa, Aisha, Khalil, Muhammad, Amir, and Al-ameen. You are my companions on this road of growth and learning – thank you for your unwavering support, your belief in me, and the bond we share. This thesis is a personal achievement and a testament to the collaborative spirit and encouragement you've provided. I want to thank you for celebrating my successes and standing by me during challenges. Your unwavering faith in my abilities has fueled my determination to excel.

My *Noury*, the love of my life, thank you for tolerating the missed calls, late calls, and even sometimes no calls. You are always in my mind throughout this journey. Fatima, thank you for your love, your unwavering support, and for being my constant inspiration. This thesis is not only a testament to my dedication but also a tribute to the love and encouragement you've showered upon me.

Lastly, I will also like to thank the Petroleum Technology Development Fund (PTDF) Nigeria for sponsoring my master's program in France in the first place. This Ph.D. is a testimony of the achievement as a return on investment. I remain grateful.

With appreciation and gratitude,
Nagode,

Kabir Shariff

Contents

List of Figures

List of Tables

Nomenclature

Acronyms

ADCP Acoustic Doppler Current Profiler

ADM Actuator Disk Method

ADM Actuator Disk Model

ADV Acoustic Doppler Velocimeter

AI Artificial Intelligence

ALM Actuator Line Model

AWAC Acoustic Wave and Current Profiler

BC Boundary condition

BEM Blade Element Model

BP Bastankhah and Porté-Agel

CFD Computational Fluid Dynamics

CPD Cell Per Diameter

ECM Electromagnetic Current Meter

FVM Finite volume method

FWHM Full-Width Half Maximum

HAT Horizontal-Axis Turbine

IEA International Energy Agency

IRENA International Renewable Energy Agency

LBM Lattice Botlzmann Method

LCOE Levelized cost of energy

LDV Laser Doppler Velocimetry

LES Large Eddy Simulation

LUSAC Laboratoire universitaire des sciences appliquées de Cherbourg

MAPE Mean Absolute Percentage Error

MRE Marine Renewable Energy

NSE Navier Stokes Equation

OEE Ocean Energy Europe

RANS Reynolds Average Navier Stokes

SSH Sea surface height

TI Turbulence intensity

TRL Technology Readiness Level

TST Tidal Stream Turbine

VAT Vertical-Axis Turbine

Greek Symbols

β	Turning parameter	
$\delta(z)$	Wake deflection coefficient	
ϵ	Turbulence dissipation	m^2/s^3
η_{farm}	Farm efficiency	
κ	Turbulent kinetic energy	$m^2 \cdot s^{-2}$
ν	Fluid viscosity	$Pa \cdot s$
ϕ	Wake correction coefficient	
ρ	Fluid density	kg/m^3
σ	Standard deviation	
θ_r	Rotor intersection angle	
θ_w	Wake intersection angle	
C_μ	$\kappa - \epsilon$ constant	

Roman Symbols

a	Axial induction factor	
A, A_∞	Rotor cross-sectional area	m^2
$a, b, c, ...$	Empirical parameters	
$A_{overlap}$	Overlap area	m^2
C_P	Power coefficient	
C_T	Thrust coefficient	
I_+	Added turbulence	
I_0	Ambient turbulence	
I_{eff}	Effective turbulence	
I_{wake}	Turbulence intensity in turbine wake	
P_{farm}	Total power in turbine farm	MW
r_0	Rotor radius	m
r_w	Wake radius	m
S_x	Axial turbine spacing	
S_y	Lateral turbine spacing	
U^*	Friction velocity	m/s
U_∞	Upstream velocity	m/s
U_D	Disk velocity	m/s
U_w	Wake velocity	m/s
z_0	Roughness height	
$\mathbf{T}$	Thrust force	N
D	Turbine diameter	m
DH	Diameter-to-depth	
H	Channel depth	m
K	Resistance coefficient	

P	Turbine power	MW

Other Symbols

$\bigtriangledown$	Gradient
$\bigtriangledown\cdot$	Divergence
ΔP	Pressure difference
$\overline{u}$	Mean velocity component
a^*	non-dimensional parameter
u'	Fluctuating velocity

Chapter 1

Introduction and Background

Contents

1.1 On the need for Energy

Global electricity production was 26,936 TWh in 2019 IEA (2022), which, with a world population of 7.67 billion, translates as an annual power output of 3.5 MWh per capita. Electricity generation has doubled since 1990 when global production was 11,854 TWh, representing an annual power output of 2.3 MWh per capita. With the increased demand, the use of conventional fossil fuel has significantly increased the CO_2 emission and other harmful pollutants contributing to global warming. Today, almost two-thirds of global electricity comes from fossil fuels. Among these about 36% of world electricity is generated by coal, contributing the highest global CO_2 emission. One-third of global electricity comes from low-carbon sources comprising renewables and nuclear power.

Renewable energy is defined as energy from resources that can be replenished at the same rate that they are used. Solar energy is a prime example of renewable energy resources. Most other renewable energies, such as biomass, wind, hydro, tidal, and wave would directly or indirectly be coming from or influenced by solar energy. Renewable energy plays a crucial role in clean energy transitions and deploying renewable power is one of the main enablers of keeping the rise in average global temperatures below 1.5^oC. Figure 1.1 shows in 2022, renewable sources generated 29.9% of global electricity which increased by almost 9% in the past decade (REN21, 2022). The need for renewable energy has become increasingly important as we continue to grow as a society and rely more on technology. Renewable energy sources are sustainable and have a lower impact on the environment compared to non-renewable sources such as coal and oil.

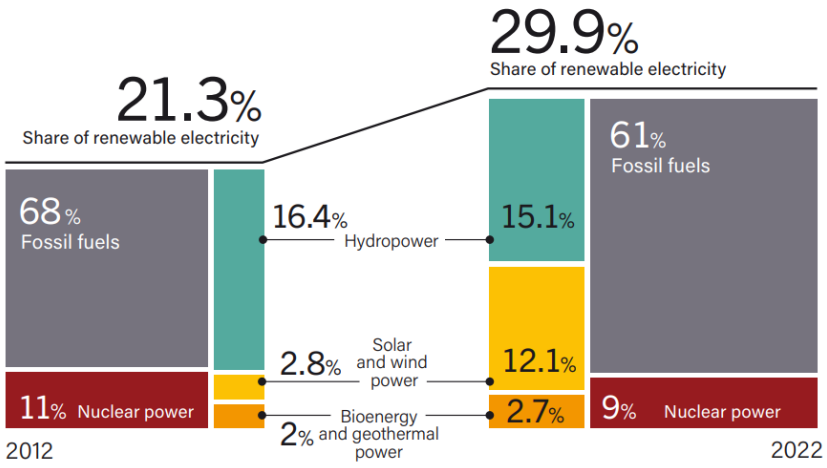

Figure 1.1 Share of Renewable Electricity Generation, by Energy Source, 2012 and 2022. (Source: REN21 (2022) Global status report).

1.2 Why Marine Renewable Energy?

The ocean is vast, covering 363 million square kilometers, equivalent to approximately 72 percent of the earth's surface. With nearly 2.4 billion people or 37% of the global population, living within 100 kilometers of the coast (UN, 2017), ocean energy presents a convenient solution to tackle climate change while contributing to a more sustainable future. For nations with coastal and ocean territories, the development and exploitation of marine renewable energy provide an attractive potential contribution to the targeted renewable energy mix.

Ocean energy, also called Marine Renewable Energy (MRE) or blue energy technologies, exploits the ocean's power to produce electricity. Figure 1.2 presents different forms of MRE including kinetic energy (offshore winds and currents), potential energy (tidal amplitude), mechanical energy (waves), and thermal potential (vertical temperature gradients). MREs are an alternative to conventional fossil fuels and their resources depend on the characteristics of the local marine environment; wind, waves, tides, currents, temperature, etc.

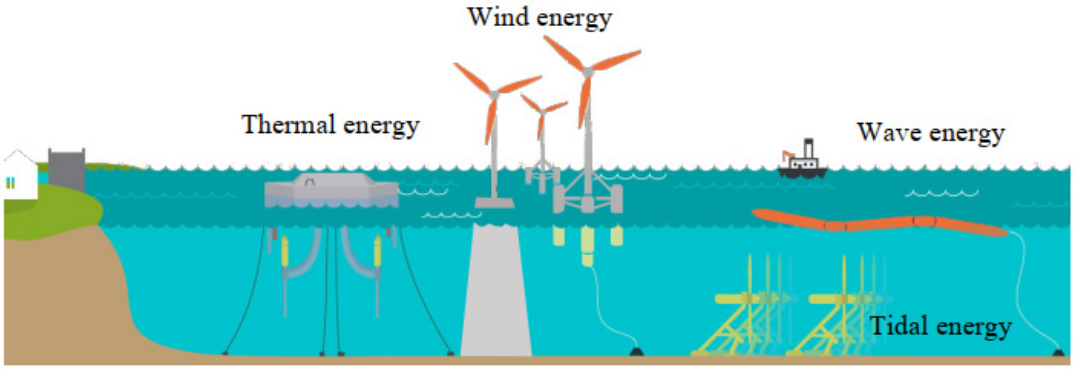

Figure 1.2 Diagram showing the types of Marine Renewable Energy (MRE) technologies. (Courtesy: Taormina (2019)).

The theoretical potential for all ocean energy technologies combined ranges from 45,000 Terawatt-hours (TWh) to well above 130,000 TWh per year (IRENA, 2020). Currently, most ocean energy technologies have not reached commercialization. They are still in the developmental stages, with the majority of technologies being in the prototype phase except for some reaching early commercialization. However, the past decade has seen noticeable progress in wave and tidal energy. According to IRENA (2020) reports, the cumulative installed capacity across all ocean technology is 537.4 MW, with a large proportion of it being tidal barrage (see Figure 1.3). Tidal energy is presently one of the favored forms of marine renewable energy because, due to its origins in (astronomical) tide-generating forces, it is predictable.

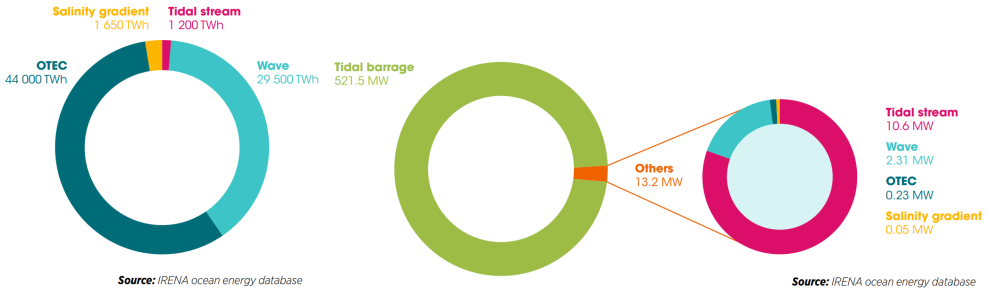

(a) Resource potential (TWh/yr)

(b) Current deployment (MW)

Figure 1.3 Global ocean energy resource potential and deployment. (Source: IRENA 2020).

1.3 Tidal energy

A tide is a natural phenomenon that is caused by the gravitational pull of the moon and the sun and the rotation of the Earth on its axis. Tides originate in the oceans and progress toward the coastlines where they appear as the regular rise and fall of the sea surface. These tides last for about 12 hours and 25 minutes for semi-diurnal tide. Spring tides are those variations observed during the full moon and new moon as the earth, sun, and moon line up as illustrated in Figure 1.4. If the earth-moon and the earth-sun relationship are at right angles, the gravitational forces are subtractive, causing neap tides that are subdued or low. Tidal currents are turbulent and complex in nature (Hardisty, 2012). It accelerates, decelerates, and reverse over varying depth in each tidal cycle. Tidal energy converts the energy obtained from tides into a valuable form of power, mainly electricity.

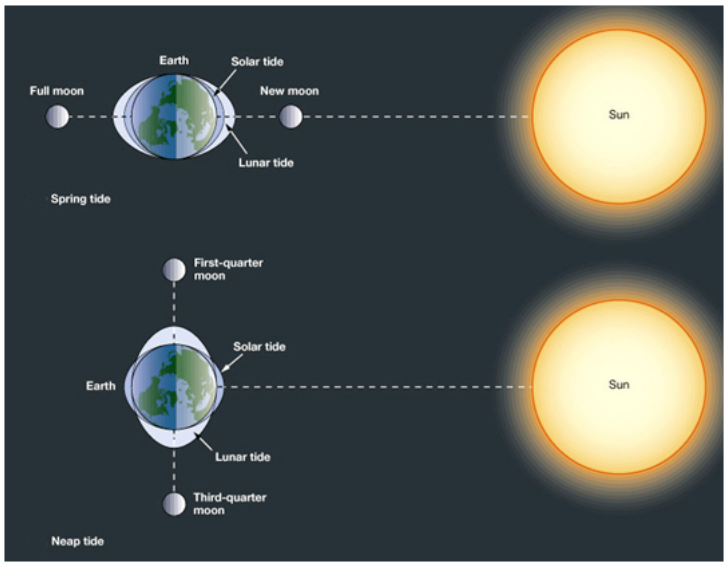

Figure 1.4 Relative positions of the sun, moon, and Earth during spring and neap tides - Pearson Prentice Hall, Inc.

The estimation of global tidal power varies but is wildly acceptable to exceed 100 GW (Figure 1.5), capable of generating 800 - 1200 TWh (IRENA, 2020). Tidal energy is categorized into two types; tidal barrage and tidal stream energy are described hereafter.

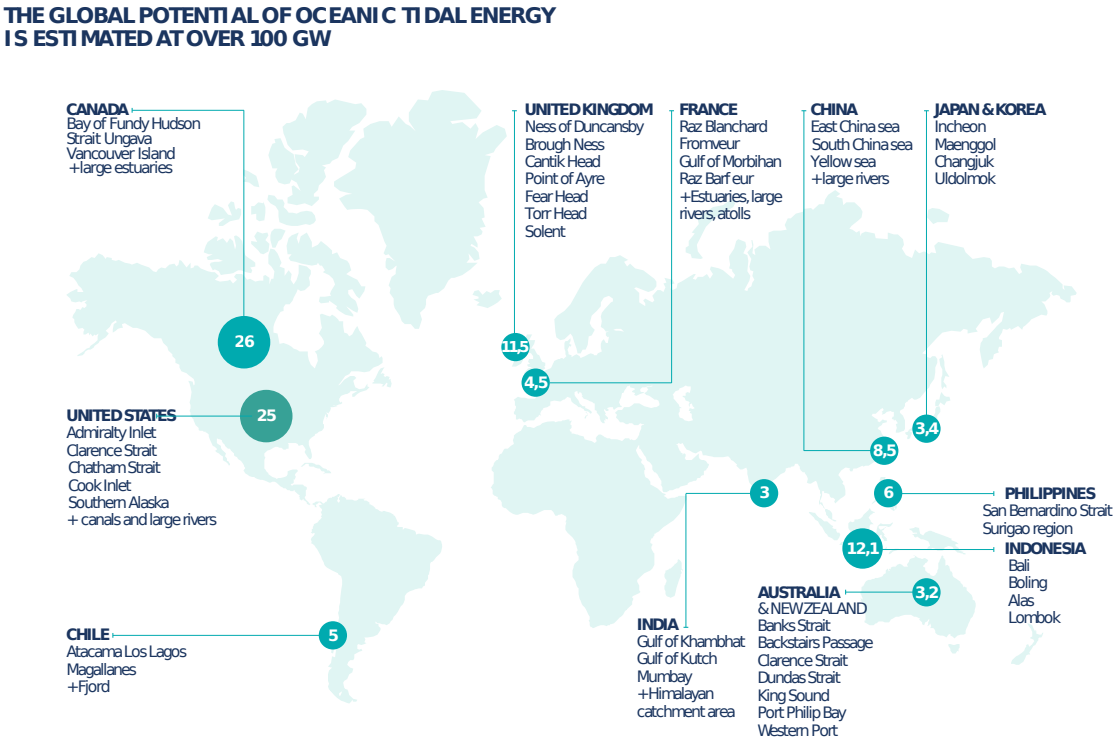

Figure 1.5 Global location of tidal energy resources (Source: Observatoire des énergies de la mer).

1.4 Tidal barrage energy

Tidal barrages and lagoons function by creating a reservoir of water behind a barrier to capture the rise and fall of the tides. Tidal barrage systems work similarly to hydropower and have sluices that control the tidal flow to drive turbines and generate electricity. Water enters an enclosed tidal basin at high tide and is released at low tide to generate electricity by passing through turbines as shown in Figure 1.6. The highest tidal range in the world is 16 m amplitude located at the Bay of Fundy in Canada (Capareda, 2019) followed by Mount Saint Michel Bay in France with amplitude reaching up to 15 m (Billeaud et al., 2009). Common tidal ranges are around 5 m in most areas while other locations with higher tidal ranges are located on the coast of Argentina, north-western Australia, Brazil, France, India, the UK, and the USA. Most of these locations with high tidal ranges are situated in unfavorable sites difficult to access and usually far from the coastline.

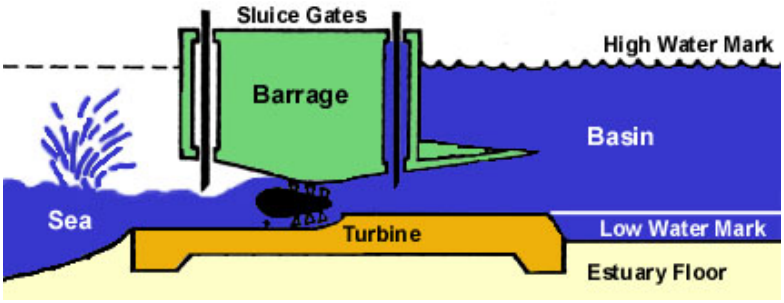

Figure 1.6 Illustration of tidal barrage energy. Adapted from Shetty and Priyam (2022).

Today, the tidal range dominates the total cumulative global installed capacity for ocean energy technologies. The tidal range has about 98% share of global installed capacity at present (IRENA, 2020), thanks to the two large installations: the 240 MW La Rance tidal plant deployed in France in 1966, and the 254 MW Shiwa plant deployed in the Republic of Korea in 2011. This leads the barrage system to reach Technology Readiness Level (TRL) 9. TRL 9 signifies economic validation where several commercial units are tested at sea for an extended period.

1.4.1 Tidal barrage energy in France

The world-first commercial tidal power plant, the La Rance plant was built in 1966 on the estuary of La Rance in France. It has 24 units of 10 MW bulb turbine generating around 500 GWh/year of electricity. The La Rance plant, shown in Figure 1.7 operates in two different modes; the ebb operation or flood and ebb operation.

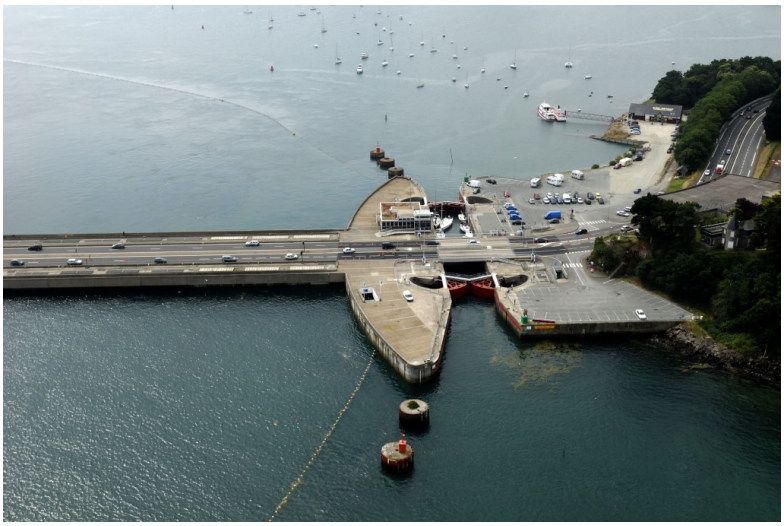

Figure 1.7 La Rance tidal power plant (Photo Credit: EDF).

1.5 Tidal stream energy

In contrast to tidal ranges, tidal stream turbines (TSTs) use the kinetic energy of the tide directly to harness energy. TSTs allow water to pass through and around them and do not require the storage of water. Therefore the local tide velocity, turbulence, bathymetry, depth, seabed mounting, and local shipping regulations are concerns associated with marine fishes and mammals and are some key issues facing the development of tidal stream devices.

1.5.1 Tidal stream energy technologies

Today, tidal stream energy with its considerable potential and predictability is still in the pre-commercialization phase of development. Tidal stream energy has traditionally suffered from relatively high costs and limited availability of sites with sufficiently high flow velocities and relatively high ambient turbulence, thereby hindering its availability. The maturity level of technology is determined using the Technology Readiness Level (TRL) defined in Table 1.1. Technologies to harness tidal energy with different TRLs shown in Figure 1.8 are briefly discussed hereafter.

- **Horizontal-Axis Turbine:** HATs are devices with a rotational axis parallel to the tidal flow. The tidal stream causes the rotors to rotate around the horizontal axis and generate power. Depending on the number of blades and the pitch mechanism, there are several types of HAT. The HAT is the most widely used due to its high efficiency and improved technology. HAT is currently at TRL 8 with several full-scale turbines tested at demonstration sites.

- **Vertical-Axis Turbine:** VATs devices have a rotational axis perpendicular to the tidal flow direction. VAT can operate regardless of the tidal flow direction and does not require a pitch or yaw mechanism to rotate the blades. It generates less noise and is suitable for low current flow (Greaves and Iglesias, 2018). VAT has recently reached TRL 6 with the 1 MW prototype of HYDROQUEST tested for 2 years at sea in Paimpol-Bréhat in France.

- **Venturi Effect Devices:** These devices are funnel-like duct that concentrates the flow through the device and increase the stream velocity. The flow of water can drive a turbine directly or the induced pressure differential in the system can drive the turbine.

- **Oscillating hydrofoils:** These devices use an oscillating motion rather than a rotary motion and can consist of a hydrofoil that is mounted on a pivot arm. The tidal current flowing on either side of a wing results in a lift. This motion then drives fluid in a hydraulic system to be converted into electricity.

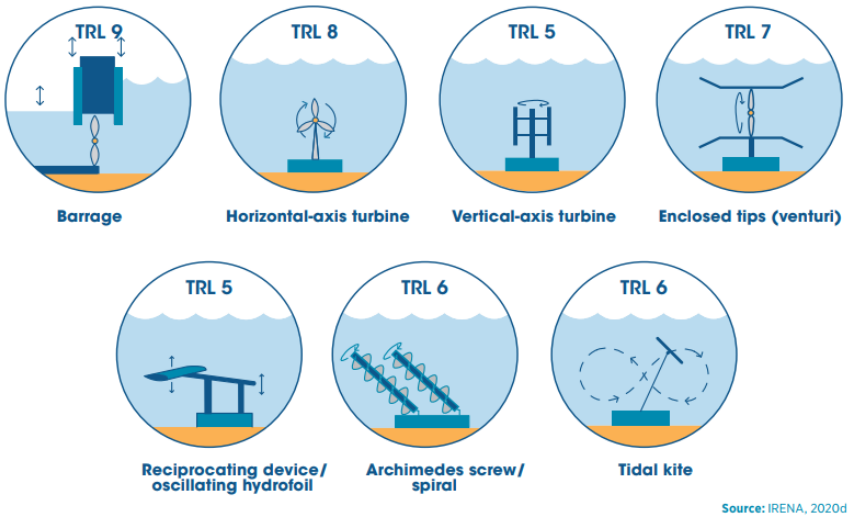

Figure 1.8 Different tidal energy technologies. (Source: IRENA, 2020).

- **Archimedes' screw:** The Archimedes screw is a helical corkscrew-shaped device (a helical surface surrounding a central cylindrical shaft). The device draws power from the tidal stream as the water moves up/through the spiral turning the turbines.

- **Tidal Kite:** A tidal kite is tethered to the sea bed and carries a turbine below the wing. The kite 'flies' in the tidal stream, swooping in a figure-of-eight shape to increase the speed of the water flowing through the turbine.

Table 1.1 Technology Readiness Level definition in tidal steam energy.

Task	**Tidal current development protocol**	
TRL 1-3	Tidal-current energy conversion concept formulated	Stage 1
TRL 4	Intermediate scale subsystem testing, Computational Fluid Dynamics, Finite Element Analysis, Dynamic Analysis	Stage 2
TRL 5-6	Subsystem testing at large scale	Stage 3
TRL 7-8	Full-scale prototype tested at sea	Stage 4
TRL 9	Commercial demonstrator tested at sea for an extended period.	Stage 5

1.5.2 Tidal stream resource characterization

Investigating the harsh marine environment is complex and expensive, with risks including turbulence, overload due to excessive waves, bathymetry, salt-induced corrosion, and algae growth (Tasiopoulos and Feketovà, 2021). An illustration of a tidal turbine in a marine environment is presented in Figure 1.9. The failure of the first-generation tidal energy converter among others is attributed to a poor understanding of turbulence-induced loading (Walker and Thies, 2021). In recent years, researchers have developed a methodology to characterize the tidal flow principally using Doppler devices. These instruments such as the Acoustic Doppler Current Profiler (ADCP) with divergent beams or the Acoustic Doppler Velocimeter (ADV) measure the instantaneous velocity, the Reynolds stresses, the turbulence kinetic energy, and the integral length scale.

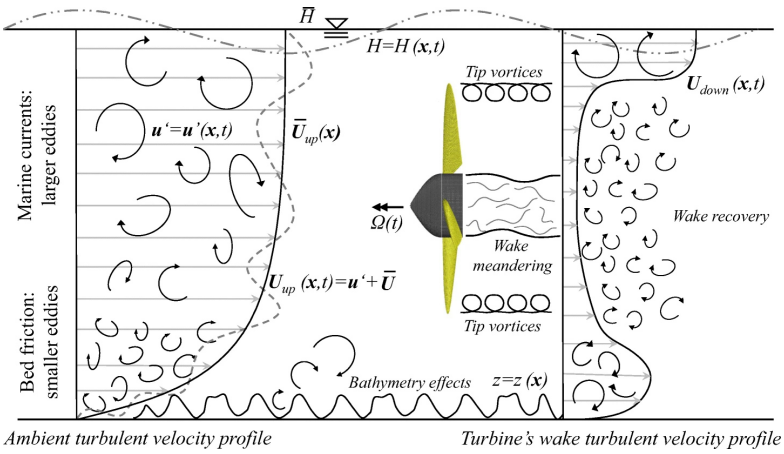

Figure 1.9 Sketch of the harsh environmental conditions faced by tidal turbines. (Source: Ouro and Stoesser (2019)).

Understanding hydrodynamics is vital to both researchers and developers. Although the mean flow characteristics of tidal energy sites are relatively well understood and easily measured, concern about turbulence characteristics is causing reluctance on the part of investors due to the perceived risk of device failure (Walker and Thies, 2021). The field measurements at tidal sites presented in Table 1.2 do not provide the global conditions in these sites due to depth variation and bathymetric effects, but rather a local measurement at a point of interest. The average tidal current and turbulent intensity (TI) in these sites ranges from 1.5 - 3.5 m/s and falls into sub-classes B ($10\% < \text{TI} < 15\%$) and C ($\text{TI} < 10\%$) of the marine energy classification system (Neary, 2019). For instance, mean time series data measured using ADCP at Alderney Race by Thiébaut et al. (2020) is shown in Figure 1.10. The observation data shows a variation of hydrodynamics data with the tidal cycles. A mean hydrodynamics metric of different tidal sites around the world is presented in Table 1.2.

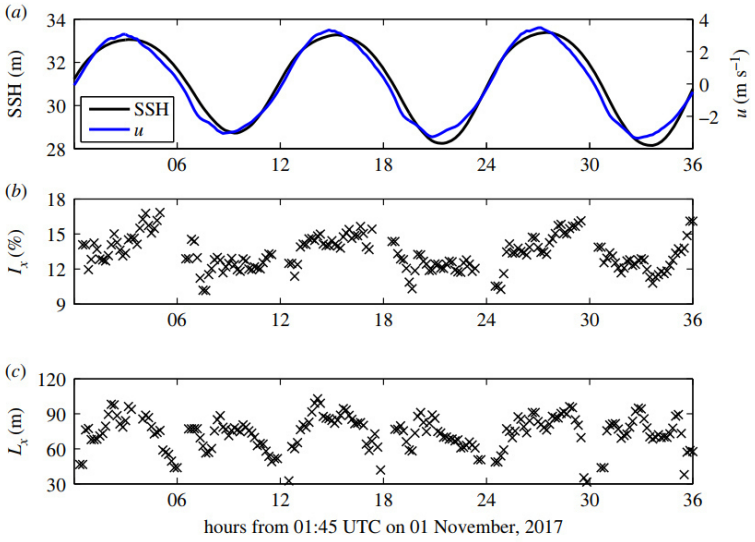

Figure 1.10 Time series of the (a) sea surface height (SSH) and velocity, (b) turbulence intensity, (c) and integral length scale, associated with the streamwise direction, at 12 m height in the Alderney Race. Source: Thiébaut et al. (2020).

Table 1.2 Mean field observation metrics of tidal channel sites around the world.

Location	*Method*	$U(m/s)$	$TI_x(\%)$	$H(m)$	*Reference*
Alderney Race, France	ADCP	1.5 - 4.0	8 - 14	35	Thiébaut et al. (2020)
East River, NY	ADCP	1.5 - 2.3	16 - 24	9.2	Li et al. (2010)
Puget Sound, USA	AWAC	2.0 - 3.2	8 - 11	56	Thomson et al. (2012)
Sound of Islay, UK	ADV	2.0 - 2.5	11 - 13	55	Milne et al. (2013)
Strangford Lough, UK	ECM	1.5 - 3.5	4 - 9	24	MacEnri et al. (2013)
EMEC Orkney, UK	ADCP	1.9 - 3.0	11 - 16	43	Sellar et al. (2018)
Uldolmok Strait, Korea	ADCP	2.0 - 2.7	10 - 18	20	Li et al. (2014)
Cook Inlet, USA	ADCP	2.0	14	34	Wang and Yang (2020)
Fromveur Strait, France	ADCP	1.5 - 2.0	-	53	El Tawil et al. (2019)
Menai Strait, Wales	ADCP	2.5	-	46	Togneri et al. (2017)
Sea Scheldt, Belgium	ADCP	0.8 - 1.4	4 - 5	10	Sentchev et al. (2020)
Jiaozhou Bay, China	ADCP	2.0	-	60	Liu et al. (2021)
Zhoushan, China	ADCP	2.0	-	60	Liu et al. (2021)
Bank Strait, Australia	ADCP	1.2 - 2.2	10 - 16	60	Perez et al. (2021)
Clarence Strait, Australia	ADCP	1.4 - 2.5	10 - 20	40	Perez et al. (2021)
Ramsey Sound, UK	ADCP	1.2 - 3.0	8 - 16	40	Togneri and Masters (2016)
Yarmouth Habour, UK	ADCP	2.0	-	25	Sentchev and Thiébaut (2015)
Dover Strait, UK	ADCP	1.0 - 1.5	-	25	Thiébaut and Sentchev (2016)
Morbihan Gulf, France	ADCP	2.5	-	28	Sedrati et al. (2015)
Race Rock, Canada	ADCP	3.0	-	22	Bhuyan and Darou (2007)
Paimpol-Bréhat, France	ADCP	1.0 - 3.0	-	30	Mercier and Guillou (2022)

1.5.3 Tidal stream energy in France

Campbell et al. (2017) identified 20 potential sites for the extraction of tidal stream energy along the French coast. The estimated power of sites with an average current exceeding 1.5 m/s ranges from 1.46 to 9.78 GW for pessimistic and optimistic cases respectively. Figure 1.11 shows potential sites in France including the Alderney Race (Raz Blanchard), the Barfleur race in Cherbourg Peninsula, the Fromveur race, Paimpol-Bréhat, the Gironde near Bordeaux, and Morbihan. The Alderney Race is one of the promising sites with the highest kinetic tidal power density in France with a local tidal range exceeding 6 m and a peak spring current reaching up to 5 m/s and a maximum potential exceeding 5 GW (Coles et al., 2017). This site has become attractive for research on tidal power farms that will contribute to the energy mix in France.

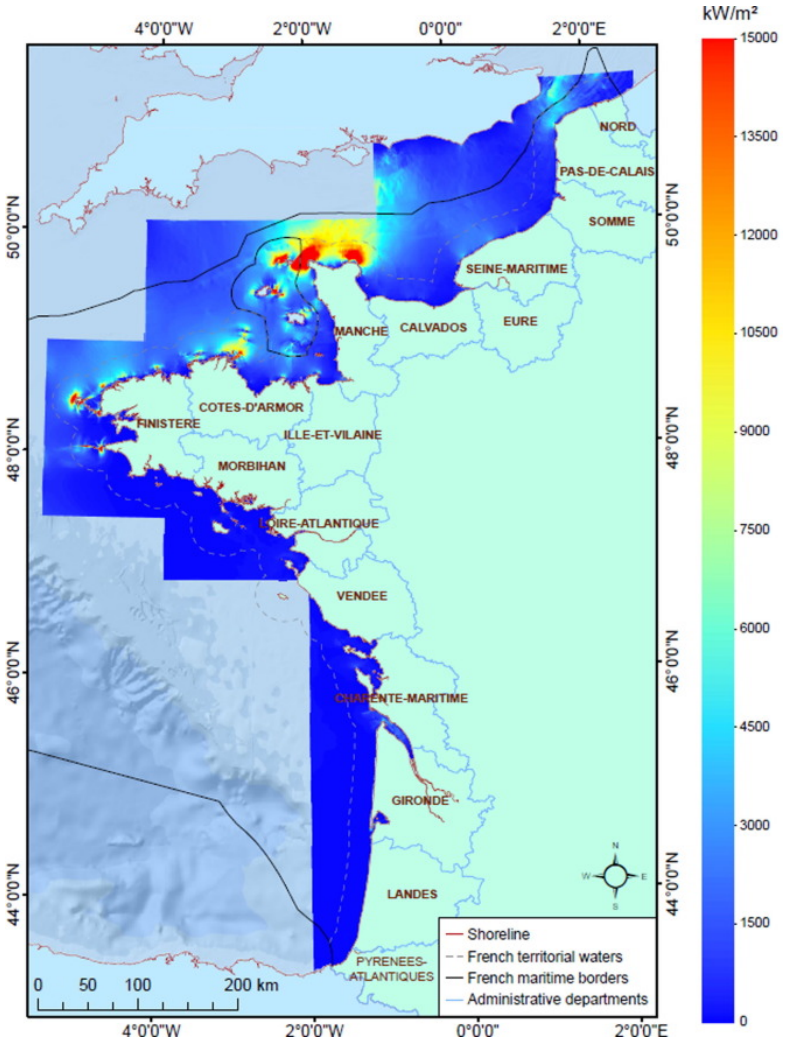

Figure 1.11 Tidal stream energy (kW/m^2) distribution along the French coasts. Adapted from Campbell et al. (2017).

1.6 Tidal stream turbine (TST)

Over the last decade, the tidal energy industry has recorded successful deployment and testing of full-scale TST at dedicated test sites and commercial project locations with units rating up to 1 MW (see Figure 1.12). In 2021, Ocean Energy Europe (OEE) reported the global cumulative installation of TST at 39.6 MW with 11.5 MW active in the water. Several technologies have been proposed to harness tidal energy as outlined in Section §1.5.1. However, the most promising technology so far is the HAT.

A study by Magagna and Uihlein (2015) shows 76% of research and development (R&D) of TST is dedicated to the HAT. Considerable studies that focus on the turbine performance (Jeffcoate et al., 2015), fluid-structure interaction (Ullah et al., 2019; Brousseau et al., 2021), and also interaction effects in array (Bai et al., 2013; Vennell and Adcock, 2014; Thiébot et al., 2015, 2020) has been conducted to improve the efficiency of HAT. The industrial preference for HAT results from the matured technology of wind turbines, economics, and high efficiency. As presented in Figure 1.13, the TST is seeing a convergence in technology with 13 of the 16 active devices dedicated to horizontal axis turbines.

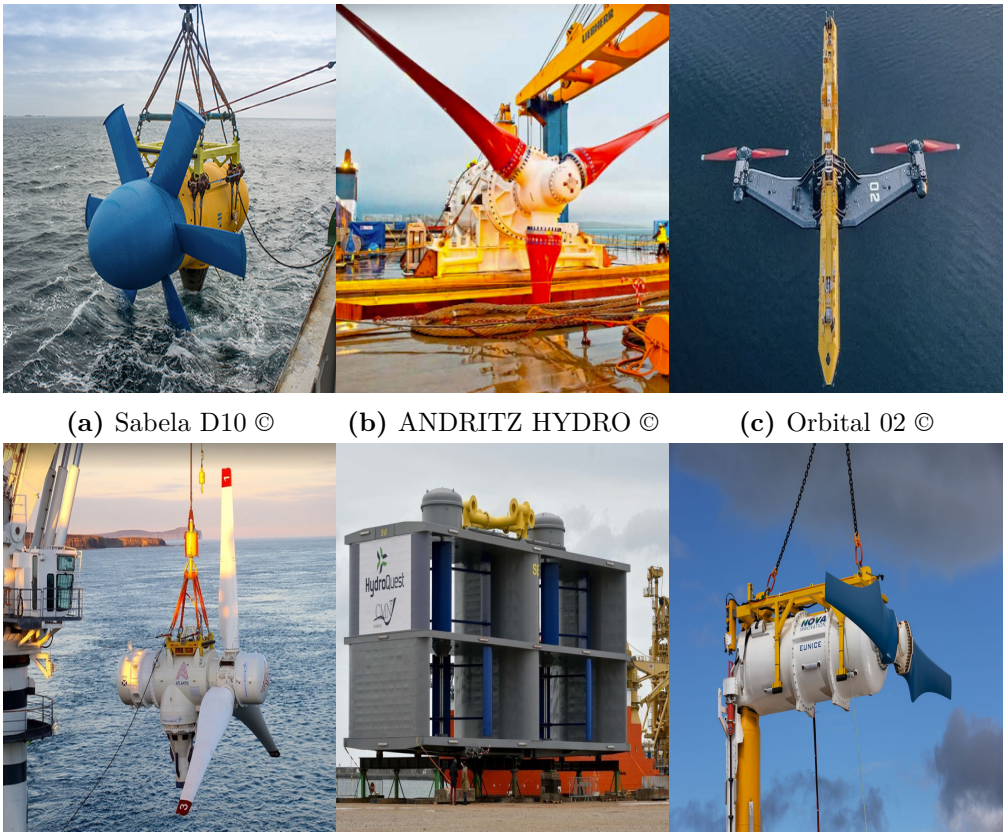

(a) Sabela D10 © **(b)** ANDRITZ HYDRO © **(c)** Orbital 02 ©

(d) Atlantis © **(e)** HydroQuest © **(f)** Nova Innovations ©

Figure 1.12 Examples of tidal stream turbine technologies.

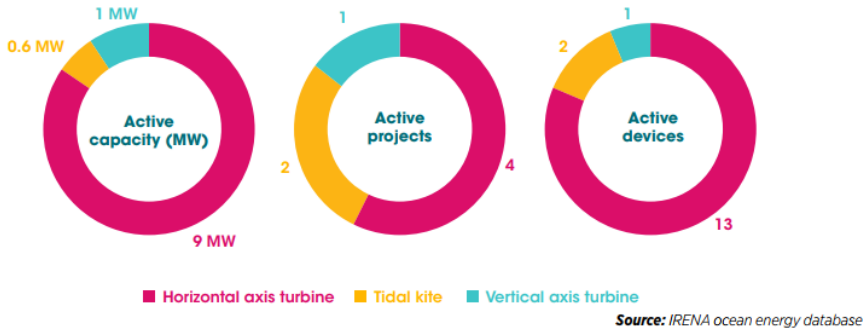

Figure 1.13 Active tidal stream by technology. (Source: IRENA, 2021).

However, for commercial-scale energy production, TSTs are expected to be arranged in a cluster network to generate electricity. This is due to the spatial power density of renewable energy including tidal current. TST is steadily moving towards commercialization with several pilot farms in the pipeline. Recently, the Normandie Région in France has consented to the development of two pilot farm projects in the Alderney Race; the 11 MW Normandie Hydrolienne and the 17.5 MW Flowatt project (Moon, 2022). A cluster network of turbine arrays can reduce costs by sharing infrastructure, and collective maintenance, reducing the learning rates, and ultimately minimizing the Levelized cost of energy (LCOE). However, turbine interaction in the park affects the turbine performance in the form of the wake (Djama Dirieh et al., 2022).

1.7 Turbine wake

The study of the tidal turbine in an array of cluster turbines has recently gained a lot of interest in research and industrial applications. This development is due to the availability of high energy density that can be harnessed to generate electricity production in tidal turbine clusters. The study of wake interaction is of paramount importance to optimize the energy extracted in a tidal turbine cluster. Wake is defined as a region of a disturbed flow behind the turbine that affects the power production of the downstream turbine. Wake is a topic of interest in research in wind and tidal farms because it affects the performance of the downstream turbine which operates in the wake of the upstream turbine. The two main characteristics of wake are listed. The first is a significant **velocity deficit** that reduced the power extracted by the downstream turbine. This power reduction in a wind park can be quite significant reaching as high as 20% (Chamorro and Porté-Agel, 2009). The second is the **increased turbulence** that induced a fatigue loading on the turbine blade which can seriously affect the life span of the turbine blade. It is therefore imperative to study the wake interaction in order to optimize the power production in a park.

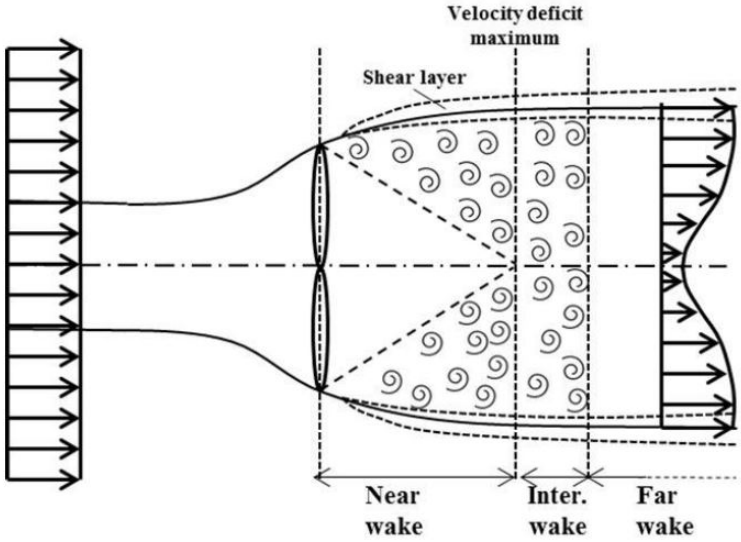

Figure 1.14 Wake behind a tidal turbine. (Source: Lo Brutto (2016)).

The wake behind a turbine can be categorized into three regions (Vermeer et al., 2003). These regions are the near, the intermediate, and the far wake. The characteristic feature of the wake defines the limit of each region.

1. **Near wake:** The flow in this region is dominated by the relaxation of axial and radial pressure gradients caused by the extraction of kinetic energy from the main flow. The minimum centreline velocity is reached at one to two diameters downstream (Crespo and Hernandez, 1996). Tip vortices generated by the turbine rotor amplify the turbulence in this region. A developed shear layer also contributes to the turbulence in the near wake region. As fluid progresses downstream, this shear layer becomes thicker, extending outwards into free-stream and inwards towards the centreline while simultaneously decreasing in strength (Ebdon et al., 2021). The location 4D downstream of the turbine marks the end of the near wake region. Research in this region is mainly focused on the performance of a turbine rather than the interaction between adjacent turbines. The length of the near wake is an important parameter in developing the empirical relation of turbulence. A method for calculating the near wake distance x_n is proposed by Vermeulen (1980) as Eq. (1.1):

$$x_n = \frac{\sqrt{(0.214 + 0.1443)}\left(1 - \sqrt{(0.134 + 0.124m)}\right)}{\left(1 - \sqrt{(0.214 + 0.144m)}\right)\sqrt{(0.134 + 0.124m)}} \frac{r_0}{(dr/dx)}, \tag{1.1}$$

where dr/dx is the growth rate by the contribution of ambient, shear, and turbine generated turbulence defined in Eq. (1.2), m and r_0 are parameters

given as:

$$\frac{\mathrm{dr}}{\mathrm{dx}} = \sqrt{\left(\left(\frac{\mathrm{dr}}{\mathrm{dx}}\right)_{\mathrm{a}}^{2} + \left(\frac{\mathrm{dr}}{\mathrm{dx}}\right)_{\mathrm{s}}^{2} + \left(\frac{\mathrm{dr}}{\mathrm{dx}}\right)_{\mathrm{t}}^{2}\right)}$$
$$(\mathrm{dr/dx})_{\mathrm{a}} = 2.5\mathrm{l_a} + 0.005, \qquad (\mathrm{dr/dx})_{\mathrm{s}} = \frac{(1-\mathrm{m})\sqrt{1.49+\mathrm{m}}}{9.76(1+\mathrm{m})}, \qquad (\mathrm{dr/dx})_{\mathrm{t}} = 0.012\ \mathrm{B}\lambda$$
$$m = \frac{1}{\sqrt{1-C_T}}, \qquad r_0 = R\sqrt{\frac{m+1}{2}} \tag{1.2}$$

2. **Intermediate wake:** This region is characterized by the dissipation of blade-generated vortices. It is a transition zone between near and far wake that extends to 6D. The physics of this region is not very well understood and hence remains an area of active research.

3. **Far wake:** Beyond 7D, the shape of mean velocity and turbulence remains constant with increasing downstream distance. The characteristics of the wake are self-similar in the far wake region. The wake has a weak memory of the turbine-generated turbulence and its decay is largely controlled by ambient turbulence. Table 1.3 shows the distribution of turbulence behind the turbine.

Table 1.3 Turbulence in the wake of TST (Vermeer et al. (2003)).

Turbulence origin	Region		
	Near wake <4D	Intermediate wake 4-6D	Far wake >7D
Ambient	High	High	High
Shear generated	High	Very high	Medium
Turbine generated	High	Medium	Low

1.8 Review of related work

The investigation of turbine wake is largely focused on the estimation of velocity deficit as it directly affects the power extracted by the turbine ($P \propto U^3$). Many studies have been carried out to investigate turbine wake. These studies are divided into three categories; experimental, numerical, and analytical methods. Each of these methods has its own advantages and drawbacks. These hydrodynamics modeling approaches are presented hereafter.

1.8.1 Experimental works

The TST industry has seen approximately 54% successful deployments of the 57 full-size TST turbines identified by Walker and Thies (2021). However, a limited understanding of the complex tidal flow, coupled with high deployment and

operating costs, and perceived risk hinder the development of full-scale TST. In addition, the limited data available is mostly confidential in its entirety, hindering the research and development of the TST. Because of this, researchers are limited to small-scale experiments that do not cover the complexity and scales of tidal currents but provide significant results in investigating the TST wake.

Several experimental studies on tidal turbine wake were performed using both porous disks (Bahaj et al., 2007; Myers and Bahaj, 2012; Blackmore et al., 2014; Chen et al., 2019) and reduced tidal turbine models (Stallard et al., 2013; Vinod and Banerjee, 2019; Zhang et al., 2021). For instance, the experimental study of Mycek et al. (2014b) (presented in Figure 1.15) found the wake shape, length, and strength are significantly affected by the ambient turbulence but slightly affect the performance parameters. The enhanced recovery due to high ambient turbulence is also reported by several authors (Maganga et al., 2010; Vinod and Banerjee, 2019; Zhang et al., 2021). Blackmore et al. (2014) also found the ambient turbulence and the integral length scale affect the drag coefficient of the rotor. However, Ebdon et al. (2021) suggests that though ambient turbulence significantly affects the wake, the turbulence length scale is insignificant. Experimental measurements by Stallard et al. (2015) show that wake generation and recovery in a shallow flow can be considered in several regions.

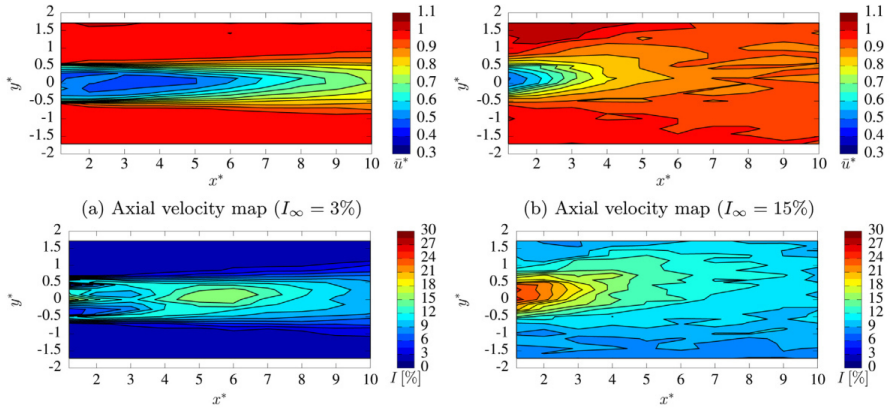

Figure 1.15 The contour of velocity deficit(top) and turbulence intensity (bottom) behind a tidal turbine wake at low (left) and high (right) ambient turbulence. Adapted from Mycek et al. (2014b).

Also, Chen et al. (2019) studied the effects of rotor diameter-to-depth ratios. The results show the increased rotor diameter-to-depth ratio is comparable to an increase in thrust coefficient. Zhang et al. (2021) investigate the hydrodynamics of wake at three different rotor diameter-to-depth ratios. The results show the shear layer at a high rotor diameter-to-depth ratio is elliptical as reported by Stallard et al. (2015) as a result of the wake compression due to the limited channel depth. Besides, considerable studies to analyze the effect of turbine loading have been reported. To illustrate, Gaurier et al. (2020) examined the load effect of

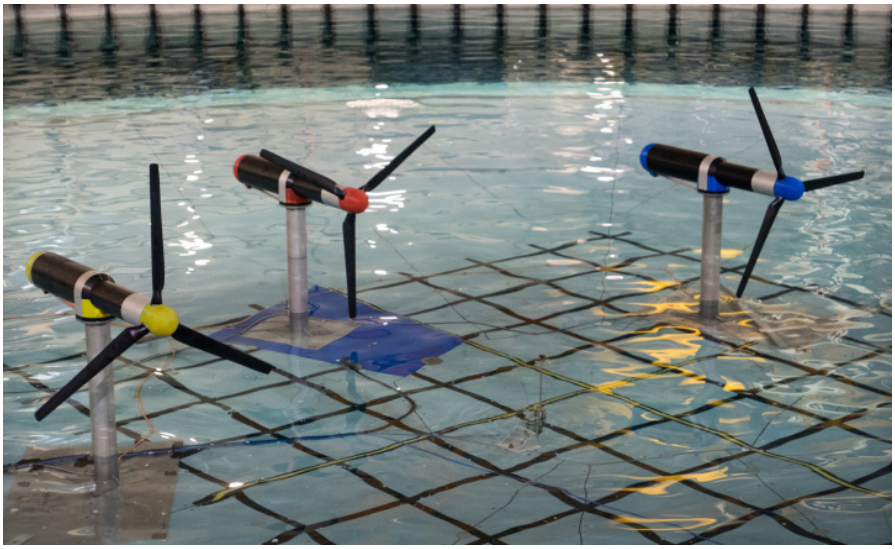

Figure 1.16 Turbine array setup at the FloWave Ocean Research Facility. (Credit: Noble et al. (2020)).

bathymetry-generated turbulence on a turbine. The effect of wake rotation has also been analyzed and it is shown to be limited to the near region (Vinod and Banerjee, 2019; Zhang et al., 2021).

In addition, the wake interaction of multiple turbines has also been studied as shown in Figure 1.16. Mycek et al. (2014a) studied the interaction of two axially aligned turbines and the performance of the downstream turbine is affected at low turbulent intensity. Myers et al. (2011) studied the effect of spacing on the downstream turbine. Improper spacing can result in a decrease in power and an increase in fatigue loading. As noted, the small experimental setup could allow sufficient control of the system to investigate a particular wake feature. Yet, the complexity of high turbulent tidal flows coupled with the sudden variation of depth, wave effect, and bathymetry can not be effectively investigated using the reduced experimental setup. The intricate flow hydrodynamics is therefore studied using numerical simulations.

1.8.2 Numerical modeling

High-fidelity numerical models are developed to complement the experimental data to provide good results to serve as basics for a full-scale turbine model. These CFD models solve the Navier-Stokes equation with turbulence closure to find the velocity magnitude at every location in the domain. Numerical models are used to investigate the performance of both reduced and full-scale tidal turbines.

The blade resolved model is the most accurate model that provides realistic turbine loading (Ahmed et al., 2017), however, it is computationally expensive. The Actuator Line Model (ALM) is an extension of the Blade Element Model

(BEM) that accounts for the non-uniform loading on the turbine blades and provides a good representation of both near and far wake (Jump et al., 2020). TST can also be simulated using the Lattice Boltzmann Method (LBM). The LES-LBM provides good turbulent features of the TST (Grondeau et al., 2022). There exists also the Actuator Disk Model (ADM) that represents the turbine as a porous disk, this model neglects the turbulence generated at the blade's tip but has good representation in the far wake. The ADM is widely used in large farms due to its low computational cost.

Apart from isolated turbines, numerical investigation of wake interaction in the tidal park has been carried out by several authors (Bai et al., 2013; Abolghasemi et al., 2016; Rahman et al., 2018; Nguyen et al., 2019; Thiébot et al., 2016, 2021; Djama Dirieh et al., 2022) as shown in Figure 1.17. These studies show higher energy production occurs at a lateral spacing of 2 - 3 D while maximizing the longitudinal spacing. The minimal lateral spacing can accelerate the flow for the downstream turbine while the large longitudinal spacing ensures flow recovery. For this reason, the staggered array produces higher energy than the rectilinear array with the same number of turbines in a particular site (Turnock et al., 2011). Although the recent increase in computational capacity allows the simulation of tidal farms (Abolghasemi et al., 2016; Lo Brutto et al., 2016b; Thiébot et al., 2020; Djama Dirieh et al., 2022), calculating large turbine arrays remains a challenge due to high computational cost.

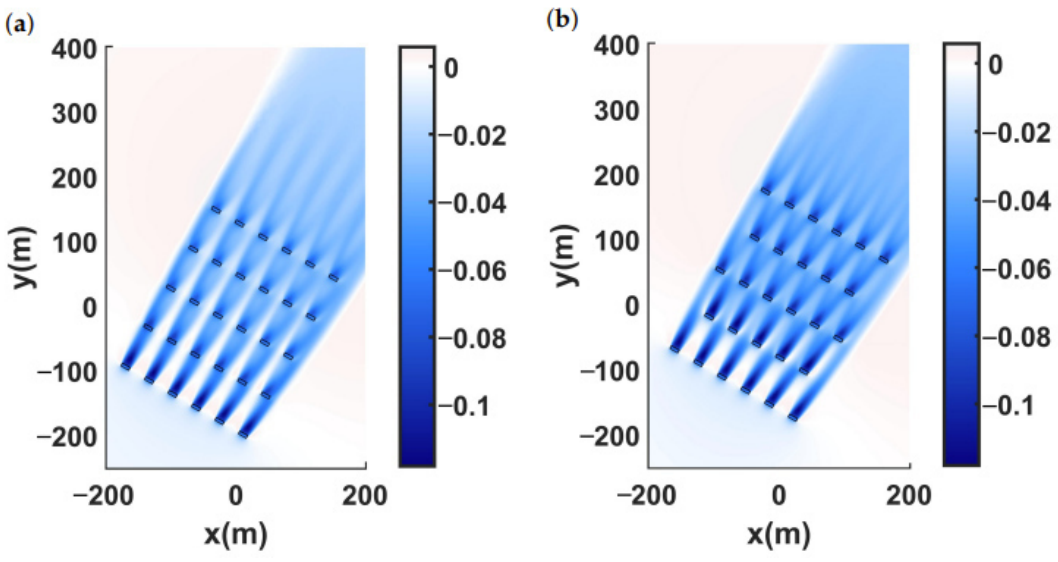

Figure 1.17 Numerical simulation of tidal turbine farm in (a) rectilinear and (b) staggered array using ADM obtained by Djama Dirieh et al. (2022).

1.8.3 Analytical model

Researchers have developed analytical models based on simple theoretical flow function and shape function relationships to estimate the wake behind a turbine. The analytical models, also called kinematic models, are based on self-similar properties of the flow. These analytical models remain the preferred method for estimating turbine hydrodynamics, especially in a large array due to their low computational cost (Crespo and Hernandez, 1996; Qian and Ishihara, 2021). Despite the availability of high-fidelity numerical models like the blade resolved model, wind farm designs are still based on analytical wake models because they are computationally affordable.

In the last 2 - 3 decades, several analytical models were developed from the simple model developed by Jensen (1983) to more complex Artificial Intelligence (AI) based models (Syed Ahmed Kabir et al., 2020; Ti et al., 2021) to estimate the velocity deficit in the far-wake of a wind turbine. The self-similar property allows the models to be defined as a product of stream functions and shape functions. The stream function representing the velocity deficit is obtained from the conservation equations of mass and momentum while the shape function is a self-similar velocity distribution. For a rotor operating in full-wake or partial-wake conditions, having the proper wake shape is essential because the wrong shape can result in inaccurate power estimation.

In 1983, Jensen proposed a top-hat shape function to estimate the velocity deficit in a far wake. The wake shape representation is adopted in several models including one proposed by Frandsen et al. (2006). However, the top-hat shape function clearly underestimates velocity deficit at the center of the wake and overestimates it at the wake edges in comparison with experimental and numerical data (Bastankhah and Porté-Agel, 2014) as shown in Figure 1.18. Therefore, a new analytical model using the Gaussian distribution profile is provided by Bastankhah and Porté-Agel (2014) to estimate the velocity deficit in the far wake. The Gaussian profile is widely used as it is consistent with the measured data in the far wake (Cheng et al., 2019). Next, Ishihara and Qian (2018) modified the Bastankhah and Porté-Agel by introducing a correction term in the near wake. Recently, Blondel and Cathelain (2020) proposed a super-Gaussian function that evolves from a nearly top-hat shape in the near wake to a Gaussian shape in the far wake, which is consistent with observations and measurements of wind turbine wakes. The analytical models for wind turbines have developed over the years and are currently used in commercial tools like WindPRO, WindSim, and OpenWind to estimate the power production in wind farms.

Overall, these analytical models lay the groundwork for estimating the velocity deficit of tidal turbine wake. Some researchers calibrate these models of wind turbines for tidal turbine applications (Palm et al., 2010; Yazicioglu et al., 2016; Lo Brutto et al., 2016a; Pyakurel et al., 2017). The calibration becomes necessary in high turbulent tidal current with a limited channel depth compare to the wind turbines in the atmospheric boundary layer. A pioneer analytical model for the

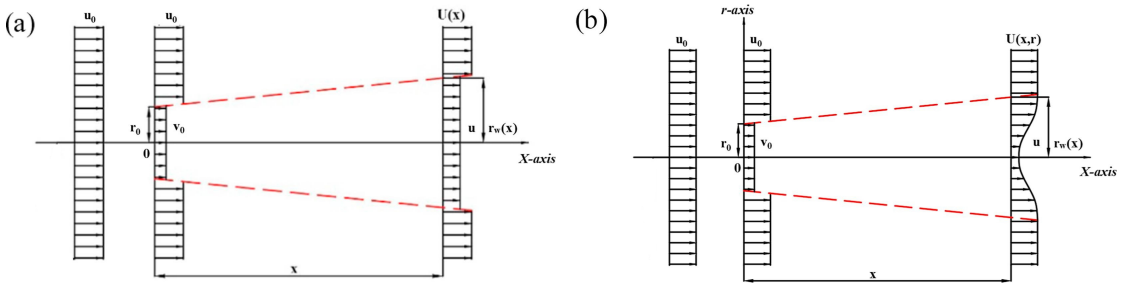

Figure 1.18 Schematic diagrams of analytical wake models showing (a) top-hat; and (b) Gaussian wake distribution. Source: Sun and Yang (2018).

velocity deficit of the tidal turbine model is reportedly developed by Lam et al. (2015) and validated with a 3-bladed tidal turbine experiment by Maganga et al. (2010). Also, a semi-empirical model for velocity deficit in the wake of the tidal turbine is proposed by Lo Brutto et al. (2016b). In this model, the velocity deficit is predicted using the Jensen equation but an exponential law of wake expansion is proposed against the linear law of Jensen. Furthermore, Stallard et al. (2015) proposed an expression to estimate the far-wake velocity deficit in a shallow channel. The model is based on an experimental campaign of TST at 60% rotor diameter to depth ratio. Pyakurel et al. (2017) use the empirical models of a wind turbine to optimize the coefficient with tidal turbine numerical data at different turbulent intensities. Note that these analytical models allow only for the representation of mean velocity without regard to the turbulence effect. For a single turbine model, the effect of turbulence wake may not affect the performance of the turbine, however, it can significantly affect the energy production of downstream turbines in a park (Bai et al., 2013).

1.8.4 Tidal arrays

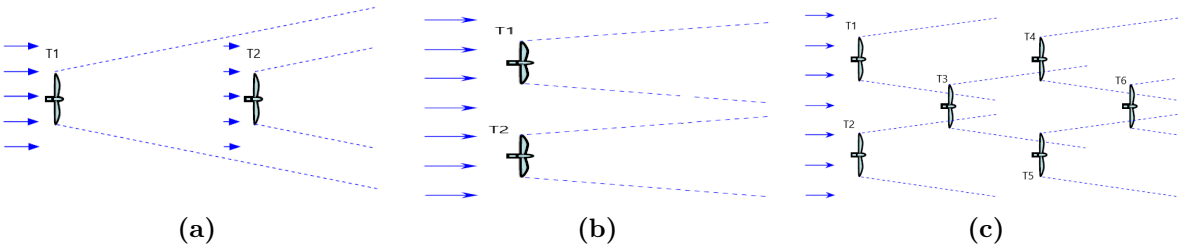

Figure 1.19 Schematic of turbine-wake interaction; (a) fully immersed (b) no interaction and (c) partially immersed in the wake of the upstream turbine. Source: Palm et al. (2010).

The single turbine models were extended to estimate the velocity deficit in turbine arrays (Palm et al., 2010; Funke et al., 2014; Lo Brutto et al., 2016b; Stansby

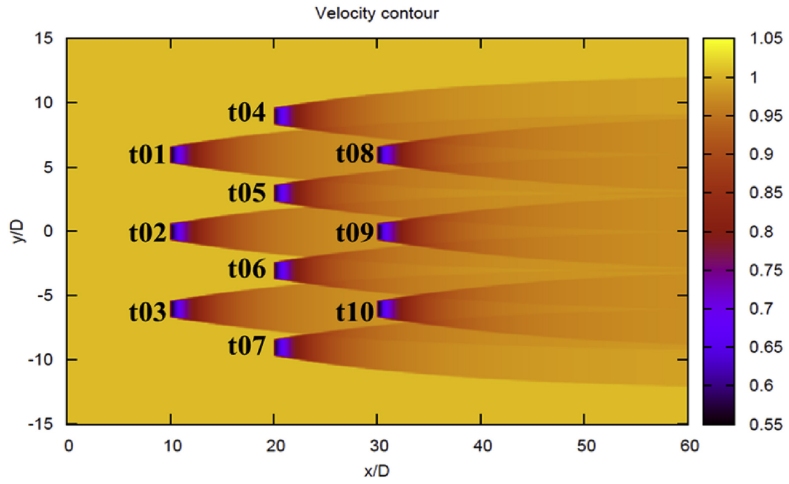

Figure 1.20 Normalised velocity contour in a tidal farm obtained by Lo Brutto et al. (2016a).

and Stallard, 2016; Pinon et al., 2017). The wake of upstream turbines interacts with downstream turbines affecting energy production. In multiple turbine farms, the three main interactions are full immersion, partial, and no interaction as shown in Fig. 1.19. To estimate the turbine-wake interaction, several superposition methods are proposed in the literature (Pookpunt and Ongsakul, 2013; Qian and Ishihara, 2021; Niayifar and Porté-Agel, 2016) to estimate the wake of a turbine. Lissaman (1979) proposes a model for the cumulative velocity deficit based on the linear superposition of velocity deficits. Other authors (Katic et al., 1987; Lo Brutto et al., 2016b; Qian and Ishihara, 2021) use the kinetic energy deficit. The kinetic energy deficit of multiple wakes is equivalent to the sum of the energy deficits for the individual wakes at the downstream position. The velocity deficit model in an array of 10 turbines by Lo Brutto et al. (2016a) is presented in Figure 1.20. These models only take into account the flow's ambient turbulence. Turbine interaction in a farm has been shown to increase turbulence intensity both experimentally and numerically. The turbulence intensity in the farm should be taken into account for an accurate estimation of the power produced in the farm using the analytical models.

1.8.5 Turbulence in turbine wake

As the number and accuracy of analytical models to estimate the velocity deficit increases over the decades, the techniques for quantifying turbulence remain immature. Turbines in a cluster network operate in the region of turbulent flow from the upstream turbine. These turbulent regions are associated with fatigue stresses that can affect both the structural integrity and power generation of turbines at the park. Adequate knowledge of understanding wake turbulence is therefore required. The turbulent intensity in turbine wake is expressed by Quarton and

Ainslie (1990) as:

$$\mathrm{I_w} = \left(\mathrm{I_0^2} + \mathrm{I_+^2}\right)^{0.5} \tag{1.3}$$

where I_w is the total turbulence in the wake, I_0 is the ambient turbulence and I_+ is the added turbulence by the rotor. The ambient turbulence is site-specific and can vary along a tidal cycle (see Fig. 1.10), while the added turbulence is the contribution of shear and turbine-generated turbulence by the turbine (see Table 1.3).

Accurate estimation of wake turbulence is essential primarily to enable the evaluation of additional fatigue loading on turbine blades and ensures a proper location for turbine placement downstream (Mullings and Stallard, 2021; Li et al., 2022). An investigation of the wake effect on the electrical model of the tidal turbine array by Lo Brutto et al. (2018) shows a significant error in the active power estimation when the turbulence effect is neglected. Mycek et al. (2014b) studies on the turbulent intensity effect in the tidal park show a modification of power coefficient C_P for a downstream turbine at low ambient turbulence. Pinon et al. (2017) studied how turbulent intensity affects energy production in TST park. The study shows an overestimation in energy production at low ambient turbulent intensity flow due to modified C_P in the downstream turbine. This overestimation can affect the project viability in long-term energy production.

Some empirical relations were developed to estimate the added turbulence of wind turbines. The added turbulence relation reported by Quarton and Ainslie (1990) is expressed as a function of the ambient turbulent intensity, the thrust coefficient, and the length of the near wake proposed by Vermeulen (1980). Though the exact length of the near wake remains a conjecture, subsequent researchers like Crespo and Hernandez (1996); Frandsen and Thøgersen (1999) express the added turbulence in terms of the downstream location rather than the length of the near wake. Other authors (Larsen et al., 1996; Frandsen and Thøgersen, 1999) argue that the turbine characteristics mainly influence added turbulence, therefore, they proposed a simple expression independent of ambient turbulence.

In contrast to wind turbines, tidal turbines are usually located in shallow water constrained by channel depth. Therefore, using a wind turbine model may result in improper estimation. Hardly any research has so far been conducted on added turbulent intensity in tidal turbine wake. To properly assess the energy production in tidal farms, a number of research questions need to be addressed. Such as, what minimum does ambient turbulence C_P remain constant as in high turbulent intensity? And at what distance, a turbine should be located downstream at different ambient turbulence to optimize energy extraction? How does the limited channel depth affect the wake recovery on the farm? A good estimation of velocity deficit and turbulence intensity in the wake of the tidal turbine is essential. The preliminary step is to estimate the added turbulence in the wake of the tidal turbine.

1.9 Scope of thesis

To accommodate the development of TST and to facilitate commercialization, the need for a low-computational analytical model cannot be overstated. In LUSAC, research in this context started with Lo Brutto (2016)'s dissertation. A semi-empirical model is developed to estimate the velocity deficit in Alderney Race. The developed model allows to set up an algorithm to calculate the energy recovery potential in a farm based on numerical data from Nguyen (2015) thesis in Alderney Race considering the flow determined by a hydrodynamic model developed by (Harrison et al., 2010b). This model is limited to a particular turbine size and does not take into account the turbulence effect on the farm.

In continuation, this thesis studies the far-wake behind a full-scale tidal turbine at an array scale. As already established in the literature, the wake behind a tidal turbine is influenced by at least three parameters; the flow condition, the turbine itself, and the site configuration. This thesis aims to develop a generic empirical model to estimate the velocity deficit and turbulence intensity in the wake of a tidal turbine considering the variation in ambient turbulence, thrust coefficient, and the rotor diameter-to-depth ratio. The study at different rotor diameter-to-depth ratios is significant as the water depth is site-specific and varies with the tidal cycle. Since the experimental data from full-scale tidal turbines are not readily available for validation. The numerical simulations will be developed using hydrodynamic data measured at potential sites.

The objectives of the thesis are as follows:

- developing a numerical model of a full-scale tidal turbine.
- validating the numerical model with benchmark experimental data.
- developing an empirical model of added turbulence in a tidal turbine wake.
- developing a generic tidal turbine wake model for velocity and turbulent intensity using realistic conditions.
- applying the generic model in tidal farms considering the turbine-wake interaction.

The rest of the thesis is structured into the following chapters:

- **Chapter 2** is the methodology which begins by presenting the basic governing equations of fluid mechanics. Different Computational Fluid Dynamics (CFD) modelings of tidal stream turbine (TST) are presented with elaborating details on the actuator disk model (ADM). A detailed implementation of Reynolds Average Navier-Stokes (RANS-ADM) in OpenFOAM is provided. A numerical model is developed and validated with a porous disk experiment of Bahaj et al. (2007) and a tidal turbine experiment of Mycek et al. (2014b).

- **Chapter 3** presents the added turbulence model in the full-scale tidal turbine. The chapter starts with a description of turbulence in turbine wake and a summary of the existing turbulence model for wind turbine application. Then, a full-scale numerical tidal turbine model is developed to provide reference data for the analytical model. Lastly, an empirical model of wake radius, and added turbulence is developed and compared with numerical data.

- **Chapter 4** begins by introducing existing models for velocity deficit for both wind and tidal turbines. These models are mainly based on mass conservation or momentum theory to express the stream function that characterizes the wake. A numerical model at different rotor diameter-to-depth ratios is presented to develop a generic model to estimate the velocity deficit and turbulent intensity in tidal turbine wake. The generic model is developed and validated with experimental data.

- In **Chapter 5**, the wake interaction in tidal farm is presented. The effect of turbine interaction for each turbine is calculated and evaluated using the superposition principle. The effect of turbine spacing, ambient condition, and rotor diameter-to-depth ratio is investigated. The farm efficiency at different configurations is studied.

- Finally, **Chapter 6** presents the overall concluding remarks and the perspective for future works.

Chapter 2

Methodology

Contents

This chapter focuses on the numerical modeling of the tidal turbine. The different numerical modeling approaches are presented with an emphasis on the actuator disk model. The actuator disk model is implemented in OpenFOAM v2006 to simulate a tidal turbine. In the end, the model is validated with a porous disk experiment of Bahaj et al. (2007) and a tidal turbine experiment of Mycek et al. (2014b).

2.1 Introduction

The cornerstone of computational fluid dynamics is the fundamental governing equations of fluid dynamics — the continuity, momentum, and energy equations. These equations relate flow variables and their rate of change in space and time. Since the density is constant in an incompressible flow, the equations of mass and momentum must be solved. This section presents these two equations only because the study does not require the use of an energy equation.

2.1.1 Conservation of mass (continuity)

It says that matter is conserved in a flow, meaning that the difference between the entering and exiting flow is equal to the mass rate. For a steady incompressible flow, the equation in vectorial form reduces to:

$$\nabla \cdot \vec{V} = \frac{\partial u_i}{\partial x_j} = 0. \tag{2.1}$$

where u_i is the component of velocity in x, y and z directions.

2.1.2 Momentum conservation (Navier–Stokes equations)

The equation is derived from the classical Newton Second law that states the rate of change of momentum is equal to the sum of external forces in a closed volume. The general expression of conservation of momentum is given as:

$$\frac{\partial}{\partial t} + \int_V \rho \mathbf{u}\, dV + \int_A (\rho \mathbf{u}\mathbf{u}) \,.\, \mathbf{n}\, dA = -\int_A p \,.\, \mathbf{n}\, dA + \int_A \mu(\bigtriangledown \mathbf{u}) \,.\, \mathbf{n}\, dA + \int \rho \mathbf{f}\, dV \tag{2.2}$$

For incompressible flow, the conservative form of the NSE reduces to:

$$\frac{\partial u_i}{\partial t} + u_j \frac{\partial u_i}{\partial x_j} = -\frac{1}{\rho}\frac{\partial p}{\partial x_i} + v\frac{\partial^2 u_i}{\partial x_j \partial x_j} + f_i \tag{2.3}$$

in which ν, p, and f_i denote the viscosity, pressure, and external forces respectively.

2.1.3 Turbulence

Turbulence is a property of the flow that is associated with random motion, generation, and propagation of 3D vortices of different length scales in the flow (Lumley, 1983). Turbulence can also cause diffusion and mixing of conserved properties in the flow (Greaves and Iglesias, 2018). In the NSE, turbulence is manifested through the flow's non-linear inertia term. So far, there is no universal and efficient mathematical model for turbulence due to the complexity of the problem. The turbulence intensity is a non-dimensional scale characterizing turbulence expressed as a percentage expressed in Eq. (2.4) as:

$$\mathrm{I} = \frac{\sqrt{\overline{u'u'}}}{\overline{U}} \tag{2.4}$$

where $\overline{u'}$ is the velocity fluctuation and $\overline{U}$ is the mean velocity in the flow.

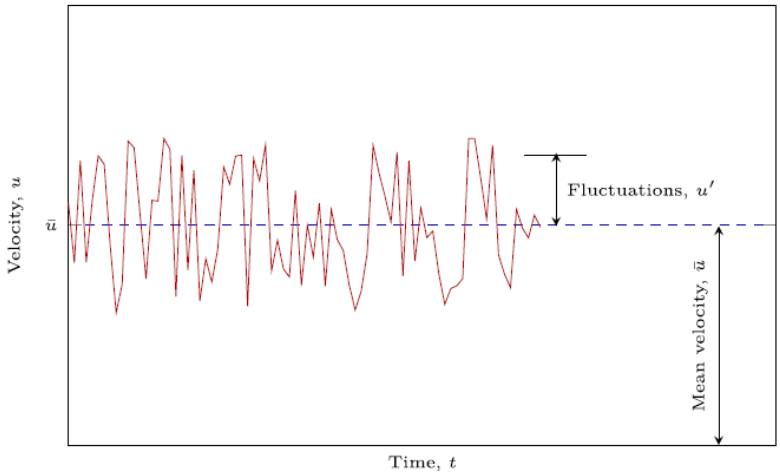

Figure 2.1 Instantaneous and average velocities. (Source: Torabi (2022)).

In turbulent flows (for example, tidal current), the velocity can be divided into an average ($\bar{u}$) and an oscillation part (u') as illustrated in Figure 2.1. This variation of speed exists in each point of the domain. By averaging the velocity over an appropriate time interval, the mean value for velocity is obtained using

$$\bar{u} = \frac{1}{\Delta t}\int_{t}^{t+\Delta t} u dt \tag{2.5}$$

in which

$$u = \bar{u} + u' \tag{2.6}$$

This averaging can be used for all flow variables, such as pressure and viscosity. It is the way to reduce computational cost in a numerical simulation.

2.2 Rotor modeling

In computational fluid dynamics (CFD), a representation of the rotor turbine is necessary. Numerical models provide low-cost solutions with details that are difficult to measure experimentally. Different numerical models have been developed with certain limitations and assumptions to perform specific tasks. Depending on the area of interest or the scope of the investigation, a particular numerical model is used. The basic numerical model for wind and tidal stream turbines is shown in Figure 2.2. We listed 4 main kinds of modeling; Blade resolved, actuator line, RANS-BEM, and constant actuator disk. These numerical models are briefly discussed hereafter.

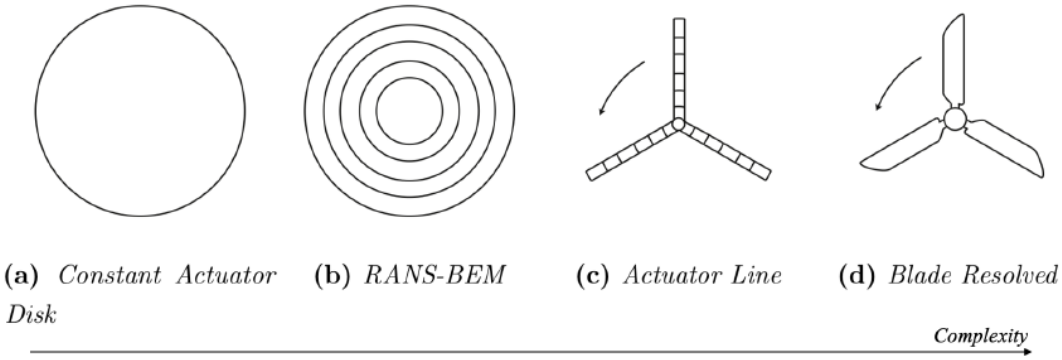

Figure 2.2 Numerical representation of turbine within the CFD (Olczak et al., 2016)

2.2.1 Blade resolved method

Blade resolved modeling (or full rotor modeling) means that the whole tower, nacelle, blades, rotor, etc., are modeled, and unsteady flow is simulated using a proper solver. This method provides accurate results with proper numerical set-up. It is worth mentioning that the computational cost of this simulation is high because of resolving the boundary layer around the blades since, for full rotor simulation, the Navier-Stokes equations and the turbulence model must be solved. Due to its high computational cost, the full rotor simulator is usually used to evaluate the performance of a turbine in the near wake.

2.2.2 Actuator line method(ALM)

In this method, instead of simulating the whole rotor, its effect is simulated inside the computational domain. The rotor blade is divided into some elements and then the hydrodynamic forces of each element are calculated. ALM uses unsteady state simulation and is computationally expensive, however less than the full rotor method. Due to its high computational cost, the ALM is largely used in the near wake to simulate the tip vortices.

2.2.3 Blade Element Momentum Theory (BEMT)

BEMT is a theory that combines both blade element theory and momentum theory. BEMT allowed for determining the aerodynamic loads of a wind and tidal turbine and thus, enabled the BEM method as a widely used design tool. This method is derived from the principles of conservation of mass and momentum based on the assumptions of steady, inviscid, incompressible flow without radial and circumferential dependency. The concept of the blade element momentum theory is that forces on the rotor can be deduced from the aerodynamic lift and drag on a blade section determined from two-dimensional airfoil theory or previously recorded experimental data (Zhao et al., 2019). This method is less computationally expensive compared to the Full rotor and ALM. However, it requires a specific blade profile and hence cannot be used for general application.

2.2.4 Actuator Disk Method (ADM)

As a simple and low-cost way, the actuator disk method (ADM) considers the turbine as a porous, permeable disk that absorbs tidal current momentum. Neglecting the boundary layer region around the blade leads to a low-cost but efficient way. The use of a one-dimensional ADM allows the analysis of the turbine without any specific turbine design by considering the energy extraction process. ADM describes the extraction of kinetic energy but does not explain which is dissipated as turbulence in the flow (Sanderse et al., 2011).

2.2.5 Why choose the ADM?

The actuator disk model is often used to model wind and tidal farms for several reasons including:

- **Simple design:** The use of an actuator disk allows a generic representation of the turbine irrespective of the blade profile and the pitch control mechanism. The ability of the ADM to adapt to a different turbine in the far wake makes it a suitable approach for developing a generic model.

- **Computational efficiency:** In a tidal farm where multiples of turbines are placed in an array. Modeling each turbine with a high-precision method is computationally expensive and time-consuming. The use of ADM drastically reduces computational resources compared to other modeling methods.

- **Parameteric studies:** Turbine farms can have various design parameters that require monitoring like the turbine spacing, turbine size, and the flow direction. Using the actuator disk model, the impact of these parameters on overall farm efficiency can be investigated without focusing too much on individual turbine performance.

- **Idea for wake effects:** In turbine farms, downstream turbines are located mainly in the far wake where the wake effect is largely self-similar. The actuator disk provides acceptable results compared to the high-fidelity numerical simulation in the far wake.

Despite its advantages, it is essential to acknowledge the limitations of ADM when applied to real-world turbines. The actual wake shape is not correctly represented and the ADM also underestimates the blade-generated turbulence in the near wake.

2.3 Actuator disk theory

The rotor of the turbine is considered an ideal permeable disk, meaning frictionless and no rotational velocity component of the wake. Upstream of the disk, the stream tube has a cross-sectional area smaller than the disk and an area larger than the disk downstream. The expansion of the stream tube in Figure 2.3 is because the mass flow rate must be the same everywhere. The disk acts as a drag device slowing down the fluid velocity from far upstream U_∞ of the rotor to U_D at the rotor plane and U_w in the wake, as shown in Figure 2.3. The conservation of mass balance along the stream tube is given in Eq. (2.7) as:

$$\rho A_\infty U_\infty = \rho A_D U_D = \rho A_w U_w \tag{2.7}$$

It is expected that the actuator disk induces a velocity variation on free stream

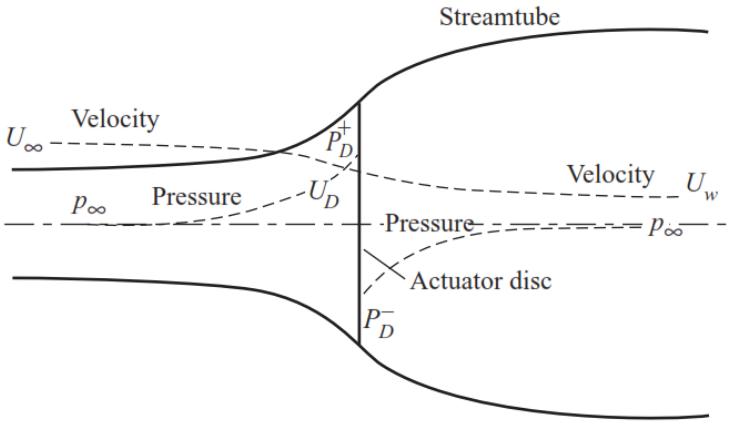

Figure 2.3 An energy-extracting actuator disk and stream-tube (Source: Hansen (2015)).

velocity in the form $-aU_\infty$, where a is the *axial induction factor*. The axial velocity at the disk location is expressed in Eq. (2.8) as:

$$U_D = U_\infty(1 - a) \tag{2.8}$$

Thrust is obtained by a pressure drop over the rotor. Close upstream of the rotor there is a small pressure rise from the atmospheric level P_∞ to P^+ before a discontinuous pressure drops ΔP over the rotor. Downstream of the rotor, the pressure recovers continuously to the atmospheric level. This thrust force T is caused by the pressure drop across the disk which can also be expressed in terms of change of momentum given in Eq. (2.9):

$$T = (P_D^+ - P_D^-)A_D = (U_\infty - U_w)\rho A_D U_D \tag{2.9}$$

Bernoulli equation (2.10) is applied separately to the upstream and downstream of the rotor to obtain the pressure drop in Eq. (2.11):

$$\frac{1}{2}\rho U^2 + p + \rho g h = const \tag{2.10}$$

$$\Delta P = \frac{1}{2}\rho(U_\infty^2 - U_w^2) \tag{2.11}$$

The Thrust force T in Eq. (2.9), can now be express as:

$$T = \frac{1}{2}\rho(U_\infty^2 - U_w^2)A_D = (U_\infty - U_w)\rho A_D U_\infty(1-a) \tag{2.12}$$

Therefore, the velocity behind the disk is defined as Eq. (2.13) is:

$$U_w = U_\infty(1-2a) \tag{2.13}$$

2.3.1 Power coefficient

The force on the fluid from Eq. (2.12) becomes:

$$T = (P_D^+ - P_D^-)A_D = 2\rho A_D U_\infty^2 a(1-a) \tag{2.14}$$

The power extracted from the fluid is given by Eq. (2.15)

$$Power = TU_D = 2\rho A_D U_\infty^3 a(1-a)^2. \tag{2.15}$$

Power coefficient C_P, is defined as the ratio of power extracted by the disk to the available power in the flow expressed by Eq. (2.16)

$$C_p = \frac{Power}{\frac{1}{2}\rho A_D U_\infty^3} \tag{2.16}$$

Therefore,

$$C_P = 4a(1-a)^2$$

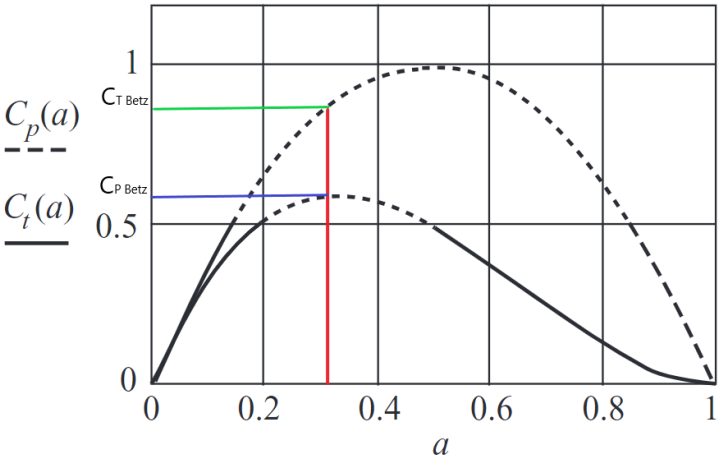

Figure 2.4 Variation of power coefficient C_p and thrust coefficients C_T with axial induction factor a (adopted from Burton et al. (2011).

The maximum C_p occurs when;

$$\frac{dC_P(a)}{da} = 0$$

According to the Betz limit, C_{Pmax} occurs at $a = 1/3$, Hence $C_{Pmax} = 16/27 = 0.593$ is the best theoretical efficiency for wind turbines. The limit is caused not by any deficiency in design, but because the stream tube has to expand upstream of the actuator disk. However, for tidal turbines, the Betz limit is reportedly exceeded due to the impact of the blockage effect (Vennell, 2013).

2.3.2 Thrust coefficient

The force on the actuator disk caused by the pressure drop, given by Eq. (2.12), can also be non-dimensionalized to give a coefficient of thrust C_T as:

$$C_T = \frac{Thrust}{\frac{1}{2}\rho A_D U_\infty^2} \tag{2.17a}$$

$$C_T = 4a(1-a) \tag{2.17b}$$

At the Betz limits ($a = 1/3$), the thrust coefficient C_{Tbetz} is 0.89. The variation of power coefficient and thrust coefficient with a is shown in Figure 2.4. A problem arises for values of $a \geq 1/2$ because the wake velocity, given by $(1-2a)U_\infty$, becomes zero, or even negative; in these conditions the momentum theory, as described, is no longer valid.

2.3.3 Actuator disk model

In the AD model, the rotor represented by a disk with a thrust force T is homogeneously distributed. The Actuator disk has the power to model far wake provided that the small-scale effect is parameterized (Blackmore et al., 2014). The pressure jump across the disk provides a thrust force, a reduction in kinetic energy, and a reduction in flow velocity as the fluid passes through the rotor. The thrust force is calculated as:

$$T = \frac{1}{2}\rho C_T A U_\infty^2 \tag{2.18}$$

The thrust force T is added as a source term in the incompressible Navier-Stokes equation to account for the energy extraction by the actuator disk. It is trivial to obtain the inflow velocity with a single turbine. However, for multiple turbines in an array, the use of upstream velocity is questionable due to the wake effect, therefore Taylor (1958) proposed an expression for resistance coefficient K, relating the upstream velocity and the local velocity of a porous media as:

$$U_\infty = U_d(1 + \frac{1}{4}K) \tag{2.19}$$

Therefore, the thrust and power coefficients are expressed as:

$$C_T = \frac{K}{(1 + \frac{1}{4}K)^2}, \qquad C_P = \frac{K}{(1 + \frac{1}{4}K)^3} \tag{2.20}$$

The modified thrust force of the actuator disk is evaluated as:

$$T = \frac{1}{2}\rho K A U_d^2 \tag{2.21}$$

This approach of simulating tidal turbine proposed by Harrison et al. (2010b) is used extensively in the literature (Harrison et al., 2010a; Nguyen et al., 2016; Thiébot et al., 2016; Rahman et al., 2018; Thiébot et al., 2020; Khaled et al., 2021; Djama Dirieh et al., 2022).

2.4 Using actuator disk method in OpenFOAM

OpenFOAM is an open-source CFD program written primarily in `C++`. The program includes a number of solvers, each designed to solve a specific fluid mechanics problem, and in addition, there are utilities for performing data manipulations. OpenFOAM is based on the finite volume method (FVM) and has implemented many numerical schemes, both for time and space integration.

OpenFOAM uses a simple model to implement ADM. To implement the model, the geometry must first be set up. The momentum equation is then modified in

such a way that the effect of the tidal turbine through body forces is included in the model. Then some necessary solver settings have to be adjusted. Finally, the problem is solved with a suitable solver and the results can be viewed with the ParaView software. OpenFOAM version *v2006* is used throughout this thesis.

2.4.1 Geometry and mesh generation with *BlockMesh*

A simple rectangular numerical domain is set up and discretized using the basic `BlockMesh`. The basic hexahedral mesh is refined around the disk region and the bottom wall using the *snappyHexMesh dict* (see Fig. 2.5). Three refinement levels, fine, medium, and coarse, are set to avoid a sudden jump in cell size. Grid sensitivity is evaluated at different mesh densities and Cells Per Diameter (CPD) in Figure 2.6. 20 CPD across the disk surface for the Δy (transverse) and Δz (depthwise) provide a good disk representation and imperceptible results as shown in Figure 2.7. The CPD along the Δx (streamwise) direction representing the thickness of the disk is 4. The region far away from the disk is represented by a coarse mesh with a geometric growth rate of 1.2.

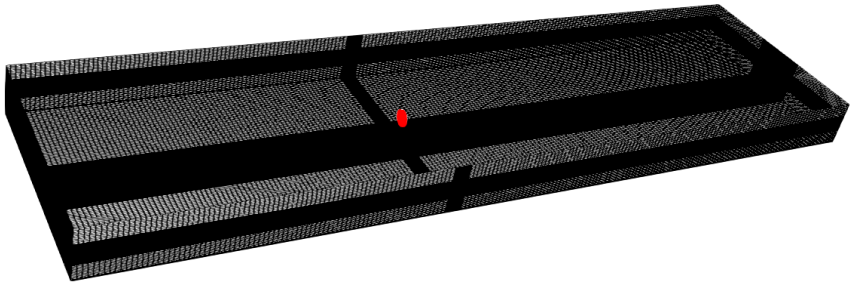

Figure 2.5 Hexahedral mesh of the numerical domain.

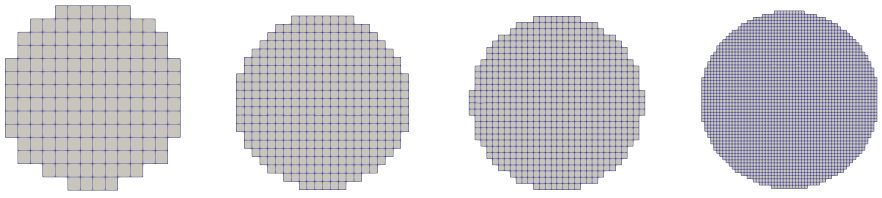

(a) n = 14 **(b)** n = 20 **(c)** n = 30 **(d)** n = 50

Figure 2.6 Mesh density among the disc surface mesh (a) - (d) corresponds to Mesh A - Mesh D in Figure 2.7

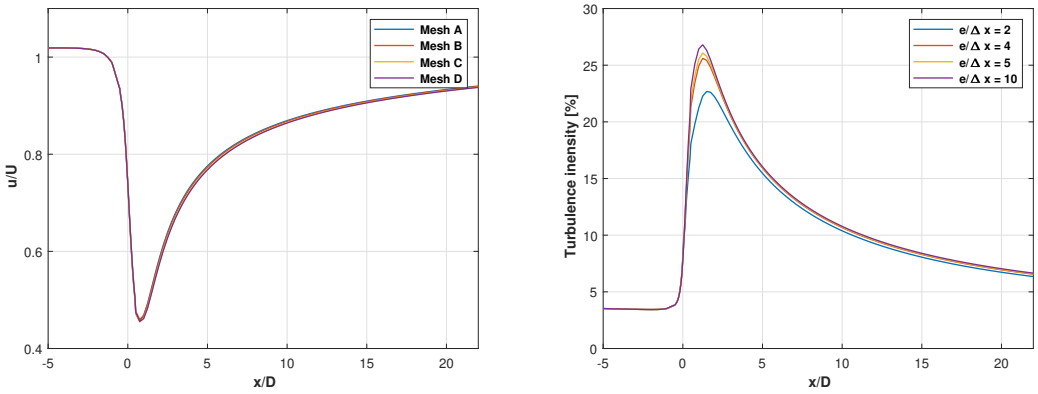

(a) Normalized velocity **(b)** Turbulence intensity

Figure 2.7 Comparison of axial normalized velocity and turbulent intensity at different mesh densities.

2.4.2 Source term definition

The `actuationDiskSource` applies a source term on the momentum equation to enable the ADM for aero/hydro thrust loading of rotary disks on the surrounding flow field in terms of energy conversion processes. The source term introduced via *fvOptions dict* (detailed in Appendix A.3) is applied to the volume cells defined in *topoSets dict* as sink term for energy extraction. `ActuatorDiskSource` provides two options to evaluate the thrust force in OpenFOAM; the `Froude` method and the `variableScaling` method. The variable scaling method is preferred for the turbine array as it uses the local velocity at the disk location to evaluate the thrust force expressed as:

$$\overrightarrow{\mathbf{T}} = \frac{1}{2}\rho A \left|\mathbf{U}_d\right| C_T^* \overrightarrow{\mathbf{U}_d} \tag{2.22}$$

where U_d is the incoming velocity average on the actuator disk, ρ is the fluid density, A is the rotor surface area and C_T^* is the calibrated thrust coefficient. C_T^* is evaluated in terms of upstream velocity, U_∞, as $C_T^* = C_T \left(\frac{|\mathbf{U}_\infty|}{|\mathbf{U}_d|}\right)^2$ and is analogous to the resistance coefficient K established in Section §2.3.3.

2.4.3 Solver selection and settings

The OpenFOAM solver used in the current study is `simpleFOAM`, which is suitable for incompressible flow. The solver utilizes the Semi-Implicit Method for Pressure Linked Equations (SIMPLE) algorithm for steady-state incompressible transport equations. The equations were discretized using the `Gaussian` integration scheme where values were interpolated from cell to face centers. A first-order bounded scheme is used for the convection and turbulence model equations. In OpenFOAM, the first-order used is referred to as `upwind`, the central interpolation

scheme `linear` is used for diffusion terms and an explicit non-orthogonal correction method `corrected` is employed for the surface-normal gradient. Interested readers can find more details on numerical schemes in the OpenFOAM User Guide (2020).

2.4.4 Turbulence modeling

The simulation of tidal current requires a mathematical model to resolve the wide range of time and length scales. Large Eddy Simulations (LES) resolve the large scales and model the small-length scales. However, for commercial-scale tidal turbines in a park, LES can be computationally expensive because it requires a fine mesh to satisfy the wall function. Therefore, several technical papers that investigated the mean wake in the wind (Rethore et al., 2009; Elgendi et al., 2023) and tidal farms (Nguyen et al., 2016; Thiébot et al., 2016, 2020) used Reynolds-Average Navier Stokes (RANS) turbulence models considering only statistically time-averaged mean flow because it is less computationally expensive and the difference between the models is reasonable in the far wake region (Rethore et al., 2009).

In OpenFOAM, the turbulence `simulationType` and the `model` are specified in *turbulenceProperties dict*. Unfortunately, there is no classical method for selecting an appropriate model. However the two primary models for turbine RANS simulation are $\kappa - \epsilon$ and $\kappa - \omega$ turbulence models. Nguyen et al. (2016) simulate tidal turbine with different RANS models and conclude that $\kappa - \epsilon$ provides good results, especially in the far wake. Moreover, several studies that investigate wind and tidal uses the $\kappa - \epsilon$ model (Rethore et al., 2009; Rahman et al., 2018; Khaled et al., 2021; Djama Dirieh et al., 2022). Hence, this study uses the standard $\kappa - \epsilon$ turbulence model for turbulence closure of Reynolds stress. The model description is presented hereafter.

2.4.4.1 $\kappa - \epsilon$ model

The $\kappa - \epsilon$ model is the most widely used two-equation turbulence model for RANS and is known to produce good results in large channel flow, however, it struggles close to walls. The RANS equations solved by numerical tools are in the form:

$$\frac{\partial(\rho U_i U_j)}{\partial x_j} = -\frac{\partial P}{\partial x_i} + \frac{\partial}{\partial x_j}\left[\mu\left(\frac{\partial U_i}{\partial x_j} + \frac{\partial U_j}{\partial x_i}\right) + \overline{u_i u_j}\right] + \rho g_i + S_i \tag{2.23}$$

where U_i is the components of the time-averaged mean velocity averaged, μ is the water dynamic viscosity, g_i are the components of the gravitational acceleration, S_i is the momentum sink term applied at the disk, and $\overline{u_i u_j}$ is the Reynolds stress tensor that must be modeled. The Boussinesq's approximation of the stress tensor

is given as:

$$-\overline{u_i u_j} = \nu_T \left(\frac{\partial U_i}{\partial x_i} + \frac{\partial U_j}{\partial x_i} \right) - \frac{2}{3} k \delta_{ij} \tag{2.24}$$

where ν_T is the eddy viscosity. Its definition and the transport equations for the turbulent kinetic energy, κ, and dissipating energy, ϵ are:

$$\nu_T = c\mu \frac{k^2}{\epsilon} \tag{2.25}$$

$$\frac{\partial k}{\partial t} + U_j \frac{\partial k}{\partial x_j} = \frac{\partial}{\partial x_j} \left[\left(\nu + \frac{\nu_T}{\sigma_k} \right) \frac{\partial k}{\partial x_j} \right] - (\overline{u_i u_j}) \frac{\partial U_i}{\partial x_j} - \epsilon \tag{2.26}$$

$$\frac{\partial \epsilon}{\partial t} + U_j \frac{\partial \epsilon}{\partial x_j} = \frac{\partial}{\partial x_j} \left[\left(\nu + \frac{\nu_T}{\sigma_\epsilon} \right) \frac{\partial \epsilon}{\partial x_j} \right] - C_{1\epsilon} (\overline{u_i u_j}) \frac{\partial U_i}{\partial x_j} \frac{\epsilon}{k} - C_{2\epsilon} \frac{\epsilon^2}{k} \tag{2.27}$$

where Eq. (2.25) is inserted into Eqs. (2.24) - (2.27) together with the constant values defined in turbulence properties are known as the $k - \epsilon$ model.

Although the $\kappa - \epsilon$ model is shown to provide good results in far wake compared to the porous disk experiments (Nguyen et al., 2016). It tends to predict faster wake recovery due to the failure to account for the turbulence generated by the turbine in the near wake region (El Kasmi and Masson, 2008). Therefore, the use of turbulence correction to complement the added turbulence generated by the turbine is suggested in the literature.

2.4.4.2 Turbulence-source term

A comparison with experimental data of tidal turbine shows the standard $\kappa - \epsilon$ model predicts faster wake recovery (Shives and Crawford, 2012). This is due to the failure to account for the energy cascade from large scale to small scale in the near wake region. To account for the proper turbulence cascading in the near wake, turbulence correction with source term has been suggested for both wind and tidal turbines (El Kasmi and Masson, 2008; Rethore et al., 2009; Abolghasemi et al., 2016; Olson et al., 2021). El Kasmi and Masson (2008) proposed to add source terms to κ and ϵ transport equation at $\pm$ 0.25D of the disk to manage the TKE dissipation rate in the near wake. These source terms are expressed in Eq. (2.28) as:

$$S_\kappa = \rho \epsilon_{amb}, \qquad S_\epsilon = \rho C_{\epsilon 2} \frac{\epsilon_{amb}^2}{\kappa_{amb}} \tag{2.28}$$

where ρ is the fluid density, $C_{\epsilon 2} = 1.92$ is $\kappa - \epsilon$ constant, κ_{amb} and ϵ_{amb} are the turbulence kinetic energy and dissipation at the inlet respectively. A source term for the vegetative canopy is also used by Rethore et al. (2009) for a wind turbine with different parameters adapted for wind turbine application. Olson

et al. (2021) later tuned the parameters by using tidal turbine experiments of Mycek et al. (2014b) as:

$$S_k = \frac{1}{2} C_x \left(\beta_{\mathrm{p}} U^3 - \beta_{\mathrm{d}} U k \right) \tag{2.29}$$

$$S_\epsilon = \frac{1}{2} C_x \left(\beta_{\mathrm{p}} C_{\epsilon 4} \frac{\epsilon}{k} U^3 - \beta_{\mathrm{d}} C_{\epsilon 5} U \epsilon \right) \tag{2.30}$$

$$C_x = \rho A_d K \tag{2.31}$$

Where C_x is the scaled term defined in terms of the resistance coefficient K (function of C_T, Eq. (2.20)), β_p, β_d, $C_{\epsilon 4}$, and $C_{\epsilon 5}$ are the turning parameters, κ is the turbulent kinetic energy, ϵ the turbulent dissipation, and U is the flow velocity. In this study, the method of Olson et al. (2021) for the tidal turbine is applied to the disk location afterward.

2.5 Validation

In this section, the performance of ADM is analyzed with well-established experimental studies. The understanding of wake interaction in a single turbine will provide vital insight into the arrays of the turbine. The reference cases to be explored here are the porous disk experimental study reported by Bahaj et al. (2007) and the flume test of a 3-bladed tidal stream turbine studied by Mycek et al. (2014b).

2.5.1 Bahaj et al. porous disk experiment

A reference experiment of the tidal turbine using a porous disk was conducted by Bahaj et al. (2007) at the University of Southampton and is used to develop a numerical model. The channel measures 21 m in length, 1.37 m wide, and has a water depth of 0.3 m. The disk, presented in Figure 2.8 has a diameter of 0.1 m with ranging porosity (ratio of open to closed areas), and the water velocity was measured at a location downstream with Acoustic Doppler Velocimeter (ADV) at a rate of 50Hz.

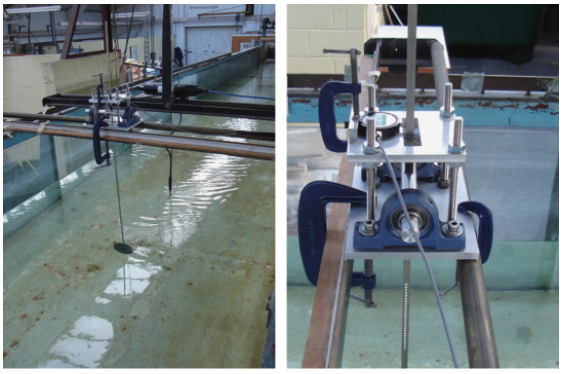

Figure 2.8 Bahaj et al. (2007) experimental setup.

2.5.1.1 Case set up

Details from the experimental setup were used to develop a similar numerical model as shown in Figure 2.9. The length of the domain is 5 m, the width is 1.36 m, and the water height is 0.3 m. The disk of 0.1 m diameter with thickness e 0.01 m is located 2 m from the inlet at the center of the water column as shown in Figure 2.9. The numerical domain has a blockage ratio of 1.92%, where the blockage ratio is defined as the ratio between the actuator disk to the total cross-sectional area of the domain. The numerical domain is discretized as elaborated in Section § 2.4.1.

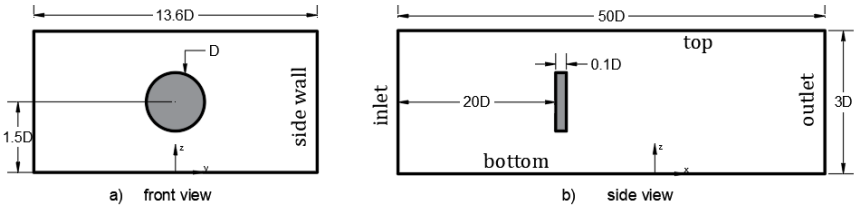

Figure 2.9 Schematic representation of the numerical domain.

2.5.1.2 Boundary Condition

At the inlet of the domain, a velocity profile $U(z)$ defined by the curved fitting of the Dyer boundary layer model is stated in Eq. (2.32). As defined by Harrison et al. (2010b), a constant turbulent kinetic energy, κ, and dissipation, ϵ are calculated by Eq. (2.33). The ambient turbulence intensity at the inlet is 5% as in the reference case (Harrison et al., 2010b; Nguyen et al., 2016). The bottom wall is set to no-slip while the top and sidewalls were set as free slip. The outlet pressure is set to zero gradients. Table 2.1 summarize the numerical settings for the simulation.

$$U(z) = 2.5U^* \ln\left(\frac{zU^*}{\nu}\right) + A \tag{2.32}$$

$$k = \frac{3}{2}I^2U^2, \qquad \epsilon = C_\mu^{\frac{3}{4}}\frac{k^{\frac{3}{2}}}{l} \tag{2.33}$$

where the friction velocity is $U^* = 0.00787\text{m s}^{-1}$, $A = 0.197$ m s^{-1}, ν is the kinematic viscosity, U is the mean inlet velocity, $I_H(z)$ is the turbulence intensity, l is $0.07H$ and is the characteristic length, $C_\mu = 0.09$, and z_o is the roughness length.

Table 2.1 CFD model parameters for the simulation of the actuator disk.

Numerical parameter	**settings**
Turbulence model	Standard k-epsilon
Inlet	Eqs. (2.32) and (2.33)
Outlet	Zero gradient (von Neumann BC)
Bottom	No-slip condition (Dirichlet BC)
Top and side walls	Symmetry (von Neumann BC)
Resistance coefficient, K	2 (corresponds to $C_T = 0.89$)

2.5.1.3 Comparison with experiments

Figure 2.10 shows the numerical result is in good agreement with both the CFD result of Nguyen et al. (2016) and the experimental result of Bahaj et al. (2007). The velocity deficit in the near wake is higher due to the extraction of energy by the rotor. This region is characterized to have the highest turbulence intensity due to the contribution of shear and porous disk as shown in Fig. 2.10b. As the flow propagates downstream, the velocity deficit increases up to 90% at 20 D downstream where the ambient turbulence in the flow recovers. The recovery to the upstream condition is delayed as a result of low ambient turbulence. The vertical profile presented in Fig. 2.11 shows that the Dyer Boundary layer significantly captures the experimental velocity profile at different locations downstream. A no-slip at the wall and free-slip surface tally well with the experiment. The delayed recovery of inlet condition is due to a slow mixing process at low ambient turbulence intensity. The distance $1 < z/D < 2$, represents the location from the disk, wherein near the wake (<7 D) the wake shape is highly affected by the turbine. From 10 D downstream on-wards, the velocity deficit profile and turbulent intensity assume a self-similarity.

In summary, the simple actuator disk approach mimics energy extraction through a porous disk. The ADM with κ-ϵ model does not require additional source term to represent the porous disk, but is it required for a tidal turbine? Next, the

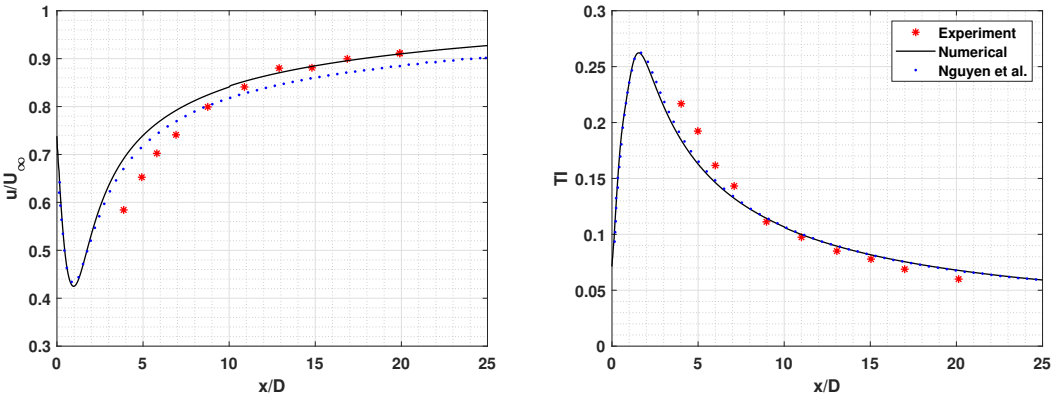

(a) **(b)**

Figure 2.10 Model validation with experimental results of Bahaj et al. (2007) and CFD results of Nguyen et al. (2016); (a) normalized axial velocity and (b) turbulence intensity along the disk axis.

application of the ADM to the actual turbine will be examined in order to answer this question. This model will give way to our subsequent investigation of arrays where wake interaction is the main area of interest.

2.5.2 Mycek et al. TST experiment

An experimental study of 3-bladed TST is conducted at IFREMER with a turbine diameter D of 0.7 m positioned at the center of the tank as illustrated in Figure 2.12. The tank is 18 m long, 4 m wide and 2 m deep. Flow measurement was performed with Laser Doppler Velocimetry (LDV) systems on the grid from 1.2 D to 10 D downstream of the turbine. The turbulent intensity in the tank is 15%, and the upstream velocity in the channel is 0.83 m/s. The thrust and power coefficient recorded are $C_T = 0.75$ and $C_P = 0.38$ respectively. Interested readers can refer to Mycek et al. (2014b) for more details on the experimental configuration.

(a) TST prototype **(b)** Schematic side view

Figure 2.12 TST experimental setup of Mycek et al. (2014b) at IFREMER.

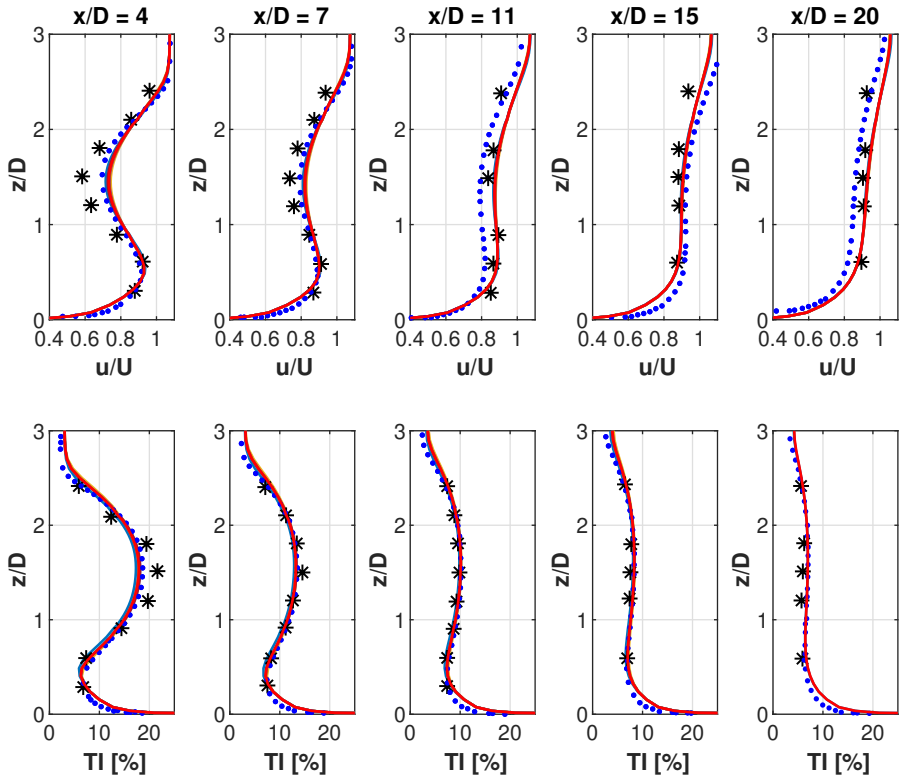

Figure 2.11 Vertical profile of velocity and turbulence intensity at different locations downstream. The solid line presents the CFD solution, the $*$ presents the experimental result reported by Bahaj et al. (2007) and the dot presents the CFD result of Nguyen et al. (2016).

2.5.2.1 Case set up

The numerical domain with dimension reported by Mycek et al. is developed as shown in Figure 2.13. The TST is modeled as an actuator disk as defined in Section § 2.4.2. Similarly, the numerical domain is discretized with optimized mesh presented in Section § 2.4.1. The domain has a blockage ratio of 4.81%.

2.5.2.2 Boundary condition

At the inlet boundary, a logarithmic velocity is set using the *atmBoundaryLayer* in *OpenFOAM* as expressed in Eq. (2.34). A constant turbulent kinetic energy and dissipation following Eq. (2.33) is imposed. At the outlet, a zero-pressure condition is imposed. Whereas, a no-slip wall condition is fixed at the bottom, and a symmetry condition is used at the top surface and the lateral walls.

$$U = \frac{U^*}{\kappa} \ln\left(\frac{z + z_0}{z_0}\right) \tag{2.34}$$

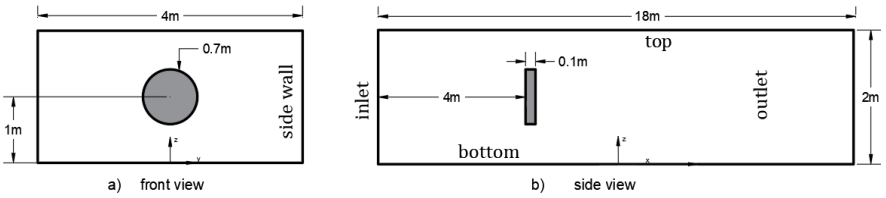

Figure 2.13 Schematic diagram of Mycek et al. experiment showing the (a) front and (b) side view.

Where U^* is the frictional velocity of $U_{ref} = 0.83$m/s, $\kappa = 0.41$ is the von Karman constant, z is the channel depth, z_0 is the roughness and L is the turbulent length scale defined as the turbine diameter.

2.5.2.3 Comparison with experiment

Figure 2.14 shows the numerical model is comparable with the experimental data, especially in the far wake. The added source term compensates for the turbulent intensity in the near wake due to blade rotation and the mean shear at the blade's tip. Although there is no significant effect of the source term in the velocity deficit profile at 2 D downstream, the AD is able to capture the flow in the far-wake region. Starting from 6 D downstream (i.e. the far wake region), the numerical and experimental results superimpose downstream. The effect of the added source term is negligible in both normalized velocity and turbulent intensity in the far wake. The wake recovery is observed at 7 D where the wake profile can be largely defined as self-similar.

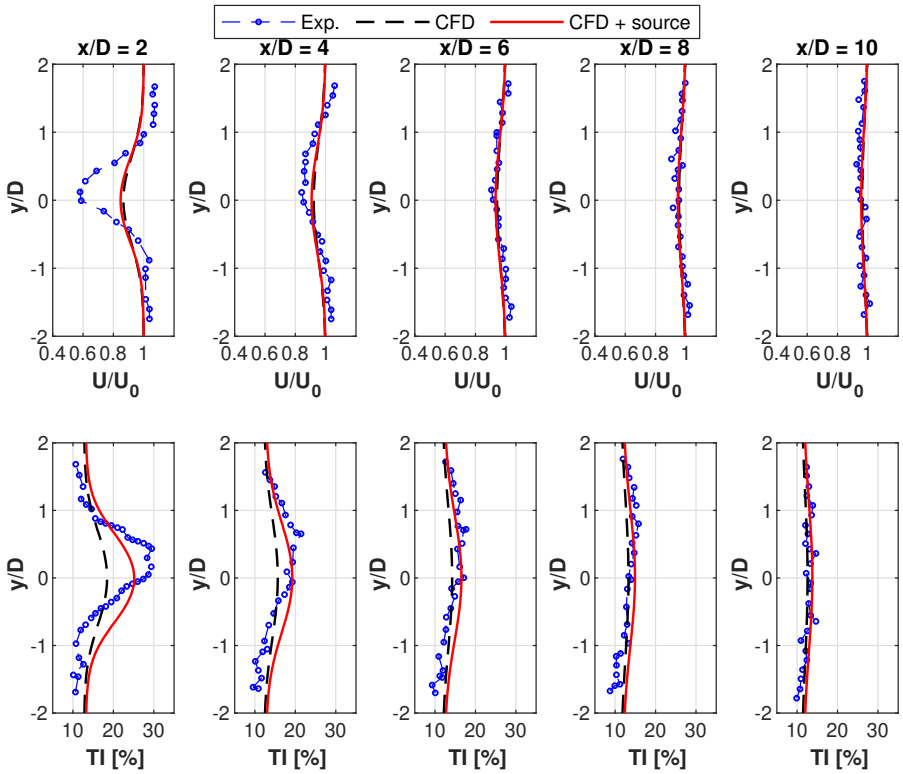

Figure 2.14 Comparison of a numerical model with TST experimental results Mycek et al. (2014b) at 15% ambient turbulence showing (a) Normalized velocity and (b) turbulence intensity along the lateral plane.

2.6 Synthesis

As already established in the literature, the ADM model with standard $\kappa - \epsilon$ model predicts the wake recovery at a much faster rate in the near wake than the experimental data due to high eddy viscosity (Rethore et al., 2009). The numerical model developed using a simple actuator disk representation has proven to provide a good estimation of the velocity deficit and turbulence intensity, especially in the far wake. The model is validated with a porous disk and a real tidal turbine experiment.

For a simple porous disk experiment, the standard $\kappa - \epsilon$ model is able to predict the flow characteristics without the use of a source term, but the source term is needed to compensate for additional turbulence production in tidal turbine experiments. In addition, The tidal turbine experimental results are not truly axisymmetrical as reported by Maganga et al. (2010) and Mycek et al. (2014b). The ADM does not detect the asymmetry because (a) the thrust is uniformly applied on the disk, (b) there is no turbine tower presentation in the actuator disk model, and (c) no swirling effect due to turbine rotation (Grondeau et al., 2022). Therefore, the average wake characteristics are modeled using the RANS

with correct turbulence parameters when the far wake is of interest.

We have seen that the ambient condition significantly affects the recovery rate. For high turbulence intensity, the inlet conditions were recovered at 7 D downstream. In the low ambient turbulence case, the inlet conditions of the porous disk experiment were not recovered until 20 D downstream. This shows how the turbulent intensity affects the flow recovery in the tidal turbine wake. Finally, the ADM can be used when studying the far-wake which is the scope of this thesis. Thus this numerical model will provide the basis for the full-scale TST model. A number of turbine arrays will be simulated for several configurations of an ideal Alderney Race site. This will be used as a reference for comparison with our proposed analytical model.

Chapter 3

Added turbulence model

Contents

This chapter aims to develop a model to estimate the added turbulence in turbine wake. A numerical simulation of a full-scale tidal turbine at different ambient conditions is used as a reference for the empirical model. The model aims to provide a good estimation of velocity deficit in the wake of a tidal farm. This chapter is an extended version of the author's article published in Applied Ocean Research (Shariff and Guillou, 2022b).

3.1 Introduction

Although there is considerable research work to estimate the velocity deficit and the power production in turbine farms, little work is established to estimate the turbulence intensity in tidal turbine wake. Turbulence in the turbine wake is associated with increased fatigue and decreased output power which may lead to premature turbine failure. Tidal turbines are deployed in turbulent flows, with sudden variations of flow characteristics along tidal cycles. Typically, turbines operate in clusters in farms which causes the downstream turbines to operate in the turbulent wake of upstream turbines. A proper estimation of turbulence wake is important as it will improve reliability and improve the confidence of developers and investors. This chapter aims to develop a simple empirical model using data fitting from numerical simulation of a non-rotational actuator disk model to estimate the added turbulence in realistic tidal stream conditions similar to the Alderney Race, with a turbine rotor diameter to depth ratio of 40%.

3.2 Turbulence in turbine wake

Turbulent intensity is defined as a ratio of standard deviation (σ) or turbulent velocity fluctuation ($\overline{u'}$) to the mean velocity ($\overline{U}$) expressed as Eq. (3.1):

$$\mathrm{I} = \frac{\sigma_{\mathrm{u}}}{\mathrm{U}} = \frac{\sqrt{\overline{u'u'}}}{\overline{U}} \tag{3.1}$$

Turbulence in turbine wake is the contribution of both the ambient and added turbulence generated by the turbine. The ambient, non-obstruct turbulence is defined as the 'normal' turbulence at a site that would be experienced by a single, stand-alone turbine. While added turbulence is the increased turbulence in the turbine wake associated with a strong shear layer between the wake and ambient flow and the turbulence generated by the turbine blade. The turbulence in the turbine wake is expressed as:

$$\mathrm{I}_{\mathrm{wake}} = \left(\mathrm{I}_0^2 + \mathrm{I}_+^2\right)^{0.5} \tag{3.2}$$

where I_{wake} is the total turbulence in the wake, I_0 is the ambient turbulence and I_+ is the added turbulence by the rotor.

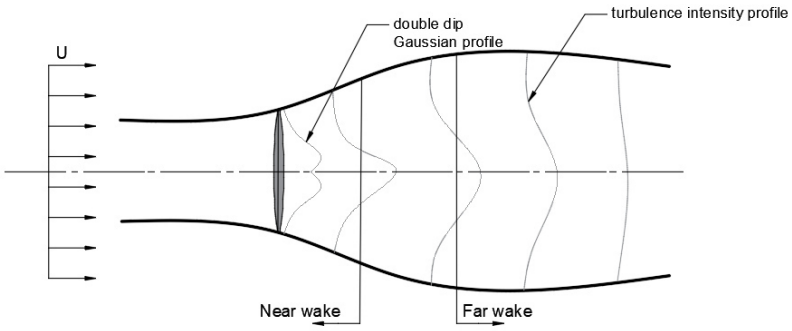

Figure 3.1 Schematic representation of the wake behind a tidal turbine showing the evolution of turbulent intensity downstream along the lateral plane.

The turbine wake is broadly categorized into two regions; near wake and far wake (Quarton and Ainslie, 1990; Vermeer et al., 2003). The intensity of turbulence varies depending on the location. The near wake region is attributed to the highest turbulence due to the additional contribution of the shear and turbine-generated turbulence, while the far wake region is mainly influenced by the ambient turbulence in the flow, as shown in Table 1.3. The estimation of far-wake turbulence is important for the proper placement of turbines in a park.

Semi-empirical turbulence models for wind turbines have been developed to estimate the far wake turbulence by calibrating experimental data and high-fidelity numerical simulations. These models, though providing approximate values yield relatively good results in the far wake region. Shamshirband et al. (2014) classify these surrogate turbulence models into four categories as follows:

1. Added turbulence model – calculated for the wake after a single turbulence

2. Added turbulence model – calculated for all surrounding turbines

3. Total turbulence model – calculated for the wake after a single turbulence

4. Total turbulence model – calculated for all surrounding turbines.

Model categories (1) and (2) estimated the added turbulence due to the turbine effect. To obtain the turbulence in the wake, the ambient turbulence is added as presented in Eq. (3.2). Model (3) provides the turbulence in the turbine wake, in a cluster network, these models will require the interaction effect of surrounding turbines. Model (4) is developed by considering the cumulative turbulence of a turbine and the surrounding effects. The following section presents the existing turbulence model for wind turbine wakes.

3.3 Existing turbulence models

Analytical models for added turbulence have been developed mainly for wind turbine applications. These models mainly provide a single value for the centreline added turbulence (Quarton and Ainslie, 1990; Hassan, 1993; Crespo and Hernandez, 1996; Frandsen, 2007) and more recently the spatial variation at any location downstream (Ishihara and Qian, 2018; Syed Ahmed Kabir et al., 2020). Recently, artificial intelligence (AI) tools like the Generic Programming (Syed Ahmed Kabir et al., 2020), and the Artificial Neural Network (Shamshirband et al., 2014; Liu et al., 2023) have been used to parameterize the added turbulence model. A brief description of these models is presented hereafter:

3.3.1 Quarton and Ainslie model

A theoretical model to predict the centerline added turbulence based on experimental data of wind turbines is proposed by Quarton and Ainslie (1990). The added turbulence in the wake is a function of the thrust coefficient C_T, the ambient turbulence, the length of the near wake, and the location downstream. The added turbulence model is expressed as Eq. (3.3):

$$I_+ = 4.8\mathrm{C_T^{0.7}I_0^{0.68}}\left(x/X_n\right)^{-0.57} \tag{3.3}$$

where C_T is the thrust coefficient, I_0 is the ambient turbulence, x is the distance downstream and X_n is the length of the near wake defined in Eq. (1.1).

3.3.2 Crespo and Hernandez model

Crespo and Hernandez (1996) propose a similar empirical relation for estimating the added turbulence in the wake of a wind turbine. The model quantitatively agrees with the Quarton and Ainslie model but demands an axial induction factor, a, instead of C_T. However, a and C_T are related in the actuator disk model (Burton et al., 2011). As the actual length of the near wake remains a conjecture, Crespo and Hernandez express the added turbulence based on well-known downstream distance as Eq. (3.4):

$$I_+ = 0.73\mathrm{a}^{0.8325}\mathrm{I_0^{0.0325}}(x/D)^{-0.32} \tag{3.4}$$

This model is applicable to far wake provided $5 < x/D < 15, 0.07 < I_0 < 0.14$, and $0.1 < a < 0.4$.

3.3.3 Frandsen and Thøgersen model

Frandsen and Thøgersen (1999) developed an empirical relation for added turbulence to account for the fatigue loading of an offshore wind farm. The model is

expressed as Eq. (3.5):

$$I_+ = \frac{1}{1.5 + 0.8\frac{x/D}{\sqrt{C_T}}} \tag{3.5}$$

where x/D is the downstream position normalized by the turbine diameter and C_T is the thrust coefficient. The Frandsen and Thøgersen model is adopted as International Electrotechnical Commission IEC 61400 standards for wind turbine design.

3.3.4 Ishihara and Qian model

A new 3D model that accounts for the spatial variation for added turbulence was developed by Ishihara and Qian (2018). This model uses a Gaussian distribution to capture the maximum turbulence intensity at the tip of the rotor. A correction term is added to account for the double Gaussian profile in the near wake, likewise $\delta(z)$ to weaken the turbulence intensity in the lower part of the wake as observed in the experiment of Chamorro and Porté-Agel (2009). The generalized 3D added turbulence model is outlined in Table 3.1.

Table 3.1 Summary of added turbulence model proposed by Ishihara and Qian (2018).

Wake model	Formulas	Parameters
wake width	$\sigma/D = k^\star x/D + \varepsilon$	$k^\star = 0.11C_T^{1.07}I_0^{0.20}$
added turbulence	$I_+(x,y,z) = \frac{\phi}{d+e\cdot x/D+p} - \delta(z)$	$\varepsilon = 0.23C_T^{-0.25}I_0^{0.17}$
shape function	$\phi = \left\{k_1 \exp\left(-\frac{(r-D/2)^2}{2\sigma^2}\right) + k_2 \exp\left(-\frac{(r+D/2)^2}{2\sigma^2}\right)\right\}$	$d = 2.3C_T^{-1.2}$
near-wake	$p = f(1 + x/D)^{-2}$	$e = 1.0I_0^{0.1}$
deflection	$\delta(z) = \begin{cases} 0 & (z \geq H) \\ I_0 \sin^2\left(\pi\frac{H-z}{H}\right) & (z < H) \end{cases}$	$f = 0.7C_T^{-3.2}I_0^{-0.45}$

A simplified expression for center line added turbulence is expressed in Eq. (3.6).

$$I_+ = \frac{1}{d + e.x/D} \tag{3.6}$$

3.3.5 Tian et al. model

Tian et al. (2015) proposed an empirical model for the effective turbulence in turbine wake. The added turbulence is proportional to the thrust coefficient which enhances the wake flow development. The idea of this enhancement is based on the fact that the thrust force comes from a change in pressure as the wind passes the rotor and slows down, it is a measure of the power losses caused by the presence of the turbine, and further more a measure of the flow development in the wake area. The model is expressed as Eq. (3.7):

$$I_{\text{wake}} = 0.4\frac{C_T}{x/D} + I_0 \tag{3.7}$$

3.3.6 Comments

A common feature in the model Eqs.[(3.3)-(3.7)] is that the added turbulence is a function of the ambient turbulence, turbine characteristics C_T in the wake of the wind turbine and location downstream. However, these turbulence models, like velocity deficit models, may require calibration for application in tidal turbine wake. The calibration is necessary as a result of the limited depth in shallow water, the blockage effect, the wide range of ambient turbulence in tidal sites, the bathymetry of the seabed, and the wave effect on the surface.

To the best of our knowledge, there is no empirical model to estimate the turbulent intensity in the wake of a tidal turbine. In the subsequent sections, a simple empirical model for added turbulence intensity in the wake of a full-scale tidal turbine is developed and compared with the established wind turbine models noted. As the experimental data of full-scale tidal turbines remain confidential, a numerical model is proposed to provide reference data for the turbulence model.

3.4 Tidal turbine with realistic dimension

3.4.1 Numerical model and method

Several CFD simulations of tidal turbines used steady-state solutions to provide the average hydrodynamics of the flow. Although in reality, a significant fluctuation occurs with eddies structure in a streamwise direction roughly as large as the turbine diameter (Gant and Stallard, 2008), the changes in mean performance are similar to a steady flow condition (Zhang et al., 2020a). The turbine is represented as a non-rotating porous disk using the Actuator disk Method (ADM). The ADM is widely used for full-scale turbines by several authors (Rahman et al., 2018; Nguyen et al., 2019; Thiébot et al., 2020; Djama Dirieh et al., 2022). Recall that in Section §2.5, the numerical simulation with ADM has been validated with porous disk and tidal turbine experiments with relatively good results in the far wake. The uniform thrust force applied to the disk region in Eq. (2.21) is:

$$T = \frac{1}{2}\rho K A U_d^2$$

where ρ is the fluid density (i.e sea water), K is the resistance coefficient relating to C_T, A is the turbine cross-sectional area and U_d is current velocity at the disk location.

3.4.1.1 Case set-up

The size of commercial-scale tidal turbines has been increasing recently with turbines ranging from 14 m to 20 m in diameter (Rajgor, 2016). In this study, a 20 m diameter turbine (the size for Atlantis AR2000) represented as a disk is located at 10 D from the inlet of the domain at mid-depth (see Fig. 3.2). The length of the domain is 50 D and the width is 20 D. The channel depth is 50 m similar to the Alderney Race (Lo Brutto et al., 2016b). The blockage ratio in the channel is 1.57% and the rotor diameter to depth ratio is 40%. For consistent meshing, the numerical domain is discretized by structured grid cells with refinement close to the turbine as elaborated in Section § 2.4.1.

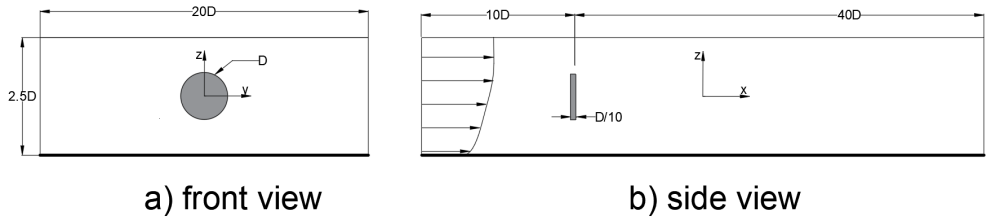

Figure 3.2 Computational domain showing the channel dimension.

3.4.1.2 Boundary conditions

A realistic boundary condition of a typical tidal stream is used for the numerical model. At the channel's inlet, a logarithmic velocity is defined and a constant turbulence kinetic energy (TKE) and dissipation are expressed in Eq. (3.8).

$$U = \frac{U^*}{\kappa} \ln\left(\frac{z}{z_0}\right), \qquad k = \frac{3}{2} I^2 U^2, \qquad \epsilon = C_\mu^{\frac{3}{4}} \frac{k^{\frac{3}{2}}}{L} \tag{3.8}$$

Where the friction velocity $U^* = 0.1109 m/s$, the mean inlet velocity $U = 2.7 m/s$ similar to the mean velocity in the Alderney Race (Thiébaut et al., 2020). The turbulence length scale $L = H/3$ is used which is shown to provide good agreement with experimental data as reported by Blackmore et al. (2011) and is also used by Rahman et al. (2018) for full-scale tidal turbine simulations. The bottom roughness of the channel is not considered in this study; a no-slip condition is set at the bottom wall with wall functions, and the top and the lateral walls are set to a symmetry condition. The outlet of the domain is set to pressure outlet conditions corresponding to atmospheric pressure.

In this study, the ambient turbulent intensity I_0 of 5% to 20% is considered to have a global representation of turbulence conditions in the tidal stream site as presented in Table 1.2. These field observations presented are usually limited to a particular location of interest and do not represent global tidal stream hydrodynamics. In the absence of complete hydrodynamic data, the local measurements

are used as ambient conditions in the channel. The thrust coefficient $C_T = 0.89$ ($K = 2$) corresponding to the Betz limit is used. It is important to clarify that experimental data are not available at this scale of a tidal turbine to fine-tune the turbulence source term parameters to account for the turbine effect, therefore a standard $\kappa - \epsilon$ is used.

However, for empirical models, a definitive value of turbulent intensity upstream of the turbine is essential which can be uncertain in simulation due to turbulence dissipation downstream, especially at high turbulent intensity. Therefore, the inlet turbulence condition is maintained in the upstream region to ensure stable turbulence upstream. This is analogous to the turbulence source term used for wind turbines by El Kasmi and Masson (2008).

3.5 Turbulent wake analysis

The turbulent intensity contour of turbine wakes at different ambient turbulence is shown in Figure 3.3. The maximum turbulent intensity in the wake occurs in the initial near wake. The initial near wake is the region behind the turbine where the pressure jump due to momentum extraction is largely recovered. Crespo and Hernandez (1996) define this length as 1-2 D for a wind turbine. This is also consistent with our numerical data as shown in Figure 3.3. The major contributor to turbulence in this region is the rotor and a mean shear layer. Experimental studies of turbine wake show the turbulent intensity profile exhibits a double Gaussian profile with maximum turbulence at the tip of the blade (Chamorro and Porté-Agel, 2009; Stallard et al., 2013). However, the profile merges downstream foaming an approximate Gaussian profile downstream. The RANS-ADM does not provide a good representation of turbulence in the near wake. This is attributed to the averaging of flow components by the RANS turbulence model and the uniform thrust force along the non-rotating actuator disk.

In the far wake, the turbine effect and the mean shear are weak compared to the near wake. The Gaussian profile is sustained for the low turbulence case (I_0 = 5%) but vanishes in high turbulent cases (see Figure 3.3). The turbulent effects vanish rapidly at high turbulence due to strong mixing. The turbulent intensity along the rotor axis and the lateral wall is imperceptible, therefore recognizing the dominance of ambient turbulence in the far wake region. High turbulence produces large turbulent scales that cascade and diminish faster than small eddies. Faster flow recovery at high ambient turbulence is reported in experiments (Mycek et al., 2014a; Vinod and Banerjee, 2019).

3.5.1 Estimation of centerline added turbulence

The centerline turbulence is the total turbulence in the wake as expressed in Eq. (3.2). Added turbulence in the wake is extracted by subtracting the root sum squared of wake turbulence at the centerline and the ambient turbulence close to

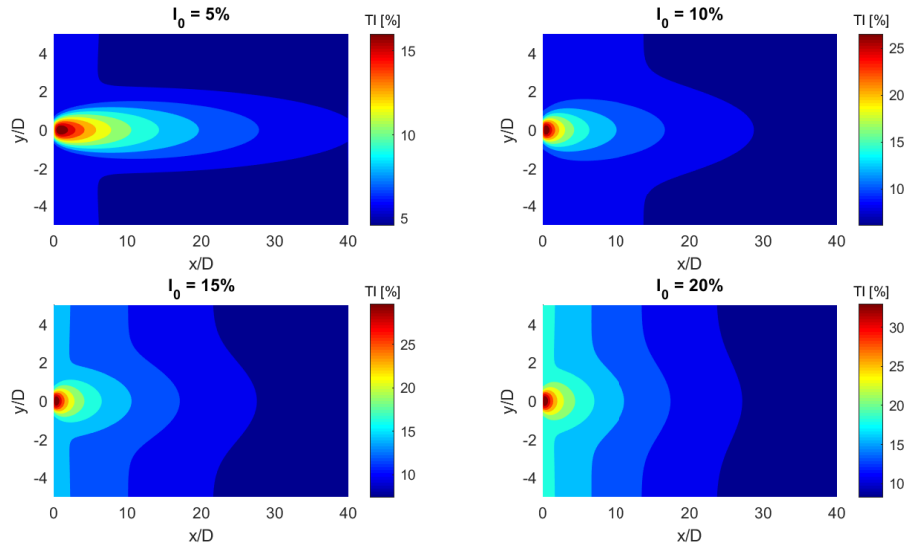

Figure 3.3 Turbulent intensity contour plot at different ambient conditions showing the effect of added turbulence by the rotor in the near wake region.

the lateral wall. The turbulent intensity close to the lateral surface is assumed at the ambient state as it is far away from the rotor, as shown in Figure 3.4.

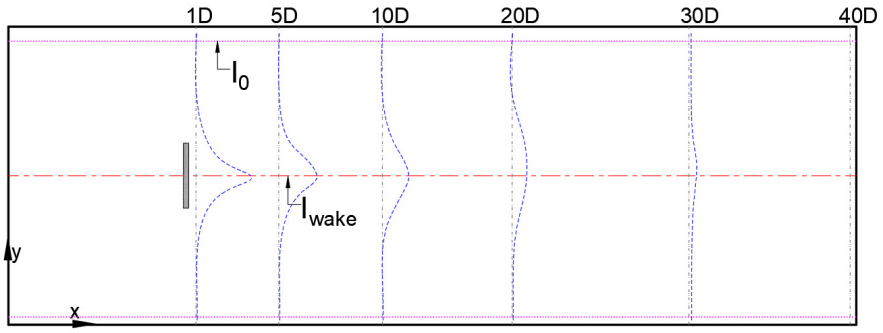

Figure 3.4 Lateral plane showing the position of ambient and total wake turbulence in the channel.

Assuming the ambient turbulence is stable in the flow. It is sufficient to propose a model for the added turbulence to estimate the turbulence in the wake. As mentioned earlier, the inlet turbulent condition is maintained upstream of the turbine to preclude dissipation due to the numerical model, as shown in Figure 3.5a. The added turbulence in Fig. 3.5b shows a slight dependence of the ambient turbulence in the flow. Added turbulence decays downstream as a result of the mixing and diffusion process in the wake. The diffusion at high ambient turbulence is accelerated leading to faster flow recovery. For instance, Fig. 3.5a shows for 5% ambient turbulence, turbulent intensity recovers around 30 D downstream

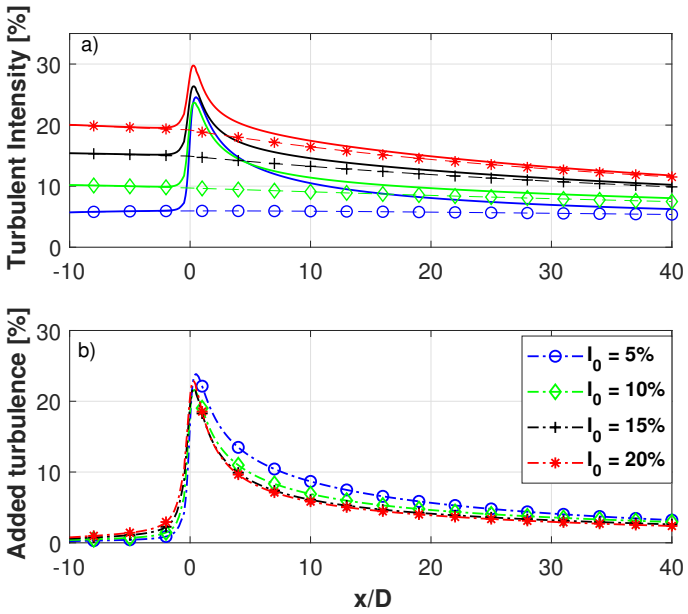

Figure 3.5 Centerline turbine wake turbulence at different ambient turbulent intensities showing (a) the total turbulence (solid) and ambient turbulence (dash); (b) the added turbulence (dash-dot).

whereas, for 15% turbulence, the recovery is around 12 D downstream.

3.5.2 Estimation of turbulent intensity wake radius

The classical turbulence theory suggests that the velocity deficit wakes behind a circular disk is approximately Gaussian and axisymmetry in the far wake region (Pope, 2000). Therefore, to develop a new method to estimate the turbulent wake radius, firstly, there is a need to verify the Gaussian and axisymmetry profile of turbulent intensity wake, as suggested for velocity deficit wake by Stallard et al. (2015). Figure 3.6 verified the Gaussian-shaped profile in the wake of turbulent intensity.

The added turbulent wake radius is estimated using a standard Gaussian profile's Full-Width Half Maximum (FWHM) approach. Turbulent intensity at the FWHM corresponds to $\sqrt{2\ln 2}\sigma$ (σ is the standard deviation). FWHM is used previously to define the radius in the velocity deficit wake of a wind turbine (Bastankhah and Porté-Agel, 2014; Ishihara and Qian, 2018). $r_{1/2}$ is the radius at the half normalized turbulent intensity I_m. The radius of the wake using the Gaussian distribution function is estimated at 3σ shown as the shaded region in Figure 3.6.

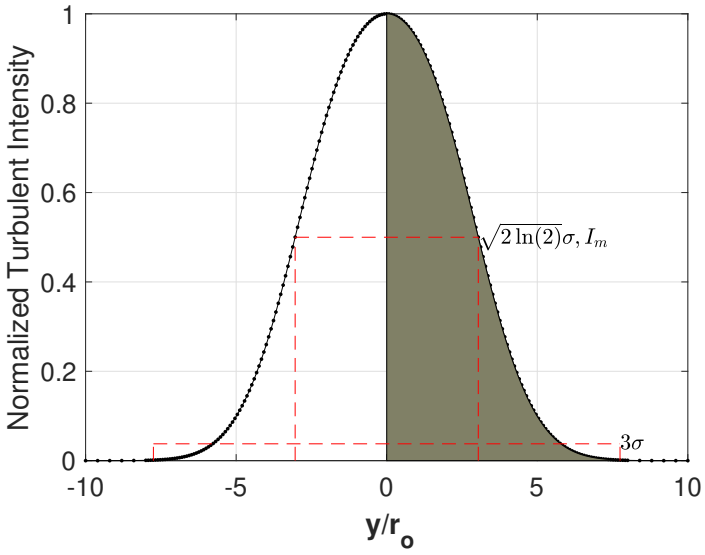

Figure 3.6 Normalized turbulent intensity profile in the transverse direction ($I_a = 10\%$; x = 10 D) follows the Gaussian law. The shaded area shows the turbulent wake radius.

3.5.3 Turbulent wake expansion

Analytical models of Jensen (1983), Bastankhah and Porté-Agel (2014) and Ishihara and Qian (2018) assume linear expansion of wake. This simple assumption allows ease of implementation into the analytical model. Lo Brutto et al. (2016a) use exponential law to define the velocity deficit wake expansion, but Frandsen et al. (2006) and Larsen et al. (1996) suggest the linear assumption is a crude representation, therefore they proposed a power law to define the wake expansion as defined in classical wake turbulence theory (Schlichting and Gersten, 1951).

The added turbulent wake radius defined in Section §3.5.2 is calculated at an interval of 1 D. Figure 3.7a shows a similar wake radius pattern at different turbulent intensities. From Figure 3.7a, it is clear that the use of the basic linear assumption of wake expansion by Jensen and Bastankhah and Porté-Agel will result in a poor estimation of added turbulent wake radius evolution. Empirical laws approximate complex relations that rely on observation data. It is necessary to verify the data can be represented by a power-law distribution. Taking the logarithm of both sides of Eq. (3.9), we see the power-law distribution is simplified as; $\ln p(x) = \alpha \ln x +$ constant. A necessary condition for power-law distribution is a straight line on a doubly logarithmic plot (Milojević, 2010). Figure 3.7b shows that one can be confident the radius approximately obeys the power-law distribution.

$$p(x) \propto x^{\alpha} \tag{3.9}$$

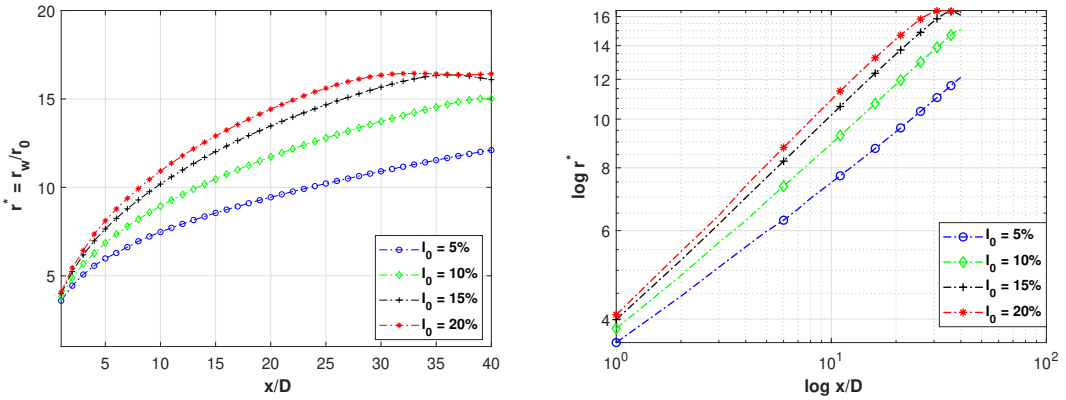

(a) Normalized turbulent wake radius **(b)** log-log plot justifying the use of power-law

Figure 3.7 Added turbulence wake radius at different ambient turbulence.

3.6 New empirical models

3.6.1 Turbulent wake radius model

A nonlinear fit in MATLAB is used to model the propagation of the wake radius as shown in Figure 3.8. The use of the power law as the model equation provides a good evolution of the radius. The empirical turbulent wake radius is valid up to the turbulent wake length and expressed as Eq. (3.10):

$$r_w^* = r/r_o = 7.41 I_0^{0.3} \left(\frac{x}{D}\right)^{0.384} \tag{3.10}$$

where r_w is the normalized turbulent wake radius, r is the local turbulent wake radius, r_o is the turbine radius, x/D is the normalized distance downstream and I_0 is the ambient turbulence in fraction form. Tidal stream turbines are located in shallow water, and the vertical boundaries limit the turbine wake expansion. This model applies to the wake of a turbine at a rotor diameter-to-depth ratio is 40%.

3.6.2 Added turbulent intensity model

The previous models of added turbulence in the wake of a wind turbine are expressed as a function of turbine and flow characteristics (Crespo and Hernandez, 1996; Frandsen and Thøgersen, 1999). Using our numerical data as reference, a simple empirical model is developed using a data fitting to estimate the added turbulence in the wake of a tidal turbine. The centerline turbulent intensity profile in Fig. 3.5b shows a decay in added turbulent intensity downstream. The new centerline added turbulent intensity model is expressed as Eq. (3.11):

$$I_+ = a\left(\frac{X - X_0}{D}\right)^{-b} \qquad \begin{cases} a = 0.16 C_T^{4.83} + 0.179 \\ b = 0.68 I_0 + 0.472 \end{cases} \tag{3.11}$$

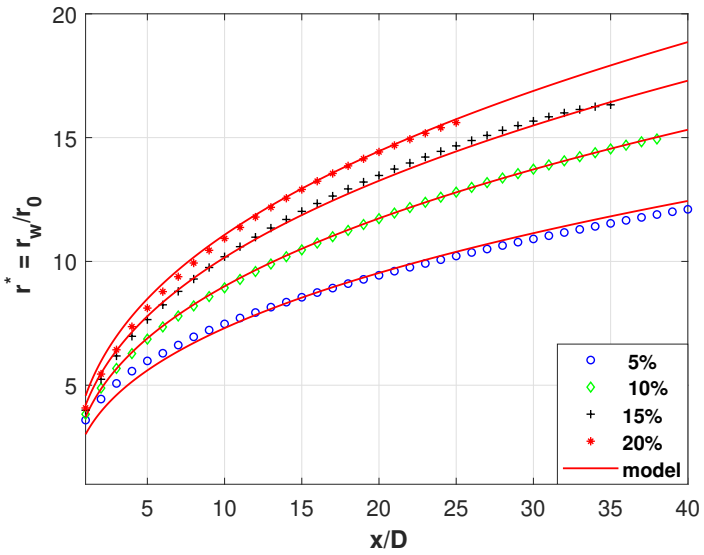

Figure 3.8 Turbulent wake radius at different ambient turbulent intensities showing the wake expansion downstream. The solid line is the empirical model fitting the numerical data at $C_T = 0.89$ (Betz limit).

The added turbulence due to the rotor is slightly dependent on ambient turbulent intensity. This is compatible with the model of Frandsen and Thøgersen (1999) which is independent of ambient turbulence (see Eq. (3.5)). Figure 3.9 compares the proposed model to the existing empirical model for a wind turbine, To our knowledge no added turbulence model was established prior to this work for the tidal turbine. The turbine wake is reconstructed using Eq. (3.2), the proposed model estimates the turbulence intensity wake at different turbulent intensities, as shown in Figures 3.10.

Furthermore, the proposed model is validated by the tidal turbine experiment of Mycek et al. (2014b) and LES simulations of Grondeau et al. (2022) as shown in Figure 3.11. The RANS and empirical model were able to provide reasonable average turbulence in the far wake compared to the LES and experimental data. The low computational cost of RANS will facilitate the study of multiple turbine configurations and flow conditions in a park. This model can provide a suitable location for turbine placements in the far wake where the ambient turbulence is largely recovered.

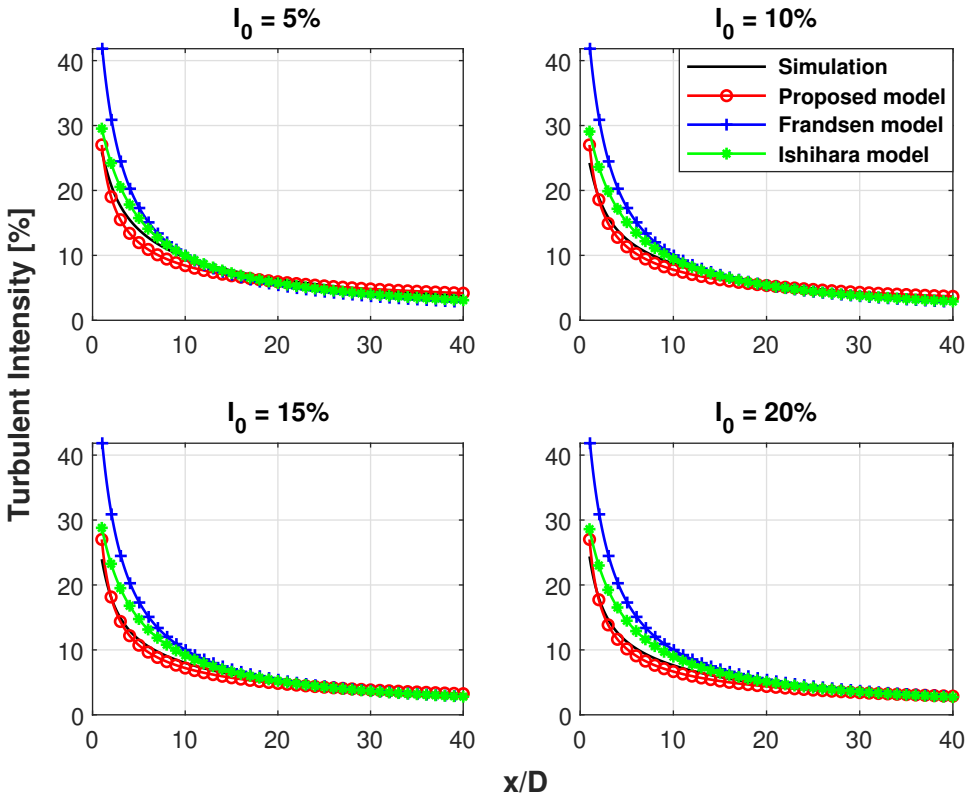

Figure 3.9 Comparison of centerline added turbulent intensity models with numerical simulation at different turbulent intensities.

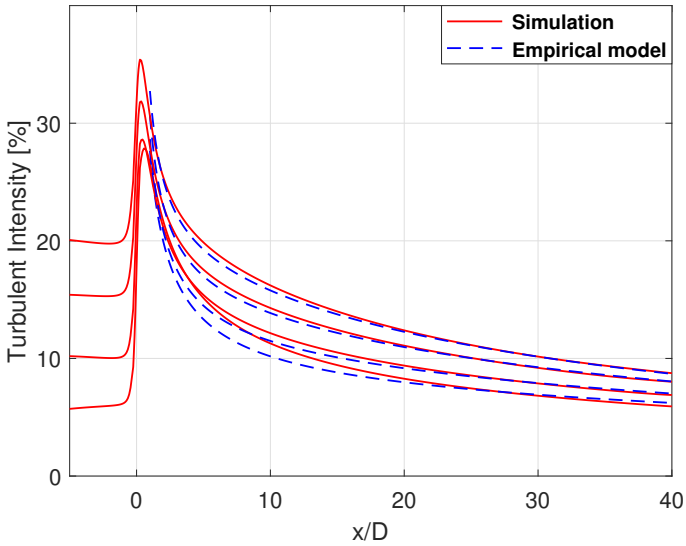

Figure 3.10 Comparison of reconstructed axial turbulence intensity from the proposed model with the numerical data.

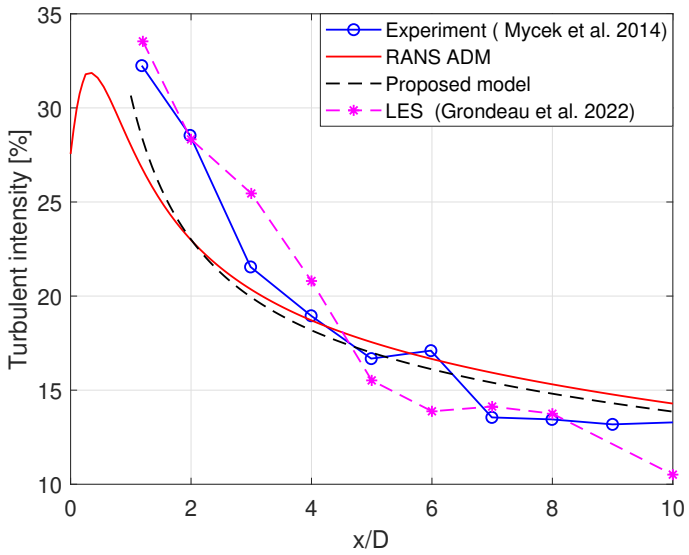

Figure 3.11 Comparison of the average turbulence intensity of the proposed empirical model with experimental data of Mycek et al. (2014b), LES data of Grondeau et al. (2022), and the RANS model with source term.

3.6.3 Goodness of fit

A measure of accuracy between the empirical and numerical model for the turbulent wake radius and the added turbulence is computed by the Mean Absolute Percentage Error (MAPE) as Eq. (3.12):

$$\text{MAPE} = \frac{1}{N}\sum_{i=1}^{N}\left|\frac{A_i - M_i}{A_i}\right| \cdot 100\% \tag{3.12}$$

where A_i is the numerical turbulent wake data and M_i is the empirical turbulent wake model at 1 D interval downstream. The mean error of the model at different ambient turbulence is given in Table 3.2. The accuracy of the model increases downstream where the turbulent characteristics are clearly defined. The near wake error may not affect the turbine placement downstream as turbines are placed at a sufficient distance downstream where the flow properties have recovered.

Table 3.2 Mean relative error of the added turbulent wake model.

Ambient turbulence I_o	5%	10%	15%	20%
Wake radius R_w (%)	2.90	0.35	1.44	2.31
Centerline I_+ (%)	8.09	6.42	5.59	6.31

3.7 Synthesis

The mixing between the high free velocity and low-velocity wake and the associated change in momentum causes the flow to recover to the upstream condition downstream. The initial wake size of the order of rotor diameter expands gradually as it propagates downstream. Ambient turbulent intensity increases the added turbulent wake radius but decreases the added turbulent wake length, as shown in Figure 3.7a. An intense mixing and diffusion of eddies that occur at high ambient turbulence promote rapid recovery of the ambient flow downstream. While in a low turbulent flow, the diffusion rate is slower, leading to propagation of the wake effect further downstream. The wake expansion far downstream at high turbulent intensity is distorted and becomes more stochastic. This might be due to (a) an ambient condition recovery as the dissipation is higher than the turbulence production effect by the disk far downstream, and (b) the limited channel depth may constrain the expansion in all directions.

The selection of power-law for turbulent wake radius is in line with the velocity deficit wake expansion model of wind turbine reported by Frandsen et al. (2006) and also in the wake theory by Schlichting and Gersten (1951) where the radius expands as $r \propto x^{1/3}$. The power-law exponent of our model is constant and comparable with that of the classical wake of a velocity deficit model. At the same time, the scaling term accommodates the dependence on ambient turbulent intensity.

The rotor's attenuation of the kinetic energy of the flow generates additional turbulence close to the turbine. As mentioned earlier, the near wake region is dominated by the turbine and shear layer-generated turbulence. Our empirical model justifies that the primary turbulence source in the near wake is attributed to the rotor. This model provides acceptable results compared with existing models for a wind turbine as no known model is available for tidal turbine application. The error between our model and existing wind turbine models can be attributed to the different wake structures. The wind turbine wake is axisymmetric Ishihara and Qian (2018), while the tidal turbine wake is largely Gaussian due to the vertically constrained channel depth (Stallard et al., 2015).

Chapter 4

A generic model for velocity deficit and turbulent intensity

Contents

This chapter aims to propose a generic model to estimate the velocity deficit and the turbulence intensity in the wake of a full-scale tidal turbine. The generic model accounts for the variation in ambient turbulence, the rotor thrust coefficient, and the rotor diameter-to-depth ratio. This chapter is an extended version of the author's article submitted to the Renewable Energy journal (Shariff and Guillou, 2023b).

4.1 Introduction

The flow behind a turbine is turbulent and quite far from the ideal case presented in Section §2.3. The axial and rotational velocities, viscosity, turbulent effects, and blade rotation generate a wake region that is associated with low speed and high turbulence compared to ideal unperturbed flow. The wake is a region of disturbed flow categorized mainly into two parts; the near and the far wake region as elaborated in detail in Section §1.7. The flow velocity and turbulent intensity upon mixing with ambient flow gradually recover as we move along the flow direction as illustrated in Figure 4.1.

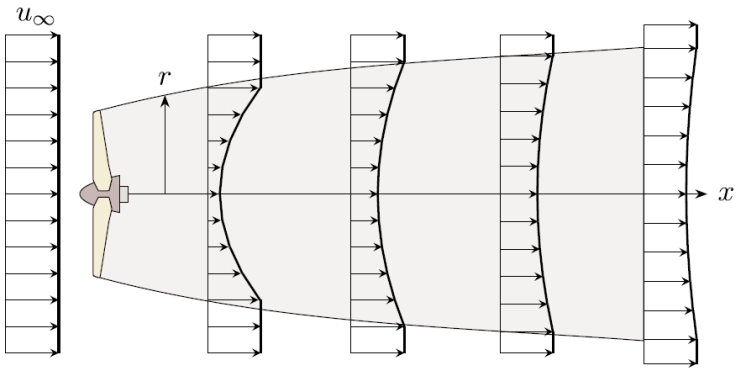

Figure 4.1 Wake behavior behind a turbine. (Source: Torabi (2022))

The investigations of turbine wake become important when dealing with several turbines on a farm. The power produced by downstream turbines is lower due to the wake effects. To have a good estimation of individual turbines, a proper wake model is required by which two main factors are to be obtained:

1. **Stream function** which is based on fundamental laws of fluid mechanics derived using mass and/or momentum conservation equations.

2. **Shape function** which describes the wake profile as it evolves downstream. The common shape functions used are top-hat, Gaussian, or cosine functions. Recently, a super-Gaussian profile has been proposed to represent both the near and far wake.

4.2 Existing velocity deficit models

The turbine wakes are studied by numerous analytical models. Some of the models are quite basic, and others are based on the principles of fluid dynamics and even turbulence modeling. To better understand the wake and its parameters, some common velocity deficit models for wind and tidal turbines are briefly discussed below. The velocity deficit in the wake of the turbine is expressed as Eq. (4.1):

$$\frac{\Delta U}{U_\infty} = \frac{U_\infty - U_w}{U_\infty} \tag{4.1}$$

where U_∞ is the upstream velocity and U_w is the wake velocity.

Table 4.1 presents a summary of the existing velocity deficit models with the proposed model.

Table 4.1 Comparison between the proposed model and the previous wake models.

Model	Principles	Profile	Wake expansion law	Added turb.	Application
Jensen (1983)	MC	top-hat	linear	–	wind turbines
Frandsen (2006)	MC & MT	top-hat	non-linear	–	wind turbines
B-P (2014)	MT	Gaussian	linear	–	wind turbines
Zhang (2020b)	MC & MT	Cosine	non-linear	Yes	wind turbines
Ishihara (2018)	MT	Gaussian	linear	–	wind turbines
Lam (2015)	MT	Gaussian	linear	–	tidal turbines
Lo Brutto (2016a)	MC	top-hat	non-linear	–	tidal turbines
Liu (2023)	MC	Gaussian	linear	–	tidal turbines
Proposed	MC	Gaussian	non-linear	Yes	tidal turbines

MC: mass conservation; MT: momentum theory.

4.2.1 Jensen model

The analytical model of the velocity deficit of wind turbines developed by Jensen (1983) and modified by Katic et al. (1987) is based on mass conservation. The velocity deficit is uniformly distributed using the top-hat shape function. This model neglects the near wake and assumes linear wake expansion as:

$$r_w = r_0 + \alpha x$$

The mass conservation of the control volume is shown by dashed lines in Fig 4.2 yields:

$$\pi r_0^2 U_{w0} + \pi(r^2 - r_0^2)U_\infty = \pi r^2 U_w \tag{4.2}$$

where U_{w0} is the velocity behind the turbine, r_0 and r are the rotor radius and the

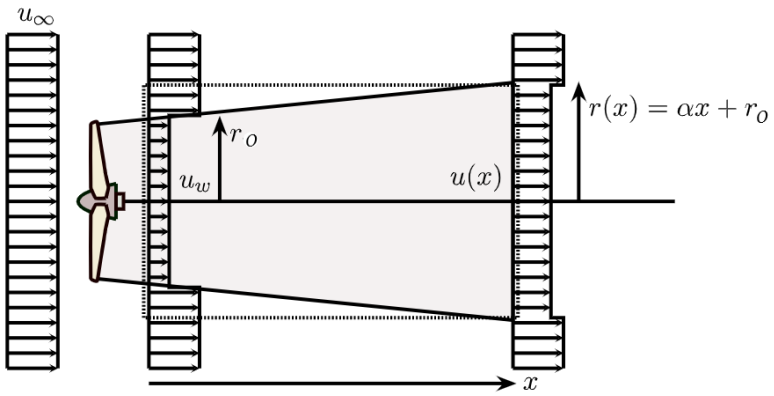

Figure 4.2 Simple linear model proposed by Jensen (Source: Torabi (2022)).

wake radius respectively. The Jensen velocity deficit is expressed as Eq. (4.3):

$$\frac{\Delta U}{U_\infty} = \frac{\left(1 - \sqrt{1 - C_T}\right)}{\left(1 + \frac{2\alpha \mathrm{x}}{D}\right)^2} \tag{4.3}$$

where C_T is the thrust coefficient, x/D is the downstream distance normalized by the turbine diameter D, and α is the rate of wake expansion coefficient. Suggested values for α are 0.075 for onshore and 0.05 for off-shore turbines (Barthelmie et al., 2006). The Jensen model is widely used by commercial tools (e.g. WindPRO, WAsP, OpenFarmer, and OpenWind).

4.2.2 Frandsen model

Frandsen et al. (2006) also assumes a top-hat shape for the velocity deficit lateral profile. In this model, the principle of mass and momentum conservation equations were applied to the control volume around the turbine. The wake expands based on the power law given in Eq. (4.4) proposed by Schlichting and Gersten (1951) is expressed as:

$$D(x) = \left(\beta^{k/2} + \alpha \mathrm{x}/D\right)^{1/k} \tag{4.4}$$

where $k = 3$ for Schlichting solution and the wake constant α determine from experiment. β is a function of C_T defined in Eq. (4.5) as:

$$\beta = \frac{1}{2}\frac{1 + \sqrt{1 - C_T}}{\sqrt{1 - C_T}} \tag{4.5}$$

The proposed wake velocity deficit is given in Eq. (4.6):

$$\frac{\Delta U}{U_\infty} = \frac{1}{2}\left(1 - \sqrt{1 - 2\frac{A_0}{A_w}C_T}\right) \tag{4.6}$$

where $A_w(x=0) = A_a$, and A_a is the cross-sectional area of the wake just after the initial wake expansion. A_a is assumed to be the area where the pressure has just reached the free state.

4.2.3 Bastankhah and Porté-Agel (B-P) model

The Bastankhah and Porté-Agel (2014) model of velocity deficit is based on the momentum conservation equation. The model uses a Gaussian shape function and also assumes a linear expansion of wind turbine wake downstream. The wake radius is evaluated at full-width half maximum of a standard Gaussian function. A linear wake expansion is considered like the one used by Jensen. The velocity deficit model is expressed as Eq. (4.7):

$$\begin{aligned}\frac{\Delta U}{U_\infty} = &\left(1 - \sqrt{1 - \frac{C_\mathrm{T}}{8\left(k^* x/d_0 + 0.2\sqrt{\beta}\right)^2}}\right) \\ &\times \exp\left(-\frac{1}{2\left(k^* x/d_0 + 0.2\sqrt{\beta}\right)^2}\left\{\left(\frac{z - z_\mathrm{h}}{d_0}\right)^2 + \left(\frac{y}{d_0}\right)^2\right\}\right)\end{aligned} \tag{4.7}$$

where β is obtained from Eq. (4.5) and k^* is the empirical constants determined by the turbulent intensity and thrust coefficient calibrated from experimental data.

4.2.4 Zhang et al. model

Zhang et al. (2020b) proposed a self-similar model for the far wake velocity deficit of wind turbines using both mass and momentum conservation equations. A trigonometric distribution using a cosine shape function is used in place of the classical Gaussian function. The velocity deficit is expressed by Eq. (4.8):

$$\begin{aligned}\frac{\Delta U}{U_\infty} = &\left(\frac{\pi^2 - 4}{3\pi^2 - 16} - \sqrt{\left(\frac{\pi^2 - 4}{3\pi^2 - 16}\right)^2 - \frac{\pi^2 C_T}{3\pi^2 - 16}\left(\frac{r_0}{r_W}\right)^2}\right) \\ &\times \left(\cos\left(\frac{\pi}{r_W} r\right) + 1\right)\end{aligned} \tag{4.8}$$

The authors maintain that the use of trigonometric functions is physically more intuitive and appealing to practice. A non-linear wake expansion model accounting for the ambient and added turbulence is used to estimate the wake radius expressed in Eq. (4.9):

$$r_w = r_0 + \frac{x}{I_0}\left(\frac{0.5\sqrt{I_0^2 + I_+^2}}{\ln\left(z_h/z_0\right)}\right) \tag{4.9}$$

The added turbulence model I_+ proposed by Crespo and Hernandez (1996)

(see Section §3.3.2 for more details) is used to estimate the turbulence in the wake as a function of thrust coefficient and ambient turbulence.

4.2.5 Ishihara and Qian model

Ishihara and Qian (2018) modified the B-P model to estimate the velocity deficit in both near and far wake. The 3-D model considers both the ambient turbulence intensity and the thrust coefficient. A wake expansion model is similar to the one proposed in the BP model. The model parameters are developed from data fitting of experimental and LES data. The model equations are summarized in Table 4.2.

Table 4.2 Summary of velocity deficit model proposed by Ishihara and Qian (2018).

Wake model	Formulas	Parameters
wake width	$\sigma/D = k^{\star}x/D + \varepsilon$	$k^{\star} = 0.11C_T^{1.07}I_a^{0.20}$
velocity deficit	$\Delta U(x,y,z)/U_h = \frac{\phi(r/\sigma)}{\{a+b\cdot x/D+c(1+x/D)^{-2}\}^2}$	$\varepsilon = 0.23C_T^{-0.25}I_a^{0.17}$
shape function	$\phi = \exp\left(-\frac{r^2}{2\sigma^2}\right)$	$a = 0.93C_T^{-0.75}I_a^{0.17}$
radius	$r = \sqrt{y^2+(z-H)^2}$	$b = 0.42C_T^{0.6}I_a^{0.2}$
		$c = 0.15C_T^{-0.25}I_a^{-0.7}$

4.2.6 Lam et al. model

Lam et al. (2015) model is potentially the first analytical model developed for the tidal turbine application. The analytical model is derived from a ship propeller. The efflux velocity (minimum velocity) at the turbine location is determined from the axial momentum equation. A Gaussian distribution represents the wake lateral wake expansion. The model predicts the double dip profile in the near wake considering the near wake. The author proposed a different parameter calibration for 3%, 8%, and 15% turbulent intensity. The model equation for the far wake velocity deficit at 8% turbulence intensity is expressed as (4.10):

$$\begin{aligned}\frac{\Delta U}{U_\infty} =& 1 - \left(0.0927\left(\frac{x}{D}\right) + 0.993\right) \\ & \times \exp\left[-0.5\left(\left(r - R_{\mathrm{mo}}\right) / \left(\left(\frac{R_{\mathrm{mo}}}{2}\right) + 0.075(x-R)\right)\right)^2\right]\end{aligned} \tag{4.10}$$

4.2.7 Lo Brutto model

Lo Brutto et al. (2016a) express the wake of a tidal turbine as a function of turbulent intensity and thrust coefficient. The proposed model is based on exponential wake expansion and a top-hat shape function developed by Jensen. The model is used to estimate the velocity deficit in tidal parks at different turbulent intensities

but is limited to a low rotor diameter-to-depth ratio (20%). The wake expansion according to exponential law depends on ambient turbulent intensity. The velocity deficit is expressed as Eq. (4.11):

$$\begin{aligned} \frac{\Delta U}{U_\infty} &= \frac{\left(1-\sqrt{1-C_T}\right)}{\left(\frac{r_w}{r_0}\right)^2} \\ r_w &= c(I_0)[5.58(1-e^{-0.051\frac{x}{D}})+1.2] \\ c(I_0) &= -15.542I_0^2+21.361I_0+0.2184 \end{aligned} \tag{4.11}$$

where r_w is the wake radius, r_0 is the rotor radius, x/D is the normalized distance downstream, and $c(I_0)$ is a quadratic function of the ambient turbulence.

4.2.8 Liu et al. model

Liu et al. (2023) recently proposed an empirical model for a ducted turbine. The ducted turbine wake profile is self-similar and approximately Gaussian, similar to the conventional HAT. However, the wake exhibits a faster recovery and a larger wake expansion. The empirical model is developed from the classical Jensen model with a Gaussian shape function. The velocity deficit is expressed as Eq. (4.12):

$$\begin{aligned} \frac{\Delta U}{U_\infty} &= \left[\frac{1-\sqrt{1-C_{T(\text{ rotor })}}}{(1+2k_wx/D)^2}+\frac{1-\sqrt{1-C_{T(\text{ duct })}}}{(1+2k_wx/D)^2}\right]\cdot\phi(r,D) \\ \phi(r,D) &= \exp\left(-\frac{\left(\frac{y-\theta}{D}\right)^2}{2\left(\frac{\theta}{D}\right)^2}\right)+\exp\left(-\frac{\left(\frac{y+\theta}{D}\right)^2}{2\left(\frac{\theta}{D}\right)^2}\right) \\ \frac{\theta}{D} &= a\frac{x}{D}+b, \quad \text{where } a=0.0315, b=0.1885, k_w=0.09 \end{aligned} \tag{4.12}$$

4.2.9 Otherworks

Other related works that calibrated the velocity deficit model parameters of wind turbines with numerical simulation for tidal application are available (Jo et al., 2014; Yazicioglu et al., 2016; Pyakurel et al., 2017). These models are extended for application in a simple tidal park (Palm et al., 2010; Lo Brutto et al., 2016b). However, these models are mainly developed for a single scenario making generic applications difficult. Unlike wind turbines, first-generation tidal turbines are located in shallow water limited by the depth which affects wake development.

In this chapter, multiple realistic scenarios are considered to develop a generic model applicable to different ambient turbulence, rotor thrust coefficient, and a range of rotor diameter to depth ratio. The proposed model is based on Jensen's mass conservation principle. The added turbulence model developed in the previ-

ous chapter (Shariff and Guillou, 2022a) is considered in evaluating the velocity deficit through the non-linear wake radius relation. A Gaussian shape function is used to estimate the wake profile in the lateral direction.

4.3 Numerical model

4.3.1 Case set-up

A full-scale turbine is located 10 D (D is turbine diameter) from the inlet, the length of the domain is 50 D, the channel width is 20 D and four-channel depths (H) are considered; 10 m, 25 m, 35 m, and 50 m representing the depth of the tidal site as shown in Table 1.2. In each case, the rotor is situated at the mid-depth of the channel. Three rotor diameter-to-depth ratios (DH) were studied with realistic flow conditions. For simplicity, the three cases are labeled as DH20, DH40, and DH60 representing the diameter-to-depth ratio of 20%, 40%, and 60% respectively. The rotor diameter corresponding to each channel configuration is presented in Table 4.3. The numerical domain has a low blockage ratio for all the configurations with 2.36% being the highest for the DH60. Figure 4.3 shows the different diameter-to-depth ratios of the three configurations.

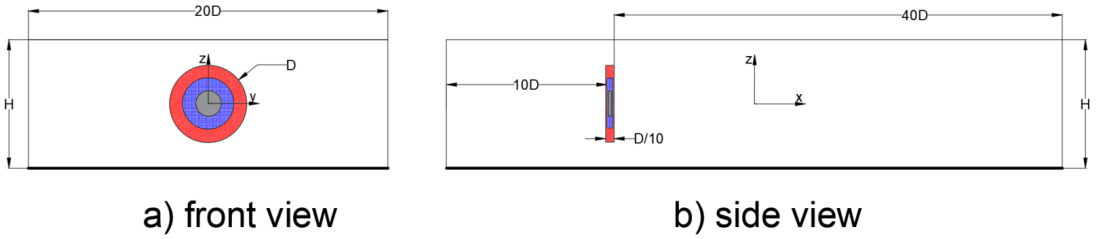

Figure 4.3 Schematic representation of the channel showing different rotor diameter to depth ratio.

Table 4.3 Rotor size at a different diameter-to-depth ratio

D/H / H(m)	20%	40%	60%
10	2	4	6
25	5	10	15
35	7	14	21
50	10	20	30

As a continuation of the previous work (Shariff and Guillou, 2022b), the numerical domain is discretized by structured grid cells using Cells Per Diameter

(CPD). 25 CPD across the disk surface for the Δy (transverse) and Δz (depth-wise) is chosen as the result is independent of mesh. This mesh based on 25 CPD is used for the different rotor diameters presented in Table 4.3.

4.3.2 Effect of the channel depth

Four different channel depths of the potential commercial tidal site are studied under the same hydrodynamic conditions. Figures 4.4 show identical center-line velocity deficit and turbulence intensity for different channel depths. Irrespective of the diameter or the channel depth under consideration given in Table 4.3, the hydrodynamics of the flow is the same for a given diameter-to-depth (DH) ratio. As the tidal turbine is bounded by limited depth, this notable parameter should be emphasized and considered in the hydrodynamics of the flow. Thus a particular channel depth with a different rotor diameter-to-depth ratio is sufficient to provide a generic representation of the channel size.

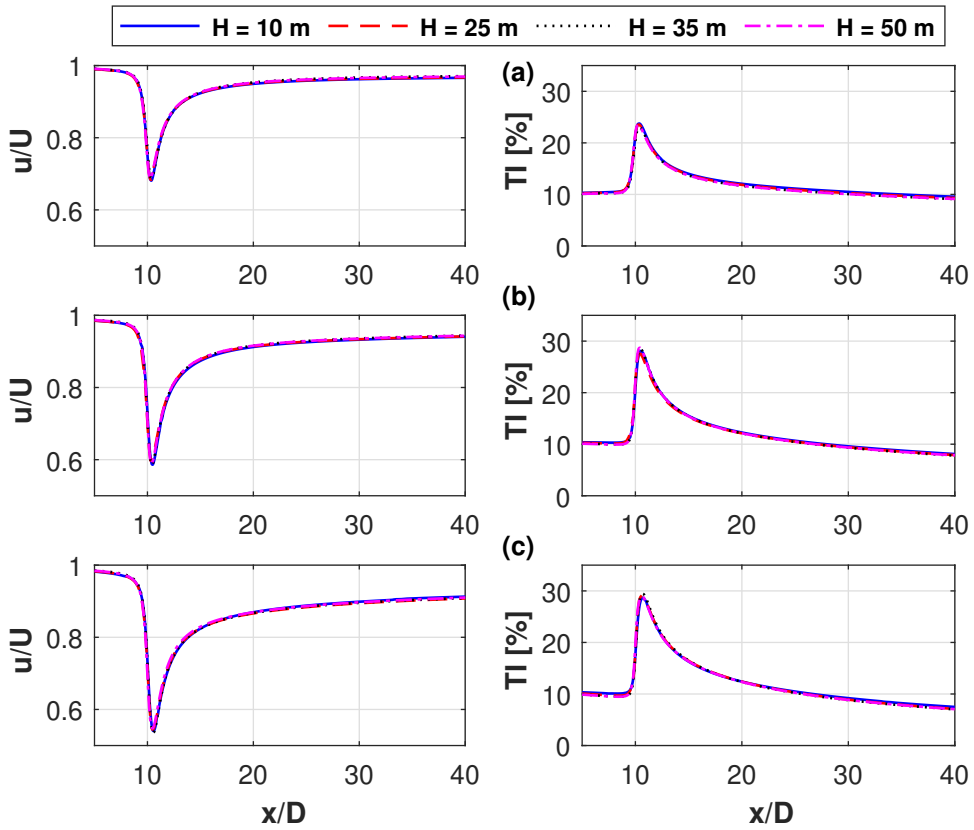

Figure 4.4 Center-line normalized velocity (left) and turbulent intensity (right) at 10% ambient turbulence showing the effect of channel depth at different rotor diameter to depth ratios (a) DH20, (b) DH40, and (c) DH60.

4.3.3 Effect of the rotor diameter to depth (DH) ratio

The DH ratio is the fraction of the rotor diameter covers along the channel depth. The rotor wake recovery is affected by the bypass flow. Bypass flow is a region around the turbine with ambient flow conditions. The momentum exchange by the rotor reduces the velocity of flow creating a wake that propagates downstream. In a low rotor diameter-to-depth ratio (i.e. DH20), the wake recovery process is faster as the flow in the bypass region is sufficient to cause mixing between the low velocity at the rotor's core and the ambient flow in the bypass region. Whereas, at a high DH ratio (i.e. DH60), the velocity deficit along the rotor is substantial compared to the free stream flow in the bypass region, therefore lagging the wake recovery to the upstream condition. The lower bypass flow region is associated with high turbulence and low velocity (bottom wall effect) while the upper bypass flow region has higher velocity and low turbulence effect (free surface effect). This causes the drift of the wake upward in a high rotor diameter-to-depth ratio as shown in Figure 4.5. Experimental studies reported the drifting of vertical profile (Chen et al., 2019) and the DH ratio is interpreted as an increase in the thrust coefficient.

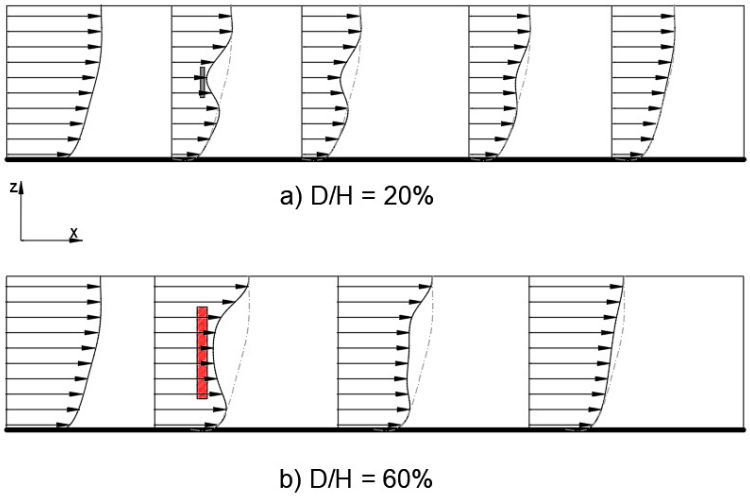

Figure 4.5 Schematic of the vertical plane showing the effect of rotor diameter to depth ratio.

The mean shear layer exists at the interface of the low velocity at the rotor core and high ambient flow (by-pass flow region). The mean shear expands from the rotor tip until it finally reaches the center line. The shear layer expansion occurs in the transverse and vertical direction at a low rotor diameter-to-depth ratio. However, an experimental investigation of the high rotor diameter to depth ratio (DH60) by Stallard et al. (2015) shows about 1.5 times the expansion rate higher in the transverse direction than in the vertical plane due to the limited channel depth. A similar compression of the radius and shear layer thickness has also

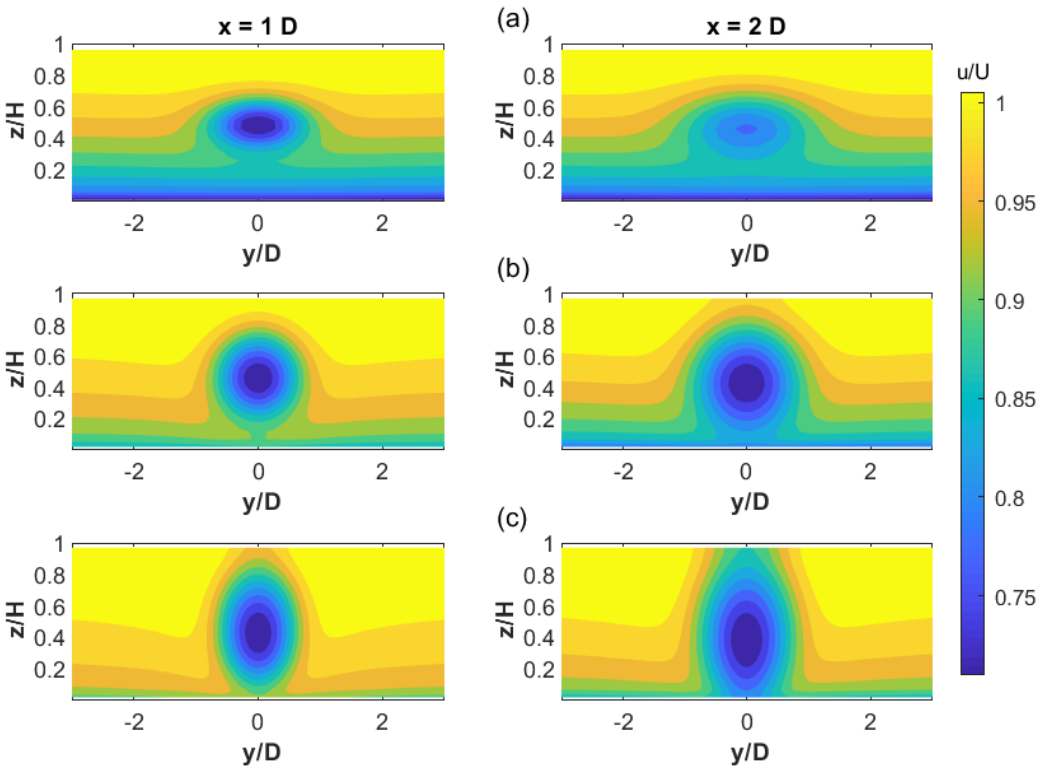

Figure 4.6 Normalized velocity contour at 10% ambient turbulence showing the wake profile at 1D (left) and 2D (right) for different rotor diameter-to-depth ratios of (a) DH20, (b) DH40, and (c) DH60.

been reported in studies by Zhang et al. (2021), forming a slightly elliptical profile by virtue of proximity to vertical boundaries. Figure 4.6 supports experimental studies that show an incomplete vertical development of wake at rotor diameter-to-depth ratio due to the limited channel depth.

4.4 Generic empirical model

To propose a generic model, the ambient turbulent intensity of 5%, 10%, 15%, and 20% is considered respectively, providing a global representation of turbulence at potential tidal sites (see Table 1.2). Similarly, a set of turbine thrust coefficients C_T allowing application at different configurations evaluated using Eq. (2.20) is presented in Table 4.4.

Table 4.4 Corresponding values of C_P and C_T for resistance coefficient K.

K	C_T	C_P
1	0.64	0.51
2	0.89	0.59
3	0.98	0.56

4.4.1 Turbulent intensity model

In the previous chapter, the centreline added turbulence intensity of a single turbine for a 20 m diameter at Betz limit was developed using curve-fitting in Matlab (Shariff and Guillou, 2022a). The approach is now generalized to accommodate a range of rotor thrust coefficients, DH ratios, and different ambient turbulent intensities. The wake expansion is represented by a Gaussian function evaluating the wake radius r_w. The generic turbulence model is expressed as Eqs. (4.13):

$$I_{eff} = \sqrt{I_0^2 + I_+^2} \tag{4.13}$$

$$I_+ = a\left(\frac{X - X_0}{D}\right)^{-b} \times \exp\left(-\frac{(y_0 - y)^2 + (z_0 - z)^2\Big)}{r_w^2}\right) \tag{4.14}$$

$$\mathrm{a} = 0.407\left(\frac{D}{H}\right)C_T^{4.83} + 0.179, \quad b = 0.681 I_0 + 0.472$$

$$r_w = c\left(\frac{X - X_0}{D}\right)^d \tag{4.15}$$

$$c = 2.7\left(\tfrac{D}{H}\right)^{-0.257}, \quad d = 0.34 \quad \text{for } 5\% \le I_0 < 10\%;$$
$$c = 3.0 + 1.5 I_{eff} \cdot \left(\tfrac{D}{H}\right)^{-1.32}, \quad d = 0.352\left(\tfrac{D}{H}\right)^{-0.145} \quad \text{for } 10\ \% \le I_0 < 20\%$$

where a, b, c, and d are the parameters depending on DH, C_T and the I_0. x_0, y_0, and z_0 are the turbine coordinates along x, the streamwise, y, the spanwise, and z, the vertical directions, respectively. I_{eff} is the effective turbulence intensity accounting for the ambient and added turbulence in the turbine wake. The turbulence intensity in the wake is reconstructed using Eq. (3.2) and compared with the tidal turbine experiment of Mycek et al. (2014b) and Stallard et al. (2013). Figure 4.7 shows the model provides reasonable results in comparison to the experimental data, especially in the far wake region.

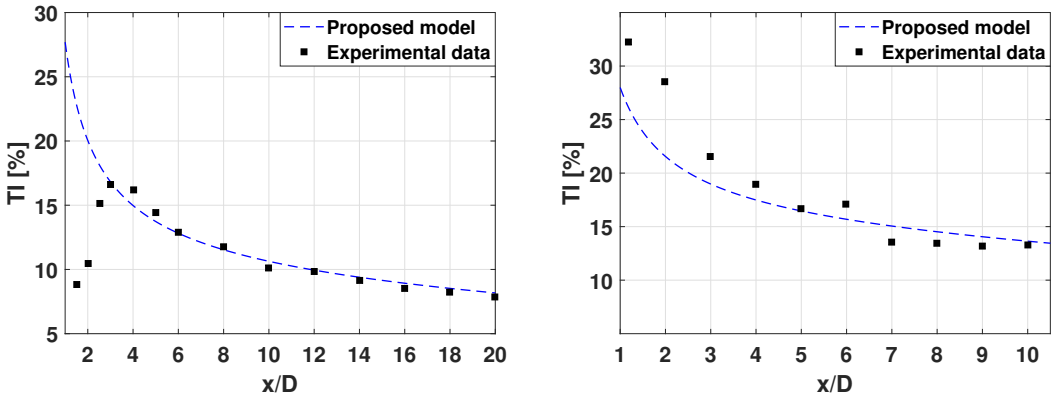

(a) Stallard et al. Stallard et al. (2013) experiment at DH60 at 12% ambient turbulence.

(b) Mycek et al. Mycek et al. (2014b) experiment at DH35 at 15% ambient turbulence.

Figure 4.7 Comparison of the proposed turbulent intensity model with tidal turbine experimental data.

4.4.2 Velocity deficit wake radius

The classical theory of turbulence shows the far wake behind a disk is axisymmetric and self-similar in a free shear flow. However, in a tidal stream, the wake is also regarded as self-similar but transmutes from axisymmetric to 2D Gaussian due to the depth constraint (Olczak et al., 2016). The wake evolution to 2D Gaussian profile increases with turbulent intensity (Lo Brutto et al., 2016a) and rotor diameter-to-depth ratio, as shown in Figure 4.8. The normalized lateral velocity profile at the mid-surface (MS) is approximately Gaussian in all the three DH ratios considered. However, as the rotor diameter-to-depth ratio increases, the wake translates from axisymmetric to 2 D Gaussian as indicated by the profile in the free surface (FS). The transition to the 2 D Gaussian profile is also amplified by an increase in turbulence intensity as shown in Figure 4.9 as reported by Lo Brutto et al. (2016a).

Similarly, the wake radius is estimated at 3σ using the Full-Width Half Maximum approach as elaborated in Section §3.5.2. The velocity deficit radius expands higher at DH20 because the wake expands in all directions to a great distance downstream before reaching the channel depth limit. As the DH increases the wake expansion is limited in the vertical plane creating an elliptical wake due to the wake compression, as shown in Figure 4.10a. The turbine wake expansion is reported to increase with turbulence intensity (Lo Brutto et al., 2016a; Shariff and Guillou, 2022b,c) due to enhanced mixing but is insensitive to the thrust coefficient as shown in Figure 4.10b. The empirical wake radius based on power law is expressed as Eq. (4.16):

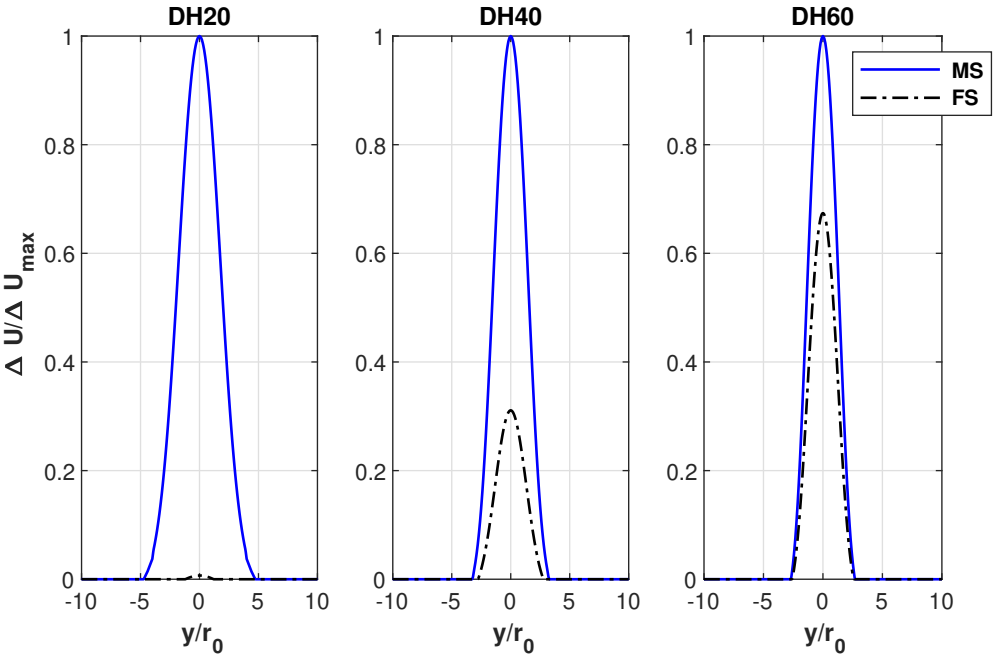

Figure 4.8 Normalized lateral velocity deficit at x/D = 3 showing the transition from axisymmetric to Gaussian profile at different DH ratios at 10% turbulence intensity.

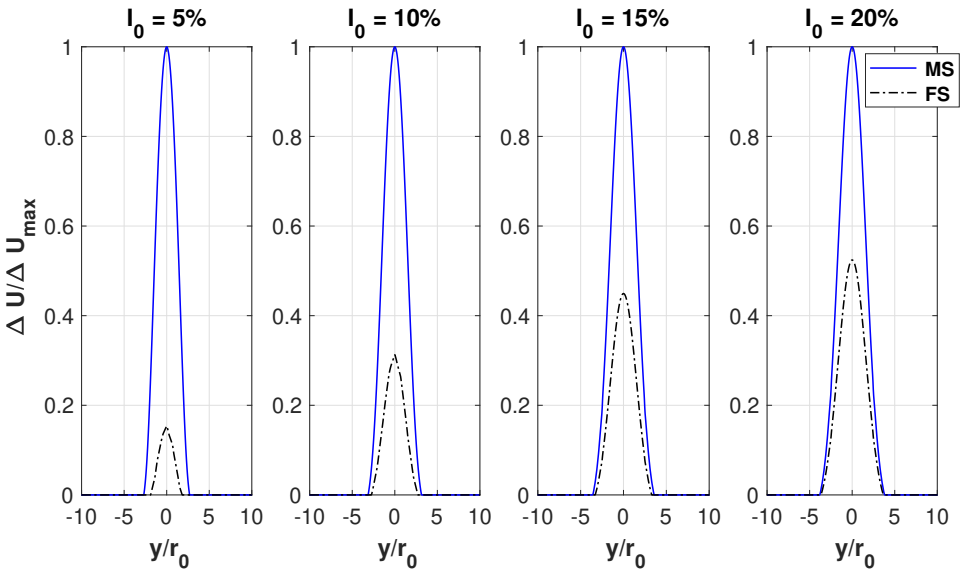

Figure 4.9 Normalized Velocity deficit at x/D = 3 showing the Gaussian lateral profile at the mid surface (MS) and free surface (FS) at a different ambient turbulent intensity at DH40.

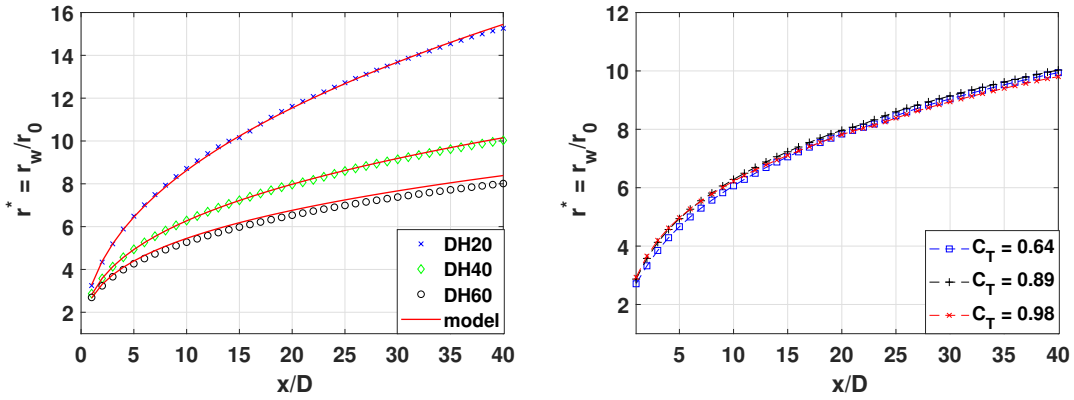

(a) Effect of rotor diameter to depth ratio **(b)** Effect of thrust coefficient

Figure 4.10 Comparison of normalized numerical velocity deficit radius and the empirical model showing the wake expansion at 10 % turbulence showing wake expansion at different (a) rotor diameter to depth ratio and (b) thrust coefficient.

$$r_w = e\left(\frac{X - X_0}{D}\right)^f \tag{4.16}$$

$$\begin{aligned} e &= 2.15\left(\tfrac{D}{H}\right)^{-0.283}, \quad f = 0.29 && \text{for } 5\ \% \leq I_0 < 10\%; \\ e &= 2.36 + 1.834\tfrac{I_{eff}}{D/H}, \quad f = 0.27\left(\tfrac{D}{H}\right)^{-0.275} && \text{for } 10\ \% \leq I_0 < 20\% \end{aligned}$$

where e and f are functions depending on the DH, C_T and I_{eff} respectively. The difference in the parameters e and f at low and high turbulence might be due to the difference in wake structure i.e. axisymmetry and 2 D Gaussian. The wake expansion is less at low ambient flow resulting in the largely axisymmetric wake whereas at high turbulence intensity, the wake expands faster to reach the vertical boundaries modifying the structure to a 2D Gaussian wake.

The wake radius model comprising the DH ratio and ambient turbulence provides good results in comparison to the numerical data as shown in Figure 4.10a. A trade-off exists between an increased wake radius at high turbulence and a decreased wake radius at a high DH ratio. The increase in wake expansion at high turbulence is due to enhanced mixing and diffusion while the decrease at high DH is due to the limited channel depth.

4.4.3 Velocity deficit model

The velocity deficit is the sum of the stream function and the shape function.

$$\frac{\Delta U}{U_\infty} = f(C_T, I_0, D/H, x/D) \cdot \phi(r_w, \sigma)$$

To estimate the centerline wake velocity of the tidal turbine, the wake radius model is substituted in the Jensen model presented in Eq. (4.3). The top-hat shape profile of the Jensen model estimates the average velocity in the wake, whereas the numerical data provides the minimum wake velocity in the form of a Gaussian profile. Assuming the velocity deficit in a lateral plane is Gaussian shape, Lo Brutto et al. (2016a) proposed a relation for maximum velocity deficit for the Jensen model as Eq. (4.17):

$$\Delta U_{\text{def ,max}} = \Delta U_{\text{def , aver}} \left(\frac{r_w}{\sigma}\right)^2 \tag{4.17}$$

where $\sigma = r_w/2.59$ is the standard deviation. The maximum velocity deficit $\Delta U_{def,max}$ henceforth ΔU_{def} can now be compared with the minimum velocity along the centreline in numerical data. In the present model, we propose to use directly a Gaussian model and then estimate directly the velocity deficit in the wake without using a correction coefficient. The modified Jensen-Gaussian velocity deficit is therefore expressed as Eq. (4.18):

$$\frac{\Delta U}{U_\infty} = \left[\frac{\left(1-\sqrt{1-C_T}\right)}{\left(\frac{r_w}{r_0}\right)^2}\right] \times \exp\left(-\frac{(y_0-y)^2+(z_0-z)^2)}{r_w^2}\right) \tag{4.18}$$

where C_T is the thrust coefficient, r_w is the wake radius downstream expressed in Eq. (4.16) and r_0 is the rotor radius. y_0 and z_0 are the turbine coordinates along y, the spanwise and z, the vertical directions, respectively. The exponential function provides the Gaussian shape profile along the lateral plane. A correction coefficient ϕ for the axisymmetric and 2D Gaussian wake derived in Appendix A.1 is expressed as Eq (4.19):

$$\phi = \begin{cases} \frac{1}{(R/\sigma)^2}, & \text{if } 2R < H \quad \text{(axisymmetry)} \\ \frac{\sqrt{\pi}/2}{R/\sigma}, & \text{otherwise} \quad \text{(2D Gaussian)} \end{cases} \tag{4.19}$$

The proposed velocity deficit model is compared with the tidal turbine experiment of Stallard et al. (2013) and Mycek et al. (2014a) as shown in Figure 4.11. The model is in good agreement with experimental data in the far wake region. However, the model is less accurate in the near wake as a limitation of the Jensen model. The parameter sensitivity of the generic model is presented in Appendix A.2.

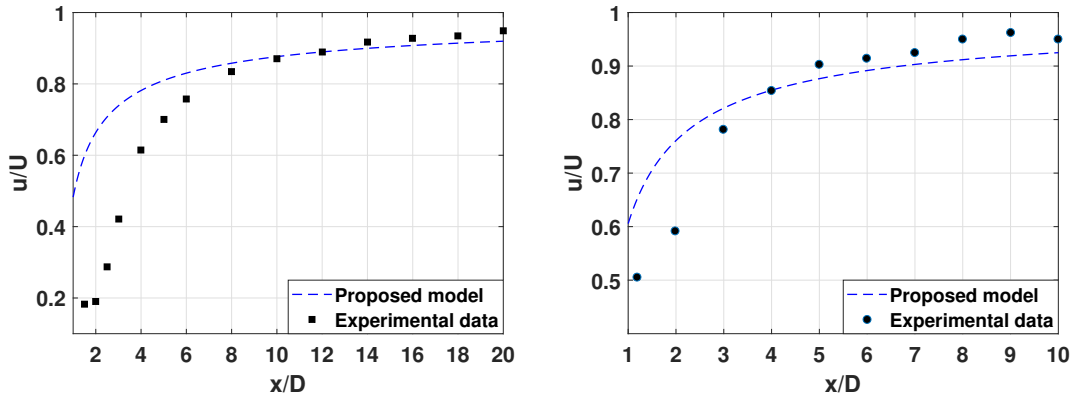

(a) Stallard et al. (2013) experiment at DH60 at 12% ambient turbulence.

(b) Mycek et al. (2014b) at DH35 at 15% ambient turbulence.

Figure 4.11 Comparison of the proposed velocity deficit model with tidal turbine experimental data.

4.5 Analysis

4.5.1 of DH ratio

The effect of DH at $C_T = 0.89$ and 10% turbulence intensity is presented in Figure 4.12. The normalized velocity is substantially affected by the DH ratio due to the wake expansion but the turbulent intensity variation at different DH ratios is minimal. The flow recovery at high DH is lessened due to the weak mixing between the low-velocity flow at the rotor core and the high-velocity bypass flow. The minimum velocity deficit is lowest at a high DH ratio. This can be interpreted by the limited free stream flow in the bypass region around the turbine. On the other hand, the turbulent intensity profile in Figure 4.12 does not show any significant variation due to the DH effect beyond 3D downstream. The centerline turbulent intensity profile is almost matching in the far wake. Figure 4.13 shows the normalized velocity contour at different DH ratios. The wake expansion decreases with an increase in the DH ratio.

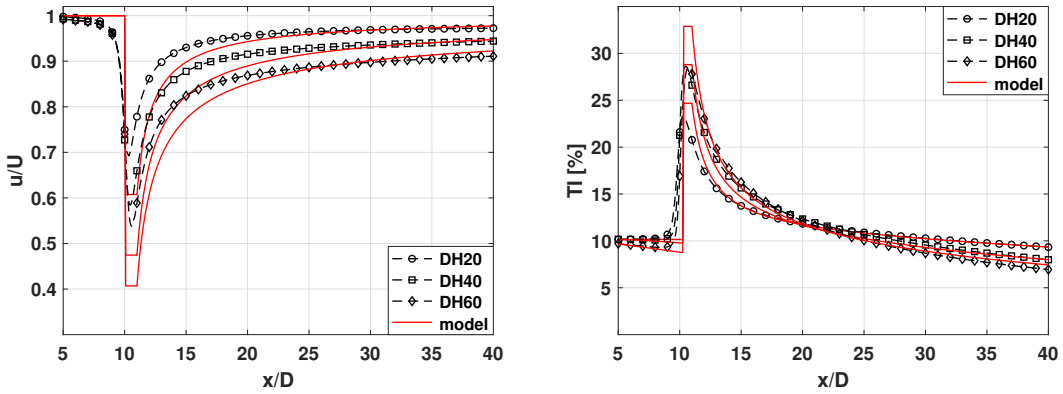

(a) Normalized velocity **(b)** Turbulent intensity

Figure 4.12 Comparison of a numerical and proposed empirical model for the (a) normalized velocity and (b) turbulent intensity showing the effect of rotor diameter to depth ratio along the centreline.

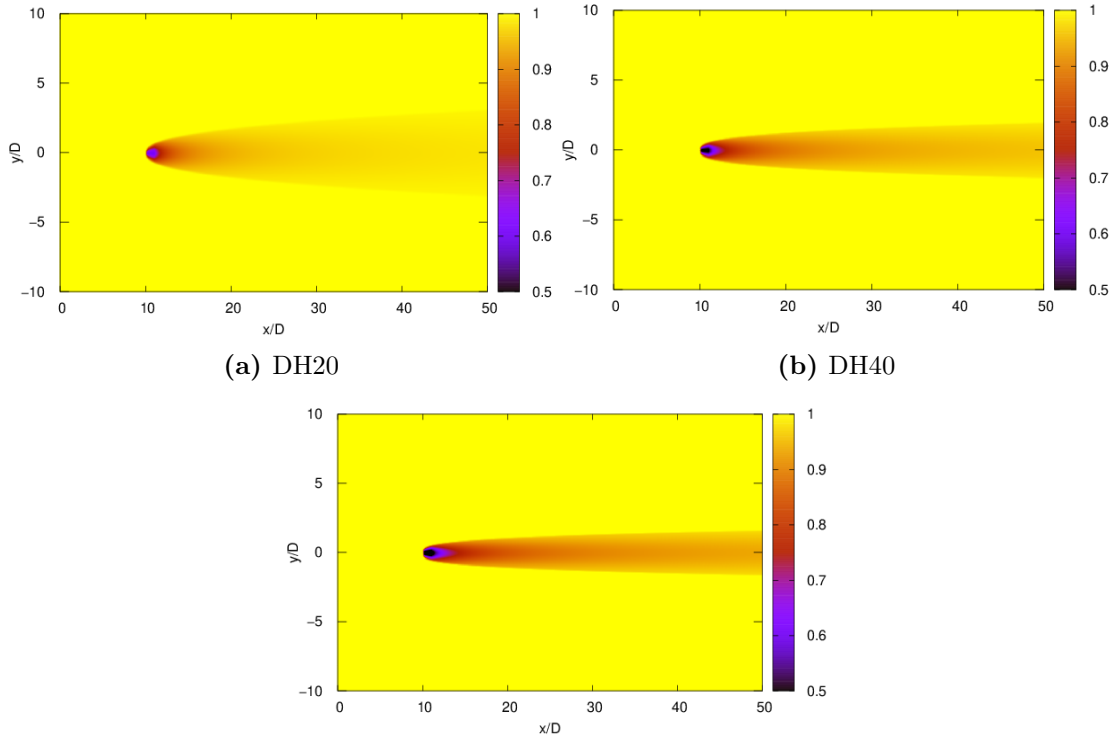

(a) DH20 **(b)** DH40

(c) DH60

Figure 4.13 Normalized velocity contour showing the wake expansion at different rotor diameter to depth ratio.

4.5.2 Effect of ambient turbulence

Figure 4.14 presents the normalized velocity and turbulent intensity at DH40 and C_T of 0.89 at different ambient turbulence. The velocity deficit and turbulence intensity recovery are faster at high ambient turbulence. The turbulence in the wake recovers at 15 D and 9 D for 10% and 15% inflow turbulence respectively. The normalized velocity recovers by more than 90%. This recovery is faster at high ambient turbulence. Other experimental (Myers et al., 2013; Mycek et al., 2014a; Blackmore et al., 2014) and numerical (Blackmore et al., 2011; Nguyen et al., 2019) studies of the wake effect illustrate the reduction in velocity deficit and quick flow recovery at high turbulent flow. The proposed model provides reasonable results compared to the numerical data, especially in the far wake region.

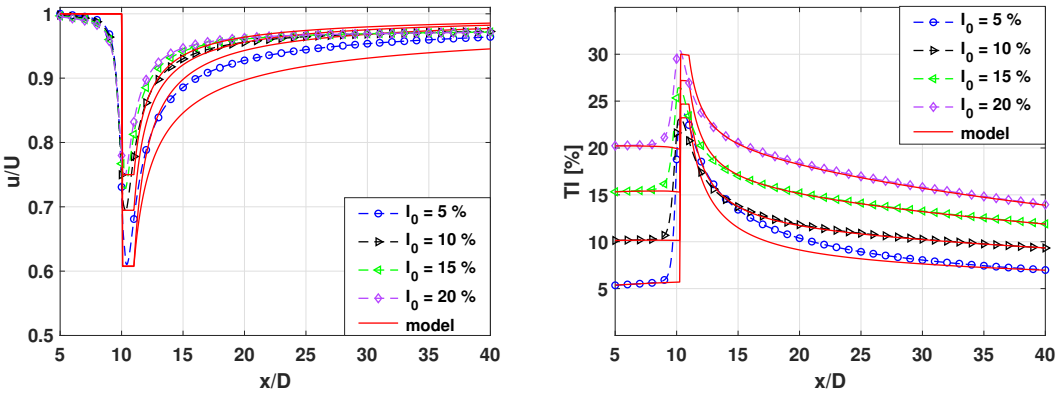

(a) Normalized velocity **(b)** Turbulent intensity

Figure 4.14 Comparison of a numerical and proposed empirical model for the (a) normalized velocity and (b) turbulent intensity showing the effect of ambient turbulence along the centreline.

The wake of turbulent intensity recovers at 5 D when the ambient turbulence is 20%. For 15% ambient turbulence, the wake recovery is achieved around 10 D downstream and 15 D for 10% ambient turbulence. At low ambient turbulence, the centerline turbulent intensity does not fully recover due to slow mixing and diffusion of the wake. The contour of normalized velocity and turbulent intensity is presented in Figure 4.15.

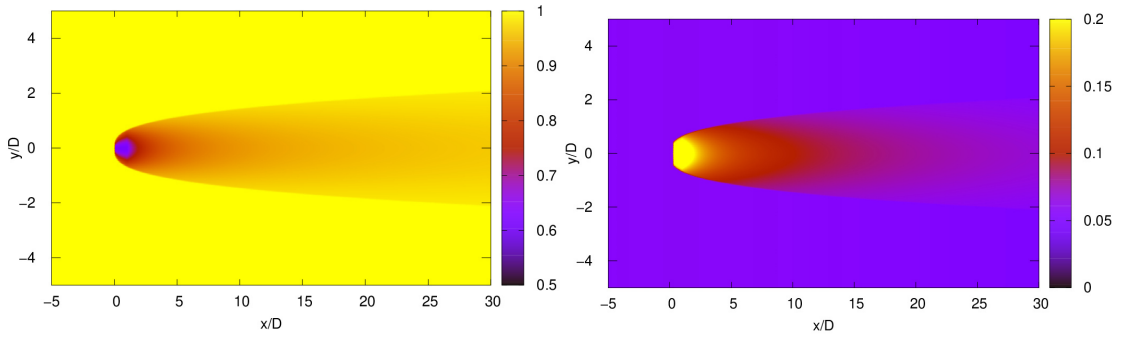

(a) $I_0 = 5\%$

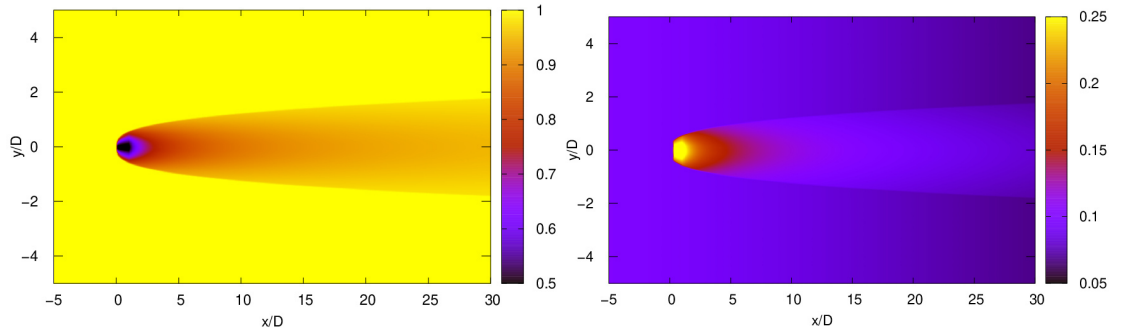

(b) $I_0 = 10\%$

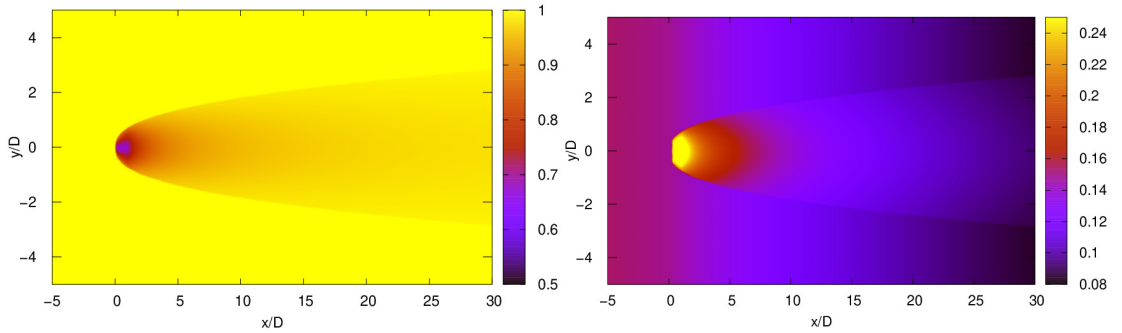

(c) $I_0 = 15\%$

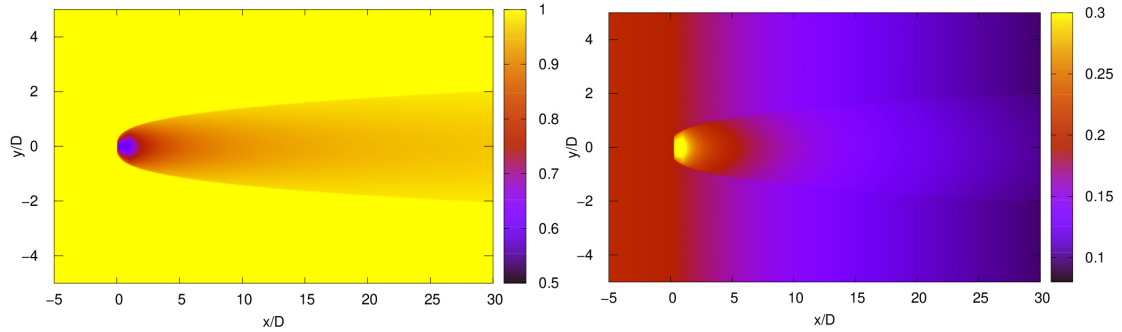

(d) $I_0 = 20\%$

Figure 4.15 Contours of normalized velocity (left) and turbulent intensity (right) using the empirical model at different ambient turbulence intensities at DH40.

4.5.3 Effect of thrust coefficient

Similarly, the effect of the thrust coefficient at 10% ambient turbulence is shown in Fig. 4.16. An increase in C_T can also be interpreted as increasing the drag force that causes the momentum exchange across the disk. High C_T creates a large velocity deficit close to the rotor producing high turbulence in the near wake. The increased thrust coefficient is largely effective in the near wake region. This variation due to the thrust coefficient is well represented by the proposed model in the near wake. However, far away from the rotor, the effect of C_T is less significant as the flow is largely homogeneous, thus reaching the recovery state.

The turbulent intensity profile in Figure 4.16b shows an increase in turbulence in the near wake in response to the increase in C_T which translates to an increase in drag. Both the normalized velocity and turbulent intensity profiles become identical in the far wake when the wake is largely uniform and far away from the rotor.

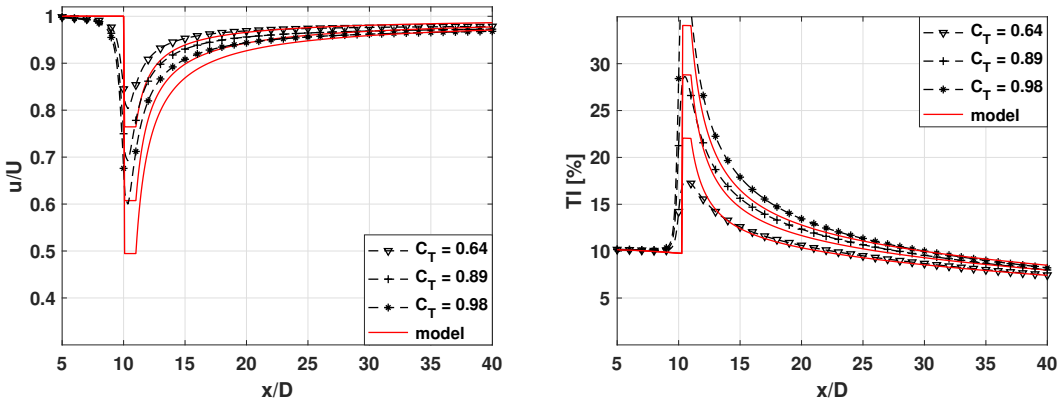

(a) Normalized velocity **(b)** Turbulent intensity

Figure 4.16 Comparison of a numerical and proposed empirical model for the (a) normalized velocity and (b) turbulent intensity showing the effect of thrust coefficient along the centreline.

4.6 Synthesis

Firstly, to propose a generic model, several numerical simulations were conducted at different channel depths and rotor diameter-to-depth ratios applicable for commercial extraction of tidal energy. The results show that the wake is independent of the channel depth but varies strongly with the rotor diameter-to-depth ratio. Therefore, further numerical simulations were carried out at a diameter-to-depth ratio of 20% to 60% which is the available range for commercial extraction of tidal energy in shallow water.

At a low DH ratio, the turbine wake expands freely, behaving like a free-shear flow with uniform expansion in lateral and vertical directions. However, as the DH ratio increases, the wake expansion is constrained along the vertical plane due to the limited water depth, thereby, transforming the wake from axisymmetric into elliptical 2D Gaussian profile. It has also been noted that the increase in ambient turbulence accelerates the transition to 2D Gaussian as a result of the rapid wake recovery in high turbulent flows. In addition, a drift in the vertical wake profile is observed at a high DH ratio due to the large velocity deficit at the turbine core and ambient flow in the bypass flow region.

With this in mind, a generic model is proposed to estimate the velocity deficit and turbulent intensity in tidal turbine wake accounting for the variation in ambient turbulence, thrust coefficient, and rotor diameter-to-depth ratio. The turbulent intensity in the wake is retraced from the added turbulence model developed and the ambient turbulence in the flow. The wake expansion model proposed is based on power law as featured in the classical turbulence model. The wake expansion model increases with ambient turbulence, decreases with the DH ratio, and is not affected by the thrust coefficient. For the velocity deficit, a modified Jensen model is used with Gaussian profile-based wake expansion.

Finally, the empirical model is compared with experimental data with reasonable results in the far wake. This low computational model is applicable in tidal turbine wake with ambient turbulence ranging from 5% to 20%, thrust coefficient range of 0.64 to 0.98, and rotor diameter to depth ratio of 20% to 60%.

Chapter 5

Tidal farm

Contents

This chapter evaluates the power generation of a large-scale tidal farm in different configurations in an ideal channel similar to the Alderney Race in the English Channel. According to the results, the farm can be resized by decreasing the lateral spacing in the rectilinear array and decreasing the longitudinal spacing in the staggered array without affecting the farm's efficiency. The reduction in farm size will reduce cable costs and provide an opportunity for future expansion. This study shows that the efficiency of a tidal farm can be increased by high ambient turbulent intensity, sufficient turbine spacing, and low diameter-to-depth ratio. This low-computational model can be useful in studying the wake interaction of tidal turbine parks in different configurations. This chapter is derived from and expands upon the authors' proceedings of the 15th European Wave and Tidal Energy Conference (Shariff and Guillou, 2023a).

5.1 Introduction

Over the last decade, the tidal energy industry has recorded successful deployment and testing of full-scale Tidal Stream Turbines (TST) at dedicated test sites with single units reaching up to 1 MW output (EMEC, 2022). The next step towards commercialization is the investigation of the turbine wake interaction in the tidal array as depicted in Figure 5.1. The wake induced on the downstream turbine can reduce the output power thereby affecting the overall efficiency of the tidal farm. In wind farms, the power loss due to the wake effect can be up to 25% (Barthelmie et al., 2006). Therefore accurate estimation is necessary to minimize loss and increase efficiency which will translate to a reduction in cost. This chapter presents the application of the empirical model in an ideal tidal turbine layout. The evaluation of turbine wake interaction and the efficiency of tidal farms is noted.

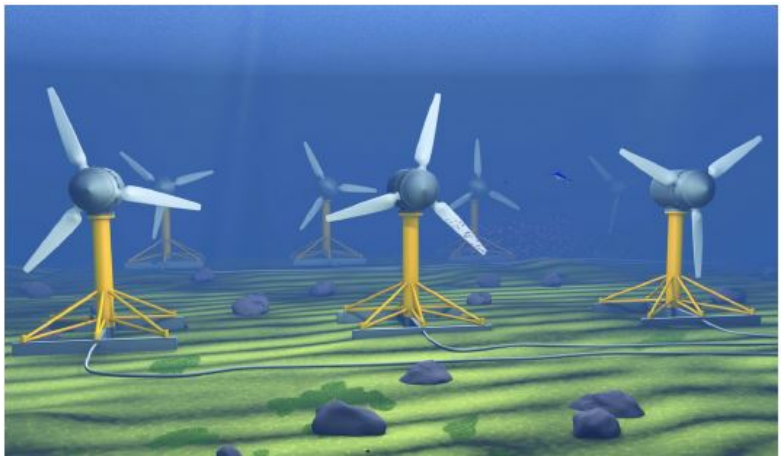

Figure 5.1 Artistic illustration of TST farm layout. © Bureau Veritas

The empirical models developed for wind and tidal turbines are used to estimate the power production in tidal farms. For example, Palm et al. (2010) uses the simple Jensen model to estimate the velocity deficit in a simple tidal farm using the Jensen model. Similarly, Lo Brutto et al. (2016b) evaluate the power produced in tidal farms using an empirical model. However, these analytical models are based on ambient turbulence in the flow. As already established, the turbine wake is a region of increased turbulence. The effective turbulence in the tidal farm is higher than the ambient turbulence due to the turbulence effect added by the individual turbine and the turbulence due to the turbine wake interaction. In this chapter, we propose a model to estimate the effective turbulence in the turbine wake taking into account the local added turbulence in the wake. Effective turbulence is used to evaluate the velocity and hence the power extracted by the turbine.

5.1.1 Turbulence in tidal farm

The turbulence in the turbine farm increases due to the kinetic energy extraction by upstream turbines and the turbine interaction in the farm. The effective turbulence in a tidal farm can be expressed as:

$$I_{eff}^2 = I_0^2 + (I_{+,i} + I_{+,ij})^2 \tag{5.1}$$

where I_0 is the ambient turbulence, I_+ is the individual added turbulence from the turbine T_i and $I_{+,ij}$ is the added turbulence on turbine T_i interacting with turbines T_j. To the best of our knowledge, there is no precise definition of $I_{+,ij}$, but the models consider only the interaction of neighboring turbines. A study by Frandsen and Thøgersen (1999) shows that only the effect of neighboring turbines is important to predict the turbulence intensity of a given turbine. Niayifar and Porté-Agel (2016) develop a model to estimate the turbulence intensity in the wake of the wind turbine array. For an individual turbine, Crespo's turbulence relation (refer to Eq. (3.4)) is used to calculate the added turbulence, then local turbulence intensity is obtained using Eq. (3.2). The turbulence contribution by wake interaction of the closest turbine is defined by Niayifar and Porté-Agel (2016) as:

$$I_{+j} = \max\left(\frac{A_w 4}{\pi d_0^2} I_{+ij}\right) \tag{5.2}$$

where I_{+j} is the added turbulence intensity at turbine j, A_w the area of the wake of turbine T_j intersecting turbine T_i, and $I_{+,ij}$ the added turbulence intensity induced by the turbine i at the turbine j. Recently, Qian and Ishihara (2021) proposed a similar model for multiple turbines. The individual added turbulence is calculated from Table 3.1 and a correction term to account for the wake interaction with the closest turbine as suggested by Frandsen and Thøgersen (1999). The interaction term is assumed to be half of the added turbulence at the tip which can be either positive for full overlap or negative in partial overlap due to a weakening velocity shear layer in the overlapped region. It is expressed in Eq. (5.3):

$$I_{+,ij} = \begin{cases} \frac{1}{2} I_{+,i} \cos^2\left(\frac{\pi r_i}{D}\right) & \text{full overlap} \\ -\frac{1}{2} I_{+,i} \sin^2\left(\frac{\pi(y-y_i)}{D_{w,i}}\right) \cos^2\left(\frac{\pi(z-H)}{L_{w,ij}}\right) & \text{partial overlap} \\ 0 & \text{else} \end{cases} \tag{5.3}$$

where r_i is the spanwise distance from the wake center of T_i, and $L_{w,ij}$ is the vertical length of the intersected wake region of T_i and T_j.

5.1.2 Wake interaction in tidal farm

To effectively estimate the wake of turbines in a tidal farm, the analytical model needs to account for the wake interaction of multiple turbines. To achieve this, single turbine models use the superposition principle to estimate the combined

effect of overlapping wakes in the farm. There are basically three types of wake interaction in tidal farms namely; full overlap (or tandem), partial overlap, and no interaction as shown in Figure 5.2. However, a turbine may be affected by a mixed wake on the farm.

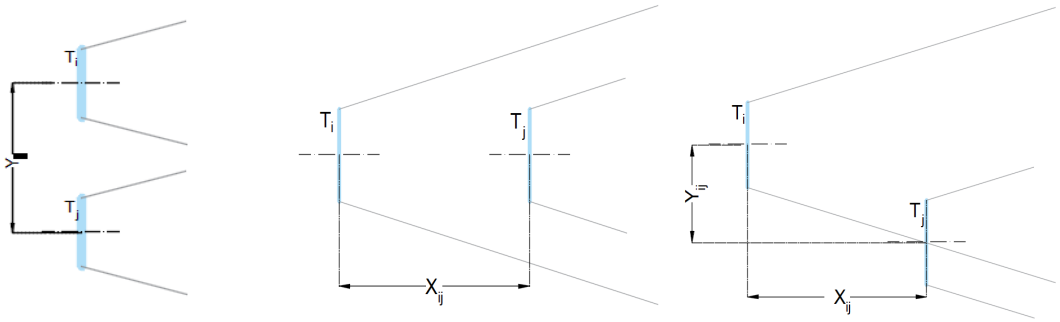

(a) **(b)** **(c)**

Figure 5.2 Schematic of turbine-wake interaction; (a) no interaction (b) full overlap and (c) partial overlap in the wake of the upstream turbine.

The wake overlap area is calculated as follows:

$$A_{overlap} = \begin{cases} 0, & if \quad r_w + r_0 \leq y \\ A_0, & if \quad r_w - r_0 \geq y \\ A_{partial}, & otherwise \end{cases} \tag{5.4}$$

where r_w and r_0 are the radius of the wake and turbine respectively, y is the lateral distance between the turbines, and $A_{partial}$ is the intersecting area between the wake area A_w and the rotor swept area A_0 as shown in Figure 5.3. The wake intersection area $A_{partial}$ is calculated using Eq. (5.5) as proposed by Pookpunt and Ongsakul (2013).

$$A_{overlap} = r_w^2 \left(\theta_w - \frac{\sin(2\theta_w)}{2}\right) + r_0^2 \left(\theta_r - \frac{\sin(2\theta_r)}{2}\right) \tag{5.5}$$

where θ_w and θ_r are the angles of the wake intersection arc and rotor intersection arc respectively and can be respectively expressed as:

$$\theta_w = \cos^{-1}\left(\frac{r_w^2 + y^2 - r_0^2}{2yr_w}\right), \theta_r = \cos^{-1}\left(\frac{r_w^2 - y^2 - r_0^2}{2yr_0}\right) \tag{5.6}$$

In order to combine the cumulative wake interaction on the downstream turbine. Different superposition methods have been proposed in the literature to estimate the wake-turbine interaction. For instance, Niayifar and Porté-Agel (2016) and Qian and Ishihara (2021) use the Linear Sum of Square (LSS) method to evaluate the wake in the wind farm. The LSS method is first adopted by Lissaman (1979) in analogy to the superposition of neighboring plume concentration

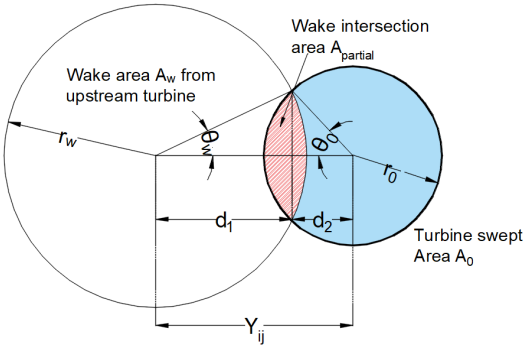

Figure 5.3 Evaluation of partial wake intersection area between a wake effect from the upstream turbine and downstream rotor.

which conserves the pollutant concentration due to linearity. LSS sum the velocity deficit of individual turbine to conserve the total momentum deficit in the wake. Another superposition method used by researchers (Lo Brutto et al., 2016b; Yang et al., 2019) to evaluate the wake interaction is the Root Square method (RSM). The RSM aims to conserve the kinetic energy deficit. These superposition models are largely empirical with no rich theoretical justification. In this study, the Root Square Method is used to evaluate the velocity deficit and turbulence intensity in the form of kinetic energy deficit and turbulence energy for the interacting turbines.

5.2 Description of the generic model in tidal farm

In Chapter 3, a model is proposed to estimate the added turbulence of a full-scale tidal turbine. Using the ambient turbulence, the wake turbulence is reconstructed and results in good estimation in comparison with numerical data. The wake turbulence model is used to evaluate the wake expansion taking into account the local added turbulence effect in the wake. A Jensen-Gaussian velocity deficit model is proposed to estimate the velocity deficit in the wake of the full-scale turbine in Chapter 4. This model is generalized to account for a range of rotor thrust coefficients, rotor diameter-to-depth ratio, and ambient turbulence. In addition, with our new model, we estimate the turbulent intensity of the wake at different hydrodynamic conditions. For a tidal farm application, the wake interaction between turbines is evaluated using trigonometric relation and estimated by superimposing the wake interacting effect to evaluate the velocity deficit and the turbulence intensity in a tidal farm. The generic velocity deficit and turbulent intensity in the tidal farm are expressed in Eq. (5.7). Figure 5.4 describes the organigram chart of the generic empirical model.

$$\left(1-\frac{u_j}{U}\right)^2=\sum_{i=1}^{n}\left(1-\frac{u_{ij}}{U}\right)^2\frac{A_{overlap}}{A_0}$$
$$I_{eff}=I_0^2+I_{+,j}^2 \tag{5.7}$$
$$I_{+,j}^2=\sum_{i=1}^{n}\left(a\left(\frac{X_{ij}-X_j}{D}\right)^{-b}\right)^2\frac{A_{overlap}}{A_0}$$

where $A_{overlap}$ is the overlap area between the expanded wake area A_w of the upstream turbine and the rotor swept area of the downstream rotor A_0 in Eq. (5.4).

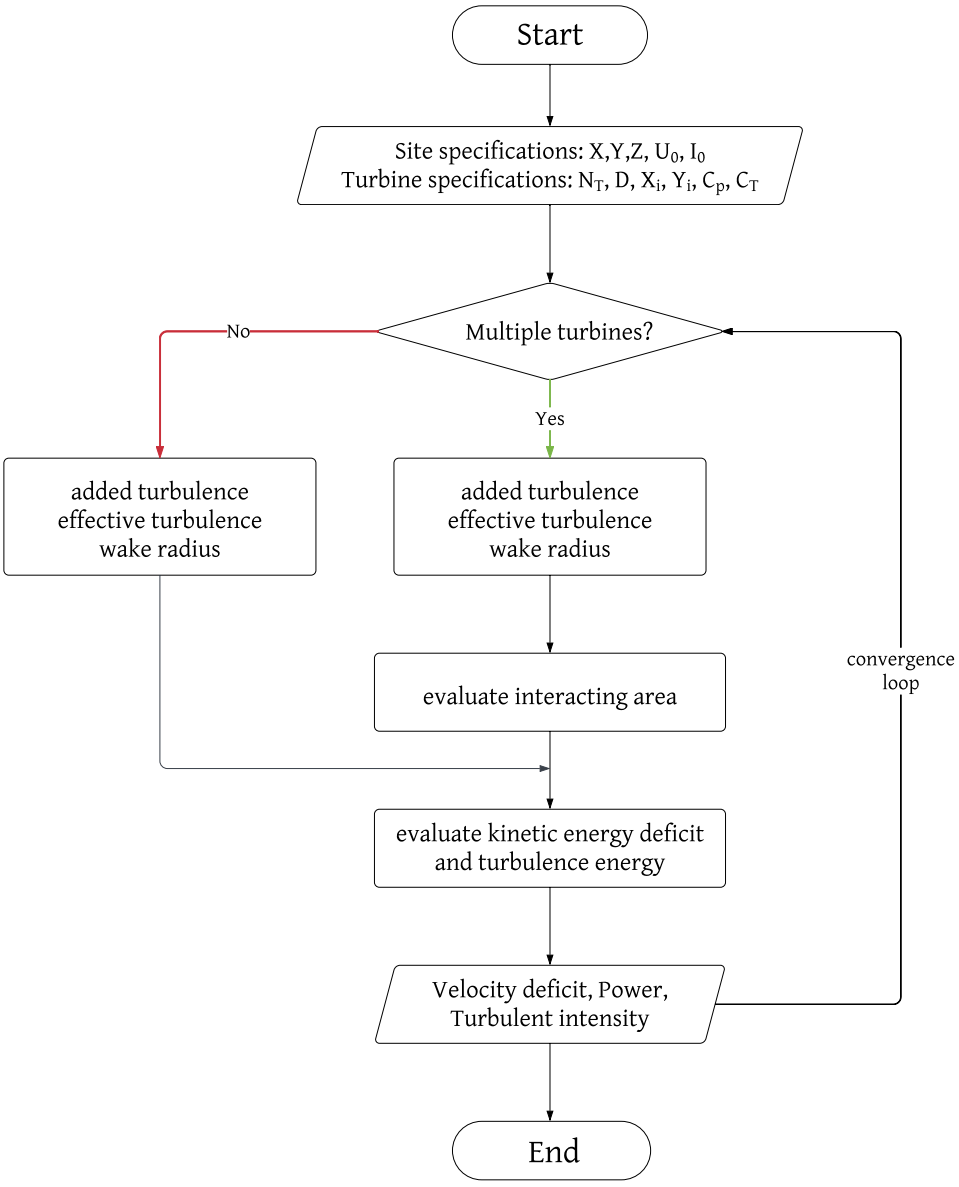

Figure 5.4 Organigram chart for the generalized empirical model.

5.3 Analysis

5.3.1 Turbine array in tandem configuration

A simple tidal farm comprising four turbines in inline configuration is studied. The rotor diameter to depth (DH) ratio of 20% is considered in the simple array. The ambient turbulence used in this case is 10% whereas the Betz thrust coefficient $C_{T,Betz}$ is used throughout this chapter unless otherwise stated. Turbines are designated as T_N where N is the turbine's position in the farm. For tandem configuration (full overlap), the downstream turbines are fully immersed in the wake of the upstream turbines as shown in Figure 5.2a. The wake interaction is evaluated as expressed in Eq. (5.4). Figure 5.5 shows the empirical model provides a good centerline estimation of the normalized velocity and turbulent intensity compared to the numerical data. At $S_x = 5D$, the downstream turbine is subjected to higher incoming turbulence compared to the upstream turbine. An incremental increase in turbulent intensity is observed due to cumulative added turbulence effects. The power produced by turbines downstream is much lower compared to the upstream turbine due to limited turbine spacing. The contour in Figure 5.6 shows that as the turbine spacing doubles, the wake largely recovered to upstream condition leading to extraction of higher power by the downstream turbines. The incoming turbulence of turbine T_2 decreases from 15.3% to 12.5% when the turbine spacing is double.

The wake effect is higher when the turbine spacing S_x is small causing an increase in the incoming turbulence intensity of the downstream turbine. In a channel at 10% ambient turbulence, the results show that the turbine downstream can detect up to 50% higher turbulence due to the successive wake effect at small turbine spacing. However, Figure 5.5 presents the maximum turbulence along the centerline (Gaussian profile), and the mean turbulence across the rotor is lower as indicated in Figure 5.6. The turbine spacing is shown to affect the power production of the turbine downstream which will affect the overall efficiency of the farm. For $I_0 = 10\%$, the turbine spacing of $S_x = 7D$ allows sufficient wake recovery and acceptable added turbulence on the downstream turbine. However, as the wake recovers faster at high ambient turbulence due to strong mixing and diffusion, (Mycek et al., 2014b; Neunaber et al., 2020) in the wake, the turbine spacing may be affected by the ambient turbulence. The effect of ambient turbulence is studied in Section 5.3.4.

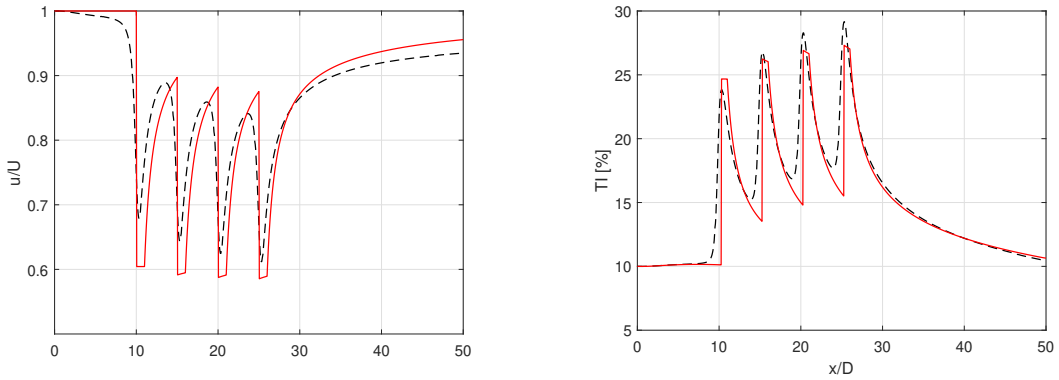

(a) $S_x = 5D$

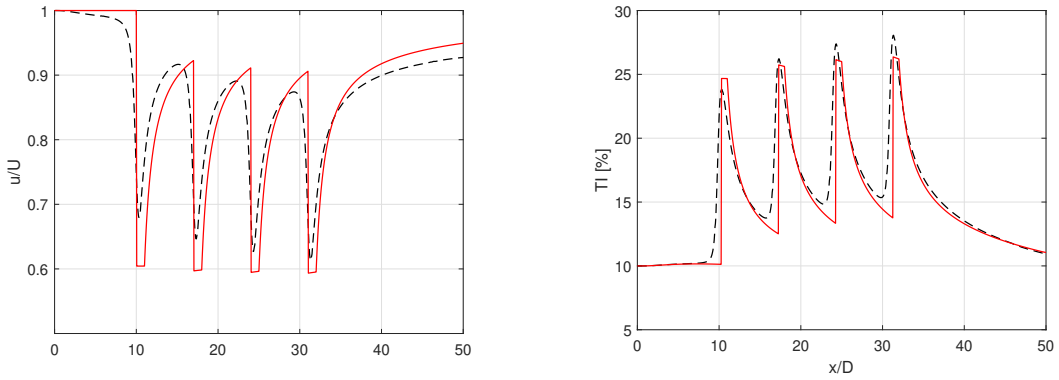

(b) $S_x = 7D$

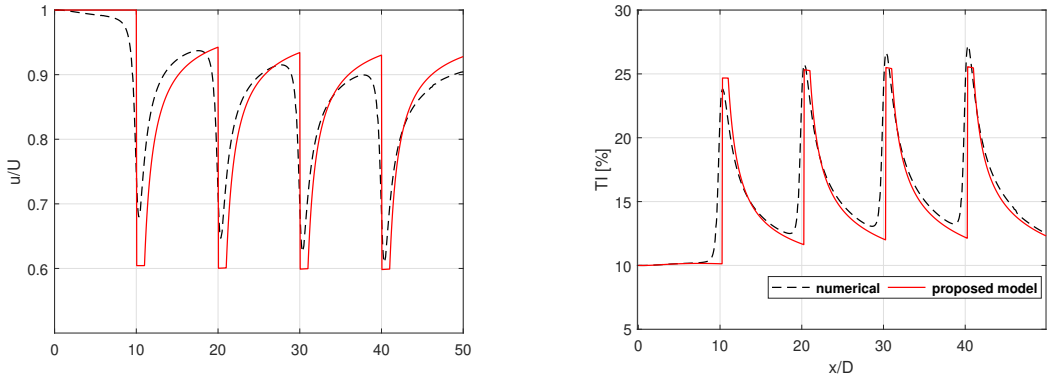

(c) $S_x = 10D$

Figure 5.5 Comparison of centerline normalized velocity (left) and turbulent intensity (right) between the numerical model and empirical model in tandem array at different turbine spacing.

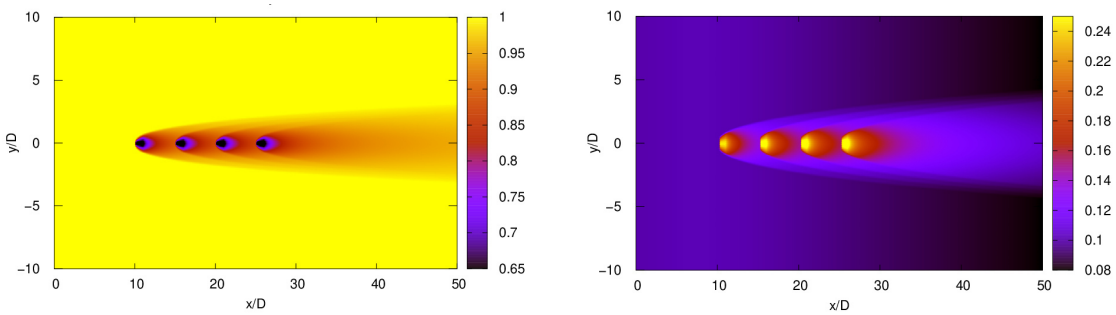

(a) $S_x = 5D$

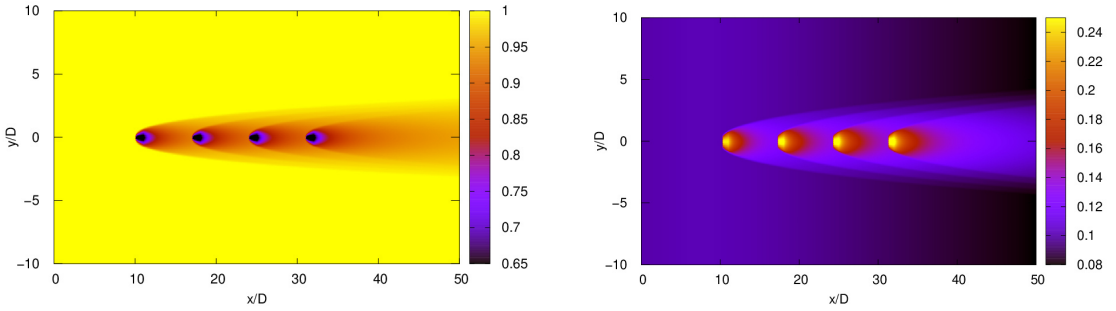

(b) $S_x = 7D$

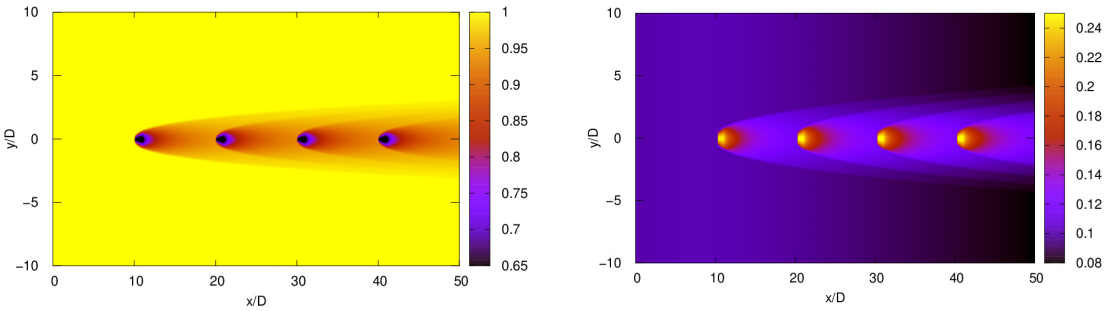

(c) $S_x = 10D$

Figure 5.6 Contour of normalized velocity (left) and turbulent intensity (right) using the empirical of tidal turbine array at different turbine spacing.

5.3.2 Power production in different array configuration

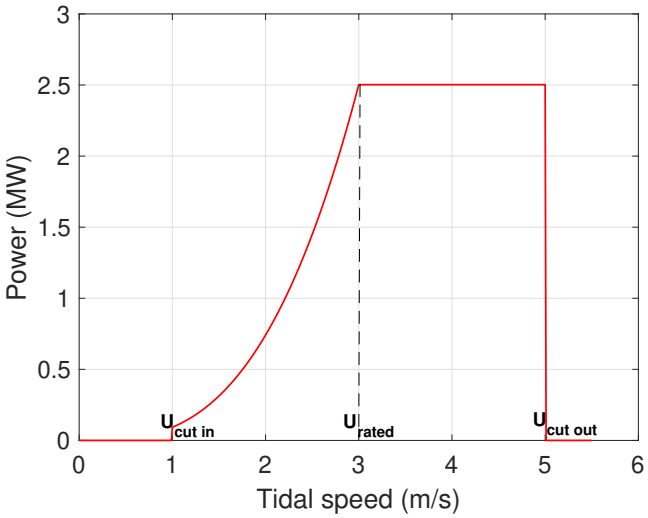

Figure 5.7 Power curve of a tidal turbine.

The power curve of a typical 20 m diameter tidal turbine is presented in Figure 5.7. The turbine cut-in speed (U_{cut-in}) is 1.0 m/s and the rated speed (U_{rated}) is 3.0 m/s. The power produced by the turbine is zero when the flow velocity is below the U_{cut-in}. The turbine begins to produce electricity from the cut in speed to the rated speed. The optimum performance of the turbine is at the rated speed where the rated power is attained. When the flow speed is higher than the cut-out speed ($U_{cut-out}$), the turbine operation is suspended to prevent damage, hence the power generated is zero. The power produced by a turbine is calculated as Eq. 5.8:

$$P_i = \frac{1}{2}\rho C_p A U_i^3 \tag{5.8}$$

where ρ is the water density, C_P is the power coefficient, A is the cross-sectional area evaluated as $\pi D/4$ and U_i is the incoming velocity for turbine T_i.

In this section, the two basic tidal farm configurations rectilinear and staggered 20 m diameter turbine at DH40 are analyzed. The farm comprising N turbines ($N = 16$) in an ideal channel is illustrated in Figure 5.8. The turbines are assumed to perform at Betz operating conditions. The turbine spacing is $S_x = 7D$ and $S_y = 4D$ respectively to ensure flow recovery and benefits from accelerated flow from the upstream turbines. In the ideal farm, the ambient turbulent intensity of 10%, and a constant mean flow of 2.8 m/s is used similar to the flow in the Alderney Race (Thiébaut et al., 2020). However, the variability of the power curve with current velocity is not considered in the algorithm.

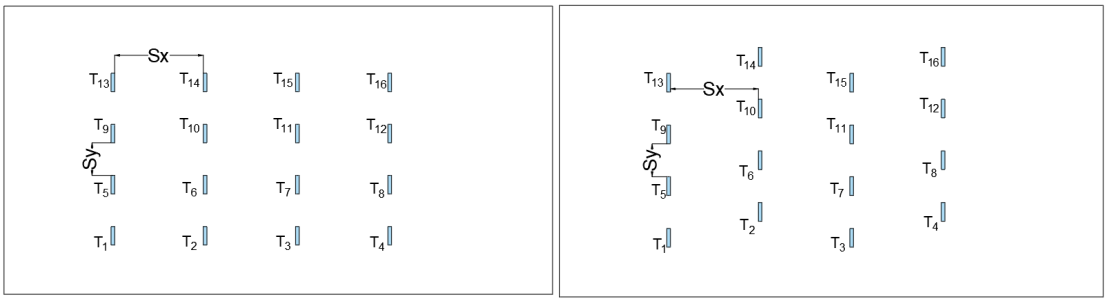

(a) Rectilinear array **(b)** Staggered array

Figure 5.8 Schematic of tidal farm array showing different turbine configurations in a farm.

Figures 5.9 compare the numerical and analytical results at different array configurations. The turbines upstream produced maximum power because they were not affected by the wake interaction. The turbine downstream produces lower power due to the wake interaction in the farm. This is consistent with the numerical results as shown in Figure 5.9.

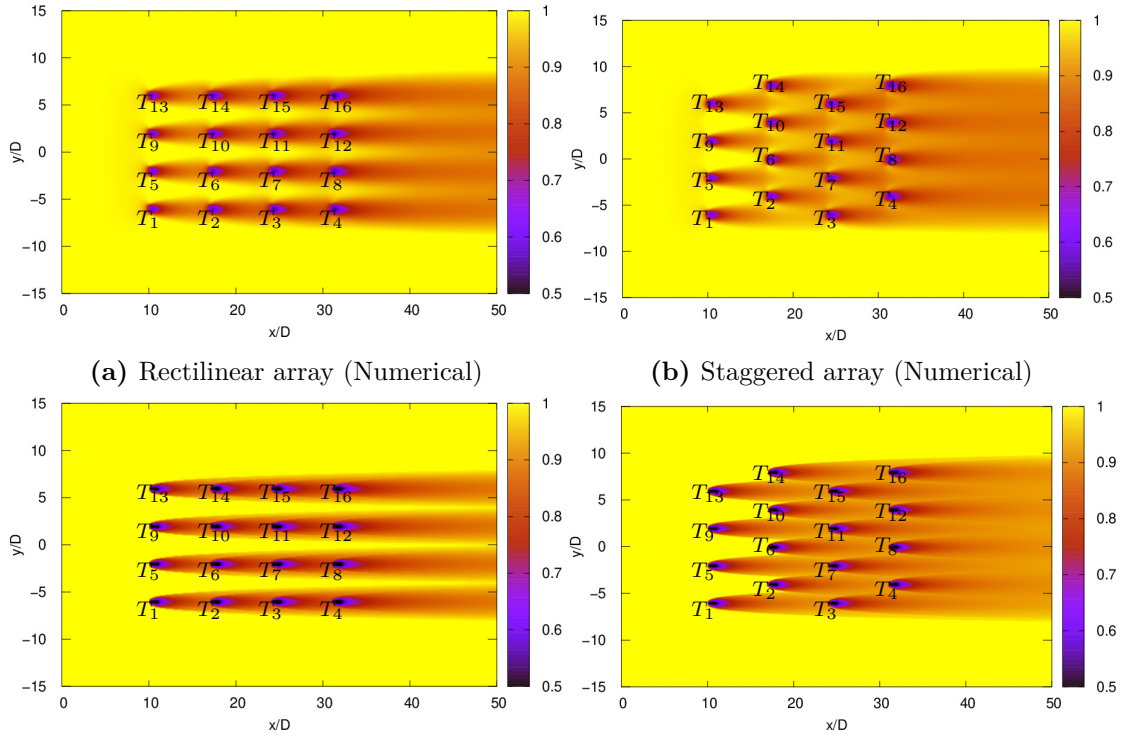

(a) Rectilinear array (Numerical) **(b)** Staggered array (Numerical)

(c) Rectilinear array (Modeled) **(d)** Staggered array (Modeled)

Figure 5.9 Comparison of numerical (top) and empirical (bottom) normalized velocity contour in rectilinear and staggered array configuration in a farm at DH40.

For the rectilinear configuration, the turbine downstream is fully in the wake of the upstream turbines. The wake interaction is evaluated as presented in Figures

5.2b. The rectilinear array (Figures 5.9a and 5.9c) identifies each turbine row independently as having no interaction between turbine rows whereas the staggered configuration shows the wake interaction in both longitudinal and lateral directions as indicated in Figures 5.9b and 5.9d. The numerical and empirical power produced by each turbine is compared in Figure 5.10. In the numerical model, the power is evaluated at a location 1.5 D away from the turbine before the pressure jump begins to develop.

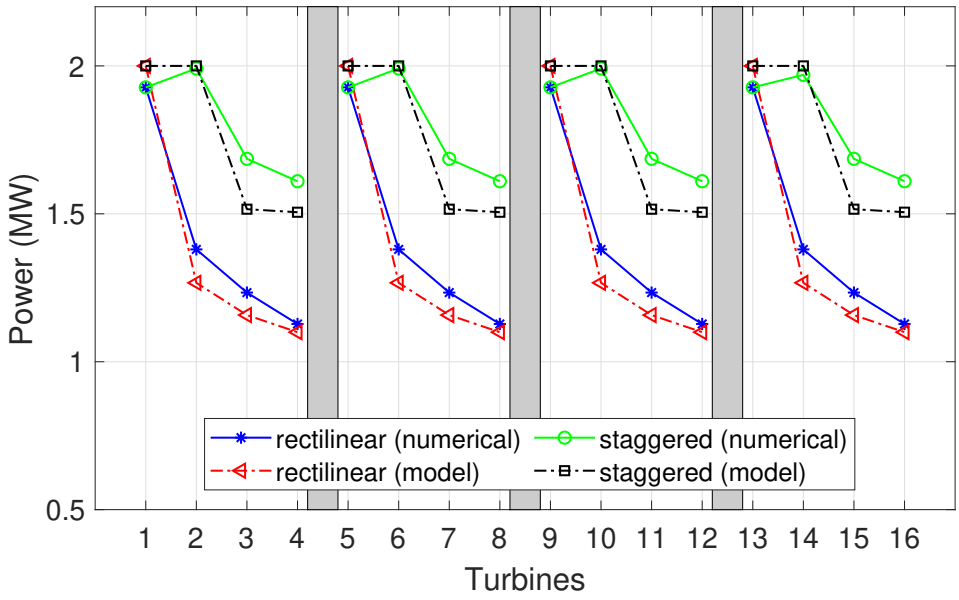

Figure 5.10 Comparison of numerical (solid line) and empirical (dash line) power produced by turbines in rectilinear and staggered array at DH40.

The power extracted by a turbine is calculated as followed by Eq. (5.8). The empirical model underpredicts the numerical power in the farm by 2.5%. A comparison of power produced by each turbine in the rectilinear and staggered array using the empirical model is presented in Figure 5.11. It is noted that the upstream turbine produces identical power output irrespective of the turbine configuration. For the rectilinear array, the power produced from turbine T_1 - T_4 decreases due to the cumulative wake effect. The downstream turbine is affected by the wake, therefore, producing less power. Similarly, for a staggered array, the turbine downstream produces less power due to the wake effect, however significantly higher than a similar turbine in a rectilinear array. For instance; a turbine T_3 with a double turbine spacing in staggered produces 23.6% more power than a corresponding T_3 in a rectilinear array. The wide turbine spacing allows a substantial recovery velocity deficit in the flow.

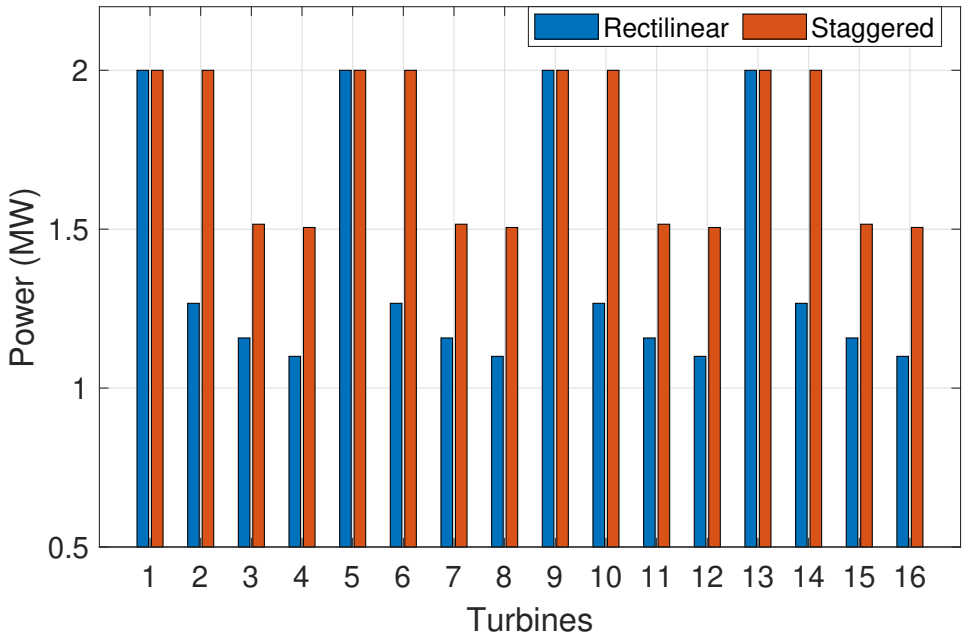

Figure 5.11 Power produced by turbines at different array configurations evaluated using the empirical model in the farm at DH40.

The cumulative power produced by N turbines in the farm is evaluated as Eq. (5.9):

$$P_{farm} = \sum_{j=i}^{N} P_i \tag{5.9}$$

The total power produced in the rectilinear and staggered farm is 22.1 MW and 28.1 MW respectively. For an identical farm size, this study shows the staggered array produces 6 MW power higher than the rectilinear configuration. This is consistent with previous tidal farm studies (Bai et al., 2013; Nguyen et al., 2019; Djama Dirieh et al., 2022). The added turbulence effect is higher in the rectilinear configuration as presented in Figure 5.12. The results show the added turbulence effect is significant in a rectilinear array as a consequence of limited turbine spacing. The turbulence intensity of the turbine downstream in the staggered array is largely recovered due to sufficient turbine spacing. The farm efficiency η_{farm} is defined as the ratio between the total power output from all turbines in a farm P_{farm} and the maximum power P_{farm}^{max} if they operate in unperturbed conditions.

$$\eta_{farm} = \frac{P_{farm}}{P_{farm}^{max}}$$

The farm efficiencies for the rectilinear and staggered array are 69.1% and 87.8% respectively. This increase in efficiency is solely due to the turbine configuration in the farm.

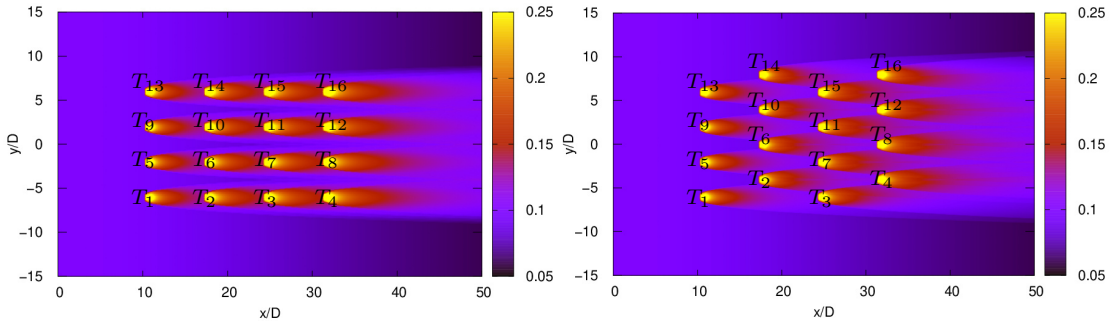

(a) rectilinear array **(b)** staggered array

Figure 5.12 Normalized turbulence intensity contour at different array configurations at DH40.

It is noted that in the rectilinear configuration, the lateral spacing S_y between turbine rows can be reduced without affecting the efficiency of the farm. But, what is the minimal turbine spacing that barely diminishes the output power? The lateral spacing S_y is reduced from $4D$ to $2D$ while maintaining the longitudinal spacing of $7D$ as shown in Figure 5.13. The cumulative power in the farm remains 22.1 MW for the different lateral spacing. However, a wake interaction effect is spotted between the turbine rows. In reality, there may be some slight differences as the model evaluates the power using the centerline velocity instead of the average velocity across the rotor. In the staggered array, Figure 5.14 compares the velocity contour for longitudinal spacing S_x reduction from $7D$ to $5D$ (i.e. the effective inline spacing is reduced from $14D$ to $10D$). The total power extracted from the farm dropped from 28.1 MW to 27.1 MW. The 3.1% reduction in efficiency can be tolerated in regard to the reduction in the farm size. Reducing the farm size whilst maintaining efficiency is essential because it will drastically reduce cable costs and will present an opportunity for future expansion of the farm.

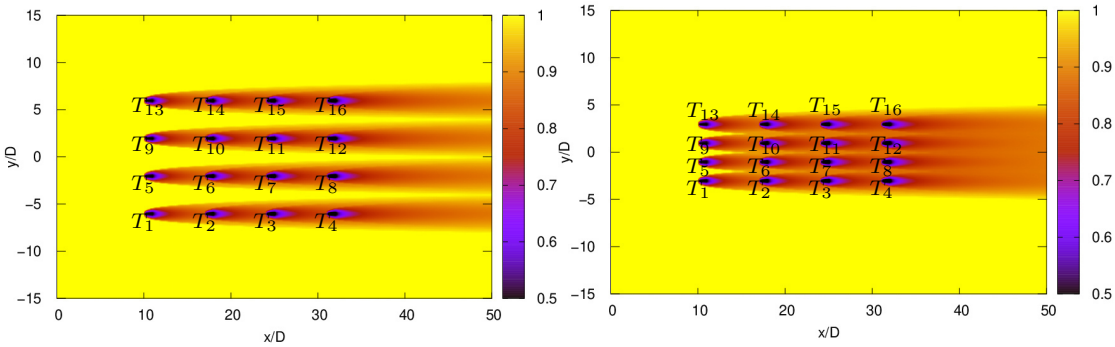

(a) Lateral spacing $S_y = 4D$ **(b)** Lateral spacing $S_y = 2D$

Figure 5.13 Comparison of normalized velocity contour at a different lateral spacing in rectilinear array at DH40.

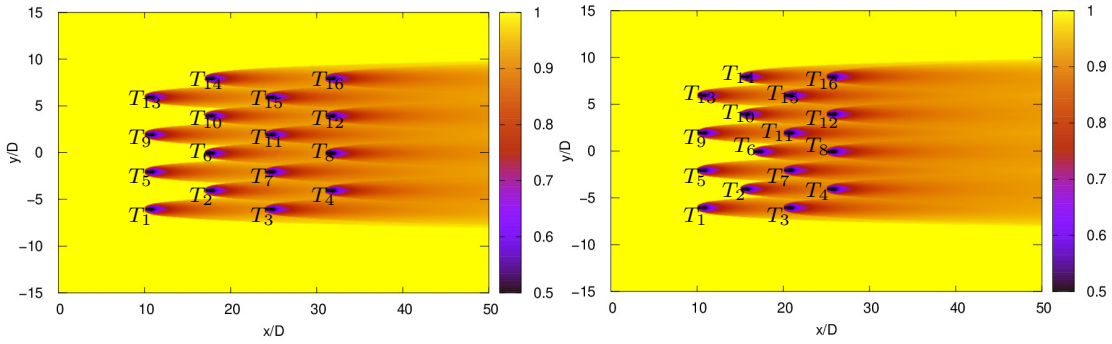

(a) Longitudinal spacing $S_x = 7D$ **(b)** Longitudinal spacing $S_x = 5D$

Figure 5.14 Comparison of normalized velocity contour at a different longitudinal spacing in staggered array at DH40.

5.3.3 Effect of rotor DH ratio in tidal farm

The effect of the rotor DH ratio on tidal farms is also investigated. The DH ratio is the rotor diameter to the channel depth. The rotor wake recovery is affected by the bypass flow. Figure 5.15 shows at a low rotor diameter to depth ratio, the wake expansion is higher and the interaction is higher. The power produced by the downstream turbine decreases with an increase in DH ratio as shown in Figure 5.16. The total farm power P_{farm} at DH20, DH40, and DH60 is 29.8 MW, 28.1 MW, and 26.9 MW respectively. In a low rotor diameter-to-depth ratio (i.e. DH20), the wake recovery process is faster as the flow in the bypass region is sufficient to cause mixing between the low velocity at the rotor's core and the ambient flow in the bypass region. However, at a high DH ratio (i.e. DH60), the velocity deficit along the rotor is substantial compared to the free stream flow in the bypass region, therefore lagging the wake recovery to the upstream condition. This implies that for an identical turbine size, the power extracted can vary with the channel diameter-to-depth ratio.

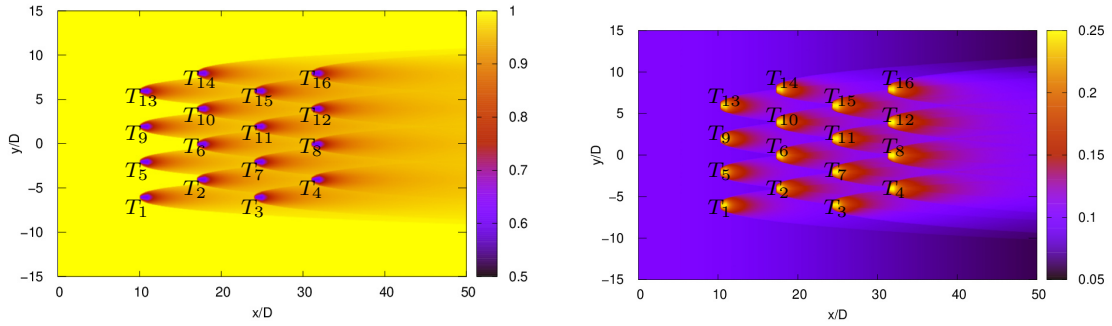

(a) $DH20$

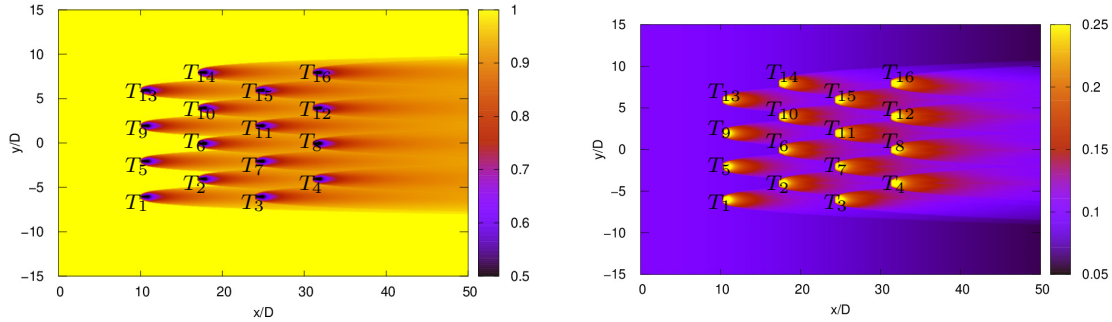

(b) $DH40$

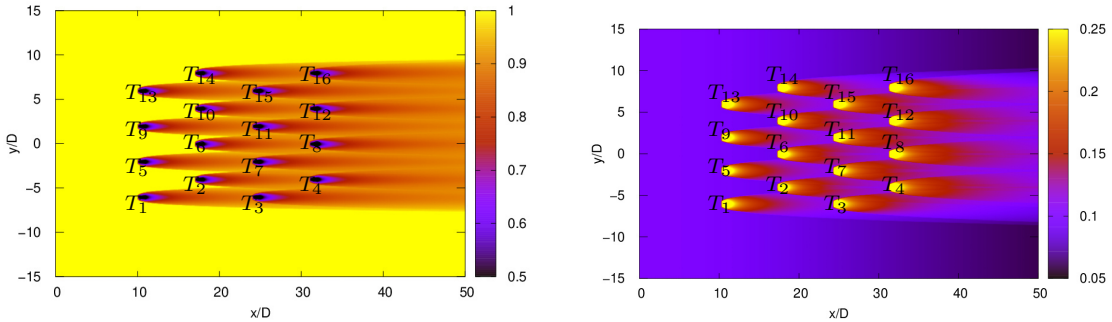

(c) $DH60$

Figure 5.15 Comparison of normalized velocity contour at different rotor diameter to depth ratio in staggered array at 7 D turbine spacing.

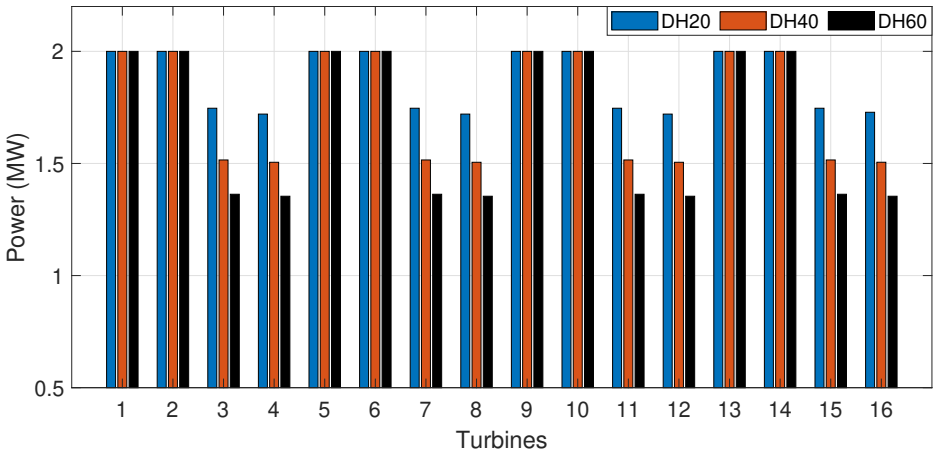

Figure 5.16 Power produced by the turbines in staggered array at different rotor diameter to depth ratio using the empirical model.

5.3.4 Effect of ambient turbulence on tidal farm

To investigate the effect of ambient turbulence on the power produced in a pilot farm, we studied a rectilinear array farm at DH40 with inter-device spacing $S_x = 7D$ as presented in Section 5.3.2 at 5%, 10%, 15%, and 20% ambient turbulence. Figure 5.17 shows an increase in wake expansion as a result of the increase in ambient turbulent intensity as discussed in Chapter 3. At $S_y = 4D$, the inline turbines act independently due to sufficient lateral spacing. The power extracted by individual turbines in the row is presented in Figure 5.18. The results indicated a decrease in power by virtue of the cumulative wake effect along in-line turbines. The power produced by the upstream turbine is identical for all ambient turbulence because the incoming flow for the upstream turbine is stable and not affected by any perturbation in the flow. Similarly, the power production is identical for each row at a given ambient turbulence. The continuous decrease in power for in-line turbines in a row at a given ambient turbulence results from the wake effect. However, at higher ambient turbulence, the wake recovery is faster, therefore, producing relatively higher power as shown in Table A.2. To clarify, turbine T_2 records a 24% increase in power due to increasing turbulent intensity from 5% to 20%. This increase in power extracted is noted for each turbine downstream. The wake recovery is accelerated by increasing ambient turbulence, thus producing more power. The farm efficiency increases with an increase in ambient turbulence as a result of increased wake recovery as shown in Table A.2.

In essence, the ambient turbulence can affect power production by downstream turbines. A low turbulent tidal site will require large turbine spacing to establish flow recovery and reduce the added turbulence effect on the downstream turbine. In contrast, a highly turbulent site can benefit from accelerated flow recovery permitting smaller turbine spacing in the array. The predicted power extracted

by the rotor in the first row remains identical for different ambient turbulence because the incoming flow is equal. There is no added turbulence effect upstream for the isolated turbine to hasten the flow recovery.

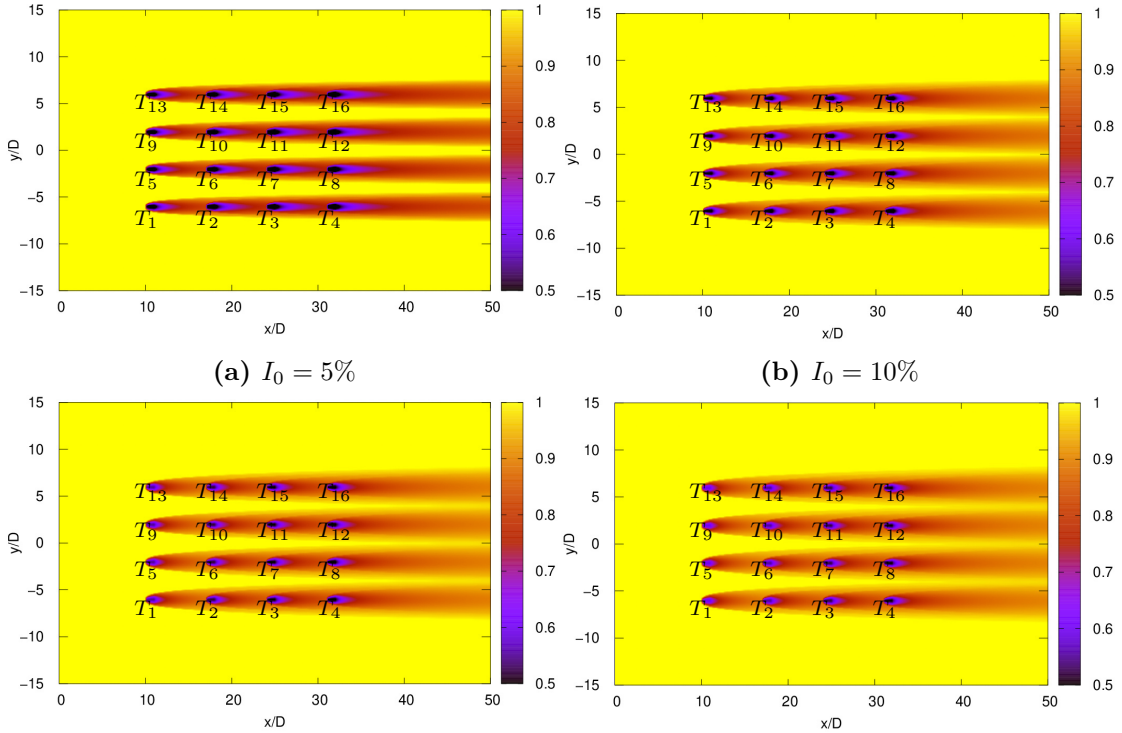

(a) $I_0 = 5\%$ **(b)** $I_0 = 10\%$

(c) $I_0 = 15\%$ **(d)** $I_0 = 20\%$

Figure 5.17 Comparison of normalized velocity contour at a different ambient turbulent intensity at DH40.

Table 5.1 Power extracted by turbines at different ambient turbulence in a rectilinear array.

	Power (MW)			
T_N \ I_0	5%	10%	15%	20%
T_1	2.04	2.04	2.04	2.04
T_2	1.10	1.30	1.39	1.45
T_3	0.95	1.18	1.26	1.32
T_4	0.87	1.12	1.19	1.24
P_{row}	4.96	5.64	5.88	6.05
η_{row}	60.80 %	69.20 %	72.10 %	74.10 %

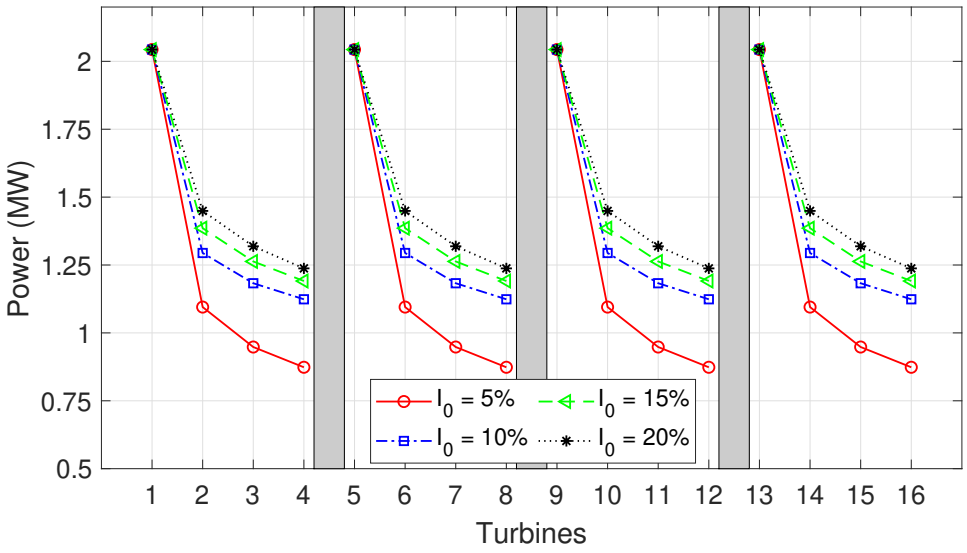

Figure 5.18 Comparison of power produced by 20 m diameter turbines in rectilinear array at different ambient turbulence.

5.3.5 Effect of C_T on rectilinear array

This section presents the effect of the thrust coefficient on the turbine array. The turbine diameter is 20 m and the rotor diameter to depth ratio is 40%. We consider a rectilinear tidal farm consisting of 16 turbines with 4 turbines in each row as shown in Figure 5.19. The first row named, R_1 has identical Betz thrust of coefficient for all turbine T_1 to T_4 (see Table 5.2). Similarly, second-row R_2 turbines have identical thrust coefficients ($C_T = 0.7$). Turbine T_1 in the third row R_3 has a thrust coefficient of 0.75 whereas the rest of the turbines in the row have identical Betz thrust coefficients (see Table 5.2). The turbines in Row_4 have different thrust coefficients in ascending order as shown in Table 5.2.

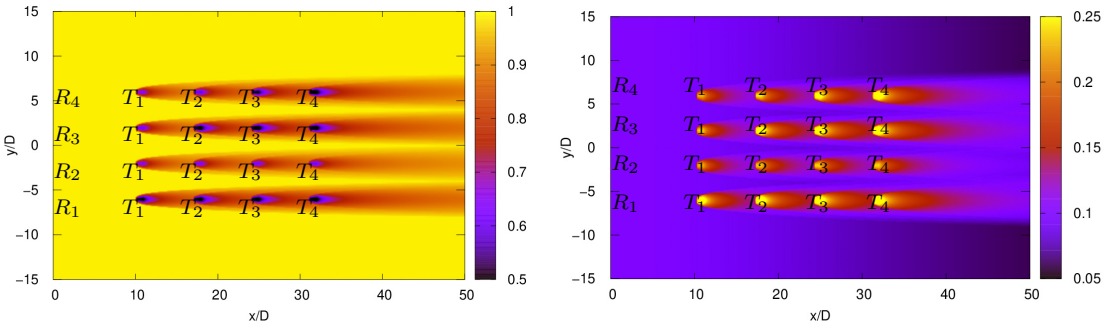

(a) Normalized velocity **(b)** Turbulent intensity

Figure 5.19 Contour of normalized velocity and turbulent intensity in a rectilinear farm with turbines at different thrust coefficients at DH40.

Table 5.2 Power extracted by turbines at different ambient turbulence in a rectilinear array.

	T_N	C_T	$U(m/s)$	$P_i(MW)$
	T_1	0.89	2.78	2.00
	T_2	0.89	2.39	1.27
	T_3	0.89	2.32	1.16
	T_4	0.89	2.27	1.10
Row_1				5.53
	T_1	0.70	2.78	1.83
	T_2	0.70	2.51	1.35
	T_3	0.70	2.46	1.27
	T_4	0.70	2.44	1.23
Row_2				5.68
	T_1	0.75	2.78	1.90
	T_2	0.89	2.49	1.43
	T_3	0.89	2.34	1.20
	T_4	0.89	2.29	1.12
Row_3				5.65
	T_1	0.70	2.78	1.83
	T_2	0.75	2.51	1.40
	T_3	0.85	2.44	1.34
	T_4	0.89	2.35	1.21
Row_4				5.78

Figure 5.20a shows the power production by the turbine presented in Table 5.2. The total power produced in the turbine row is comparable. The upstream turbine T_1 produces the highest power as it is not affected by the upstream turbine wake. The turbine T_1 in Row_1 with the highest C_T produces the maximum power whereas the turbine in Row_3 with minimum C_T produces the least power as shown in Table 5.2.

However, the power produced in Row_2 with a lower turbine thrust coefficient is 2.64% higher than Row_1 with $C_{T,Betz}$. Increasing the thrust coefficient is interpreted as increasing the drag causing a momentum exchange. The velocity recovery of turbines with lower thrust coefficient is faster leading to higher upstream velocity for the downstream turbines. Similarly, comparing Row_1 and Row_3, an increase of 0.12 MW in Row_3 is observed due to the lower thrust coefficient in turbine T_1. The low thrust coefficient of turbine T_1 allows faster wake recovery of the downstream turbines. The turbines in Row_4 produce the highest power of 5.78 MW in the tidal farm. The turbine thrust coefficient affects the wake of the downstream turbine. Figure 5.20b shows the recommended strategy in the tidal farm is turbines arranged with increasing thrust coefficient (i.e. Row_4). However,

the overall increase in power due to the variation in thrust coefficient is limited in a small tidal array. This effect can be significant in a large array and, therefore, should be considered in optimizing the tidal turbine farm.

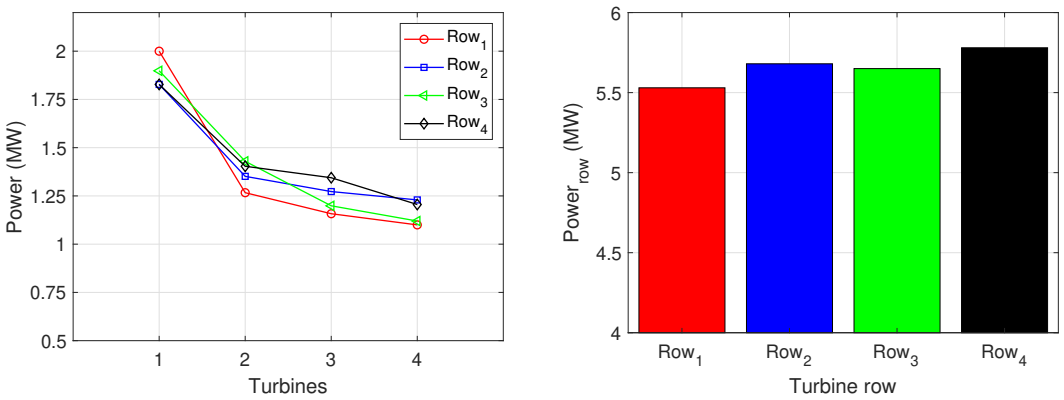

Figure 5.20 Comparison of power production in the rectilinear array by (a) by the individual turbine and (b) turbine row at different thrust coefficients.

5.4 Applications

5.4.1 Large tidal farm

A tidal farm size of $500m \times 500m$ is considered with $10m$ diameter turbines. The power production in staggered and rectilinear configurations is evaluated at 10% ambient turbulence, $C_{T,Betz}$, and DH20. The array layout is organized so that inter-device spacing S_x is $10D$ for both the rectilinear and staggered configuration to ensure flow recovery. Section 5.3.2 has shown that the lateral spacing in the rectilinear array can be reduced without affecting the power. Therefore, a lateral spacing of $3D$ and $5D$ is used in rectilinear and staggered arrays respectively. The velocity and turbulence contour in the large tidal farm is shown in Figure 5.21. The power produced in the farm is summarized in Table 5.3. The rectilinear array produces more power due to the higher number of turbines. The efficiency of both arrays is more than 85%, this high efficiency is obtained due to the large turbine spacing. At 10 D turbine spacing, the wake of the upstream turbine is largely recovered which overall increases the farm efficiency. However, this spacing is chosen arbitrarily.

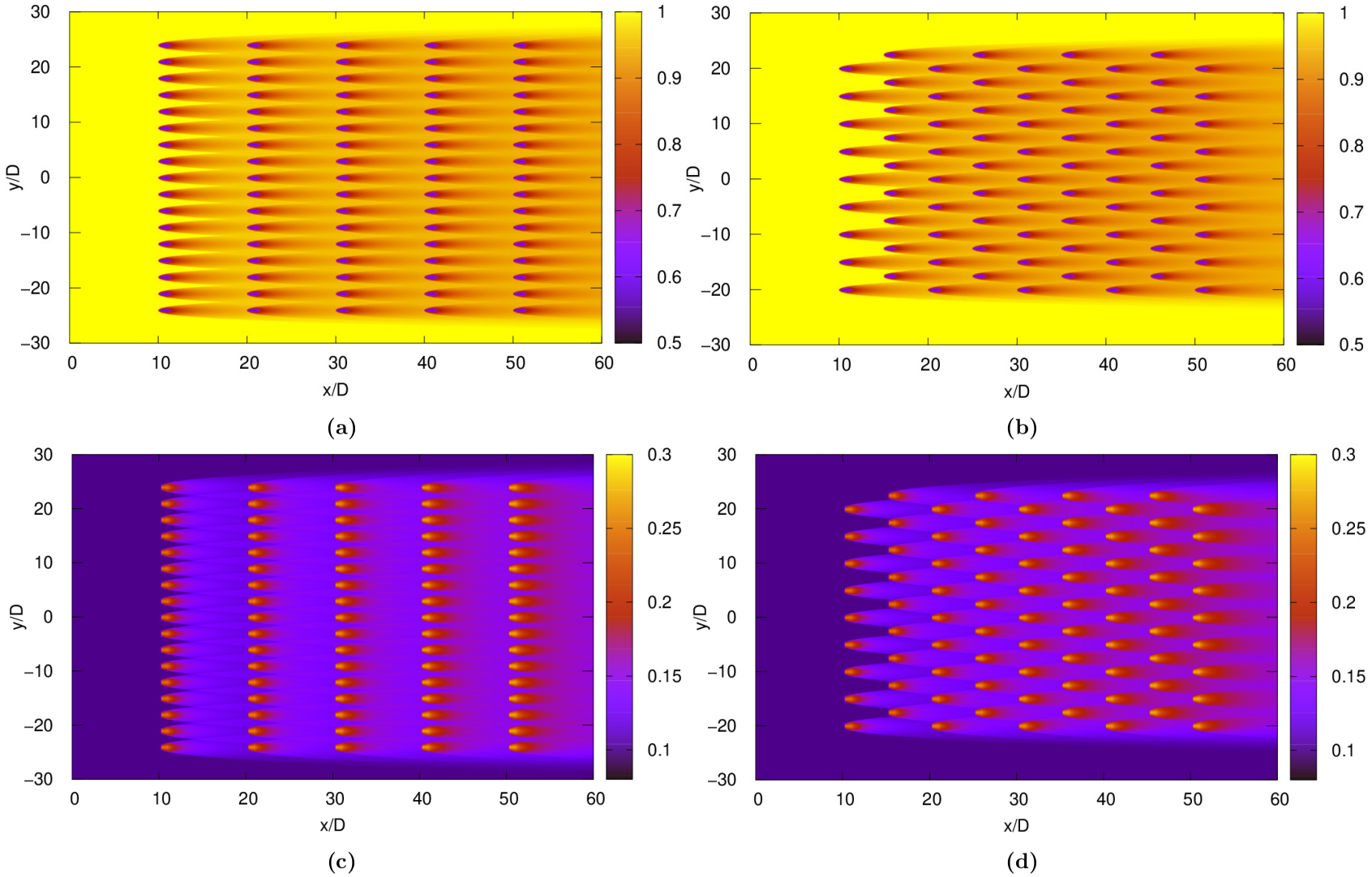

Figure 5.21 Contour of normalized velocity (top) and turbulent intensity (bottom) in (a) rectilinear (left) and (b) staggered array (right) at 10% ambient turbulent intensity and DH20.

Table 5.3 Summary of results on a large tidal farm.

Array	Rectilinear	Staggered
N_T	85	81
S_x	$10D$	$5D$
S_y	$5D$	$3D$
$P_{farm}(MW)$	45.45	43.56
$\eta_{farm}[\%]$	85.1	85.6

Similarly, the turbulent intensity contour in Figure 5.21 shows a sufficient wake recovery at the location of downstream turbines. In the farm with large turbine spacing, the effect of added turbulence on the downstream turbine is diminished therefore having less impact on downstream turbines. To harness maximum power in tidal farms, a multi-objective function algorithm is required to optimize the turbine placement considering the variation in ambient turbulence, the thrust coefficient, the rotor diameter-to-depth ratio, and the effect of added turbulence on the turbine downstream.

5.4.2 Lo Brutto optimize tidal farm

Lo Brutto et al. (2016b) uses Particle Swarm Optimization to evaluate the power production in tidal turbine farms. The best turbine configuration for uni-directional flow is from the optimization presented in Figure 5.22. The tidal farm comprises a 10 m diameter turbine in a channel with a rotor diameter to depth ratio of 20%. The low DH ratio will allow more wake expansion for the downstream turbine. The minimum turbine spacing is set as 5 D in both longitudinal and lateral directions. The average turbine spacing in the longitudinal and lateral directions in the optimized farm is 7.16 D and 14.06 D respectively. The turbine spacing is sufficiently large to ensure the wake recovery for a downstream turbine.

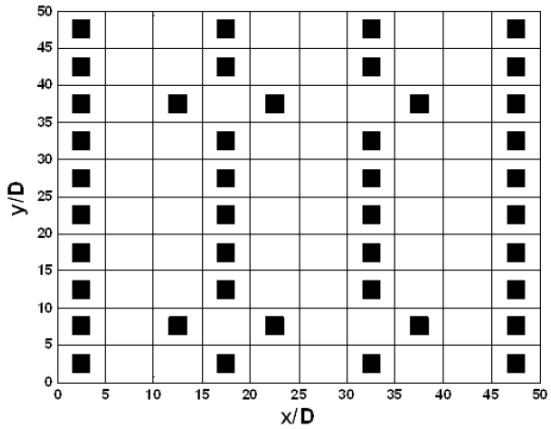

Figure 5.22 Optimized turbine layout configuration of Lo Brutto et al. (2016b).

Figures 5.23 to 5.25 presents the contour of the normalized velocity and turbulent intensity at different velocities. At cut-in speed, the power produced in the farm is very low as turbines do not produce electricity below the cut-in speed. Table 5.4 shows an increase in ambient turbulence increases the power extracted by the turbine. The power produced in the farm increases significantly with an increase in upstream velocity from 2 m/s to the rated speed of 3 m/s. This large increase in power for a given turbulent intensity is attributed to the increase in the incoming velocity in the farm. The power extracted is proportional to the cube of the velocity ($P \propto U^3$).

For example, at 5% ambient turbulence, P_{farm} increases by 14.7 MW when the upstream velocity increases from 2.0 m/s to 3.0 m/s as shown in Table 5.4. For a given incoming velocity, an increase in ambient turbulence increases the power produced in the tidal farm. The tidal farm attains a maximum efficiency of 91.46% when the ambient turbulence is 15%.

Table 5.4 Summary of power extracted at different hydrodynamic conditions in an optimized tidal turbine farm.

$U(m/s)$ \ I_0		5%	10%	15%
1.0	P_{farm} (MW)	0.773	0.872	0.894
2.0	P_{farm} (MW)	6.187	6.976	7.151
3.0	P_{farm} (MW)	20.881	23.545	24.135
	η_{farm} [%]	79.13	89.22	91.46

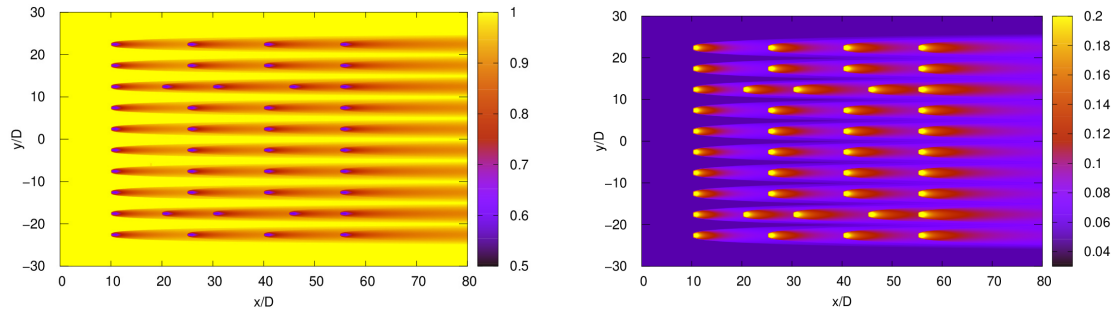

(a) $U = 3.0m/s; I_0 = 5\%$

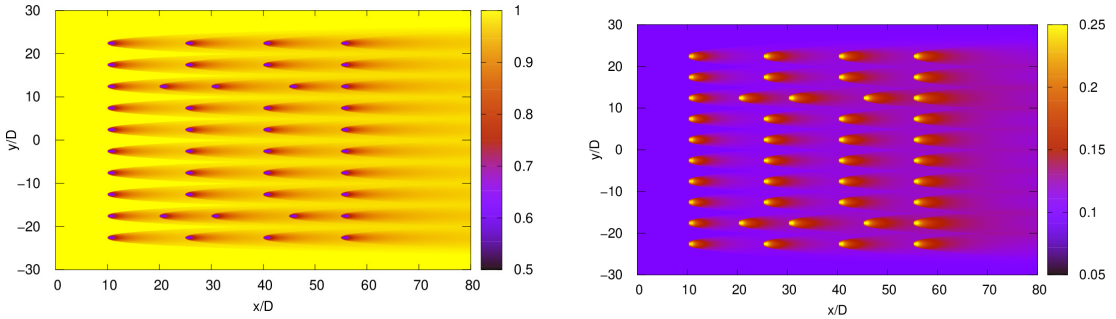

(b) $U = 3.0m/s; I_0 = 10\%$

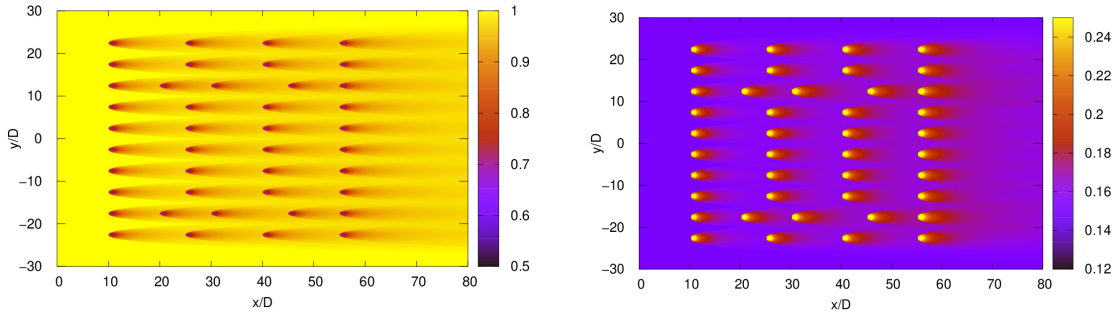

(c) $U = 3.0m/s; I_0 = 15\%$

Figure 5.23 Contour of normalized velocity (left) and turbulent intensity (right) of optimized tidal turbine farm of Lo Brutto et al. (2016b) at different ambient turbulent intensities.

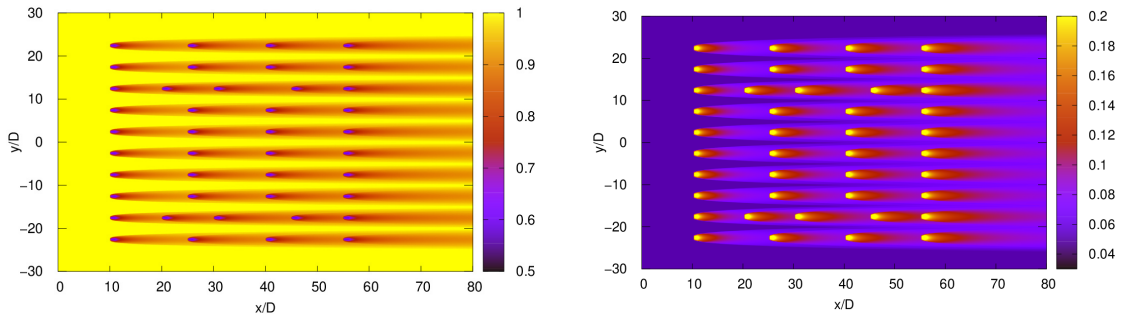

(a) $U = 2.0m/s; I_0 = 5\%$

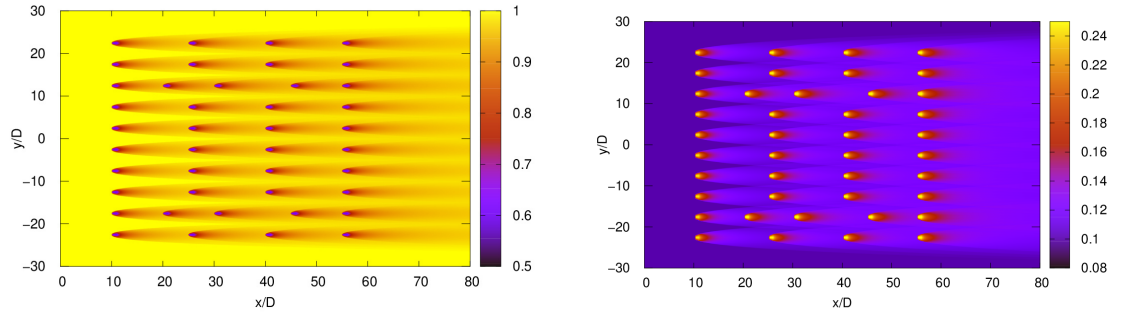

(b) $U = 2.0m/s; I_0 = 10\%$

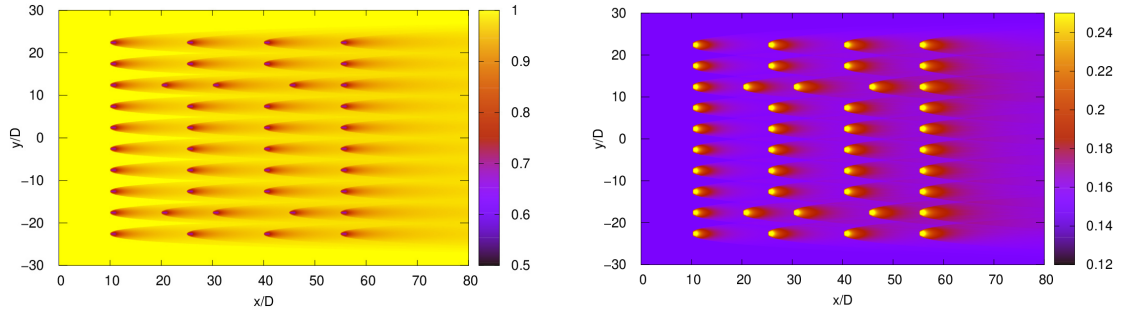

(c) $U = 2.0m/s; I_0 = 15\%$

Figure 5.24 Contour of normalized velocity (left) and turbulent intensity (right) of optimized tidal turbine farm of Lo Brutto et al. (2016b) at different ambient turbulent intensities.

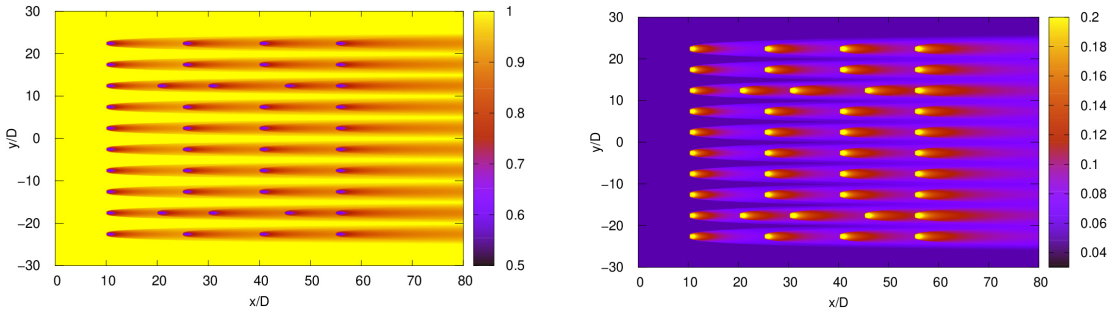

(a) $U = 1.0m/s; I_0 = 5\%$

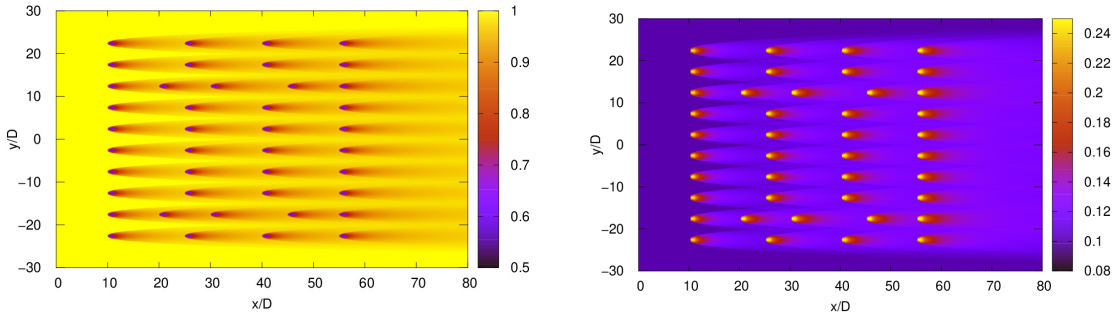

(b) $U = 1.0m/s; I_0 = 10\%$

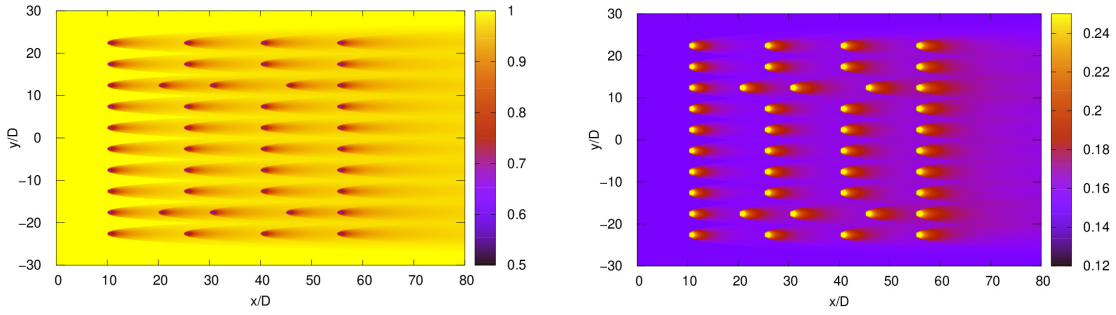

(c) $U = 1.0m/s;\ I_0 = 15\%$

Figure 5.25 Contour of normalized velocity (left) and turbulent intensity (right) of optimized tidal turbine farm of Lo Brutto et al. (2016b) at different ambient turbulent intensities.

5.5 Synthesis

In this chapter, a model for estimating the wake in tidal farms is developed considering the wake interaction effects between turbines. The cumulative wake interaction is evaluated using RSM which aims to conserve the kinetic energy deficit and turbulence energy. In the model, the user inputs the site specification details such as the farm size, the hydrodynamic conditions (ambient turbulence and mean current flow), and the farm specification (i.e. number of turbines, turbine size, position, and performance parameters). Next, the added turbulence is evaluated, then the effective turbulence is reconstructed to calculate the wake radius. If there is turbine interaction in the farm, the interacting area is assessed to estimate the velocity deficit and turbulent intensity in the farm.

Firstly, a simple array comprising 4 turbines in tandem is studied at different turbine spacing. At a small turbine spacing, the downstream turbine is subjected to higher turbulence compared to the upstream turbines. As the turbine spacing increases, the wake recovers faster and the downstream turbine extracts more power.

Next, a comparison of power production in rectilinear and staggered farms is studied in an identical farm comprising 16 turbines. In this study, the longitudinal and lateral turbine spacing is 7 D and 4 D respectively, to ensure sufficient wake recovery. The efficiency of the staggered arrangement is 18% higher than that of the in-line arrangement. The increase in efficiency is solely due to the turbine configuration in the park. It also notes that the turbine configuration can be reduced without sacrificing tidal farm efficiency. Reducing farm size reduces cable costs and frees up room for future expansion.

Moreover, the effect of the rotor diameter-to-depth ratio on power production in tidal farms is investigated. The results show that the pilot farm produces more power at a low DH ratio. This is due to the sufficient bypass flow region assisting the wake recovery. In addition, the effect of ambient turbulence on power production in tidal farms is studied. For an ideal farm, the farm efficiency increases with ambient turbulence.

Similarly, the effect of ambient turbulence on power extracted in tidal farms is investigated. The power extracted by the upstream turbines is not affected by the increase in ambient turbulence as no wake effect preceding the turbines. However, for the downstream turbines, the power extracted is substantially affected by the ambient turbulence in the flow. In a low ambient flow, the wake recovery is slow, therefore the subsequent turbines downstream are preceded by low velocity and high turbulence flow. Contrarily, in a high turbulent flow, the wake recovers faster within a short distance downstream providing high velocity and low turbulence to downstream turbines. For instance, a turbine array comprising 4 turbines at 20% ambient turbulence produces 1 MW power higher than an identical array at 5% ambient turbulence.

In addition, the turbine thrust coefficient can affect the wake power production

in turbine farms. Turbine array with low C_T (Row_2) produces more power than array with high C_T (Row_1). This increase in power is related to the speedy flow recovery due to the low-velocity deficit in the near wake when the thrust coefficient is low. The maximum power recorded in the farm is at Row_4 with an ascending thrust coefficient. The recommended strategy for turbine placement in tidal farms is a progressive increase in the thrust coefficient. However, the overall effect of C_T on power produced in a small array is limited. This effect can be significant in large arrays.

To sum up, our study shows that the efficiency of a tidal farm can be increased by (1) high ambient turbulent intensity, (2) sufficient turbine spacing, and (3) low rotor diameter-to-depth ratio. These factors improve the wake recovery to allow more energy to be extracted by a downstream turbine.

Chapter 6

Conclusions and perspectives

6.1 Conclusions

This thesis focuses on developing a low computational model to estimate the velocity deficit and the turbulent intensity of a horizontal axis tidal turbine on a farm. The main aim of the work is to develop a generic model to estimate power production in tidal turbine farms. The general contribution and main finding of this thesis are summarized as follows.

Firstly, the turbine is represented as a porous media using the Actuator Disk Method. The ADM applies a uniform thrust force to replicate the momentum exchange by the turbine. The ADM provides relatively good results in the far wake which is the scope of our study. In this thesis, the ADM is validated with good results with an established porous disk experiment and tidal turbine experiment. As the ADM rotor is stationary, a source term is added to complement the turbine-generated turbulence in the near wake.

After the model validation, a series of numerical simulations of a full-scale rotor at 20 m diameter is performed at different ambient turbulence corresponding to the range of turbulent intensity at tidal sites. Using the RANS-ADM, the turbine wake is found to be approximately Gaussian as reported in several studies in the literature. The turbine wake radius is estimated using the Full-Width Half Maximum of the Standard Gaussian function at 3σ. It was observed that the wake radius increases with ambient turbulent intensity whereas the wake length decreases. The increase in wake radius is due to a strong mixing and diffusion process at high turbulent intensity. A wake radius model is proposed based on power law that depends on the ambient turbulent intensity and the distance downstream. The use of power law is in agreement with the classical theory of wake. A centerline-added turbulence model is developed by curve fitting. The model is barely dependent on ambient turbulence. This is also observed by the Frandsen model which is used as the IEC standard for modeling the turbine of wind turbine wake. The added turbulence is primarily dominated in the near wake where the turbine-generated turbulence is highest. The turbulence in the turbine wake is reconstructed with

ambient turbulence and provides good results.

Similarly, a model is proposed to estimate the velocity deficit of a single turbine. To propose a generic model, numerical simulations are conducted at different channel depths and rotor diameter to depth (DH) ratio. The result shows that the results are identical for the same DH ratio irrespective of the channel depth. Commercial scale tidal turbines are expected to be located in shallow water where the rotor diameter to depth ratio varies from 20 - 60%. For this reason, different DH ratios (i.e. DH20, DH40, and DH60 for a rotor diameter to depth ratio of 20%, 40%, and 60% respectively) are considered to provide a generic model to estimate the velocity deficit and turbulent intensity in turbine wake. In addition to the range of ambient turbulence studied, a variation in thrust coefficient is also considered to ensure the wide applicability of the model.

Furthermore, the generic velocity deficit radius model is proposed using the FWHM approach. A new velocity model is based on the classical Jensen model. The choice of the Jensen model is guided by its simplicity, relative accuracy in the far wake, and wide application in commercial tools. However, the Jensen model is based on the top-hat shape function that clearly underestimates the velocity deficit at the center of the wake and overestimates it at the wake edges compared to experimental data. For this reason, our model uses the Gaussian shape function to estimate the wake expansion in the lateral direction as proposed in wake turbulence theory.

Not to mention, the turbine wake is generally assumed to be axisymmetry, this is true for wind turbines where the atmospheric layer is large compared to the turbine diameter. However, for a tidal turbine in shallow water, the wake transmutes from axisymmetric to 2D Gaussian due to the limited channel depth. Increasing the DH ratio decreases the wake expansion due to the low bypass flow region around the turbine. The increase in DH is interpreted as an increase in thrust coefficient that affects the wake close to the rotor. The model shows an increase in ambient turbulence increases the wake recovery due to better mixing and diffusion processes. There is a trade-off between increasing ambient turbulence and increasing the DH. The thrust coefficient is shown to affect the near wake by creating a large velocity deficit close to the turbine. As noted, the tidal turbine wake is dependent on at least three parameters; the ambient turbulence, the thrust coefficient, and the rotor diameter-to-depth ratio.

Next, the single turbine model is used to estimate the velocity deficit and turbulence in the tidal farm. The turbine-wake interaction is evaluated using kinetic energy deficits. The new model accounts for wake added turbulence intensity effect and the wake interaction in the farm. A simple array of turbines in tandem configuration shows the turbine spacing is pivotal to the energy produced by the downstream turbine. It has been observed that for a 10% ambient turbulence, both the normalized velocity and turbulent intensity are affected by the inter-device spacing. The wake of the upstream turbine has not recovered therefore the turbine at position S_x will be subjected to a highly turbulent and low incoming

flow. The normalized velocity successively decreases due to the wake effect. However, at 10 D spacing, the turbine spacing is sufficiently large that the flow fully recovered to 90% for the turbines downstream.

Furthermore, the power production in a rectilinear and staggered array comprising 16 turbines is compared. Profiting from the turbine arrangement, the staggered array produces about 6 MW power higher than the rectilinear array under the same condition. The increase in power is attributed to sufficient wake recovery in the former configuration. The comparison with different turbine spacing has shown that the rectilinear and staggered array can benefit from reduced lateral and longitudinal spacing without affecting the efficiency of the farm.

Also, the result obtained shows that in shallow water, the channel depth can affect the overall power production in a farm. An increase in power is observed when the rotor diameter-to-depth (DH) ratio is low. This resulted from a large wake expansion due to a sufficient bypass flow region that hastened the flow recovery at a low DH ratio. Specifically, the power produced drops by 5.7% when the DH ratio increases from DH20 to DH40. Lastly, the effect of turbulent intensity on farm efficiency is studied. For a farm with 7 D inter-device spacing, the total farm efficiency between 5% and 20% ambient turbulence increases from 60.8% to 74.1%. This 13.3% increase in power is attributed to better wake recovery at high ambient turbulence.

Overall, in this thesis, we have proposed potentially the first turbulence intensity model for horizontal axis tidal turbines and established a new relation for the rotor diameter to depth ratio. This turbulence model along with the modified Jensen-Gaussian model can be used to provide preliminary insight into power production in tidal farms. The efficiency of a tidal farm can be increased by high ambient turbulent intensity, sufficient turbine spacing, and low diameter-to-depth ratio. This low-computational model can be useful in studying the wake interaction of tidal turbine parks in different configurations. The applicability of the model over a wide range makes it useful in realistic tidal sites under ideal conditions.

6.2 Perspectives

Firstly, the numerical data can be improved by using a more accurate turbulence modeling approach like the LES-ALM. In reality, the wake of the turbulent intensity profile behind a turbine shows a two-dip Gaussian profile with maximum turbulence at the tip of the rotor. The use of RANS-ADM does not provide accurate wake shape, especially in the near wake. However, the use of LES-ALM can provide a better wake shape and a better prediction in both the near and the far wake. Moreover, the turbulence dissipation upstream of the turbine will be minimized, therefore, the use of a turbulence source may not be necessary. This is subjected to further investigation.

Secondly, empirical models are based on approximations which lead to a large error margin. The velocity deficit and turbulent intensity model can be improved

by providing a better model equation and more accurate coefficients. More accurate parameters can be obtained by using machine learning such as artificial neural network (ANN) for the wake radius, velocity deficit, and turbulent intensity.

Thirdly, the model is developed based on a constant incoming velocity in the farm. Investigating the applicability of the time-vary flow will be appealing in validating the model. The variability of the power curve should be considered in future work. Apart from this, the current flow in some tidal sites has incidence with respect to the predominant direction reaches up to 20°(Nguyen et al., 2019). The influence of the current direction on the energy production on a tidal farm using the empirical model should also be investigated.

Further, this study is developed for a turbine position at mid-depth in the channel. In practice, tidal turbines are located close to the bottom where the flow velocity is affected by the bathymetry of the seabed. The model can be improved by introducing a correction term to account for better estimation in realistic conditions as proposed by Orgiazzi et al. (2019).

Finally, the wake of velocity deficit and turbulence intensity shows dependence on a number of parameters. Therefore a multi-objective function optimization algorithm like the Particle Swarm Optimization (PSO) is required for turbine placement to maximize the power production in tidal turbine farms.

Bibliography

M. A. Abolghasemi, M. D. Piggott, J. Spinneken, A. Viré, C. J. Cotter, and S. Crammond. Simulating tidal turbines with multi-scale mesh optimisation techniques. *Journal of Fluids and Structures*, 66:69–90, Oct. 2016. ISSN 08899746. doi: 10.1016/j.jfluidstructs.2016.07.007. URL `https://linkinghub.elsevier.com/retrieve/pii/S0889974615301729`. 1.8.2, 2.4.4.2

U. Ahmed, D. D. Apsley, I. Afgan, T. Stallard, and P. K. Stansby. Fluctuating loads on a tidal turbine due to velocity shear and turbulence: Comparison of CFD with field data. *Renewable Energy*, 112:235–246, Nov. 2017. ISSN 0960-1481. doi: 10.1016/j.renene.2017.05.048. URL `https://www.sciencedirect.com/science/article/pii/S0960148117304330`. 1.8.2

A. S. Bahaj, L. E. Myers, M. D. Thomson, and N. Jorge. Characterising the wake of horizontal axis marine current turbines. In *Proceedings of 13th European Wave and Tidal Energy Conference*, volume 9, page 10, Porto, Portugal, 2007. (document), 1.8.1, 1.9, 2, 2.5, 2.5.1, 2.8, 2.5.1.3, 2.10, 2.11, C.2.4

G. Bai, J. Li, P. Fan, and G. Li. Numerical investigations of the effects of different arrays on power extractions of horizontal axis tidal current turbines. *Renewable Energy*, 53:180–186, May 2013. ISSN 0960-1481. doi: 10.1016/j.renene.2012.10.048. URL `https://www.sciencedirect.com/science/article/pii/S0960148112006982`. 1.6, 1.8.2, 1.8.3, 5.3.2, C.1.4, C.5.3.2

R. J. Barthelmie, G. C. Larsen, S. T. Frandsen, L. Folkerts, K. Rados, S. C. Pryor, B. Lange, and G. Schepers. Comparison of Wake Model Simulations with Offshore Wind Turbine Wake Profiles Measured by Sodar. *Journal of Atmospheric and Oceanic Technology*, 23(7):888 – 901, 2006. doi: 10.1175/JTECH1886.1. URL `https://journals.ametsoc.org/view/journals/atot/23/7/jtech1886_1.xml`. Place: Boston MA, USA Publisher: American Meteorological Society. 4.2.1, 5.1

M. Bastankhah and F. Porté-Agel. A new analytical model for wind-turbine wakes. *Renewable Energy*, 70:116–123, Oct. 2014. ISSN 09601481. doi: 10.1016/j.renene.2014.01.002. URL `https://linkinghub.elsevier.com/retrieve/pii/S0960148114000317`. (document), 1.8.3, 3.5.2, 3.5.3, 4, 4.1, 4.2.3, C.3.2.2

G. Bhuyan and G. Darou. Integrated Tidal Current Demonstration Project at Race Rocks, British Columbia, Canada. Technical report, European Commission Coordinated Action on Ocean Energy (CA-OE), Copenhagen, Copenhagen, Denmark, 2007. URL https://racerocks.ca/integrated-tidal-current-demonstration-project-at-race-rocks/. 1.2

I. Billeaud, B. Tessier, and P. Lesueur. Impacts of late Holocene rapid climate changes as recorded in a macrotidal coastal setting (Mont-Saint-Michel Bay, France). *Geology*, 37(11):1031–1034, Nov. 2009. ISSN 0091-7613. doi: 10.1130/G30310A.1. URL https://doi.org/10.1130/G30310A.1. 1.4

T. Blackmore, W. M. J. Batten, M. E. Harrison, and A. S. Bahaj. The Sensitivity of Actuator-Disc RANS Simulations to Turbulence Length Scale Assumptions. In *9th European Wave and Tidal Energy Conference*, page 10, Southampton, United Kingdom, Sept. 2011. URL http://eprints.soton.ac.uk/id/eprint/372458. 3.4.1.2, 4.5.2

T. Blackmore, W. M. J. Batten, and A. S. Bahaj. Influence of turbulence on the wake of a marine current turbine simulator. *Proceedings of the Royal Society A: Mathematical, Physical and Engineering Sciences*, 470(2170):20140331, Oct. 2014. ISSN 1364-5021, 1471-2946. doi: 10.1098/rspa.2014.0331. URL https://royalsocietypublishing.org/doi/10.1098/rspa.2014.0331. 1.8.1, 2.3.3, 4.5.2, C.2.2

F. Blondel and M. Cathelain. An alternative form of the super-Gaussian wind turbine wake model. *Wind Energy Science*, 5(3):1225–1236, Sept. 2020. ISSN 2366-7443. doi: 10.5194/wes-5-1225-2020. URL https://wes.copernicus.org/articles/5/1225/2020/. Publisher: Copernicus GmbH. 1.8.3

P. Brousseau, M. Benaouicha, and S. Guillou. Fluid-structure interaction effects on the deformable and pitching plate dynamics in a fluid flow. *Applied Ocean Research*, 113:102720, Aug. 2021. ISSN 0141-1187. doi: 10.1016/j.apor.2021.102720. URL https://www.sciencedirect.com/science/article/pii/S0141118721001978. 1.6

T. Burton, N. Jenkins, D. Sharpe, and E. Bossanyi. *Wind Energy Handbook*. John Wiley & Sons, 2nd edition, May 2011. ISBN 978-1-119-99392-6. (document), 2.4, 3.3.2

R. Campbell, A. Martinez, C. Letetrel, and A. Rio. Methodology for estimating the French tidal current energy resource. *International Journal of Marine Energy*, 19:256–271, Sept. 2017. ISSN 2214-1669. doi: 10.1016/j.ijome.2017.07.011. URL https://www.sciencedirect.com/science/article/pii/S2214166917300553. (document), 1.5.3, 1.11

S. C. Capareda. *Introduction to Renewable Energy Conversions*. Number 9780429199103. CRC Press, Boca Raton, 1st edition, Aug. 2019. ISBN 978-0-429-58342-1. 1.4

L. P. Chamorro and F. Porté-Agel. A Wind-Tunnel Investigation of Wind-Turbine Wakes: Boundary-Layer Turbulence Effects. *Boundary-Layer Meteorology*, 132(1):129–149, July 2009. ISSN 0006-8314, 1573-1472. doi: 10.1007/s10546-009-9380-8. URL http://link.springer.com/10.1007/s10546-009-9380-8. 1.7, 3.3.4, 3.5, C.1.3

Y. Chen, B. Lin, J. Sun, J. Guo, and W. Wu. Hydrodynamic effects of the ratio of rotor diameter to water depth: An experimental study. *Renewable Energy*, 136:331–341, June 2019. ISSN 0960-1481. doi: 10.1016/j.renene.2019.01.022. URL https://www.sciencedirect.com/science/article/pii/S0960148119300229. 1.8.1, 1.8.1, 4.3.3

Y. Cheng, M. Zhang, Z. Zhang, and J. Xu. A new analytical model for wind turbine wakes based on Monin-Obukhov similarity theory. *Applied Energy*, 239:96–106, Apr. 2019. ISSN 03062619. doi: 10.1016/j.apenergy.2019.01.225. URL https://linkinghub.elsevier.com/retrieve/pii/S0306261919302454. 1.8.3

D. S. Coles, L. S. Blunden, and A. S. Bahaj. Assessment of the energy extraction potential at tidal sites around the Channel Islands. *Energy*, 124:171–186, Apr. 2017. ISSN 0360-5442. doi: 10.1016/j.energy.2017.02.023. URL https://www.sciencedirect.com/science/article/pii/S0360544217301974. 1.5.3

A. Crespo and J. Hernandez. Turbulence characteristics in wind-turbine wakes. *Journal of Wind Engineering and Industrial Aerodynamics*, 61(1):71–85, June 1996. ISSN 0167-6105. doi: 10.1016/0167-6105(95)00033-X. URL https://www.sciencedirect.com/science/article/pii/016761059500033X. (document), 1, 1.8.3, 1.8.5, 3, 3.3, 3.3.2, 3.5, 3.6.2, 4.2.4, C.1.4, C.3.1

N. Djama Dirieh, J. Thiébot, S. Guillou, and N. Guillou. Blockage Corrections for Tidal Turbines—Application to an Array of Turbines in the Alderney Race. *Energies*, 15(10):3475, Jan. 2022. ISSN 1996-1073. doi: 10.3390/en15103475. URL https://www.mdpi.com/1996-1073/15/10/3475. Number: 10 Publisher: Multidisciplinary Digital Publishing Institute. (document), 1.6, 1.8.2, 1.17, 2.3.3, 2.4.4, 3.4.1, 5.3.2, C.5.3.2

T. Ebdon, M. J. Allmark, D. M. O'Doherty, A. Mason-Jones, T. O'Doherty, G. Germain, and B. Gaurier. The impact of turbulence and turbine operating condition on the wakes of tidal turbines. *Renewable Energy*, 165:96–116, Mar. 2021. ISSN 0960-1481. doi: 10.1016/j.renene.2020.11.065. URL https://www.sciencedirect.com/science/article/pii/S0960148120318085. 1, 1.8.1

A. El Kasmi and C. Masson. An extended model for turbulent flow through horizontal-axis wind turbines. *Journal of Wind Engineering and Industrial Aerodynamics*, 96(1):103–122, Jan. 2008. ISSN 01676105. doi: 10.1016/j.jweia.2007.03.007. URL https://linkinghub.elsevier.com/retrieve/pii/S0167610507000943. 2.4.4.1, 2.4.4.2, 3.4.1.2

T. El Tawil, N. Guillou, J.-F. Charpentier, and M. Benbouzid. On Tidal Current Velocity Vector Time Series Prediction: A Comparative Study for a French High Tidal Energy Potential Site. *Journal of Marine Science and Engineering*, 7(2):46, Feb. 2019. ISSN 2077-1312. doi: 10.3390/jmse7020046. URL https://www.mdpi.com/2077-1312/7/2/46. Number: 2 Publisher: Multidisciplinary Digital Publishing Institute. 1.2

M. Elgendi, M. AlMallahi, A. Abdelkhalig, and M. Y. E. Selim. A review of wind turbines in complex terrain. *International Journal of Thermofluids*, 17:100289, Feb. 2023. ISSN 2666-2027. doi: 10.1016/j.ijft.2023.100289. URL https://www.sciencedirect.com/science/article/pii/S2666202723000113. 2.4.4

EMEC. Tidal clients : EMEC: European Marine Energy Centre, 2022. URL https://www.emec.org.uk/about-us/our-tidal-clients/. 5.1

S. Frandsen. *Turbulence and turbulence-generated structural loading in wind turbine clusters*. PhD thesis, Technical University of Denmark, Denmark, Jan. 2007. URL https://www.osti.gov/etdeweb/biblio/20685756. 3.3, 6.1, C.3.1

S. Frandsen and M. L. Thøgersen. Integrated Fatigue Loading for Wind Turbines in Wind Farms by Combining Ambient Turbulence and Wakes. *Wind Engineering*, 23(6):327–339, 1999. ISSN 0309-524X. URL https://www.jstor.org/stable/43749903. Publisher: Sage Publications, Ltd. (document), 1.8.5, 3, 3.3.3, 3.3.3, 3.6.2, 3.6.2, 5.1.1, 5.1.1

S. Frandsen, R. Barthelmie, S. Pryor, O. Rathmann, S. Larsen, J. Højstrup, and M. Thøgersen. Analytical modelling of wind speed deficit in large offshore wind farms. *Wind Energy*, 9(1-2):39–53, Jan. 2006. ISSN 1095-4244, 1099-1824. doi: 10.1002/we.189. URL http://doi.wiley.com/10.1002/we.189. 1.8.3, 3.5.3, 3.7, 4.1, 4.2.2

S. W. Funke, P. E. Farrell, and M. D. Piggott. Tidal turbine array optimisation using the adjoint approach. *Renewable Energy*, 63:658–673, Mar. 2014. ISSN 0960-1481. doi: 10.1016/j.renene.2013.09.031. URL https://www.sciencedirect.com/science/article/pii/S0960148113004989. 1.8.4

S. Gant and T. Stallard. Modelling a Tidal Turbine in Unsteady Flow. In *Proceedings of the Eighteenth (2008) International Offshore and Polar Engineering Conference*, page 8, Vancouver, Canada, 2008. ISBN 978-1-880653-70-8. 3.4.1

B. Gaurier, M. Ikhennicheu, G. Germain, and P. Druault. Experimental study of bathymetry generated turbulence on tidal turbine behaviour. *Renewable Energy*, 156:1158–1170, Aug. 2020. ISSN 0960-1481. doi: 10.1016/j.renene.2020.04.102. URL https://www.sciencedirect.com/science/article/pii/S0960148120306340. 1.8.1

D. Greaves and G. Iglesias. *Wave and Tidal Energy*. John Wiley & Sons, 1st edition, Mar. 2018. ISBN 978-1-119-01447-8. URL https://onlinelibrary.wiley.com/doi/abs/10.1002/9781119014492.ch4. 1.5.1, 2.1.3

M. Grondeau, S. S. Guillou, J. C. Poirier, P. Mercier, E. Poizot, and Y. Méar. Studying the Wake of a Tidal Turbine with an IBM-LBM Approach Using Realistic Inflow Conditions. *Energies*, 15(6):2092, Jan. 2022. ISSN 1996-1073. doi: 10.3390/en15062092. URL https://www.mdpi.com/1996-1073/15/6/2092. Number: 6 Publisher: Multidisciplinary Digital Publishing Institute. (document), 1.8.2, 2.6, 3.6.2, 3.11, C.2.4, C.3.3.2

O. U. Guide. *OpenFOAM User Guide*. OpenCFD Limited, v2006 edition, June 2020. URL https://www.openfoam.com/documentation/user-guide. 2.4.3

M. O. L. Hansen. *Aerodynamics of Wind Turbines*. Routledge, 3rd edition, 2015. ISBN 978-1-138-77507-7. (document), 2.3

J. Hardisty. The Tidal Stream Power Curve: A Case Study. *Energy and Power Engineering*, 04:132–136, Jan. 2012. doi: 10.4236/epe.2012.43018. 1.3

M. E. Harrison, W. M. J. Batten, and A. S. Bahaj. A blade element actuator disc approach applied to tidal stream turbines. Seattle, WA, Sept. 2010a. IEEE. ISBN 978-1-4244-4332-1. URL http://ieeexplore.ieee.org/document/5664564/. 2.3.3

M. E. Harrison, W. M. J. Batten, L. E. Myers, and A. S. Bahaj. Comparison between CFD simulations and experiments for predicting the far wake of horizontal axis tidal turbines. *IET Renewable Power Generation*, 4(6):613–627, Nov. 2010b. ISSN 1752-1424. doi: 10.1049/iet-rpg.2009.0193. URL https://digital-library.theiet.org/content/journals/10.1049/iet-rpg.2009.0193. Publisher: IET Digital Library. 1.9, 2.3.3, 2.5.1.2

U. Hassan. A wind tunnel investigation of the wake structure within small wind turbine farms. Technical report ETSU-WN-5113, Garrad, Hassan and Partners, Bristol, United Kingdom, Nov. 1993. URL https://www.osti.gov/etdeweb/biblio/10195365. 3.3

IEA. Renewable Electricity – Analysis. Technical report, IEA, Paris, 2022. URL https://www.iea.org/reports/renewable-electricity. 1.1

S. IEC. *IEC 61400–1,Wind energy generation systems*. IEC, 1.0 2019-04 edition, 2001. 3.3.3

IRENA. Innovation outlook: Ocean energy technologies. Technical report, International Renewable Energy Agency, Abu Dhabi, 2020. URL :www.irena.org/Publications. 1.2, 1.3, 1.4, C.1.1

T. Ishihara and G.-W. Qian. A new Gaussian-based analytical wake model for wind turbines considering ambient turbulence intensities and thrust coefficient effects. *Journal of Wind Engineering and Industrial Aerodynamics*, 177:275–292, June 2018. ISSN 01676105. doi: 10.1016/j.jweia.2018.04.010. URL https://linkinghub.elsevier.com/retrieve/pii/S0167610517306396. (document), 1.8.3, 3, 3.3, 3.3.4, 3.1, 3.5.2, 3.5.3, 3.7, 4, 4.1, 4.2.5, 4.2, C.3.1, C.3.2.2

P. Jeffcoate, R. Starzmann, B. Elsaesser, S. Scholl, and S. Bischoff. Field measurements of a full scale tidal turbine. *International Journal of Marine Energy*, 12:3–20, Dec. 2015. ISSN 2214-1669. doi: 10.1016/j.ijome.2015.04.002. URL https://www.sciencedirect.com/science/article/pii/S221416691500017X. 1.6

N. O. Jensen. A note on wind generator interaction. Technical Report 2411, Risø National Laboratory, Roskilde, Denmark, 1983. (document), 1.8.3, 3.5.3, 4, 4.1, 4.2.1, 4.2.3, 4.2.7, C.3.2.2

C.-H. Jo, J.-H. Lee, Y.-H. Rho, and K.-H. Lee. Performance analysis of a HAT tidal current turbine and wake flow characteristics. *Renewable Energy*, 65:175–182, May 2014. ISSN 0960-1481. doi: 10.1016/j.renene.2013.08.027. URL https://www.sciencedirect.com/science/article/pii/S0960148113004291. 4.2.9

E. Jump, A. Macleod, and T. Wills. Review of tidal turbine wake modelling methods. *International Marine Energy Journal*, 3(2):91–100, Sept. 2020. ISSN 2631-5548. doi: 10.36688/imej.3.91-100. URL https://www.marineenergyjournal.org/imej/article/view/57. Number: 2. 1.8.2

I. Katic, J. Højstrup, and N. Jensen. A Simple Model for Cluster Efficiency: European Wind Energy Association Conference and Exhibition. *EWEC'86. Proceedings. Vol. 1*, pages 407–410, 1987. Place: Rome Publisher: A. Raguzzi. 1.8.4, 4.2.1

F. Khaled, S. Guillou, and Y. Méar. Impact of the blockage ratio on the transport of sediment in the presence of a hydrokinetic turbine: Numerical modeling of the interaction sediment and turbine | Elsevier Enhanced Reader. 2021. doi: 10.1016/j.ijsrc.2021.02.003. URL https://www.sciencedirect.com/science/article/pii/S1001627921000056. 2.3.3, 2.4.4

W.-H. Lam, L. Chen, and R. Hashim. Analytical wake model of tidal current turbine. *Energy*, 79:512–521, Jan. 2015. ISSN 03605442. doi: 10.1016/

j.energy.2014.11.047. URL https://linkinghub.elsevier.com/retrieve/pii/S0360544214013024. (document), 1.8.3, 4, 4.1, 4.2.6

G. C. Larsen, J. Hoejstrup, and H. A. Madsen. Wind fields in wakes. In *1996 European Union Wind Energy Conference*, pages 764–768, Goeteborg ,Sweden, Dec. 1996. URL https://www.osti.gov/etdeweb/biblio/634807. 1.8.5, 3.5.3

L. Li, Z. Huang, M. Ge, and Q. Zhang. A novel three-dimensional analytical model of the added streamwise turbulence intensity for wind-turbine wakes. *Energy*, 238:121806, Jan. 2022. ISSN 0360-5442. doi: 10.1016/j.energy.2021.121806. URL https://www.sciencedirect.com/science/article/pii/S0360544221020545. 1.8.5

Y. Li, J. A. Colby, N. Kelley, R. Thresher, B. Jonkman, and S. Hughes. Inflow Measurement in a Tidal Strait for Deploying Tidal Current Turbines: Lessons, Opportunities and Challenges. In *29th International Conference on Ocean, Offshore and Arctic Engineering: Volume 3*, pages 569–576, Shanghai, China, Jan. 2010. ASMEDC. ISBN 978-0-7918-4911-8. doi: 10.1115/OMAE2010-20911. URL https://asmedigitalcollection.asme.org/OMAE/proceedings/OMAE2010/49118/569/345899. 1.2

Y. Li, J.-H. Yi, H. Song, Q. Wang, Z. Yang, N. D. Kelley, and K.-S. Lee. On the natural frequency of tidal current power systems—A discussion of sea testing. *Applied Physics Letters*, 105(2):023902, July 2014. ISSN 0003-6951, 1077-3118. doi: 10.1063/1.4886797. URL http://aip.scitation.org/doi/10.1063/1.4886797. 1.2

P. B. S. Lissaman. Energy Effectiveness of Arbitrary Arrays of Wind Turbines. *Journal of Energy*, 3(6):323–328, 1979. ISSN 0146-0412. doi: 10.2514/3.62441. URL https://doi.org/10.2514/3.62441. Publisher: American Institute of Aeronautics and Astronautics _eprint: https://doi.org/10.2514/3.62441. 1.8.4, 5.1.2

X. Liu, Z. Chen, Y. Si, P. Qian, H. Wu, L. Cui, and D. Zhang. A review of tidal current energy resource assessment in China. *Renewable and Sustainable Energy Reviews*, 145:111012, July 2021. ISSN 1364-0321. doi: 10.1016/j.rser.2021.111012. URL https://www.sciencedirect.com/science/article/pii/S1364032121003026. 1.2

X. iu, H. u, B. ang, Y. ang, C. i, Y. i, P. ian, and D. hang. An analytical double-Gaussian wake model of ducted horizontal-axis tidal turbine. *Physics of Fluids*, 35(4):043103, Apr. 2023. ISSN 1070-6631. doi: 10.1063/5.0146196. URL https://doi.org/10.1063/5.0146196. (document), 3.3, 4, 4.1, 4.2.8

O. Lo Brutto. *Energy management in a tidal farm. Application to the Alderney Race (Raz Blanchard).* These de doctorat, Université de Caen, Cherbourg, Jan. 2016. URL https://www.theses.fr/2016CAEN2037. (document), 1.14, 1.9

O. A. Lo Brutto, V. T. Nguyen, S. S. Guillou, J. Thiébot, and H. Gualous. Tidal farm analysis using an analytical model for the flow velocity prediction in the wake of a tidal turbine with small diameter to depth ratio. *Renewable Energy*, 99:347–359, Dec. 2016a. ISSN 09601481. doi: 10.1016/j.renene.2016.07.020. URL https://linkinghub.elsevier.com/retrieve/pii/S0960148116306164. (document), 1.8.3, 1.20, 1.8.4, 3.5.3, 4.1, 4.2.7, 4.4.2, 4.4.2, 4.4.3

O. A. Lo Brutto, J. Thiébot, S. S. Guillou, and H. Gualous. A semi-analytic method to optimize tidal farm layouts – Application to the Alderney Race (Raz Blanchard), France. *Applied Energy*, 183:1168–1180, Dec. 2016b. ISSN 03062619. doi: 10.1016/j.apenergy.2016.09.059. URL https://linkinghub.elsevier.com/retrieve/pii/S0306261916313617. (document), 1.8.2, 1.8.3, 1.8.4, 3.4.1.1, 4.2.9, 5.1, 5.1.2, 5.4.2, 5.22, 5.23, 5.24, 5.25

O. A. L. Lo Brutto, M. R. Barakat, S. S. Guillou, J. Thiébot, and H. Gualous. Influence of the Wake Effect on Electrical Dynamics of Commercial Tidal Farms: Application to the Alderney Race (France). *IEEE Transactions on Sustainable Energy*, 9(1):321–332, Jan. 2018. ISSN 1949-3037. doi: 10.1109/TSTE.2017.2731839. Conference Name: IEEE Transactions on Sustainable Energy. 1.8.5

J. L. Lumley. Turbulence modeling. *ASME Journal of Applied Mechanics*, 50:1097–1103, Dec. 1983. ISSN 0021-8936. URL https://ui.adsabs.harvard.edu/abs/1983ATJAM..50.1097L. ADS Bibcode: 1983ATJAM..50.1097L. 2.1.3

J. MacEnri, M. Reed, and T. Thiringer. Influence of tidal parameters on SeaGen flicker performance. *Philosophical Transactions of the Royal Society A: Mathematical, Physical and Engineering Sciences*, 371(1985):20120247, Feb. 2013. ISSN 1364-503X, 1471-2962. doi: 10.1098/rsta.2012.0247. URL https://royalsocietypublishing.org/doi/10.1098/rsta.2012.0247. 1.2

D. Magagna and A. Uihlein. Ocean energy development in Europe: Current status and future perspectives. *International Journal of Marine Energy*, 11:84–104, Sept. 2015. ISSN 2214-1669. doi: 10.1016/j.ijome.2015.05.001. URL https://www.sciencedirect.com/science/article/pii/S2214166915000181. 1.6

F. Maganga, G. Germain, J. King, G. Pinon, and E. Rivoalen. Experimental characterisation of flow effects on marine current turbine behaviour and on its wake properties. *IET Renewable Power Generation*, 4(6):498, 2010. ISSN 17521416. doi: 10.1049/iet-rpg.2009.0205. URL https://digital-library.theiet.org/content/journals/10.1049/iet-rpg.2009.0205. 1.8.1, 1.8.3, 2.6, C.2.4

P. Mercier and S. S. Guillou. Spatial and temporal variations of the flow characteristics at a tidal stream power site: A high-resolution numerical

study. *Energy Conversion and Management*, 269:116123, 2022. ISSN 0196-8904. doi: https://doi.org/10.1016/j.enconman.2022.116123. URL https://www.sciencedirect.com/science/article/pii/S0196890422009062. 1.2

I. A. Milne, R. N. Sharma, R. G. J. Flay, and S. Bickerton. Characteristics of the turbulence in the flow at a tidal stream power site. *Philosophical Transactions of the Royal Society A: Mathematical, Physical and Engineering Sciences*, 371 (1985):20120196, Feb. 2013. ISSN 1364-503X, 1471-2962. doi: 10.1098/rsta.2012.0196. URL https://royalsocietypublishing.org/doi/10.1098/rsta.2012.0196. 1.2

S. Milojević. Power law distributions in information science: Making the case for logarithmic binning. *Journal of the American Society for Information Science and Technology*, 61(12):2417–2425, Dec. 2010. ISSN 15322882. doi: 10.1002/asi.21426. URL https://onlinelibrary.wiley.com/doi/10.1002/asi.21426. 3.5.3

S. Moon. Le Raz Blanchard demonstration site, 2022. URL https://interregtiger.com/expanding-the-marine-energy-market/development-sites-and-procurement/le-raz-blanchard/. 1.6

H. Mullings and T. Stallard. Assessment of Dependency of Unsteady Onset Flow and Resultant Tidal Turbine Fatigue Loads on Measurement Position at a Tidal Site. *Energies*, 14(17):5470, Jan. 2021. ISSN 1996-1073. doi: 10.3390/en14175470. URL https://www.mdpi.com/1996-1073/14/17/5470. Number: 17 Publisher: Multidisciplinary Digital Publishing Institute. 1.8.5

P. Mycek, B. Gaurier, G. Germain, G. Pinon, and E. Rivoalen. Experimental study of the turbulence intensity effects on marine current turbines behaviour. Part II: Two interacting turbines. *Renewable Energy*, 68:876–892, Aug. 2014a. ISSN 09601481. doi: 10.1016/j.renene.2013.12.048. URL https://linkinghub.elsevier.com/retrieve/pii/S0960148114000196. 1.8.1, 3.5, 4.4.3, 4.5.2, C.3.2, C.4.2.2

P. Mycek, B. Gaurier, G. Germain, G. Pinon, and E. Rivoalen. Experimental study of the turbulence intensity effects on marine current turbines behaviour. Part I: One single turbine. *Renewable Energy*, 66:729–746, June 2014b. ISSN 09601481. doi: 10.1016/j.renene.2013.12.036. URL https://linkinghub.elsevier.com/retrieve/pii/S096014811400007X. (document), 1.8.1, 1.15, 1.8.5, 1.9, 2, 2.4.4.2, 2.5, 2.5.2, 2.12, 2.5.2.1, 2.13, 2.14, 2.6, 3.6.2, 3.11, 4.4.1, 4.7b, 4.11b, 5.3.1, C.2.4, C.3.3.2

L. Myers, K. Shah, and P. Galloway. Design, commissioning and performance of a device to vary the turbulence in a recirculating flume. In *10th European Wave and Tidal Energy Conference*, page 8, Aalborg, Denmark, Sept. 2013. URL https://eprints.soton.ac.uk/356974/. 4.5.2

L. E. Myers and A. S. Bahaj. An experimental investigation simulating flow effects in first generation marine current energy converter arrays. *Renewable Energy*, 37(1):28–36, Jan. 2012. ISSN 0960-1481. doi: 10.1016/j.renene.2011.03.043. URL https://www.sciencedirect.com/science/article/pii/S0960148111001716. 1.8.1

L. E. Myers, B. Keogh, and A. Bahaj. Experimental investigation of inter-array wake properties in early tidal turbine arrays. In *OCEANS'11 MTS/IEEE KONA*, pages 1–8, Sept. 2011. doi: 10.23919/OCEANS.2011.6107150. ISSN: 0197-7385. 1.8.1

V. S. Neary. Marine energy classification systems: Tools for resource assessment and design. Technical Report SAND2019-13817PE, Sandia National Lab. (SNL-NM), Albuquerque, NM (United States), Nov. 2019. URL https://www.osti.gov/biblio/1646261. 1.5.2

I. Neunaber, M. Hölling, R. J. A. M. Stevens, G. Schepers, and J. Peinke. Distinct Turbulent Regions in the Wake of a Wind Turbine and Their Inflow-Dependent Locations: The Creation of a Wake Map. *Energies*, 13(20):5392, Jan. 2020. doi: 10.3390/en13205392. URL https://www.mdpi.com/1996-1073/13/20/5392. Number: 20 Publisher: Multidisciplinary Digital Publishing Institute. 5.3.1

V. T. Nguyen. *Modélisation de l'interaction entre hydroliennes et le courant dans un courant de marée comme celui du Raz Blanchard*. These de doctorat, Université de Caen, Cherbourg, Jan. 2015. URL https://www.theses.fr/2015CAEN2036. 1.9

V. T. Nguyen, S. S. Guillou, J. Thiébot, and A. Santa Cruz. Modelling turbulence with an Actuator Disk representing a tidal turbine. *Renewable Energy*, 97:625–635, Nov. 2016. ISSN 09601481. doi: 10.1016/j.renene.2016.06.014. URL https://linkinghub.elsevier.com/retrieve/pii/S0960148116305353. (document), 2.3.3, 2.4.4, 2.4.4.1, 2.5.1.2, 2.5.1.3, 2.10, 2.11, C.2.3

V. T. Nguyen, A. Santa Cruz, S. S. Guillou, M. N. Shiekh Elsouk, and J. Thiébot. Effects of the Current Direction on the Energy Production of a Tidal Farm: The Case of Raz Blanchard (France). *Energies*, 12(13):2478, June 2019. ISSN 1996-1073. doi: 10.3390/en12132478. URL https://www.mdpi.com/1996-1073/12/13/2478. 1.8.2, 3.4.1, 4.5.2, 5.3.2, 6.2, C.5.3.2

A. Niayifar and F. Porté-Agel. Analytical Modeling of Wind Farms: A New Approach for Power Prediction. *Energies*, 9(9):741, Sept. 2016. ISSN 1996-1073. doi: 10.3390/en9090741. URL http://www.mdpi.com/1996-1073/9/9/741. 1.8.4, 5.1.1, 5.1.2

D. R. Noble, S. Draycott, A. Nambiar, B. G. Sellar, J. Steynor, and A. Kiprakis. Experimental Assessment of Flow, Performance, and Loads for Tidal Turbines in a Closely-Spaced Array. *Energies*, 13(8):1977, Jan. 2020. ISSN 1996-1073. doi: 10.3390/en13081977. URL https://www.mdpi.com/1996-1073/13/8/1977. Number: 8 Publisher: Multidisciplinary Digital Publishing Institute. (document), 1.16

A. Olczak, T. Stallard, T. Feng, and P. K. Stansby. Comparison of a RANS blade element model for tidal turbine arrays with laboratory scale measurements of wake velocity and rotor thrust. *Journal of Fluids and Structures*, 64:87–106, July 2016. ISSN 0889-9746. doi: 10.1016/j.jfluidstructs.2016.04.001. URL https://www.sciencedirect.com/science/article/pii/S088997461530058X. (document), 2.2, 4.4.2

S. S. Olson, J. C. P. Su, H. Silva, C. C. Chartrand, and J. D. Roberts. Turbulence-parameter estimation for current-energy converters using surrogate model optimization. *Renewable Energy*, 168:559–567, 2021. ISSN 0960-1481. doi: 10.1016/j.renene.2020.12.036. URL https://www.sciencedirect.com/science/article/pii/S0960148120319625. 2.4.4.2, 2.4.4.2, 2.4.4.2

C. Orgiazzi, S. S. Guillou, O. A. L. Brutto, A. S. Cruz, C. Mayousse, M. N. S. Elsouk, and A. Jean-Marie. Analytical Wake Model of a Seabed-Mounted Tidal Turbine. In *13th European Wave and Tidal Energy Conference*, page 7, Naples, Sept. 2019. 6.2

P. Ouro and T. Stoesser. Impact of Environmental Turbulence on the Performance and Loadings of a Tidal Stream Turbine. *Flow, Turbulence and Combustion*, 102(3):613–639, Mar. 2019. ISSN 1573-1987. doi: 10.1007/s10494-018-9975-6. URL https://doi.org/10.1007/s10494-018-9975-6. (document), 1.9

M. Palm, R. Huijsmans, M. Pourquie, and A. Sijtstra. Simple Wake Models for Tidal Turbines in Farm Arrangement. In *29th International Conference on Ocean, Offshore and Arctic Engineering: Volume 3*, pages 577–587, Shanghai, China, Jan. 2010. ASMEDC. ISBN 978-0-7918-4911-8. doi: 10.1115/OMAE2010-20966. URL https://asmedigitalcollection.asme.org/OMAE/proceedings/OMAE2010/49118/577/345920. (document), 1.8.3, 1.19, 1.8.4, 4.2.9, 5.1

L. Perez, R. Cossu, A. Grinham, and I. Penesis. Seasonality of turbulence characteristics and wave-current interaction in two prospective tidal energy sites. *Renewable Energy*, 178:1322–1336, Nov. 2021. ISSN 0960-1481. doi: 10.1016/j.renene.2021.06.116. URL https://www.sciencedirect.com/science/article/pii/S0960148121009824. 1.2

G. Pinon, M. F. Hurst, and E. Lukeba. Semi-analytical estimate of energy production from a tidal turbine farm with the account of ambient turbulence.

International Journal of Marine Energy, 19:70–82, Sept. 2017. ISSN 2214-1669. doi: 10.1016/j.ijome.2017.05.003. URL https://www.sciencedirect.com/science/article/pii/S2214166917300516. 1.8.4, 1.8.5

S. Pookpunt and W. Ongsakul. Optimal placement of wind turbines within wind farm using binary particle swarm optimization with time-varying acceleration coefficients. *Renewable Energy*, 55:266–276, July 2013. ISSN 0960-1481. doi: 10.1016/j.renene.2012.12.005. URL https://www.sciencedirect.com/science/article/pii/S0960148112007604. 1.8.4, 5.1.2

S. B. Pope. *Turbulent Flows*. Cambridge University Press, Aug. 2000. ISBN 978-0-521-59886-6. 3.5.2

P. Pyakurel, W. Tian, J. H. VanZwieten, and M. Dhanak. Characterization of the mean flow field in the far wake region behind ocean current turbines. *Journal of Ocean Engineering and Marine Energy*, 3(2):113–123, May 2017. ISSN 2198-6452. doi: 10.1007/s40722-017-0075-9. URL https://doi.org/10.1007/s40722-017-0075-9. 1.8.3, 4.2.9

G.-W. Qian and T. Ishihara. Wind farm power maximization through wake steering with a new multiple wake model for prediction of turbulence intensity. *Energy*, 220:119680, Apr. 2021. ISSN 0360-5442. doi: 10.1016/j.energy.2020.119680. URL https://www.sciencedirect.com/science/article/pii/S0360544220327870. 1.8.3, 1.8.4, 5.1.1, 5.1.2, C.1.4

D. C. Quarton and J. F. Ainslie. Turbulence in Wind Turbine Wakes. *Wind Engineering*, 14(1):10, 1990. URL https://www.jstor.org/stable/43749409. (document), 1.8.5, 1.8.5, 3, 3.2, 3.3, 3.3.1, 3.3.2, C.1.4.1, C.1.4.1, C.3.1

A. Rahman, V. Venugopal, and J. Thiebot. On the Accuracy of Three-Dimensional Actuator Disc Approach in Modelling a Large-Scale Tidal Turbine in a Simple Channel. *Energies*, 11(8):2151, Aug. 2018. ISSN 1996-1073. doi: 10.3390/en11082151. URL http://www.mdpi.com/1996-1073/11/8/2151. 1.8.2, 2.3.3, 2.4.4, 3.4.1, 3.4.1.2

G. Rajgor. Tidal developments power forward. *Renewable Energy Focus*, 17(4):147–149, July 2016. ISSN 1755-0084. doi: 10.1016/j.ref.2016.06.006. URL https://www.sciencedirect.com/science/article/pii/S1755008416300679. 3.4.1.1

REN21. Renewables 2023 Global Status Report collection. Renewables in Energy Supply, REN21, Paris, 2022. URL https://www.ren21.net/gsr-2022. (document), 1.1, 1.1

P.-E. Rethore, N. N. Sørensen, A. Bechmann, and F. Zhale. Study of the atmospheric wake turbulence of a CFD actuator disc model. In *Proceedings of*

2009 European Wind Energy Conference, page 10, Marseille, France., Mar. 2009. WindEurope. ISBN 978-1-61567-746-7. 2.4.4, 2.4.4.2, 2.4.4.2, 2.6, C.2.3

B. Sanderse, S. Pijl, and B. Koren. Review of computational fluid dynamics for wind turbine wake aerodynamics: Review of CFD for wind turbine wake aerodynamics. *Wind Energy*, 14(7):799–819, Oct. 2011. ISSN 10954244. doi: 10.1002/we.458. URL http://doi.wiley.com/10.1002/we.458. 2.2.4

H. Schlichting and K. Gersten. *Boundary-Layer Theory*. Springer Science & Business Media, 9th edition, 1951. ISBN 978-3-540-66270-9. URL https://link.springer.com/content/pdf/10.1007/978-3-662-52919-5.pdf. 3.5.3, 3.7, 4.2.2

M. Sedrati, R. Le Gall, and J. Bertier. Etude de définition du potentiel énergétique d'origine hydrolienne sur deux sites du Golfe du Morbihan. Technical report, Centre de Recherche Yves Coppens, 2015. 1.2

B. Sellar, G. Wakelam, D. Sutherland, D. Ingram, and V. Venugopal. Characterisation of Tidal Flows at the European Marine Energy Centre in the Absence of Ocean Waves. *Energies*, 11(1):176, Jan. 2018. ISSN 1996-1073. doi: 10.3390/en11010176. URL https://www.mdpi.com/1996-1073/11/1/176. 1.2

A. Sentchev and M. Thiébaut. Monitoring tidal currents off the Yarmouth harbour with a towed ADCP system. Technical report, Laboratoire d'Océanologie et de Géosciences(LOG), Wimereux, France, 2015. 1.2

A. Sentchev, M. Thiébaut, and F. G. Schmitt. Impact of turbulence on power production by a free-stream tidal turbine in real sea conditions. *Renewable Energy*, 147:1932–1940, Mar. 2020. ISSN 0960-1481. doi: 10.1016/j.renene.2019.09.136. URL https://www.sciencedirect.com/science/article/pii/S0960148119314806. 1.2

S. Shamshirband, D. Petković, N. B. Anuar, and A. Gani. Adaptive neuro-fuzzy generalization of wind turbine wake added turbulence models. *Renewable and Sustainable Energy Reviews*, 36:270–276, Aug. 2014. ISSN 1364-0321. doi: 10.1016/j.rser.2014.04.064. URL https://www.sciencedirect.com/science/article/pii/S1364032114003025. 3.2, 3.3

K. B. Shariff and S. S. Guillou. Developing an empirical model for added turbulence in a wake of tidal turbine. In *25ème Congrès Français de Mécanique*, page 10, Nantes, France, 2022a. 4.2.9, 4.4.1, C.4

K. B. Shariff and S. S. Guillou. An empirical model accounting for added turbulence in the wake of a full-scale turbine in realistic tidal stream conditions. *Applied Ocean Research*, 128:103329, Nov. 2022b. ISSN 0141-1187. doi: 10.1016/j.apor.2022.103329. URL https://www.sciencedirect.com/science/article/pii/S0141118722002619. 3, 4.3.1, 4.4.2

K. B. Shariff and S. S. Guillou. An empirical wake model accouting for the velocity deficit and turbulence intensity in a simple tidal park. In *18è Journées de l'Hydrodynamique*, page 10, Poitiers, Nov. 2022c. Université de Poitiers. URL https://normandie-univ.hal.science/hal-03976984/. 4.4.2

K. B. Shariff and S. S. Guillou. A comparative study of power production using a generic empirical model in a tidal farm. In *Proceedings of the 15th European Wave and Tidal Energy Conference (EWTEC)*, page 8, Bilbao, Sept. 2023a. doi: https://doi.org/10.36688/ewtec-2023-199. 5

K. B. Shariff and S. S. Guillou. A generalized empirical model for velocity deficit and turbulent intensity in tidal turbine wake accounting for the effect of rotor diameter to depth ratio, 2023b. 4

C. Shetty and A. Priyam. A review on tidal energy technologies. *Materials Today: Proceedings*, 56:2774–2779, Jan. 2022. ISSN 2214-7853. doi: 10.1016/j.matpr.2021.10.020. URL https://www.sciencedirect.com/science/article/pii/S2214785321064993. (document), 1.6

M. Shives and C. Crawford. Developing an empirical model for ducted tidal turbine performance using numerical simulation results. *Proceedings of the Institution of Mechanical Engineers, Part A: Journal of Power and Energy*, 226(1):112–125, Feb. 2012. ISSN 0957-6509, 2041-2967. doi: 10.1177/0957650911417958. URL http://journals.sagepub.com/doi/10.1177/0957650911417958. 2.4.4.2

T. Stallard, R. Collings, T. Feng, and J. Whelan. Interactions between tidal turbine wakes: experimental study of a group of three-bladed rotors. *Philosophical Transactions of the Royal Society A: Mathematical, Physical and Engineering Sciences*, 371(1985):20120159, Feb. 2013. doi: 10.1098/rsta.2012.0159. URL https://royalsocietypublishing.org/doi/full/10.1098/rsta.2012.0159. Publisher: Royal Society. 1.8.1, 3.5, 4.4.1, 4.7a, 4.4.3, 4.11a, C.4.2.2

T. Stallard, T. Feng, and P. Stansby. Experimental study of the mean wake of a tidal stream rotor in a shallow turbulent flow. *Journal of Fluids and Structures*, 54:235–246, Apr. 2015. ISSN 08899746. doi: 10.1016/j.jfluidstructs.2014.10.017. URL https://linkinghub.elsevier.com/retrieve/pii/S0889974614002485. 1.8.1, 1.8.1, 1.8.3, 3.5.2, 3.7, 4.3.3

P. Stansby and T. Stallard. Fast optimisation of tidal stream turbine positions for power generation in small arrays with low blockage based on superposition of self-similar far-wake velocity deficit profiles. *Renewable Energy*, 92:366–375, July 2016. ISSN 0960-1481. doi: 10.1016/j.renene.2016.02.019. URL https://www.sciencedirect.com/science/article/pii/S0960148116301203. 1.8.4

H. Sun and H. Yang. Study on an innovative three-dimensional wind turbine wake model. *Applied Energy*, 226:483–493, Sept. 2018. ISSN 0306-2619. doi: 10.1016/j.apenergy.2018.06.027. URL https://www.sciencedirect.com/science/article/pii/S0306261918308924. (document), 1.18

I. F. Syed Ahmed Kabir, F. Safiyullah, E. Ng, and V. W. Tam. New analytical wake models based on artificial intelligence and rivalling the benchmark full-rotor CFD predictions under both uniform and ABL inflows. *Energy*, 193:116761, Feb. 2020. ISSN 03605442. doi: 10.1016/j.energy.2019.116761. URL https://linkinghub.elsevier.com/retrieve/pii/S0360544219324569. 1.8.3, 3.3

B. Taormina. *Potential impacts of submarine power cables from marine renewable energy projects on benthic communities*. PhD thesis, Université de Bretagne occidentale, Brest, Dec. 2019. URL https://theses.hal.science/tel-03078936. (document), 1.2

G. Tasiopoulos and S. Feketovà. Tackling turbine failures enhances tidal energy viability. Technical report, European Commossion, 2021. URL https://cordis.europa.eu/article/id/421948-tackling-turbine-failures-enhances-tidal-energy-viability. 1.5.2

G. I. Taylor. *The Scientific Papers of Sir Geoffrey Ingram Taylor: Mechanics of solids*, volume 1. CUP Archive, 1958. 2.3.3, C.2.2

M. Thiébaut and A. Sentchev. Tidal stream resource assessment in the Dover Strait (eastern English Channel). *International Journal of Marine Energy*, 16:262–278, Dec. 2016. ISSN 2214-1669. doi: 10.1016/j.ijome.2016.08.004. URL https://www.sciencedirect.com/science/article/pii/S2214166916300637. 1.2

M. Thiébaut, J.-F. Filipot, C. Maisondieu, G. Damblans, C. Jochum, L. F. Kilcher, and S. Guillou. Characterization of the vertical evolution of the three-dimensional turbulence for fatigue design of tidal turbines. *Philosophical Transactions of the Royal Society A: Mathematical, Physical and Engineering Sciences*, 378(2178):20190495, Aug. 2020. ISSN 1364-503X, 1471-2962. doi: 10.1098/rsta.2019.0495. URL https://royalsocietypublishing.org/doi/10.1098/rsta.2019.0495. (document), 1.5.2, 1.10, 1.2, 3.4.1.2, 5.3.2

J. Thiébot, P. Bailly du Bois, and S. Guillou. Numerical modeling of the effect of tidal stream turbines on the hydrodynamics and the sediment transport – Application to the Alderney Race (Raz Blanchard), France. *Renewable Energy*, 75:356–365, Mar. 2015. ISSN 0960-1481. doi: 10.1016/j.renene.2014.10.021. URL https://www.sciencedirect.com/science/article/pii/S096014811400648X. 1.6

J. Thiébot, S. Guillou, and V. T. Nguyen. Modelling the effect of large arrays of tidal turbines with depth-averaged Actuator Disks. *Ocean Engineering*, 126:265–275, Nov. 2016. ISSN 00298018. doi: 10.1016/j.oceaneng.2016.09.021. URL https://linkinghub.elsevier.com/retrieve/pii/S0029801816303985. 1.8.2, 2.3.3, 2.4.4

J. Thiébot, N. Guillou, S. Guillou, A. Good, and M. Lewis. Wake field study of tidal turbines under realistic flow conditions. *Renewable Energy*, 151: 1196–1208, 2020. ISSN 0960-1481. doi: https://doi.org/10.1016/j.renene.2019.11.129. URL https://www.sciencedirect.com/science/article/pii/S0960148119318233. 1.6, 1.8.2, 2.3.3, 2.4.4, 3.4.1

J. Thiébot, N. Djama Dirieh, S. Guillou, and N. Guillou. The Efficiency of a Fence of Tidal Turbines in the Alderney Race: Comparison between Analytical and Numerical Models. *Energies*, 14(4):892, Jan. 2021. ISSN 1996-1073. doi: 10.3390/en14040892. URL https://www.mdpi.com/1996-1073/14/4/892. Number: 4 Publisher: Multidisciplinary Digital Publishing Institute. 1.8.2

J. Thomson, B. Polagye, V. Durgesh, and M. C. Richmond. Measurements of Turbulence at Two Tidal Energy Sites in Puget Sound, WA. *IEEE Journal of Oceanic Engineering*, 37(3):363–374, July 2012. ISSN 0364-9059, 1558-1691. doi: 10.1109/JOE.2012.2191656. URL http://ieeexplore.ieee.org/document/6200383/. 1.2

Z. Ti, X. W. Deng, and M. Zhang. Artificial Neural Networks based wake model for power prediction of wind farm. *Renewable Energy*, 172:618–631, July 2021. ISSN 0960-1481. doi: 10.1016/j.renene.2021.03.030. URL https://www.sciencedirect.com/science/article/pii/S0960148121003840. 1.8.3

L. Tian, W. Zhu, W. Shen, N. Zhao, and Z. Shen. Development and validation of a new two-dimensional wake model for wind turbine wakes. *Journal of Wind Engineering and Industrial Aerodynamics*, 137:90–99, Feb. 2015. ISSN 01676105. doi: 10.1016/j.jweia.2014.12.001. URL https://linkinghub.elsevier.com/retrieve/pii/S0167610514002505. (document), 3, 3.3.5, C.3.1

M. Togneri and I. Masters. Micrositing variability and mean flow scaling for marine turbulence in Ramsey Sound. *Journal of Ocean Engineering and Marine Energy*, 2(1):35–46, Feb. 2016. ISSN 2198-6452. doi: 10.1007/s40722-015-0036-0. URL https://doi.org/10.1007/s40722-015-0036-0. 1.2

M. Togneri, M. Lewis, S. Neill, and I. Masters. Comparison of ADCP observations and 3D model simulations of turbulence at a tidal energy site. *Renewable Energy*, 114:273–282, Dec. 2017. ISSN 0960-1481. doi: 10.1016/j.renene.2017.03.061. URL https://www.sciencedirect.com/science/article/pii/S0960148117302537. 1.2

F. Torabi. *Fundamentals of Wind Farm Aerodynamic Layout Design*. Academic Press, London, 1st edition, Jan. 2022. ISBN 978-0-12-823437-2. (document), 2.1, 4.1, 4.2

S. R. Turnock, A. B. Phillips, J. Banks, and R. Nicholls-Lee. Modelling tidal current turbine wakes using a coupled RANS-BEMT approach as a tool for analysing power capture of arrays of turbines. *Ocean Engineering*, 38(11):1300–1307, Aug. 2011. ISSN 0029-8018. doi: 10.1016/j.oceaneng.2011.05.018. URL https://www.sciencedirect.com/science/article/pii/S0029801811001089. 1.8.2

H. Ullah, M. Hussain, N. Abbas, H. Ahmad, M. Amer, and M. Noman. Numerical investigation of modal and fatigue performance of a horizontal axis tidal current turbine using fluid–structure interaction. *Journal of Ocean Engineering and Science*, 4(4):328–337, Dec. 2019. ISSN 2468-0133. doi: 10.1016/j.joes.2019.05.008. URL https://www.sciencedirect.com/science/article/pii/S2468013319301007. 1.6

R. Vennell. Exceeding the Betz limit with tidal turbines. *Renewable Energy*, 55:277–285, July 2013. ISSN 0960-1481. doi: 10.1016/j.renene.2012.12.016. URL https://www.sciencedirect.com/science/article/pii/S096014811200780X. 2.3.1, C.2.1

R. Vennell and T. A. A. Adcock. Energy storage inherent in large tidal turbine farms. *Proceedings of the Royal Society A: Mathematical, Physical and Engineering Sciences*, 470(2166):20130580, June 2014. doi: 10.1098/rspa.2013.0580. URL https://royalsocietypublishing.org/doi/full/10.1098/rspa.2013.0580. Publisher: Royal Society. 1.6

L. Vermeer, J. Sørensen, and A. Crespo. Wind turbine wake aerodynamics. *Progress in Aerospace Sciences*, 39(6-7):467–510, Aug. 2003. ISSN 03760421. doi: 10.1016/S0376-0421(03)00078-2. URL https://linkinghub.elsevier.com/retrieve/pii/S0376042103000782. (document), 1.7, 1.3, 3.2, C.1.3

P. E. J. Vermeulen. An experimental analysis of wind turbine wakes. pages 431–450, Jan. 1980. URL https://ui.adsabs.harvard.edu/abs/1980wes..symp..431V. Conference Name: 3rd International Symposium on Wind Energy Systems ADS Bibcode: 1980wes..symp..431V. 1, 1.8.5, C.1.4.1

A. Vinod and A. Banerjee. Performance and near-wake characterization of a tidal current turbine in elevated levels of free stream turbulence. *Applied Energy*, 254:113639, Nov. 2019. ISSN 0306-2619. doi: 10.1016/j.apenergy.2019.113639. URL https://www.sciencedirect.com/science/article/pii/S0306261919313261. 1.8.1, 1.8.1, 3.5, C.3.2

S. R. J. Walker and P. R. Thies. Failure and reliability growth in tidal stream turbine deployments. In *Proceedings of 14th European Wave and Tidal Energy Conference*, volume 1, page 6, Plymouth, United kingdom, Sept. 2021. URL http://hdl.handle.net/10871/127470. 1.5.2, 1.5.2, 1.8.1, C.1.4

T. Wang and Z. Yang. A Tidal Hydrodynamic Model for Cook Inlet, Alaska, to Support Tidal Energy Resource Characterization. *Journal of Marine Science and Engineering*, 8(4):254, Apr. 2020. ISSN 2077-1312. doi: 10.3390/jmse8040254. URL https://www.mdpi.com/2077-1312/8/4/254. 1.2

K. Yang, G. Kwak, K. Cho, and J. Huh. Wind farm layout optimization for wake effect uniformity. *Energy*, 183:983–995, Sept. 2019. ISSN 0360-5442. doi: 10.1016/j.energy.2019.07.019. URL https://www.sciencedirect.com/science/article/pii/S0360544219313465. 5.1.2

H. Yazicioglu, K. M. M. Tunc, M. Ozbek, and T. Kara. Simulation of electricity generation by marine current turbines at Istanbul Bosphorus Strait. *Energy*, 95:41–50, Jan. 2016. ISSN 0360-5442. doi: 10.1016/j.energy.2015.11.038. URL https://www.sciencedirect.com/science/article/pii/S0360544215015881. 1.8.3, 4.2.9

Y. Zhang, E. Fernandez-Rodriguez, J. Zheng, Y. Zheng, J. Zhang, H. Gu, W. Zang, and X. Lin. A Review on Numerical Development of Tidal Stream Turbine Performance and Wake Prediction. *IEEE Access*, 8:79325–79337, 2020a. ISSN 2169-3536. doi: 10.1109/ACCESS.2020.2989344. URL https://ieeexplore.ieee.org/document/9075239/. 3.4.1

Y. Zhang, Z. Zhang, J. Zheng, J. Zhang, Y. Zheng, W. Zang, X. Lin, and E. Fernandez-Rodriguez. Experimental investigation into effects of boundary proximity and blockage on horizontal-axis tidal turbine wake. *Ocean Engineering*, 225:108829, Apr. 2021. ISSN 00298018. doi: 10.1016/j.oceaneng.2021.108829. URL https://linkinghub.elsevier.com/retrieve/pii/S002980182100264X. 1.8.1, 1.8.1, 4.3.3

Z. Zhang, P. Huang, and H. Sun. A Novel Analytical Wake Model with a Cosine-Shaped Velocity Deficit. *Energies*, 13(13):3353, Jan. 2020b. ISSN 1996-1073. doi: 10.3390/en13133353. URL https://www.mdpi.com/1996-1073/13/13/3353. Number: 13 Publisher: Multidisciplinary Digital Publishing Institute. (document), 4, 4.1, 4.2.4

D. Zhao, N. Han, E. Goh, J. Cater, and A. Reinecke. Chapter 7 - Aerodynamics of horizontal axis wind turbines and wind farms. In D. Zhao, N. Han, E. Goh, J. Cater, and A. Reinecke, editors, *Wind Turbines and Aerodynamics Energy Harvesters*, pages 431–461. Academic Press, Jan. 2019. ISBN 978-0-12-817135-6. doi: 10.1016/B978-0-12-817135-6.00007-7. URL https://www.sciencedirect.com/science/article/pii/B9780128171356000077. 2.2.3

Appendix A

Appendix

A.1 Wake correction coefficient ϕ

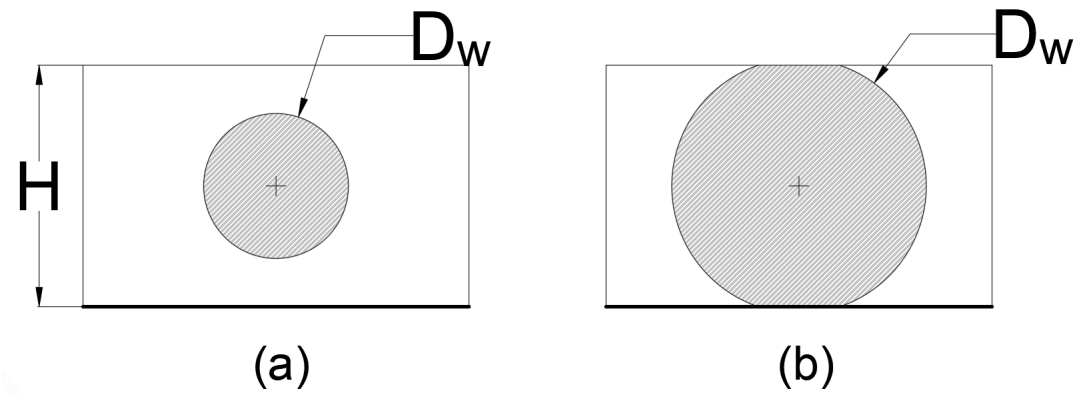

Figure A.1 Schematic of (a) axisymmetric and (b) 2 D Gaussian wake surface in lateral plane

The surface area of a standard Gaussian function in general form is expressed as:

$$\int\int_R \mathrm{e}^{-(x^2+y^2)}\mathrm{d}x\mathrm{d}y = \int_0^{2\pi}\int_0^{\infty} \mathrm{e}^{-r^2} r\mathrm{d}r\mathrm{d}\theta \tag{A.1}$$

The area under axisymmetric wake can be expressed as:

$$A = \int_0^{2\pi}\int_0^{R} \mathrm{e}^{-\left(\frac{R}{\sigma}\right)^2} r \ \mathrm{d}r \ \mathrm{d}\theta \tag{A.2}$$

By changing variable

$$A = 2\pi\sigma^2 \int_0^{R/\sigma} y\mathrm{e}^{-y^2}\mathrm{d}y$$

$$A = 2\pi\sigma^2 \cdot \left(\frac{1}{2} - \frac{\mathrm{e}^{-\frac{R^2}{\sigma^2}}}{2}\right) = 2\pi\sigma^2 C$$

The correction term is expressed as:

$$\frac{A}{\pi R^2} = \frac{2\pi\sigma^2 C}{\pi R^2} = 2C \cdot \left(\frac{\sigma}{R}\right)^2 = \frac{1}{(R/\sigma)^2} \tag{A.3}$$

The area under a 2 D Gaussian wake can be expressed as:

$$B = \int_0^H \int_{-R}^{R} \mathrm{e}^{-\left(\frac{y}{\sigma}\right)^2} \mathrm{d}y\mathrm{d}z \tag{A.4}$$

$$B = H\sqrt{\pi}\,\mathrm{erf}\left(\frac{R}{\sigma}\right)\sigma \simeq H\sigma\sqrt{\pi}$$

The correction term is expressed as:

$$\frac{B}{2HR} = \frac{H\sigma\sqrt{\pi}}{2HR} = \frac{\sqrt{\pi}}{2} \cdot \frac{1}{R/\sigma} \tag{A.5}$$

$$\phi = \begin{cases} \frac{1}{(R/\sigma)^2} & \text{if } 2R < H \qquad \text{axisymmetry} \\ \frac{\sqrt{\pi}/2}{R/\sigma} & \text{otherwise} \qquad \text{2D Gaussian} \end{cases} \tag{A.6}$$

A.2 Parameter sensitivity of generic model

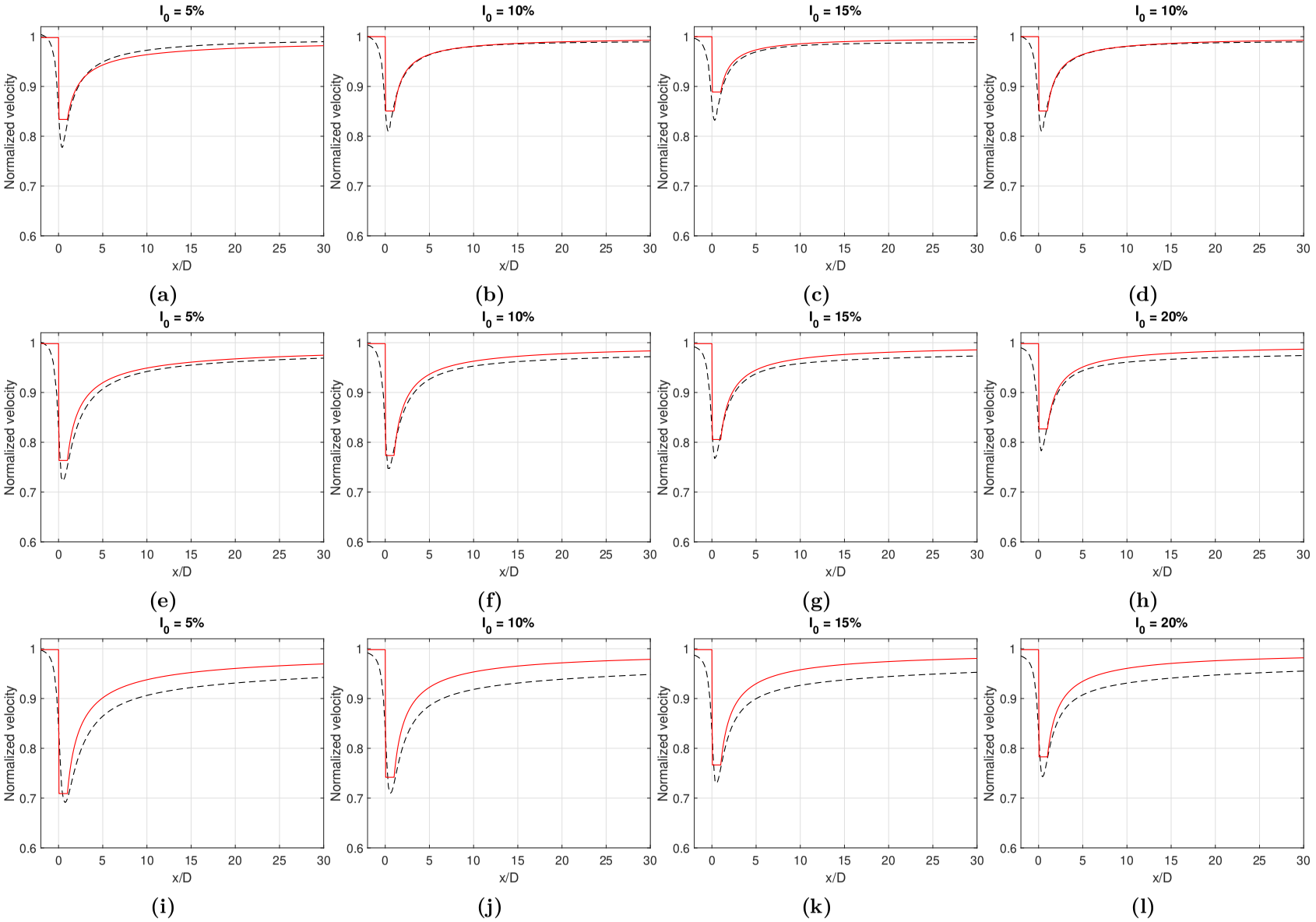

Figure A.2 Comparison of the normalized velocity of numerical data (solid) and proposed model (dash) at DH20 (a-d), DH40 (e-h) and (i-l) at $C_T = 0.64$

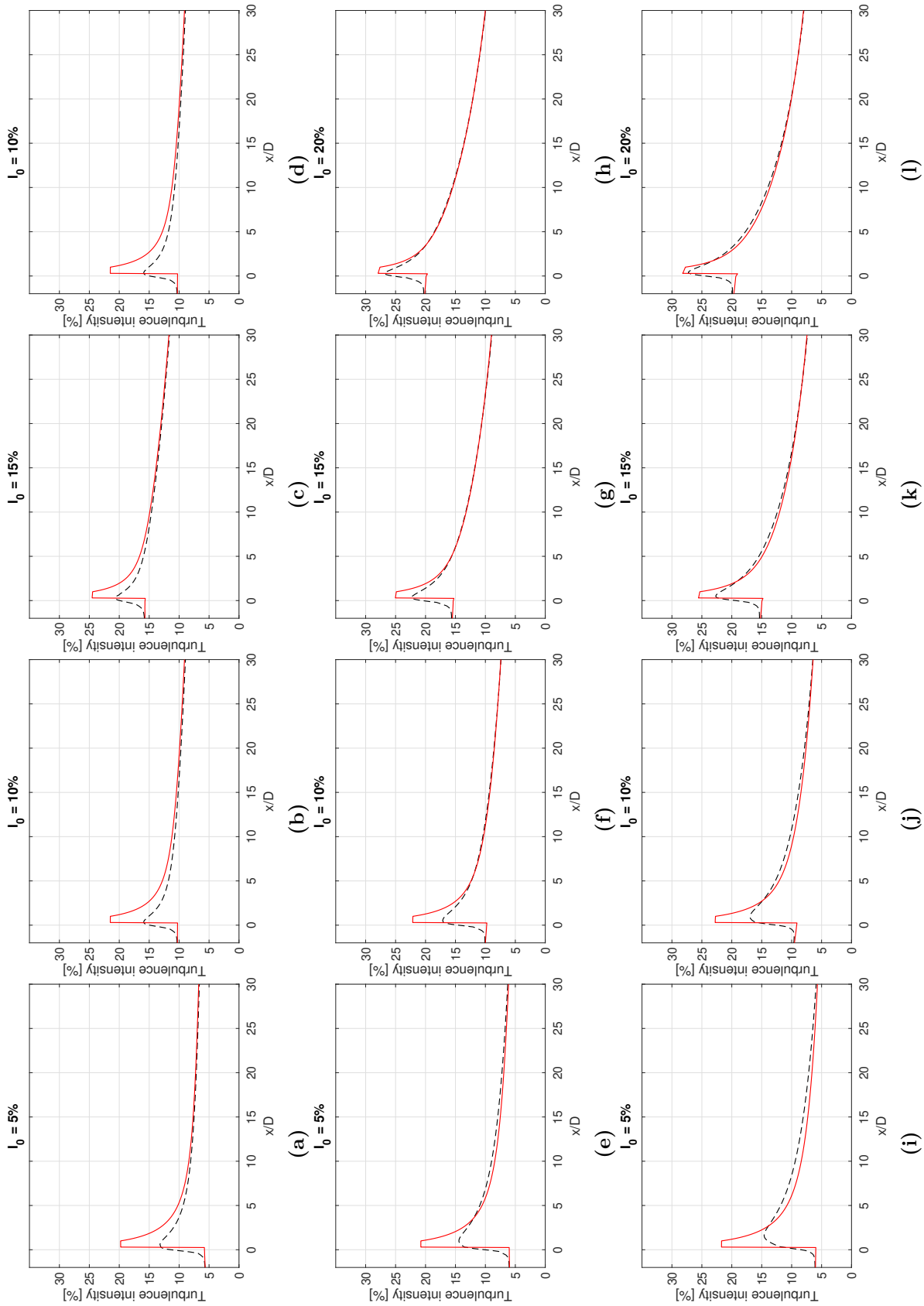

Figure A.3 Comparison of turbulence intensity of numerical data (solid) and proposed model (dash) at DH20 (a-d), DH40 (e-h) and (i-l) at $C_T = 0.64$

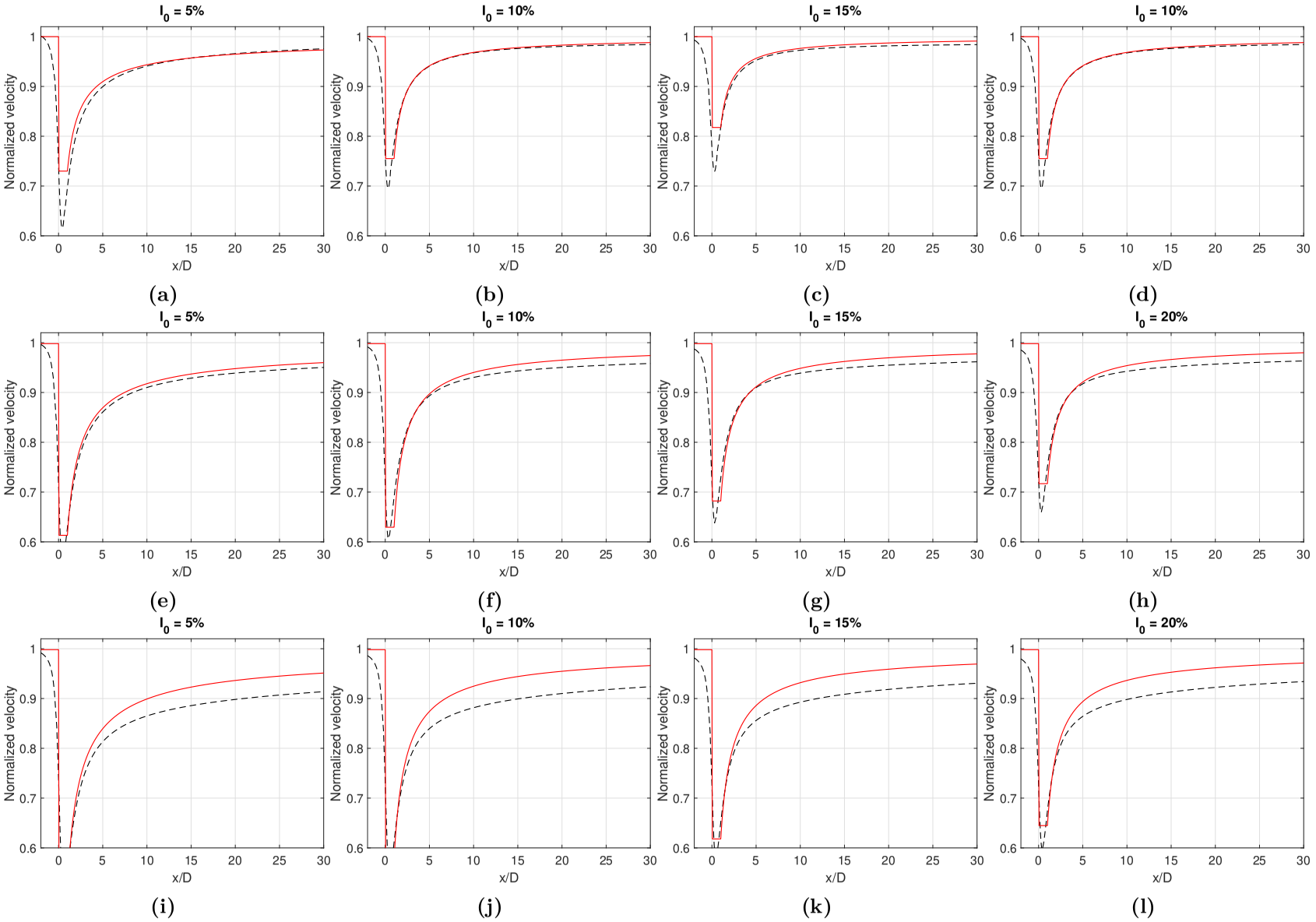

Figure A.4 Comparison of the normalized velocity of numerical data (solid) and proposed model (dash) at DH20 (a-d), DH40 (e-h) and (i-l) at $C_T = 0.89$

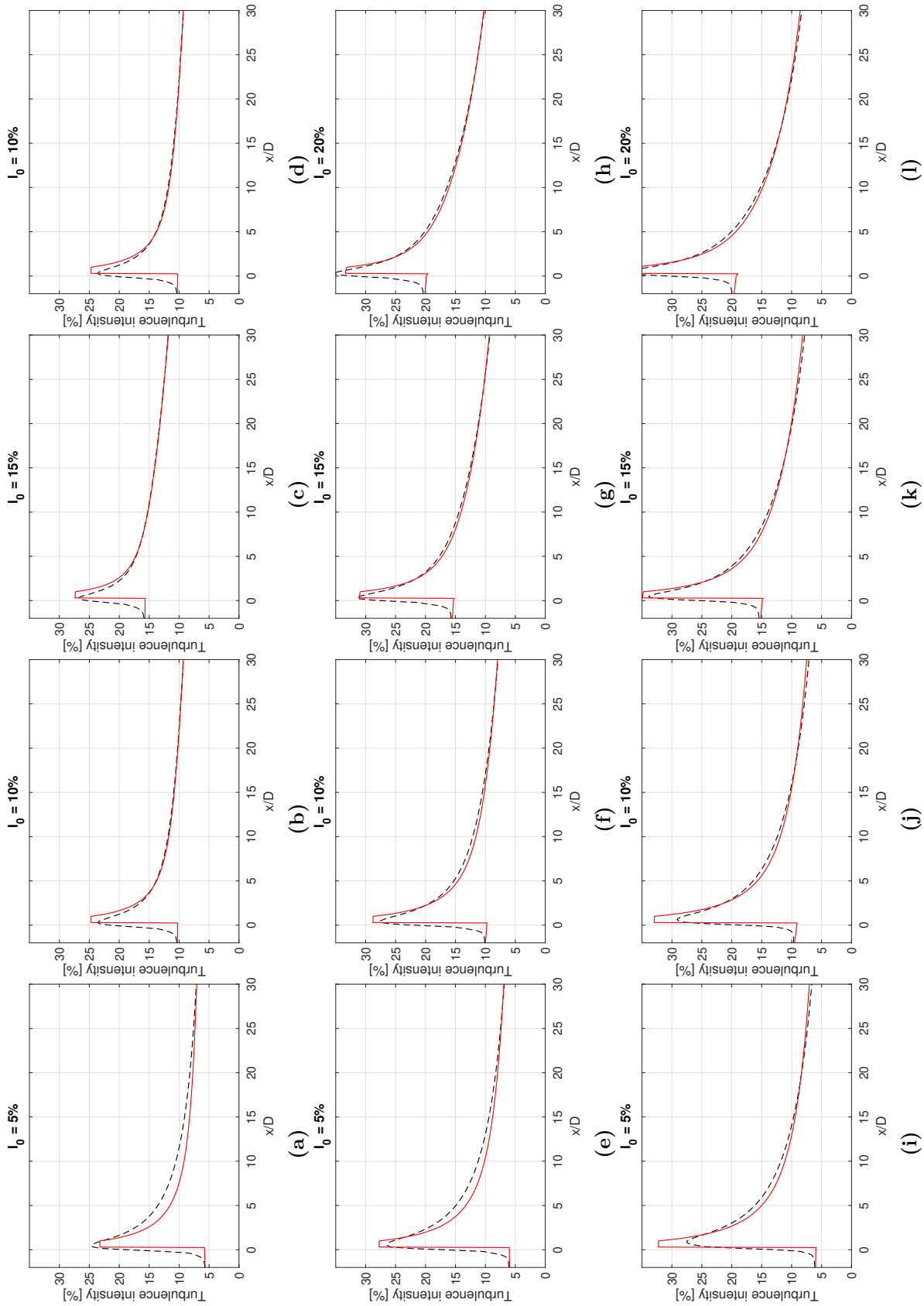

Figure A.5 Comparison of turbulence intensity of numerical data (solid) and proposed model (dash) at DH20 (a-d), DH40 (e-h) and (i-l) at $C_T = 0.89$

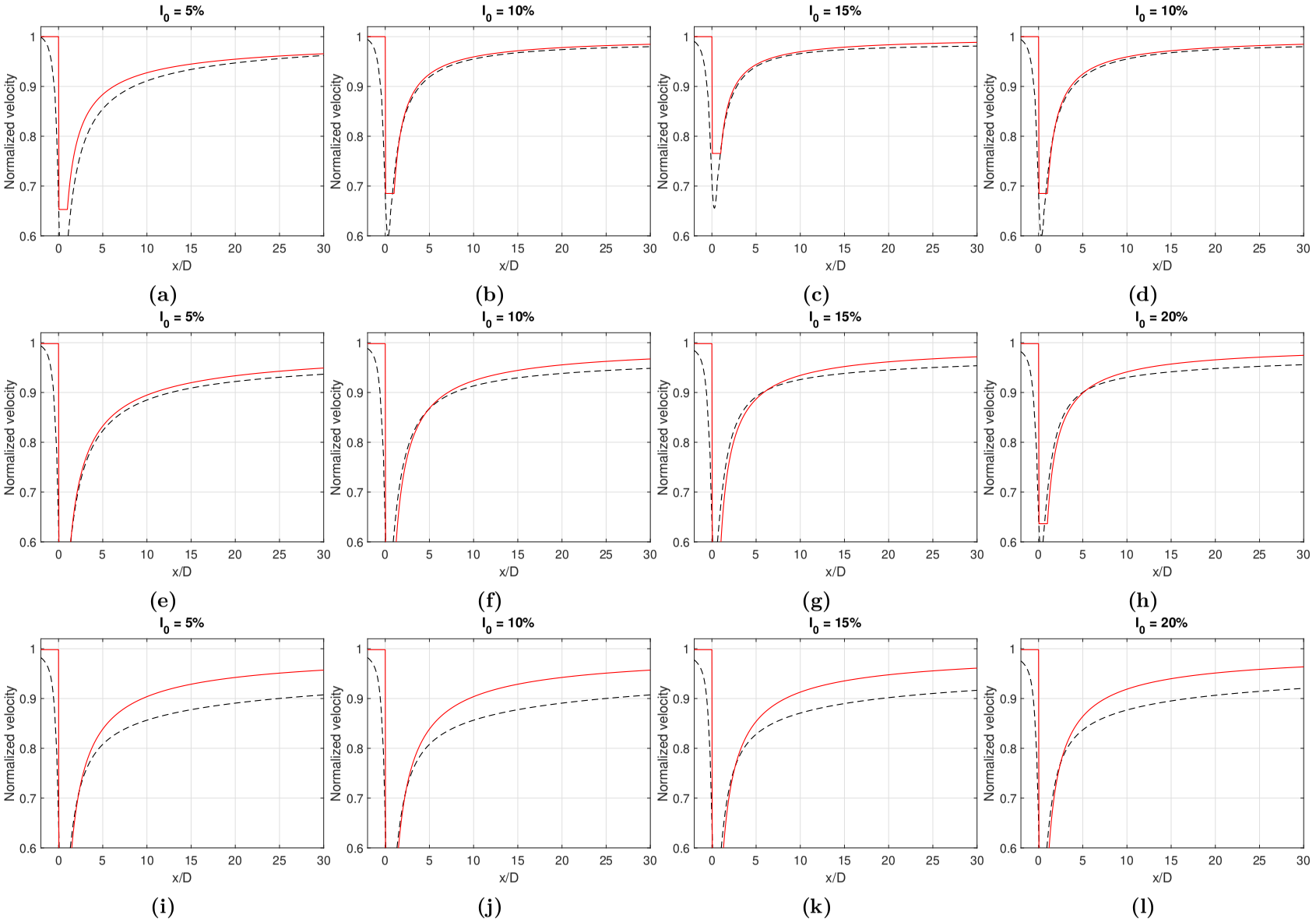

Figure A.6 Comparison of the normalized velocity of numerical data (solid) and proposed model (dash) at DH20 (a-d), DH40 (e-h) and (i-l) at $C_T = 0.98$

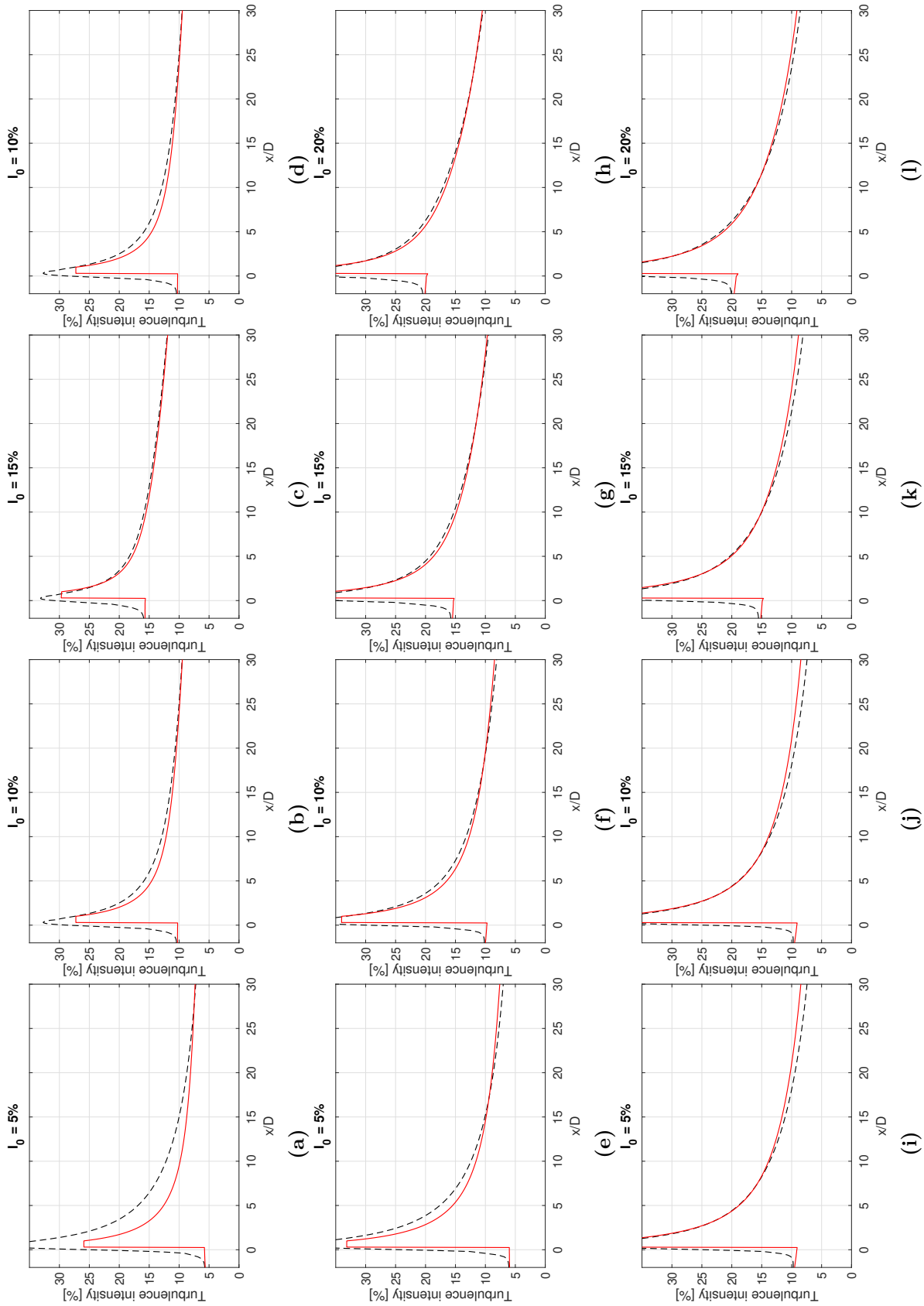

Figure A.7 Comparison of turbulence intensity of numerical data (solid) and proposed model (dash) at DH20 (a-d), DH40 (e-h) and (i-l) at $C_T = 0.98$

Table A.1 Relative error analysis of turbulence intensity

$C_T = 0.64$												
	I_0	DH20				DH40				DH60		
x/D		5%	10%	15%	20%	5%	10%	15%	20%	5%	10%	15%	20%
1		53.38	42.41	26.56	17.51	44.11	32.14	18.40	11.44	55.30	33.98	15.89	8.43
3		17.00	14.28	7.49	4.09	2.63	4.28	1.97	0.45	2.40	0.83	2.12	2.83
5		9.50	8.53	4.20	2.10	3.41	0.44	0.17	0.45	8.93	4.97	3.52	3.31
7		6.10	6.09	2.86	1.32	5.30	0.73	0.34	0.64	10.50	5.91	3.57	3.06
10		3.73	4.29	1.97	0.88	5.89	1.19	0.47	0.64	10.76	5.96	3.06	2.42
15		2.30	2.86	1.33	0.57	5.42	1.18	0.28	0.32	9.39	4.78	1.97	1.42
20		1.80	2.24	1.04	0.43	4.30	0.72	0.05	0.02	7.63	3.26	0.82	0.47
30		1.58	1.74	0.87	0.32	2.23	0.38	0.75	0.53	3.76	0.63	0.92	0.78
$C_T = 0.89$													
	I_0	DH20				DH40				DH60			
x/D		5%	10%	15%	20%	5%	10%	15%	20%	5%	10%	15%	20%
1		1.65	17.63	15.35	11.09	9.18	14.02	11.45	8.04	17.40	17.48	12.41	8.39
3		13.29	1.87	2.27	1.00	9.22	2.50	1.19	1.70	5.49	1.66	1.87	2.81
5		14.94	0.49	0.55	0.07	11.11	4.41	2.47	2.37	7.10	4.28	3.50	3.69
7		14.57	1.06	0.10	0.37	10.87	4.73	2.63	2.36	6.95	4.70	3.54	3.38
10		12.80	1.10	0.26	0.46	9.42	4.33	2.40	2.07	5.65	4.07	2.65	2.37
15		9.21	0.87	0.32	0.50	6.45	3.08	1.52	1.29	2.68	1.68	0.64	0.61
20		6.01	0.53	0.29	0.38	3.68	1.61	0.63	0.54	0.50	0.95	1.24	0.96
30		1.11	0.10	0.17	0.22	0.80	0.94	0.81	0.51	6.03	5.51	4.43	3.14
$C_T = 0.98$													
	I_0	DH20				DH40				DH60			
x/D		5%	10%	15%	20%	5%	10%	15%	20%	5%	10%	15%	20%
1		23.80	0.74	6.50	5.45	9.28	2.02	6.11	5.07	6.63	6.63	8.58	7.04
3		26.94	8.33	1.96	1.65	13.61	5.65	2.28	2.43	0.20	0.20	0.27	1.00
5		25.45	8.20	2.51	1.95	12.17	5.84	3.14	3.11	0.50	0.50	1.13	2.05
7		23.20	7.18	2.38	1.87	10.12	5.15	3.21	3.06	0.10	0.10	1.00	1.74
10		19.33	5.53	2.06	1.64	6.84	3.81	2.69	2.52	1.48	1.48	0.247	0.60
15		12.76	3.42	1.66	1.40	1.93	1.42	1.39	1.42	4.83	4.83	2.83	1.70
20		7.02	2.00	1.27	1.14	2.15	0.75	0.14	0.47	8.25	8.25	5.27	3.68
30		1.60	0.25	0.72	0.69	8.28	4.43	1.90	1.05	13.96	13.96	9.30	6.53

Table A.2 Relative error normalized velocity

	$C_T = 0.64$											
	DH20				DH40				DH60			
I_0 / x/D	5%	10%	15%	20%	5%	10%	15%	20%	5%	10%	15%	20%
1	2.61	0.35	2.27	3.17	3.31	0.04	0.51	0.88	3.23	3.42	2.58	2.16
3	1.65	1.96	2.41	2.66	4.08	3.13	2.64	2.48	7.39	6.66	5.28	4.68
5	1.11	1.84	2.18	2.39	3.15	2.86	2.57	2.54	6.09	6.00	5.16	4.81
7	0.92	1.80	2.12	2.33	2.75	2.78	2.64	2.68	5.59	5.78	5.17	4.92
10	0.82	1.80	2.13	2.35	2.50	2.79	2.78	2.85	5.29	5.64	5.18	4.99
15	0.80	1.87	2.22	2.44	2.39	2.88	2.94	3.01	5.09	5.48	5.11	4.94
20	0.83	1.95	2.30	2.51	2.38	2.94	3.01	3.07	4.95	5.32	5.00	4.83
30	0.92	2.10	2.43	2.61	2.37	2.96	3.04	3.08	4.68	5.00	4.73	4.58
	$C_T = 0.89$											
	DH20				DH40				DH60			
I_0 / x/D	5%	10%	15%	20%	5%	10%	15%	20%	5%	10%	15%	20%
1	6.59	2.17	1.65	3.76	0.66	7.11	4.65	4.64	4.11	3.85	3.44	2.68
3	4.03	1.79	2.45	2.96	3.15	1.55	1.30	1.55	4.74	5.06	4.23	4.13
5	2.88	1.83	2.19	2.54	2.77	2.18	1.94	2.15	5.02	5.92	5.32	5.25
7	2.40	1.84	2.12	2.43	2.64	2.51	2.37	2.57	5.38	6.40	5.86	5.77
10	2.04	1.85	2.14	2.42	2.60	2.84	2.79	2.98	5.75	6.73	6.22	6.10
15	1.76	1.93	2.24	2.51	2.65	3.16	3.17	3.31	6.02	6.83	6.32	6.17
20	1.63	2.02	2.34	2.59	2.72	3.33	3.33	3.44	6.07	6.74	6.24	6.08
30	1.50	2.16	2.49	2.69	2.79	3.43	3.44	3.50	5.91	6.43	5.97	5.81
	$C_T = 0.98$											
	DH20				DH40				DH60			
I_0 / x/D	5%	10%	15%	20%	5%	10%	15%	20%	5%	10%	15%	20%
1	13.81	2.88	0.85	3.96	3.76	13.76	10.50	13.33	13.32	11.90	8.58	9.71
3	7.29	2.45	2.43	3.13	3.03	0.48	0.19	3.29	3.29	2.48	0.27	2.79
5	5.21	2.39	2.18	2.62	2.91	1.81	1.20	5.61	5.65	4.91	1.13	5.04
7	4.31	2.29	2.12	2.48	2.87	2.40	1.98	6.66	6.66	5.98	1.00	6.02
10	3.58	2.20	2.15	2.47	2.88	2.93	2.67	7.37	7.39	6.67	0.247	6.61
15	2.94	2.16	2.27	2.56	2.96	3.39	3.24	7.67	7.67	6.95	2.83	6.82
20	2.56	2.18	2.38	2.65	3.03	3.62	3.50	7.64	7.64	6.93	5.27	6.77
30	2.12	2.26	2.53	2.76	3.10	3.77	3.67	7.32	7.32	6.69	9.30	6.53

A.3 OpenFOAM files

TopoSet

```
FoamFile
{
    version     2.0;
    format      ascii;
    class       dictionary;
    object      topoSetDict;
}

actions
(
    // actuationDisk1        // Rotor ID
    {
        name    actuationDisk1CellSet;
        type    cellSet;
        action  new;
        source  cylinderToCell;
        sourceInfo
        {
            radius 10.0;
                p1 (200 200 25);
                p2 (204 200 25);
        }
    }
    {
        name    actuationDisk1;
        type    cellZoneSet;
        action  new;
        source  setToCellZone;
        sourceInfo
        {
            set actuationDisk1CellSet;
        }
    }
    // source2
    {
        name    source2CellSet;
        type    cellSet;
        action  new;
        source      boxToCell;
        box (0 0 0) (200 400 50);
    }
    {
        name    source2;
        type    cellZoneSet;
        action  new;
        source  setToCellZone;
        sourceInfo
        {
            set source2CellSet;
        }
    }

);
```

fvOptions

```
FoamFile
{
    version     2.0;
    format      ascii;
    class       dictionary;
    location    "constant";
    object      fvOptions;
}

disk1
{
    type            myActuationDiskSource;
    variant         Resistance;
    selectionMode   cellSet;
    cellSet         actuationDisk1;
    diskArea        314.16;
    diskDir         (1 0 0);
    writeToFile     true;
    sink            true;
    K               2.0;

    monitorMethod   points;
    monitorCoeffs
    {
        points
        (
            (160 200 25)
        );
    }
}
```

Appendix B

List of publications

B.1 Articles published in peer-reviewed journals

1. Shariff, K.B, and Guillou, S.S. (2022). An empirical model accounting for added turbulence in the wake of a full-scale turbine in realistic tidal stream conditions. Applied Ocean Research (IF 3.761) https://doi.org/10.1016/j.apor.2022.103329.

B.2 Article submitted

1. Shariff, K.B, and Guillou, S.S. (2023). A generalized empirical model for velocity deficit and turbulent intensity in tidal turbine wake accounting for the effect of rotor diameter to depth ratio. Submitted to Renewable Energy (IF 8.634).

B.3 International conferences with proceedings

1. Shariff, K.B, and Guillou, S.S. (2023). A comparative study of power production using a generic empirical model in a tidal farm, 15th European Wave and Tidal Energy Conference Proceeding, Bilbao, 5-9 Sept. 2023.

B.4 National conferences with proceedings

1. Shariff, K.B, and Guillou, S.S. (2022). Developing an empirical model for added turbulence in a wake of tidal turbine. Congrès Français de Mécanique, Nantes 29 Aug - 02 Sept, 2022.

2. Shariff, K.B, and Guillou, S.S. (2022). An empirical wake model accounting for the velocity deficit and turbulence intensity in a simple tidal park, 18èmes Journées de l'Hydrodynamique, Poitiers, 22 - 24 Nov, 2022.

B.5 International conferences without proceedings

1. Emrsim2022: Simulation and Optimization for Marine Renewable Energies, Roscoff, 30 May - 2 June 2021, Presentation.
2. Seanergy, Paris, 20-21 June 2023, Poster.
3. Seanergy, Le Havre, 15-17 June 2022, Poster.

B.6 National conference without proceedings

1. Experimental and numerical methods for tidal turbines organized by IFREMER, Boulogne-sur-Mer 7-8 June, 2023.

B.7 Seminaires

1. GDR EOL-EMR/ Doctoriales ANCRE 2021, Paris, 25-26 Nov. 2021.
2. Journée des doctorants du LUSAC, Cherbourg, 19 Jan. 2023.
3. Journée Ecole Doctorale JED, Le Havre, 29 Oct. 2021, Poster.

Appendix C

Résumé étendu en français

C.1 Sur le besoin d'énergie

Avec l'augmentation de la demande, l'utilisation de combustibles fossiles conventionnels a considérablement augmenté les émissions de CO_2 et d'autres polluants nocifs contribuant au réchauffement de la planète. Aujourd'hui, près des deux tiers de l'électricité mondiale proviennent de combustibles fossiles. Parmi ceux-ci, environ 36 % de l'électricité mondiale est générée par le charbon, qui est à l'origine des émissions de CO_2 les plus élevées au monde. Un tiers de l'électricité mondiale provient de sources à faible teneur en carbone, à savoir les énergies renouvelables et l'énergie nucléaire. L'énergie renouvelable est définie comme l'énergie provenant de ressources qui peuvent être reconstituées au même rythme qu'elles sont utilisées. Les énergies renouvelables jouent un rôle crucial dans les transitions énergétiques propres et leur déploiement est l'un des principaux moyens de maintenir l'augmentation des températures moyennes mondiales en dessous de $1,5^oC$.

C.1.1 Énergie des marées

L'océan est vaste, couvrant 363 millions de kilomètres carrés, soit l'équivalent d'environ 72 % de la surface de la terre. Avec près de 2,4 milliards de personnes, soit 37 % de la population mondiale, vivant à moins de 100 kilomètres des côtes (UN, 2017), l'énergie marine représente une solution pratique pour lutter contre le changement climatique tout en contribuant à un avenir plus durable. Pour les nations dotées de territoires côtiers et océaniques, le développement et l'exploitation des énergies marines renouvelables constituent une contribution potentielle intéressante au bouquet d'énergies renouvelables visé.

Le potentiel théorique de toutes les technologies de l'énergie marine combinées va de 45 000 térawattheures (TWh) à bien plus de 130 000 TWh par an (IRENA, 2020). L'énergie hydrolienne est actuellement l'une des formes privilégiées d'énergie marine renouvelable car, en raison de l'origine astronomiques les force, elle est prévisible.

C.1.2 Énergie hydrolienne

Les turbines hydroliennes (TST pour Tidal Stream Turbine) utilisent directement l'énergie cinétique de la marée pour exploiter l'énergie. Les TST permettent à l'eau de passer à travers et autour d'elles et ne requièrent. Par conséquent, la vitesse locale de la marée, la turbulence, la bathymétrie, la profondeur, l'élévation des fonds marins, les réglementations locales en matière de navigation ainsi que les préoccupations associées aux poissons et aux mammifères marins, constituent des questions clés pour le développement des hydroliennes. La figure 1.8 présente différentes technologies d'exploitation de l'énergie hydrolienne avec différents niveaux de maturité technologique (TRL). Cependant, la technologie la plus prometteuse à ce jour est la turbine à axe horizontal. La préférence de l'industrie pour la turbine à axe horizontal résulte de la technologie mature des turbines éoliennes, de leur modèle économique et de leur haute efficacité. Comme le montre la figure 1.13, 13 des 16 hydroliennes sont des aux turbines à axe horizontal.

Cependant, pour la production d'énergie à l'échelle commerciale, on s'attend à ce que les TST soient disposées en parcs pour produire de l'électricité. Cela s'explique par la densité de puissance spatiale des les courants de marée. Une architecture en ferme de turbines peut réduire les coûts en partageant l'infrastructure et la maintenance collective, en réduisant les taux d'apprentissage et, en fin de compte, en minimisant le coût de l'énergie (Levelized cost of energy, LCOE). Cependant, l'interaction des turbines dans le parc due à leur sillage respectif affecte leurs performances.

C.1.3 Sillage de la turbine

L'étude de la turbine hydrolienne au sein d'une ferme a récemment suscité beaucoup d'intérêt dans la recherche et les applications industrielles. L'étude de l'interaction du sillage est d'une importance capitale pour optimiser l'énergie extraite dans une ferme de turbines hydroliennes. Le sillage est défini comme une région d'écoulement perturbé derrière la turbine qui affecte la production d'énergie de la turbine en aval. Les deux principales caractéristiques du sillage sont énumérées. La première est un **déficit de vitesse** significatif qui réduit la puissance extraite par la turbine en aval. Cette réduction de puissance dans un parc éolien peut être très importante et atteindre 20 % (Chamorro and Porté-Agel, 2009). La seconde est la **turbulence accrue** qui induit une charge de fatigue sur la pale de la turbine, ce qui peut sérieusement affecter la durée de vie des pales. Il est donc impératif d'étudier l'interaction des sillages afin d'optimiser la production d'énergie dans un parc. Le sillage derrière une turbine peut être classé en trois régions (Vermeer et al., 2003). Ces régions sont le sillage proche, le sillage intermédiaire et le sillage lointain. La caractéristique du sillage définit la limite de chaque région.

C.1.4 Revue des études en la matière

L'étude du sillage d'une turbine est largement axée sur l'estimation du déficit de vitesse car il affecte directement la puissance extraite par la turbine ($P \propto U^3$). De nombreuses études ont été menées pour étudier le sillage des turbines. Ces études sont divisées en trois catégories: les méthodes expérimentales, numériques et analytiques. Chacune de ces méthodes présente ses propres avantages et inconvénients.

L'industrie des TST a connu environ 54 % de déploiements réussis sur les 57 turbines TST de taille normale identifiées par Walker and Thies (2021). Cependant, une compréhension limitée du flux complexe des marées, associée à des coûts de déploiement et d'exploitation élevés, ainsi qu'un risque perçu entravent le développement des turbines à échelle 1. En outre, les quelques données disponibles sont pour la plupart confidentielles dans leur intégralité, ce qui entrave la recherche et le développement des TST. Pour cette raison, les chercheurs sont limités à des expériences à petite échelle qui ne couvrent pas la complexité et les échelles des courants de marée, mais qui fournissent des résultats significatifs dans l'étude du sillage de la TST. Comme nous l'avons vu, la petite configuration expérimentale pourrait permettre un contrôle suffisant du système pour étudier une caractéristique particulière du sillage. Cependant, la complexité des flux de marée très turbulents, associée à la variation soudaine de la profondeur, à l'effet des vagues et à la bathymétrie, ne peut pas être étudiée de manière efficace en utilisant un dispositif expérimental réduit. L'hydrodynamique complexe de l'écoulement est donc étudiée à l'aide de simulations numériques.

D'autre part, des modèles numériques de haute fidélité sont développés pour compléter les données expérimentales et fournir de bons résultats qui serviront de base à un modèle de turbine grandeur nature. Ces modèles CFD résolvent les équations de Navier-Stokes avec fermeture de la turbulence pour trouver la vitesse à chaque endroit du domaine. Les modèles numériques sont utilisés pour étudier les performances des turbines hydroliennes à échelle réduite et à échelle réelle. Plusieurs modèles numériques ont été développés, notamment le modèle résolu des pales et la méthode de la ligne d'actionnement, mais ils présentent des coûts de calcul élevés, en particulier pour les parcs d'éoliennes à grande échelle. Cependant, le modèle de disque d'action qui représente la turbine comme un milieu poreux reste la méthode la plus courante pour les grandes fermes éoliennes et hydroliennes en raison de son faible coût de calcul.

En outre, les chercheurs ont développé des modèles analytiques basés sur des relations théoriques simples en fonction de l'écoulement et de fonctions de forme pour estimer le sillage derrière une turbine. Les modèles analytiques, également appelés modèles cinématiques, sont basés sur les propriétés auto-similaires de l'écoulement. Ces modèles analytiques sont privilégiés pour estimer l'hydrodynamique des éoliennes, en particulier dans une grande ferme, en raison de leur faible coût de calcul (Crespo and Hernandez, 1996; Qian and Ishihara, 2021). Les modèles analytiques pour les éoliennes se sont développés au fil des ans et sont actuellement utilisés

dans des outils commerciaux tels que WindPRO, WindSim et OpenWind pour estimer la production d'énergie dans les parcs éoliens. Il convient de noter que ces modèles analytiques ne permettent principalement que la représentation de la vitesse moyenne sans tenir compte de l'effet de turbulence. Pour un modèle de turbine unique, l'effet du sillage de turbulence peut ne pas affecter la performance de la turbine, mais il peut affecter de manière significative la production d'énergie des turbines en aval dans un parc (Bai et al., 2013).

C.1.4.1 Turbulence dans le sillage de la turbine

Alors que le nombre et la précision des modèles analytiques permettant d'estimer le déficit de vitesse ont augmenté au cours des décennies, les techniques de quantification de la turbulence restent immatures. Les turbines d'une ferme fonctionnent dans la zone d'écoulement turbulent de la turbine en amont. Ces régions turbulentes sont associées à des contraintes de fatigue qui peuvent affecter à la fois l'intégrité structurelle et la production d'énergie des turbines du parc. Il est donc nécessaire de bien comprendre la turbulence de sillage. L'intensité de la turbulence dans le sillage de la turbine est exprimée par Quarton and Ainslie (1990) comme suit:

$$\mathrm{I_w} = \left(\mathrm{I_0^2} + \mathrm{I_+^2}\right)^{0.5} \tag{C.1}$$

La turbulence ambiante (I_0) est spécifique au site et peut varier au cours d'un cycle de marée (voir Fig. 1.10), tandis que la turbulence ajoutée (I_+) est la contribution du cisaillement et de la turbulence générée par la turbine (voir Tableau 1.3).

Certaines relations empiriques ont été développées pour estimer la turbulence ajoutée par les éoliennes. La relation de turbulence ajoutée rapportée par Quarton and Ainslie (1990) est exprimée comme une fonction de l'intensité de la turbulence ambiante, du coefficient de poussée et de la longueur du sillage proche proposée par Vermeulen (1980). Contrairement aux éoliennes, les turbines hydroliennes sont généralement situées dans des eaux peu profondes, limitées par la profondeur du canal. Par conséquent, l'utilisation d'un modèle d'éolienne peut conduire à des estimations inexactes. Peu de recherches ont été effectuées sur l'intensité turbulente ajoutée dans le sillage des hydroliennes.

C.1.5 Portée de la thèse

Pour soutenir le développement des la TST et faciliter sa commercialisation, on ne saurait trop insister sur la nécessité de disposer d'un modèle analytique efficace en termes de calcul. Cette thèse étudie le sillage lointain derrière une turbine hydrolienne à l'échelle d'un parc. Le but de cette thèse est de développer un modèle empirique générique pour estimer le déficit de vitesse et l'intensité de la turbulence dans le sillage d'une turbine hydrolienne, en tenant compte des variations de la

turbulence ambiante, du coefficient de poussée et du rapport diamètre/profondeur du rotor.

Les objectifs de la thèse sont les suivants:

- développement d'un modèle numérique d'une turbine hydrolienne en vraie grandeur.
- validation du modèle numérique à l'aide de données expérimentales de référence.
- développement d'un modèle empirique de turbulence ajoutée dans le sillage d'une turbine hydrolienne.
- développement d'un modèle générique de sillage de turbine hydrolienne pour la vitesse et l'intensité des turbulences dans des conditions réalistes.
- l'application du modèle générique dans les fermes hydroliennes en tenant compte de l'interaction entre la turbine et le sillage.

C.2 Méthodologie

En dynamique des fluides numérique (CFD), une représentation de la turbine du rotor est nécessaire. Les modèles numériques fournissent des solutions rentables avec des détails qui sont difficiles à mesurer expérimentalement. Différents modèles numériques ont été développés avec certaines limitations et hypothèses pour effectuer des tâches spécifiques. Un modèle numérique particulier est utilisé en fonction du domaine d'intérêt ou de la portée de l'étude. Nous avons répertorié quatre principaux types de modélisation: pale résolue, ligne d'action, RANS-BEM et disque d'action constant. Le modèle numérique de base pour les éoliennes et les turbines hydroliennes est illustré à la figure 2.2.

C.2.1 Théorie du disque d'action

Le rotor de la turbine est considéré comme un disque perméable idéal, c'est-à-dire sans frottement et sans composante de vitesse de rotation du sillage. En amont du disque, le tube d'écoulement a une section plus petite que le disque, et en aval, il a une section plus grande que le disque, comme le montre la figure 2.3. La conservation du bilan massique le long du tube d'écoulement est donnée par l'équation (C.2):

$$\rho A_\infty U_\infty = \rho A_D U_D = \rho A_w U_w \tag{C.2}$$

La force de poussée est obtenue par une chute de pression sur le rotor. Cette force de poussée T est causée par la chute de pression à travers le disque qui peut également être exprimée en termes de changement de quantité de mouvement donné dans l'Eq. (C.3):

$$T = (P_D^+ - P_D^-)A_D = (U_\infty - U_w)\rho A_D U_D \tag{C.3}$$

La puissance extraite du fluide est donnée par l'équation (C.4)

$$T = (P_D^+ - P_D^-)A_D = (U_\infty - U_w)\rho A_D U_D \tag{C.4}$$

Le coefficient de puissance C_P est défini comme le rapport entre la puissance extraite par le disque et la puissance disponible dans le flux, exprimé par l'équation (C.5).

$$C_p = \frac{Power}{\frac{1}{2}\rho A_D U_\infty^3} \tag{C.5}$$

C'est pourquoi,

$$C_P = 4a(1-a)^2$$

La valeur maximale de C_p est atteinte lorsque ;

$$\frac{\mathrm{d}C_P(a)}{\mathrm{d}a} = 0$$

Selon la limite de Betz, C_{Pmax} se produit à $a = 1/3$, d'où $C_{Pmax} = 16/27 = 0,593$ est le meilleur rendement théorique pour les éoliennes. Cependant, pour les turbines hydroliennes, la limite de Betz pourrait être dépassée en raison de l'impact de l'effet de blocage (Vennell, 2013).

La force exercée sur le disque d'action par la chute de pression, donnée par l'Eq. (2.12), peut également être adimensionnée pour donner un coefficient de force C_T comme suit:

$$C_T = \frac{Thrust}{\frac{1}{2}\rho A_D U_\infty^2} \tag{C.6a}$$

$$C_T = 4a(1-a) \tag{C.6b}$$

A la limite de Betz (a = 1/3), le coefficient de force C_{Tbetz} est de 0,89. La variation du coefficient de puissance et du coefficient de force en fonction de a est représentée sur la figure 2.4.

C.2.2 Modèle de disque d'action

Dans le modèle ADM, le rotor représenté par un disque dont la force de poussée T est répartie de façon homogène. Le disque d'action a le capacité à modéliser le sillage lointain à condition que l'effet de petite échelle soit paramétré (Blackmore et al., 2014). Le saut de pression à travers le disque fournit une force de poussée, une réduction de l'énergie cinétique et une réduction de la vitesse d'écoulement lorsque le fluide traverse le rotor. La force de poussée est calculée comme suit:

$$T = \frac{1}{2}\rho C_T A U_\infty^2 \tag{C.7}$$

La force de poussée T est ajoutée comme terme source dans les équations de Navier-Stokes incompressible pour tenir compte de l'extraction d'énergie par le disque d'action. Il est trivial d'obtenir la vitesse d'écoulement avec une seule turbine. Cependant, pour des turbines multiples dans une ferme, l'utilisation de la vitesse en amont est discutable en raison de l'effet de sillage, c'est pourquoi Taylor (1958) a proposé une expression pour le coefficient de résistance K, reliant la vitesse en amont et la vitesse locale d'un milieu poreux comme suit:

$$U_\infty = U_d(1 + \frac{1}{4}K) \tag{C.8}$$

Par conséquent, les coefficients de force et de puissance s'expriment comme suit:

$$C_T = \frac{K}{(1 + \frac{1}{4}K)^2}, \qquad C_P = \frac{K}{(1 + \frac{1}{4}K)^3} \tag{C.9}$$

La force de poussée modifiée du disque d'action est évaluée comme:

$$T = \frac{1}{2}\rho K A U_d^2 \tag{C.10}$$

C.2.3 Utilisation de la méthode du disque d'action dans OpenFOAM

Un domaine numérique rectangulaire simple est mis en place et discrétisé à l'aide du `BlockMesh` de base. Un test de maillage est effectué à différentes densités de maillage pour sélectionner le maillage optimisé, comme le montre la figure 2.7. La commande `actuationDiskSource` applique un terme source à l'équation de la quantité de mouvement pour permettre d'appliquer le disque d'action représentant la turbine. Le terme source introduit via *fvOptions dict* est appliqué aux cellules de volume définies dans *topoSets dict* en tant que terme puits pour l'extraction d'énergie.

Le solveur OpenFOAM utilisé dans la présente étude est `simpleFOAM`, qui convient aux écoulements incompressibles. Les équations ont été discrétisées à l'aide du schéma d'intégration `Gaussian` où les valeurs ont été interpolées des centres des cellules aux faces. Dans cette thèse, les modèles de turbulence aux moyennes de Reynolds (Reynolds-Averaged Navier Stokes, RANS) ne prennent en compte que l'écoulement moyen statistiquement moyenné dans le temps, car ils sont moins coûteux en termes de calcul et la différence entre les modèles est raisonnable dans la région du sillage lointain (Rethore et al., 2009). Nguyen et al. (2016) ont simulé une turbine hydrolienne avec différents modèles RANS et concluent que $\kappa - \epsilon$ fournit de bons résultats, en particulier dans le sillage lointain. Par conséquent, le

modèle de turbulence le modèle $\kappa - \epsilon$ est adopté dans cette thèse.

C.2.4 Validation du modèle

Les performances du dique d'action sont analysées à l'aide d'études expérimentales bien établies. La compréhension de l'interaction du sillage dans une turbine unique fournira des informations importantes sur les réseaux de turbines. Les cas de référence étudiés ici sont l'étude expérimentale du disque poreux rapportée par Bahaj et al. (2007) et l'essai en cannal flume d'une turbine hydrolienne à 3 pales étudiée par Mycek et al. (2014b).

Pour une expérience de disque poreux simple, le modèle standard $\kappa - \epsilon$ est capable de prédire les caractéristiques de l'écoulement sans l'utilisation d'un terme source, mais le terme source est nécessaire pour compenser la production de turbulence supplémentaire dans les expériences de turbine hydrolienne. En outre, les résultats expérimentaux des turbines hydroliennes ne sont pas vraiment axisymétriques comme indiqué par Maganga et al. (2010) et Mycek et al. (2014b). L'ADM ne détecte pas l'asymétrie car (a) la force est appliquée uniformément au disque, (b) il n'y a pas de représentation de la tour de la turbine dans le modèle du disque d'action, et (c) il n'y a pas d'effet de turbulence dû à la rotation de la turbine (Grondeau et al., 2022). Par conséquent, les caractéristiques moyennes du sillage sont modélisées à l'aide d'un model de RANS avec des paramètres de turbulence corrects lorsque le sillage lointain présente un intérêt.

Nous avons vu que les conditions ambiantes ont un effet significatif sur le taux de récupération. Pour une intensité de turbulence élevée, les conditions d'entrée ont été récupérées à 7 D en aval. Dans le cas d'une faible turbulence ambiante, les conditions d'entrée de l'expérience du disque poreux n'ont pas été rétablies avant 20 D en aval. Cela montre comment l'intensité de la turbulence peut affecter la récupération de l'écoulement dans le sillage de la turbine hydrolienne. Enfin, l'ADM peut être utilisé pour étudier le sillage lointain, ce qui est l'objet de cette thèse. Ainsi, ce modèle numérique constituera la base du modèle TST à grande échelle. Un certain configuration de parcs de turbines seront simulés pour différentes configurations d'un site idéal de Raz Blanchard. Ce modèle servira de référence pour la comparaison avec le modèle analytique proposé.

C.3 Modèle de turbulence supplémentaire

Bien que l'estimation du déficit de vitesse et de la production d'énergie dans les parcs de turbines ait fait l'objet de recherches considérables, peu de travaux ont été consacrés à l'estimation de l'intensité de la turbulence dans le sillage des turbines hydroliennes. Les turbulences dans le sillage des turbines sont associées à une fatigue accrue et à une réduction de la production d'énergie, ce qui peut entraîner une défaillance prématurée des turbines.

C.3.1 Turbulence dans le sillage des turbines

L'intensité turbulente est définie comme un rapport entre l'écart-type (σ) ou la fluctuation de la vitesse turbulente ($\overline{u'}$) et la vitesse moyenne ($\overline{U}$), exprimée par l'équation suivante (C.11):

$$\mathrm{I} = \frac{\sigma_{\mathrm{u}}}{\mathrm{U}} = \frac{\sqrt{\overline{u'u'}}}{\overline{U}} \tag{C.11}$$

La turbulence dans le sillage de la turbine est la contribution de la turbulence ambiante et de la turbulence ajoutée générée par la turbine. La turbulence dans le sillage de la turbine est exprimée par l'équation (C.12):

$$\mathrm{I}_{\mathrm{wake}} = \left(\mathrm{I}_0^2 + \mathrm{I}_+^2\right)^{0.5} \tag{C.12}$$

où I_{wake} est la turbulence totale dans le sillage, I_0 est la turbulence ambiante et I_+ est la turbulence ajoutée par le rotor.

Une caractéristique commune du modèle (Quarton and Ainslie, 1990; Crespo and Hernandez, 1996; Frandsen, 2007; Ishihara and Qian, 2018; Tian et al., 2015) est que la turbulence ajoutée est une fonction de la turbulence ambiante, des caractéristiques de la turbine C_T dans le sillage de l'éolienne et de l'emplacement en aval. Cependant, ces modèles de turbulence, comme les modèles de déficit de vitesse, peuvent nécessiter une calibration pour une application dans le sillage des turbines hydroliennes. L'étalonnage est nécessaire en raison de la profondeur limitée dans les eaux peu profondes, de l'effet de blocage, de la large gamme de turbulences ambiantes dans les sites à marée.

À notre connaissance, il n'existe pas de modèle empirique permettant d'estimer l'intensité des turbulences dans le sillage d'une turbine hydrolienne. Dans les sections suivantes, un modèle empirique simple pour l'intensité de turbulence ajoutée dans le sillage d'une turbine hydrolienne à échelle réelle est développé et comparé aux modèles établis pour les turbines éoliennes mentionnés ci-dessus. Comme les données expérimentales des turbines hydroliennes grandeur nature restent confidentielles, un modèle numérique est proposé pour fournir des données de référence pour le modèle de turbulence.

C.3.2 Analyse du sillage turbulent

La figure 3.3 montre le contour de l'intensité turbulente des sillages de turbine à différentes turbulences ambiantes. L'intensité turbulente maximale dans le sillage se produit dans le sillage initial proche. Le sillage initial proche est la région située derrière la turbine, où le saut de pression dû à l'extraction de la quantité de mouvement est largement récupéré.

Dans le sillage lointain, l'effet de la turbine et le cisaillement moyen sont faibles par rapport au sillage proche. Le profil gaussien se maintient dans le cas d'une faible turbulence ($I_0 = 5$ %) mais disparaît dans les cas de forte turbulence (voir

la figure 3.3). Les effets turbulents disparaissent rapidement en cas de forte turbulence en raison d'un mélange important. L'intensité turbulente le long de l'axe du rotor et de la paroi latérale est imperceptible, ce qui confirme la prédominance de la turbulence ambiante dans la région du sillage lointain. Une forte turbulence produit de grandes échelles de turbulence qui cascadent et s'atténuent plus rapidement que les petits tourbillons. Une récupération plus rapide de l'écoulement en cas de forte turbulence ambiante est signalée dans les expériences (Mycek et al., 2014a; Vinod and Banerjee, 2019).

C.3.2.1 Estimation de la turbulence ajoutée à l'axe central

La turbulence de la ligne médiane est la turbulence totale dans le sillage, comme l'exprime l'équation (C.12). La turbulence ajoutée dans le sillage est extraite en soustrayant la racine de la somme des carrés de la turbulence de sillage à la ligne centrale et de la turbulence ambiante près de la paroi latérale. L'intensité turbulente à proximité de la surface latérale est supposée à l'état ambiant car elle est éloignée du rotor, comme le montre la figure 3.4. En supposant que la turbulence ambiante stable dans l'écoulement. Il suffit de proposer un modèle pour la turbulence ajoutée afin d'estimer la turbulence dans le sillage.

C.3.2.2 Estimation du rayon de sillage de l'intensité turbulente

Le rayon du sillage turbulent ajouté est estimé à l'aide de l'approche pleine largeur et demi-maximum (FWHM) d'un profil gaussien standard. L'intensité turbulente à la FWHM est égale à $\sqrt{2\ln 2}\sigma$ (où σ est l'écart-type). Le FWHM est précédemment utilisé pour définir le rayon dans le sillage de déficit de vitesse d'une éolienne (Bastankhah and Porté-Agel, 2014; Ishihara and Qian, 2018). $r_{1/2}$ est le rayon à la moitié de l'intensité de turbulence normalisée I_m. Le rayon du sillage utilisant la fonction de distribution gaussienne est estimé à 3σ, représenté par la région ombrée dans la figure 3.6.

Le rayon de sillage turbulent supplémentaire est calculé à un intervalle de 1 D. La figure 3.7a montre une configuration similaire du rayon de sillage à différentes intensités de turbulence. La figure 3.7a montre clairement que l'utilisation de l'hypothèse linéaire de base de l'expansion du sillage par Jensen et Bastankhah and Porté-Agel conduit à une mauvaise estimation de l'évolution du rayon du sillage turbulent supplémentaire. En prenant le logarithme des deux côtés de l'éq. (3.9), nous voyons que la distribution de la loi de puissance est simplifiée comme; $\ln p(x) = \alpha \ln x +$ constante. La figure 3.7b montre que l'on peut être sûr que le rayon suit approximativement la distribution en loi de puissance.

C.3.3 Nouveau modèle empirique

C.3.3.1 Modèle de rayon de sillage turbulent

L'utilisation de la loi de puissance comme équation modèle permet une bonne évolution du rayon. Le rayon empirique du sillage turbulent est valable jusqu'à la longueur du sillage turbulent, comme le montre la figure 3.8, et s'exprime sous la forme de l'équation suivante (C.13):

$$r_w^* = r/r_o = 7.41 I_0^{0.3} \left(\frac{x}{D}\right)^{0.384} \tag{C.13}$$

C.3.3.2 Modèle d'intensité turbulente ajoutée

Le profil d'intensité turbulente de la ligne médiane de la figure 3.5b montre une diminution de l'intensité turbulente ajoutée en aval. Le nouveau modèle d'intensité turbulente ajoutée à la ligne médiane est exprimé par l'équation suivante (C.14):

$$I_+ = a\left(\frac{X - X_0}{D}\right)^{-b} \qquad \begin{cases} a = 0.16 C_T^{4.83} + 0.179 \\ b = 0.68 I_0 + 0.472 \end{cases} \tag{C.14}$$

Le sillage de la turbine est reconstruit à l'aide de l'Eq. (3.2), le modèle proposé estime le sillage d'intensité de turbulence à différentes intensités turbulentes ambiantes, comme le montrent les figures 3.10. En outre, le modèle proposé est validé par l'expérience de la turbine hydrolienne de Mycek et al. (2014b) et les simulations LES de Grondeau et al. (2022) avec des résultats acceptables dans le sillage lointain, comme le montre la figure 3.11.

C.4 Un modèle générique pour le déficit de vitesse et l'intensité turbulente

La vitesse d'écoulement et l'intensité turbulente lors du mélange avec l'écoulement ambiant se rétablissent progressivement à mesure que l'on se déplace dans la direction de l'écoulement, comme l'illustre la figure 4.1. Pour obtenir une bonne estimation des turbines individuelles, il est nécessaire de disposer d'un modèle de sillage approprié permettant d'obtenir deux facteurs principaux: la fonction d'écoulement et la fonction de forme. Le déficit de vitesse dans le sillage de la turbine est exprimé par l'équation suivante (C.15):

$$\frac{\Delta U}{U_\infty} = \frac{U_\infty - U_w}{U_\infty} \tag{C.15}$$

où U_∞ est la vitesse en amont et U_w est la vitesse de sillage. Le tableau 4.1 présente un résumé des modèles de déficit de vitesse existants avec le modèle proposé.

Dans cette thèse, de multiples scénarios réalistes sont envisagés pour développer un modèle générique applicable à différentes turbulences ambiantes, au coefficient de poussée du rotor et à une gamme de rapports diamètre/profondeur du rotor. Le modèle proposé est basé sur le principe de conservation de la masse de Jensen. Le modèle de turbulence ajouté développé dans la section précédente (Shariff and Guillou, 2022a) est pris en compte dans l'évaluation du déficit de vitesse par le biais de la relation non linéaire du rayon de sillage. Une fonction de forme gaussienne est utilisée pour estimer le profil du sillage dans la direction latérale.

C.4.1 Modèle numérique

Une turbine à échelle réelle est située à 10 D (D est le diamètre de la turbine) de l'entrée, la longueur du domaine est de 50 D, la largeur du canal est de 20 D et quatre profondeurs de canal (H) sont considérées ; 10 m, 25 m, 35 m et 50 m représentant la profondeur du site de la turbine hydrolienne comme indiqué dans le tableau 1.2. Par souci de simplicité, les trois cas sont désignés par DH20, DH40 et DH60, représentant le rapport diamètre-profondeur de 20 %, 40 % et 60 % respectivement. La figure 4.3 montre les différents rapports diamètre-profondeur des trois configurations.

C.4.1.1 Effet du rapport diamètre-profondeur (DH) du rotor

Le rapport DH est la fraction du diamètre du rotor qui couvre la profondeur du canal. La récupération du sillage du rotor est affectée par le flux de contournement. Lorsque le rapport diamètre/profondeur du rotor est faible (c'est-à-dire DH20), le processus de rétablissement du sillage est plus rapide car le flux dans la zone de contournement est suffisant pour provoquer un mélange entre la faible vitesse au cœur du rotor et le flux ambiant dans la zone de contournement. En revanche, lorsque le rapport DH est élevé (DH60), le déficit de vitesse le long du rotor est important par rapport à l'écoulement libre dans la zone de contournement, ce qui retarde le rétablissement du sillage par rapport à l'état en amont.

C.4.2 Modèle empirique générique

Pour proposer un modèle générique, l'intensité turbulente ambiante de 5%, 10%, 15% et 20% est considérée respectivement, fournissant une représentation globale de la turbulence sur les sites potentiels de marée (voir le tableau 1.2). De même, un ensemble de coefficients de poussée de turbine C_T permettant l'application à différentes configurations évaluées à l'aide de l'Eq. (2.20) est présenté dans le tableau 4.4.

C.4.2.1 Modèle d'intensité turbulente

Le modèle de turbulence générique est exprimé par les équations suivantes (C.16):

$$I_{eff} = \sqrt{I_0^2 + I_+^2} \tag{C.16}$$

$$I_+ = a\left(\frac{X - X_0}{D}\right)^{-b} \times \exp\left(-\frac{(y_0 - y)^2 + (z_0 - z)^2\Big)}{r_w^2}\right) \tag{C.17}$$

$$\mathrm{a} = 0.407\left(\frac{D}{H}\right)C_T^{4.83} + 0.179, \quad b = 0.681 I_0 + 0.472$$

$$r_w = c\left(\frac{X - X_0}{D}\right)^{d} \tag{C.18}$$

$$\begin{aligned} c &= 2.7\left(\tfrac{D}{H}\right)^{-0.257}, & d &= 0.34 && \text{pour } 5\% \le I_0 < 10\%; \\ c &= 3.0 + 1.5 I_{eff} \cdot \left(\tfrac{D}{H}\right)^{-1.32}, & d &= 0.352\left(\tfrac{D}{H}\right)^{-0.145} && \text{pour } 10\% \le I_0 < 20\% \end{aligned}$$

La figure 4.7 montre que le modèle fournit des résultats raisonnables par rapport aux données expérimentales, en particulier dans la région du sillage lointain.

C.4.2.2 Modèle de déficit de vitesse

Dans le présent modèle, nous proposons d'utiliser directement un modèle gaussien et d'estimer directement le déficit de vitesse dans le sillage sans utiliser de coefficient de correction. Le déficit de vitesse Jensen-Gaussien modifié s'exprime donc comme suit: Eq. (C.19):

$$\frac{\Delta U}{U_\infty} = \left[\frac{\left(1 - \sqrt{1 - C_T}\right)}{\left(\frac{r_w}{r_0}\right)^2}\right] \times \exp\left(-\frac{(y_0 - y)^2 + (z_0 - z)^2)}{r_w^2}\right) \tag{C.19}$$

Le rayon de sillage empirique basé sur la loi de puissance est exprimé par l'équation suivante (C.20):

$$r_w = e\left(\frac{X - X_0}{D}\right)^{f} \tag{C.20}$$

$$\begin{aligned} e &= 2.15\left(\tfrac{D}{H}\right)^{-0.283}, & f &= 0.29 && \text{for } 5\ \% \le I_0 < 10\%; \\ e &= 2.36 + 1.834\tfrac{I_{eff}}{D/H}, & f &= 0.27\left(\tfrac{D}{H}\right)^{-0.275} && \text{for } 10\ \% \le I_0 < 20\% \end{aligned}$$

Le modèle de déficit de vitesse proposé est comparé à l'expérience de la turbine hydrolienne de Stallard et al. (2013) et Mycek et al. (2014a). Comme le montre la figure 4.11, le modèle est en bon accord avec les données expérimentales dans la région du sillage lointain. Cependant, le modèle est moins précis dans le sillage proche, ce qui constitue une limitation de l'ADM.

C.4.3 Analyse

L'effet du rapport DH à $C_T = 0{,}89$ et 10 % d'intensité de turbulence est présenté à la figure 4.12. La vitesse normalisée est considérablement affectée par le rapport DH en raison de l'expansion du sillage, mais la variation de l'intensité turbulente à différents rapports DH est minime. Le rétablissement de l'écoulement à une DH élevée est moindre en raison du faible mélange entre l'écoulement à faible vitesse au cœur du rotor et l'écoulement de dérivation à grande vitesse.

De même, la figure 4.14 présente la vitesse normalisée et l'intensité turbulente à DH40 et C_T de 0,89 à différentes turbulences ambiantes. Le déficit de vitesse et la récupération de l'intensité de la turbulence sont plus rapides lorsque la turbulence ambiante est élevée. La turbulence dans le sillage se rétablit en 15 D et 9 D pour une turbulence de 10 % et 15 % respectivement. La vitesse normalisée se rétablit de plus de 90 %. Ce rétablissement est plus rapide lorsque la turbulence ambiante est élevée.

En outre, l'effet du coefficient de poussée pour une turbulence ambiante de 10 % est illustré à la figure 4.16. Une augmentation de C_T peut également être interprétée comme une augmentation de la force de traînée qui provoque l'échange de quantité de mouvement à travers le disque. Un C_T élevé crée un déficit de vitesse important à proximité du rotor, ce qui produit une forte turbulence dans le sillage proche. L'augmentation du coefficient de poussée est largement efficace dans la région du sillage proche. Cette variation due au coefficient de poussée est bien représentée par le modèle proposé dans le sillage proche. Cependant, loin du rotor, l'effet de C_T est moins important car l'écoulement est largement homogène, ce qui permet d'atteindre l'état de récupération.

C.5 Ferme hydrolienne

L'étape suivante vers la commercialisation est l'étude de l'interaction du sillage de la turbine dans la ferme hydrolienne, comme le montre la figure 5.1. Le sillage induit sur la turbine hydrolienne en aval peut réduire la puissance de sortie, affectant ainsi l'efficacité globale de la ferme hydrolienne.

C.5.1 Interaction de sillage dans une ferme hydrolienne

Pour estimer efficacement le sillage des turbines dans une ferme hydrolienne, le modèle analytique doit tenir compte de l'interaction du sillage de plusieurs turbines. Pour ce faire, les modèles à turbine unique utilisent le principe de superposition pour estimer l'effet combiné des sillages qui se chevauchent dans le parc. Il existe fondamentalement trois types d'interaction de sillage dans les fermes hydroliennes: le chevauchement total (ou tandem), le chevauchement partiel et l'absence d'interaction, comme le montre la figure 5.2. Cependant, une turbine peut être affectée par un sillage mixte dans la ferme.

Afin de combiner l'interaction cumulative du sillage sur la turbine en aval, différentes méthodes de superposition ont été proposées dans la littérature pour estimer l'interaction sillage-turbine. Dans cette étude, nous travaillons sur l'énergie cinétique et la turbulence pour en déduire la vitesse et la turbulence dans le sillage.

C.5.2 Description du modèle générique d'une ferme hydrolienne

Pour une application dans une ferme hydrolienne, l'interaction du sillage entre les turbines est évaluée à l'aide d'une relation trigonométrique et estimée en superposant l'effet d'interaction du sillage pour évaluer le déficit de vitesse et l'intensité de la turbulence dans une ferme hydrolienne. Le déficit de vitesse générique et l'intensité des turbulences dans la ferme hydrolienne sont exprimés dans le systèmes de relations (C.21). La figure 5.4 décrit l'organigramme du modèle empirique générique.

$$\begin{aligned} \left(1-\frac{u_j}{U}\right)^2 &= \sum_{ij=1}^{n}\left(1-\frac{u_{ij}}{U}\right)^2\frac{A_{overlap}}{A_0} \\ I_{eff} &= I_0^2 + I_{+,j}^2 \\ I_{+,j}^2 &= \sum_{ij=1}^{n}\left(a\left(\frac{X_{ij}-X_i}{D}\right)^{-b}\right)^2\frac{A_{overlap}}{A_0} \end{aligned} \tag{C.21}$$

où $A_{overlap}$ est la zone de chevauchement entre la zone de sillage élargie A_w de la turbine en amont et la zone balayée du rotor en aval A_0 dans l'équation (5.4).

C.5.3 Analyse

C.5.3.1 Réseau de turbines en configuration tandem

Une ferme hydrolienne simple comprenant quatre turbines en configuration en ligne est étudiée. Le rapport diamètre/profondeur (DH) du rotor est de 20 % dans le réseau simple. La turbulence ambiante utilisée dans ce cas est de 10 %, tandis que le coefficient de poussée de Betz $C_{T,Betz}$ est utilisé tout au long de ce chapitre, sauf indication contraire. L'effet de sillage est plus important lorsque l'espacement des turbines S_x est faible, ce qui entraîne une augmentation de l'intensité de la turbulence entrante de la turbine en aval. Le contour de la figure 5.6 montre que lorsque l'espacement des turbines double, le sillage se rétablit en grande partie en amont, ce qui permet aux turbines en aval d'extraire une plus grande puissance.

C.5.3.2 Production d'énergie dans différentes configurations de réseau

La puissance produite par une turbine est calculée comme suit Eq. C.22:

$$P_i = \frac{1}{2}\rho C_p A U_i^3 \tag{C.22}$$

Les deux configurations de base de la ferme hydrolienne, rectiligne et en quinconce, avec des turbines de 20 m de diamètre à DH40 sont analysées. La ferme comprenant N turbines ($N = 16$) dans un canal idéal est illustrée dans la figure 5.8. L'espacement des turbines est respectivement de $S_x = 7D$ et $S_y = 4D$ afin d'assurer la récupération du flux et de bénéficier de l'accélération du flux provenant des turbines en amont.

La puissance cumulée produite par N turbines dans la ferme est évaluée par Eq. (C.23):

$$P_{farm} = \sum_{j=i}^{N} P_i \tag{C.23}$$

La puissance totale produite dans la ferme rectiligne et la ferme en quinconce est respectivement de 22,1 MW et de 28,1 MW. Pour une taille de ferme identique, cette étude montre que le réseau en quinconce produit une puissance supérieure de 6 MW à la configuration rectiligne. Ceci est cohérent avec les études précédentes sur les fermes hydroliennes (Bai et al., 2013; Nguyen et al., 2019; Djama Dirieh et al., 2022). L'effet de turbulence ajouté est plus important dans la configuration rectiligne présentée dans la figure 5.12. Les résultats montrent que l'effet de turbulence ajouté est significatif dans un réseau rectiligne en raison de l'espacement limité entre le turbine. La turbulence additionnelle à la turbine aval est presque négligeable dans le cas d'une ferme en quinconce en raison de l'espacement suffisant entre les turbines. Le rendement de la ferme η_{farm} est défini comme le rapport entre la puissance totale produite par toutes les turbines d'une ferme P_{farm} et la puissance maximale P_{farm}^{max} si elles fonctionnent dans des conditions non perturbées.

$$\eta_{farm} = \frac{P_{farm}}{P_{farm}^{max}}$$

Les rendements de l'exploitation pour placement rectiligne et l'organisation réseau en quinconce sont respectivement de 69,1 % et 87,8 %. Cette augmentation de l'efficacité est uniquement due à la configuration de la turbine dans la ferme.

C.5.3.3 Effet du rapport DH du rotor dans la ferme hydrolienne

La figure 5.15 montre qu'à un faible rapport diamètre/profondeur du rotor, l'expansion du sillage est plus importante et l'interaction plus forte. La puissance produite par la turbine en aval diminue avec l'augmentation du rapport DH, comme le montre la figure 5.16. La puissance totale P_{farm} à DH20, DH40 et DH60 est respectivement de 29,8 MW, 28,1 MW et 26,9 MW. Ceci implique que pour une taille de turbine identique, la puissance extraite peut varier en fonction du rapport diamètre/profondeur du canal.

C.5.3.4 Effet de la turbulence ambiante sur la ferme hydrolienne

Dans ce cas, nous avons étudié une ferme rectiligne à DH40 avec un espacement inter-dispositifs $S_x = 7D$ comme présenté dans la section 5.3.2 pour des taux de turbulence ambiante de 5%, 10%, 15%, et 20%. La puissance extraite par les différentes turbines de la rangée est présentée dans la figure 5.18. Les résultats indiquent une diminution de la puissance en raison de l'effet de sillage cumulatif le long des turbines en ligne. La puissance produite par la turbine en amont est identique pour toutes les turbulences ambiantes car le flux entrant pour la turbine en amont est stable et n'est affecté par aucune perturbation du flux. De même, la production d'énergie est identique pour chaque rangée à une turbulence ambiante donnée. La diminution continue de la puissance pour les turbines en ligne d'une rangée à une turbulence ambiante donnée résulte de l'effet de sillage. Toutefois, lorsque la turbulence ambiante est plus élevée, la récupération du sillage est plus rapide, ce qui permet de produire une puissance relativement plus élevée, comme le montre le tableau A.2.

C.5.3.5 Effet de C_T sur un réseau rectiligne

Nous considérons une ferme hydrolienne rectiligne composée de 16 turbines avec 4 turbines dans chaque rangée comme indiqué dans la figure fig:Cteffpow. Le coefficient de poussée de chaque turbine du parc est présenté dans la tableau 5.2.

La figure 5.20a indique la puissance produite par la turbine présentée dans la tableau 5.2. La puissance totale produite dans la rangée de turbines est comparable. La turbine en amont T_1 produit la puissance la plus élevée car elle n'est pas affectée par le sillage de la turbine en amont. La turbine T_1 dans Row_1 avec le C_T le plus élevé produit la puissance maximale tandis que la turbine dans Row_3 avec le C_T minimum produit la puissance la plus faible comme le montre la tableau5.2. La figure 5.20b montre que la stratégie recommandée dans la ferme hydrolienne consiste à disposer les turbines avec un coefficient de poussée croissant (c'est-à-dire Row_4). Cependant, l'augmentation globale de la puissance due à la variation du coefficient de poussée est limitée dans un petit parc. Cet effet peut être significatif dans un grand parc et doit donc être pris en compte dans l'optimisation de la ferme hydrolienne.

C.6 Conclusions et perspectives

Cette thèse porte sur le développement d'un modèle d'ordre réduit calculatoire pour estimer le déficit de vitesse et l'intensité turbulente d'une turbine hydrolienne à axe horizontal dans une ferme hydrolienne. L'objectif principal de ce travail est de développer un modèle générique pour estimer la production d'énergie dans les fermes hydroliennes. Dans cette thèse, nous avons proposé potentiellement le premier modèle d'intensité de turbulence pour les turbines hydroliennes à axe horizontal et établi une nouvelle relation pour le rapport diamètre-profondeur du rotor.

Ce modèle de turbulence ainsi que le modèle Jensen-Gaussien modifié peuvent être utilisés pour fournir un aperçu préliminaire de la production d'énergie dans les fermes hydroliennes. L'efficacité d'une ferme hydrolienne peut être augmentée par une intensité de turbulence ambiante élevée, un espacement suffisant entre les turbines et un faible rapport diamètre-profondeur. Ce modèle peu consomateur de ressources informatiques peut être utile pour étudier l'interaction du sillage des parcs de turbines hydroliennes dans différentes configurations. L'applicabilité du modèle sur une large plage le rend utile dans des sites hydrolien réalistes dans des conditions idéales.

C.6.1 Perspectives

Premièrement, les données numériques peuvent être améliorées en utilisant une approche de modélisation de la turbulence plus précise telle que le modèle LES-ALM. Deuxièmement, les modèles empiriques sont basés sur des approximations qui entraînent une grande marge d'erreur. Des valeurs plus précises peuvent être obtenues en utilisant l'apprentissage automatique tel que le réseau neuronal artificiel (ANN) pour les paramètres de rayon de sillage, de déficit de vitesse et d'intensité turbulente. Troisièmement, le modèle est développé sur la base d'une vitesse d'entrée constante dans la ferme. L'étude de l'applicabilité de l'écoulement variable dans le temps sera utile pour valider le modèle. Enfin, le sillage du déficit de vitesse et de l'intensité de la turbulence dépend d'un certain nombre de paramètres. Par conséquent, un algorithme d'optimisation de fonction multi-objectif comme l'optimisation par essaims de particules (PSO) est nécessaire pour le placement des turbines afin de maximiser la production d'énergie dans les fermes hydroliennes.

Titre: Développment d'un modèle générique d'optimisation de la production d'énergie d'un parc d'hydroliennes.

Mots clés: parc d'hydroliennes, modèle empirique, disque d'action, turbulence, puissance.

Résumé: L'industrie de l'énergie des courants de marée a réussi à déployer et à tester des turbines à courant de marée (Tidal Stream Turbine,TST) en grandeur réelle sur des sites d'essai dédiés, avec des unités individuelles atteignant jusqu'à 1 MW de puissance. L'étape suivante vers la commercialisation est l'étude de l'effet de sillage de la turbine et de l'interaction des hydroliennes au sein d'une ferme (ou parc) d'hydroliennes.
Dans cette thèse, nous avons proposé potentiellement le premier modèle empirique pour estimer la turbulence ajoutée dans le sillage de la turbine d'hydroliennes. En utilisant ce modèle, la turbulence effective est générée et utilisée pour estimer le déficit de vitesse dans le sillage de la turbine. Ce modèle de déficit de vitesse utilise l'approche Jensen-Gaussienne pour les fonctions de flux et de forme. En outre, le modèle est appliqué à une ferme hydrolienne simple pour estimer le déficit de vitesse et l'intensité de la turbulence. Un principe de superposition est choisi pour évaluer l'interaction des sillages au sein de cette ferme.
Comme les courants de marée en eaux peu profondes sont spécifiques aux sites, le modèle est généralisé pour prendre en compte la variation de la turbulence ambiante, le coefficient de poussée du rotor et le rapport diamètre-profondeur dans différentes conditions hydrodynamiques réalistes du site de marée dans un cas idéal. Le modèle est valable pour des TST réalistes en eaux peu profondes avec un coefficient de poussée allant de 0,64 - 0,98 et une turbulence ambiante de 5 - 20% dans un canal avec un rapport diamètre/profondeur du rotor de 20 - 60%.
Profitant de la disposition des turbines, l'arrangement en quinconce produit plus d'énergie que l'arrangement rectiligne dans les mêmes conditions. L'augmentation de la puissance est attribuée à une récupération suffisante du sillage dans la première configuration. La comparaison avec différents espacements de turbines a montré que les arrangments rectiligne et en quinconce peuvent bénéficier d'un espacement latéral et longitudinal réduit sans affecter l'efficacité de la ferme. Les résultats obtenus montrent également qu'en eaux peu profondes, la profondeur du canal peut affecter la production d'énergie globale d'une ferme. Une augmentation de la puissance est observée pour un faible rapport diamètre-profondeur, ce qui résulte d'une expansion suffisante du sillage pour ce rapport. Dans les fermes, l'efficacité peut être améliorée en augmentant la turbulence ambiante, en espaçant suffisamment les turbines et en ayant un faible rapport diamètre/profondeur. Ce modèle générique, quoique améliorable, permet de donner un bon aperçu de la production d'énergie produite par une ferme d'hydroliennes pour différentes conditions avant un approfondissement avec par exemple des simulations à haute résolution.

Title: Development of a generic analytical model for optimizing the electricity production of a tidal turbine park.

Keywords: Tidal farm, empirical model, actuator disk, turbulence, power.

Abstract: The tidal energy industry has recorded successful deployment and testing of full-scale Tidal Stream Turbines (TST) at dedicated test sites with single units reaching up to 1 MW output. The next step towards commercialization is the investigation of the turbine wake effect turbine interaction in the tidal array.
In this thesis, we proposed potentially the first empirical model to estimate the added turbulence in tidal turbine wake. Using this model, effective turbulence is generated and used to estimate the velocity deficit in the turbine wake. This velocity deficit model uses the Jensen-Gaussian approach for the stream and shape functions. Further, the model is applied in a simple tidal farm to estimate the velocity deficit and turbulence intensity. A superposition principle is chosen to evaluate the wake interaction in the tidal farm.
As the tidal flows in shallow water are site-specific, the model is generalized to take into account the variation in ambient turbulence, rotor thrust coefficient, and the diameter-to-depth ratio at different realistic tidal site hydrodynamic conditions in an ideal case. The model is valid for realistic TST in shallow water with a thrust coefficient ranging from 0.64 - 0.98 and ambient turbulence of 5 - 20% in a channel with a rotor diameter to depth ratio of 20 - 60%.
Profiting from the turbine arrangement, the staggered array produces higher than the rectilinear array under the same condition. The increase in power is attributed to sufficient wake recovery in the former configuration. The comparison with different turbine spacing has shown that the rectilinear and staggered array can benefit from reduced lateral and longitudinal spacing without affecting the efficiency of the farm. Also, the result obtained shows that in shallow water, the channel depth can affect the overall power production in a farm. An increase in power is observed at a low diameter-to-depth ratio, this results from sufficient wake expansion at a low rotor diameter-to-depth ratio. In tidal farms, it is noted that the efficiency can be improved by increased ambient turbulence, sufficient turbine spacing, and a low diameter-to-depth ratio. This generic model can provide insight into the power production in tidal farms under different conditions before high-fidelity numerical simulations.

Kabir Bashir Shariff
Université de Caen Normandie
Laboratoire Universitaire des Sciences Appliquées de Cherbourg (LUSAC)
60, rue Max-Pol Fouchet 50130 Cherbourg-en-Cotentin.